UNIVERSITY OF LEEDS

Design of novel integrated cathodes in electro-Fenton processes for organic contaminant and microplastic degradation in aquatic environments

Qian Ye

Submitted in accordance with the requirements for the degree of Doctor of Philosophy

University of Leeds
School of Civil Engineering
School of Chemical and Process Engineering
Supervisors: Prof. Martin R. Tillotson & Dr. Timothy N. Hunter
Date of registration: 01/10/2021
Date of submission: 20/03/2025

Intellectual property and publication statements

I confirm that the work submitted is my own, except where work that has formed part of jointly authored publications has been included. My contribution and that of the other authors to this work have been explicitly indicated below. I confirm that appropriate credit has been given within the thesis where reference has been made to the work of others.

The work in Chapter 3 of this thesis has been published as follows:
Qian Ye, Timothy N. Hunter*, Hao Xu, David Harbottle, Girish M. Kale, Martin R. Tillotson*. Synergistic effect of Fe and Ni on carbon aerogel for enhanced oxygen reduction and H_2O_2 activation in electro-Fenton process. Separation and Purification Technology. Volume 353, Part B, 2025, 128436.

The authorship contributions are:
Qian Ye: Writing – original draft, visualisation, investigation, formal analysis, conceptualisation. Timothy N. Hunter: writing – review & editing, supervision, resources, methodology, conceptualisation. Hao Xu: writing – review & editing, methodology. David Harbottle: writing – review & editing, resources. Girish M. Kale: writing – review & editing, resources. Martin R. Tillotson: writing – review & editing, supervision, resources, methodology, conceptualisation.

The work in Chapter 4 of this thesis has been published as follows:
Qian Ye, Timothy N. Hunter*, Hao Xu, David Harbottle, Girish M. Kale, Martin R. Tillotson*. CuCo carbon aerogel as a bifunctional cathode for Electro-Fenton processes: Unveiling synergistic effects and catalytic mechanisms. Separation and Purification Technology. Volume 361, Part 3, 2025, 131597.

The authorship contributions are:
Qian Ye: Writing – original draft, visualisation, investigation, formal analysis, conceptualisation. Timothy N. Hunter: writing – review & editing, supervision, resources, methodology, conceptualisation. Hao Xu: writing – review & editing, methodology. David Harbottle: writing – review & editing, resources. Girish M. Kale: writing – review & editing, resources. Martin R. Tillotson: writing – review &

editing, supervision, resources, methodology, conceptualisation.

The work in Chapter 5 of this thesis has been submitted as follows:
Qian Ye, Hao Xu, Timothy N. Hunter*, David Harbottle, Girish M. Kale, Martin R. Tillotson*. Advanced polystyrene nanoplastic remediation through electro-Fenton process: degradation mechanisms and pathways. Submitted to journal.

The authorship contributions are expected to be:
Qian Ye: Writing – original draft, visualisation, investigation, formal analysis, conceptualisation. Hao Xu: writing – visualisation, review & editing, methodology. Timothy N. Hunter: writing – review & editing, supervision, resources, methodology, conceptualisation. David Harbottle: writing – review & editing, resources. Girish M. Kale: writing – review & editing, resources. Martin R. Tillotson: writing – review & editing, supervision, resources, methodology, conceptualisation.

Acknowledgement

I would like to express my deepest gratitude to my supervisors, Prof. Martin R. Tillotson and Dr. Timothy N. Hunter, for their invaluable guidance, encouragement, and support throughout my doctoral journey. They have always been willing to listen to and respect my ideas, providing me with ample space to think and implement them. Their expertise and constructive feedback have been instrumental in shaping my research and ensuring its successful completion.

I am sincerely grateful to the China Scholarship Council, School of Civil Engineering (University of Leeds), and School of Chemical and Process Engineering (University of Leeds), for providing financial support and research platform that made this research possible. Their contribution has been vital in enabling me to pursue my studies and conduct all the experiments.

I would like to especially thank Dr. Nataliya Sergeeva and Dr. Jannis Wenk for being my viva examiners, whose valuable suggestions and inspiring discussions greatly helped to improve the quality of my thesis. Special thanks go to Dr. David Harbottle and Dr. Girish Kale, who have contributed to various aspects of this work through their experimental platform and insightful discussions. I would particularly like to acknowledge Dr. David Elliott, Mr. Morgan McGowan, and Ms. Emma Tidswell for their assistance with laboratory equipment and technical support.

On a personal note, I am deeply grateful to my family and friends for their unwavering support and understanding during this challenging yet rewarding journey. To my parents, your encouragement and belief in me have been my anchor throughout this process. Thank you to my husband for encouraging me to come to the UK. Your companionship got me through so many tough moments. The academic discussions with you also inspired me a lot.

In the end, I want to thank myself for bravely stepping out of my comfort zone and choosing this challenging yet meaningful journey. Experiencing a whole new research atmosphere, culture, and way of life in another country has been amazing, and I'll treasure these special memories for the rest of my life.

Abstract

Pharmaceutically active compounds (PhACs) and micro/nano-plastics (MP/NP) pose growing environmental threats due to their persistence and incomplete removal by conventional wastewater treatment processes. PhACs often accumulate as partially mineralised contaminants in wastewater and associated biosolids, harming ecosystems, while current methods for MP/NP removal primarily focus on physical separation rather than degradation. Heterogeneous electro-Fenton (HEF) processes, which utilise electricity to produce highly reactive oxygen species, offer a promising solution by mineralising a wide range of organic pollutants. However, challenges such as catalyst recovery, secondary pollution, and limited scalability hinder their widespread application. Despite their potential, HEF applications for MP/NP degradation remain underexplored, as existing methods rely on harsh reaction conditions or multiple chemical inputs. To bridge these gaps, this research focuses on developing novel integrated cathodes for efficient EF systems to address the challenges relating to pH adaptability, catalyst stability, and energy efficiency in the PhACs degradation process, while exploring the feasibility of the EF process for MP/NP removal.

A carbon aerogel is a synthetic porous material composed of 90–99% gas by volume. It retains a highly porous, three-dimensional network structure without undergoing significant shrinkage. Carbon aerogel (CA) was selected as a conductive substrate because of its large surface area, high porosity, excellent conductivity, and high potential for fixing metal sites. Two alloy carbon aerogels, FeNi-CA and CuCo-CA, were synthesised as integrated cathodes in HEF systems to enhance the efficient degradation of PhACs and MP/NP under environmentally friendly conditions. The FeNi-CA cathode exhibited outstanding bifunctional properties, enabling highly efficient H_2O_2 production and *in situ* activation to generate reactive radicals, which facilitated nearly complete degradation of acetaminophen across a broad pH range. This system demonstrated excellent stability and reusability, underscoring its industrial scalability. Building on these findings, the CuCo-CA cathode further improved EF performance by enhancing oxygen reduction reaction (ORR) activity, conductivity, and mass transport, achieving high tetracycline removal efficiency without external oxygen input. This cathode also outperformed FeNi-CA in acetaminophen degradation while exhibiting lower metal dissolution, contributing to long-term stability. Moreover, the CuCo-CA cathode was

successfully applied to the degradation of polystyrene nanoplastics, demonstrating efficient in situ H_2O_2 generation and ·OH-mediated polymer breakdown. The system achieved significant total organic carbon (TOC) removal, effectively mineralising toxic intermediates into safer end products.

This study successfully developed stable and efficient cathodes for targeting various organic and emerging contaminants, enhancing the applicability of the Electro-Fenton (EF) process across a wider pH range while improving energy efficiency. Additionally, it provided deeper insights into the underlying reaction mechanisms and demonstrated the environmental safety of the treated water. These findings establish a strong basis for advancing sustainable and high-performance EF technologies for water treatment applications.

Table of contents

List of figures

List of tables

List of abbreviation

In alphabetical order

AOPs	Advanced oxidation processes
AAS	Atomic absorption spectrometer
ACT	Acetaminophen
AFM	Atomic force microscopy
ACF	Activated carbon fibre
AO7	Acid orange 7
BET	Brunauer, Emmett, and Teller
BDD/CF	Boron-doped diamond/carbon-felt
BD	Biological digestion
CA	Carbon aerogel
CV	Cyclic voltammetry
CSTR	Continuous stirred tank reactor
C-F/F	Coagulation-flocculation/flotation
CD	Chemical digestion
CF	Carbon felt
CNT	Carbon nanotube
DLS	Dynamic light scattering
DMP	Dimethyl phthalate
DO	Dissolved oxygen
EF	Electro-Fenton
EDS	Energy dispersive spectrometer
ESR	Electron spin resonance
EIS	Electrochemical impedance spectroscopy
EAOPs	Electrochemical advanced oxidation processes
EO	Electrooxidation
ES	Electro-sorption
FTIR	Fourier transform infrared spectroscopy
GO	Graphene oxide
GCMS	Gas chromatography mass spectrometry
GC	Gas chromatography

GF	Graphite felt
GDE	Gas diffusion electrode
HRTEM	High resolution transmission electron microscopy
HPLC	High performance liquid chromatography
HEF	Heterogeneous electro-Fenton
ICP-MS	Inductively coupled plasma-mass spectrometry
LCMS	Liquid chromatography mass spectrometry
LDHs	Layered double hydroxides
MP/NP	Micro/nano-plastics
MOF	Metal-organic framework
MNZ	Metronidazole
NSAIDs	Non-steroidal anti-inflammatory drugs
NHE	Normal hydrogen electrode
ORR	Oxygen reduction reaction
OER	Oxygen evolution reaction
PhACs	Pharmaceutically active compounds
PS-NP	Polystyrene nanoplastic
PP	Polypropylene
PE	Polyethylene
PS	Polystyrene
PET	Polyethylene terephthalate
PES	Polyester
PA	Polyamide
PVC	Polyvinyl chloride
p-BQ	p-benzoquinone
POPs	Persistent organic pollutants
ROS	Reactive oxygen species
RRDE	Rotating ring disk electrode
RHE	Reversible hydrogen electrode
SEM	Scanning electron microscope
SDS	Sodium dodecyl sulphate
SACs	Single-atom catalysts
STEM	Scanning transmission electron microscope

SA	Salicylic acid
TOC	Total organic carbon
TC	Tetracycline
TMs	Transition metals
TBA	Tert-butanol
UV-vis	Ultraviolet-visible spectrophotometer
WWTPs	Wastewater treatment plants
XRD	X-ray diffraction
XPS	X-ray photoelectron spectroscopy

List of chemical species

AgCl	Silver chloride
$AgCl_3$	Aluminium chloride
$C_{15}H_{21}FeO_6$	Ferric acetylacetonate
$C_{10}H_{14}NiO_4$	Nickel acetylacetonate
$C_4H_6CuO_4$	Copper acetate dehydrate
$C_{15}H_{21}CoO_6$	Cobalt (II) acetylacetonate
CuCo-CA	Copper cobalt carbon aerogel
$C_{17}H_{18}FN_3O_3$	Ciprofloxacin
$C_{16}H_{18}FN_3O_3$	Norfloxacin
$C_{22}H_{24}N_2O_8$	Tetracycline
$C_{23}H_{27}N_3O_7$	Minocycline
$C_{10}H_{13}N_3O_3S$	Sulfamethoxazole
$C_{10}H_{10}N_4O_2S$	Sulfadiazine
$C_{12}H_{12}N_2O_3$	Nalidixic acid
$C_{13}H_{11}NO_5$	Oxolinic acid
$C_6H_9N_3O_3$	Metronidazole
$C_8H_{13}N_3O_4S$	Tinidazole
CeO_2	Cerium oxide
$CuCo_2S_4$	Copper cobalt sulphide
CO_2	Carbon dioxide
Cu_2O	Cuprous oxide
DMPO	5,5-Dimethyl-1-Pyrroline-N-Oxide
FeNi-CA	Iron nickel carbon aerogel
$FeCl_3$	Ferric chloride
Fe_3O_4	Magnetite
H_2O_2	Hydrogen peroxide
H_2O	Water
H_2SO_4	Sulfuric acid
KOH	Potassium hydroxide
N_2	Nitrogen
Na_2SO_4	Sodium sulphate
NaOH	Sodium hydroxide

O_2	Oxygen
$\cdot O_2^-$	Superoxide radical
$\cdot OH$	Hydroxyl radicals
PbO_2	Lead dioxide
$\cdot SO_4^-$	Sulphate radical
TiO_2	Titanium dioxide

1 Introduction

1.1 Research background

In recent years, the risks posed by pharmaceutically active compounds (PhACs) and micro/nano-plastics (MP/NP) have become significant environmental concerns. Conventional wastewater treatment processes are often unable to completely degrade or remove PhACs because of their resistant physical and chemical properties, leading to the accumulation of partially mineralised contaminants in sewage and sludge, which can negatively impact ecosystems. Therefore, effective and environmentally friendly techniques for PhAC removal remain a critical challenge in addressing the ongoing water environment crisis. MP/NP pose a significant risk to the food chain due to their ingestion by aquatic organisms at various trophic levels, ultimately leading to human consumption. These particulates can penetrate cell membranes, cross the blood-brain barrier, and have been linked to adverse health effects through exposure pathways such as inhalation, ingestion, and skin contact [1]. However, efficiently breaking down MP/NP in aquatic systems is still in its early stages, as most existing methods merely achieve physical separation without complete degradation [2].

Advanced oxidation processes (AOPs), which rely on generating highly reactive oxygen species such as hydroxyl radicals (·OH), offer a promising solution by mineralising a wide range of organic pollutants non-selectively to achieve water purification [3,4]. Despite their potential, few studies have explored the use of AOPs for MP degradation in water. For instance, some research has focused on the photodegradation of MP/NP using semiconductor-based photocatalysts, such as TiO_2 nanomaterials [5]. However, these suspended catalysts are challenging to recover, posing risks of secondary pollution and limiting large-scale application.

Immobilising catalysts on conductive substrate surfaces can address these challenges. Heterogeneous electro-Fenton (EF) processes (as one of the AOPs), with the assistance of integrated cathodes, are promising technologies for solving this problem. This method avoids the issues of catalyst shedding, dissolution, and agglomeration, thereby making it more suitable for plant-scale wastewater treatment applications. However, the application of electrochemical methods for MP/NP degradation remains underexplored. Current

electrochemical approaches require multiple chemical inputs or harsh reaction conditions (such as high current density or temperature) [6,7].

Given these research gaps and technological limitations, the research topic of this project was to develop novel integrated cathode materials and establish highly efficient heterogeneous EF systems to address practical challenges (e.g. pH range, catalyst stability, and energy consumption) in the degradation of PhACs and to explore the possibility of using mild, efficient and environmentally friendly technologies to alleviate the MP/NP pollution crisis. Carbon aerogel (CA), as a bulk cathode, exhibits high potential for generating H_2O_2 and fixing metal sites because of its large surface area, abundant porosity, and good conductivity [8]. Thus, CA was chosen as the conductive substrate to support transition metals in this project. Two transition metal alloys (FeNi and CuCo) served as effective candidates for further improving the activity of carbon aerogel for microcontaminant removal in water.

Bimetallic cathode materials have been widely studied for their potential to enhance electrochemical performance in EF systems, as they optimise electronic structures and improve conductivity compared to monometallic catalysts [9,10]. Among them, FeNi-CA is expected to exhibit high electrocatalytic activity, with Ni improving the two-electron oxygen reduction reaction (ORR) selectivity of Fe-based cathodes, leading to more efficient H_2O_2 production for EF reaction. However, the effects of Fe and Ni in a carbon aerogel matrix as an EF cathode have not yet been explored. Cu, as an important iron-free Fenton catalyst, reacts with H_2O_2 at a much higher rate than Fe^{2+} and remains effective over a wide pH range [11]. Co, with its stable Co^{2+}/Co^{3+} redox pair, further supports H_2O_2 activation to generate reactive radicals for organic pollutant degradation [12]. Thus, the CuCo-CA cathode has the potential to take advantage of the synergistic interaction between Cu and Co to enhance electrochemical activity. Despite these advantages, the combined role of Cu and Co in modifying the structure and electrochemical properties of carbon aerogels has not been fully studied, and their potential as EF cathodes for water treatment requires further investigation.

In summary, both FeNi-CA and CuCo-CA cathodes represent significant innovations in EF cathode design, addressing key limitations of existing monometallic and bimetallic catalysts. By leveraging the unique properties of Fe-Ni and Cu-Co interactions, these

materials are expected to enhance H_2O_2 generation, catalytic efficiency, and long-term stability, paving the way for more efficient and scalable EF applications in water treatment.

1.2 Research aims and objectives

This project aimed to develop effective and stable integrated cathode materials for heterogeneous electro-Fenton systems to improve the degradation efficiency of PhACs (acetaminophen and tetracycline as the model pollutants) and MP/NP (polystyrene nanoplastics as the model pollutant), which have the potential to mitigate the environmental and biological threats posed by these contaminants.

In this research, two composite alloy carbon aerogels, FeNi-CA and CuCo-CA, were synthesised as highly active cathodes for selective two-electron ORR to produce H_2O_2. Simultaneously, the fabricated cathodes served as efficient Fenton catalysts for the on-site decomposition of H_2O_2 into reactive oxygen species (such as ·OH radicals), which play a crucial role in the oxidative degradation of various organic contaminants such as PhACs and MP/NP.

The research objectives in this project included:

1. Development and optimisation of a reliable and consistent synthesis process for two types of integrated bimetallic cathodes, namely FeNi-CA and CuCo-CA.
2. Design and assembly of an electrochemical cell for electro-Fenton reactions, and evaluation of the degradation performance of acetaminophen (ACT), tetracycline (TC), and polystyrene nanoplastics (PS-NP) in optimised EF systems coupled with FeNi-CA and CuCo-CA cathodes.
3. Analysis of the physical and chemical properties of the synthesised cathodes using a range of characterisation techniques, revealing the synergistic effects of the transition metals on the microstructural features.
4. Conducting electrochemical property tests to investigate the activity and selectivity of the $2e^-$ oxygen reduction reaction and the electron transfer process during *in situ* generation and activation of H_2O_2.
5. Optimisation of the heterogeneous EF systems by assessing the degradation performance under different operating conditions and water quality parameters.
6. Establishing a comprehensive detection method for PS-NP and comparing the physicochemical properties of PS-NP before and after the reaction to investigate

the degradation process.

7. Investigation of the durability and recyclability of the synthesised cathodes and exploration of their broad applicability to various organic pollutants.
8. Study of the mechanisms of pollutant degradation by identification of reaction intermediates, understanding of degradation pathways, and evaluation of the acute toxicity of degradation products.

1.3 Research content

In the first publication, a FeNi-CA bifunctional cathode was synthesised and applied to the electro-Fenton degradation of acetaminophen (ACT, the main component of analgesics), and its degradation mechanisms and pathways were elucidated. The second publication focused on the degradation of tetracycline (TC, an antibiotic) as a model pollutant, involving the synthesis of a CuCo-CA integrated cathode and exploration of its microstructural characteristics and electro-Fenton activity. Building on the findings from the first two publications, the CuCo-CA cathode demonstrated higher activity and lower metal leaching. Therefore, in the third manuscript, CuCo-CA was selected as the cathode for an electro-Fenton system to further investigate its degradation performance and mechanisms regarding polystyrene nanoplastics (PS-NP).

The research contents in this project include:

(1) Synthesis of cathode materials

FeNi-CA and CuCo-CA, with a metal molar ratio of 1:1, were fabricated by sol-gel formation, solvent exchange, ambient drying, and calcination. In addition, single-metal carbon aerogels (Fe-CA, Ni-CA, Cu-CA, Co-CA), pure carbon aerogel (CA), and alloy CA with various metal ratios ($Fe_{0.7}Ni_{0.3}$-CA, $Fe_{0.3}Ni_{0.7}$-CA, $Cu_{0.7}Co_{0.3}$-CA, $Cu_{0.3}Co_{0.7}$-CA) were prepared to investigate the synergistic effect of these metals and to optimise the alloy metal ratios.

(2) Characterisation

To investigate the physicochemical properties and microstructural features of the synthesised cathodes and PS-NP, various characterisation techniques were utilised. These are summarised in Table 1.1.

Table 1.1: List of characterisation techniques

Technique	Materials		Purpose
	Cathodes	PS-NP	
Scanning electron microscopy (SEM)	√	√	Surface morphology and microstructure
Energy-dispersive X-ray spectroscopy (EDS)	√		Elemental component and distribution
High-resolution transmission electron microscopy (HRTEM)	√	√	Dispersion of alloy particles, lattice distance, and particle size
N_2 adsorption and desorption (Brunauer-Emmett-Teller, BET)	√		Surface area and porosity
X-ray diffraction (XRD)	√		Phase composition and crystal structure
Fourier transform infrared (FTIR) spectroscopy	√	√	Chemical bonds and functional groups
X-ray photoelectron spectroscopy (XPS)	√	√	Elemental composition and chemical state
Raman spectroscopy	√		Chemical structure, phase and polymorph, crystallinity and molecular interactions
Inductively coupled plasma-mass spectrometry (ICP-MS)	√		Content of doped metals
Atomic absorption spectroscopy (AAS)	√		Concentration of leaching metals
Atomic force microscopy (AFM)		√	Images with near-atomic resolution for measuring surface topography
Dynamic light scattering (DLS)		√	Size and distribution of particles

(3) Degradation performance and optimisation of water quality parameters and operational conditions

The prepared cathodes were evaluated by the degradation performance of PhACs and PS-

NP in electro-Fenton systems, and the setup for degradation experiments is shown in Fig. 1.1. The contribution of the electro-sorption process was also assessed by keeping the applied current at a minimal value and removing oxygen from the system. Reaction conditions such as current density, initial pH, electrolyte concentration, contaminant concentration, and aeration rate were optimised by comparing degradation efficiency under different conditions.

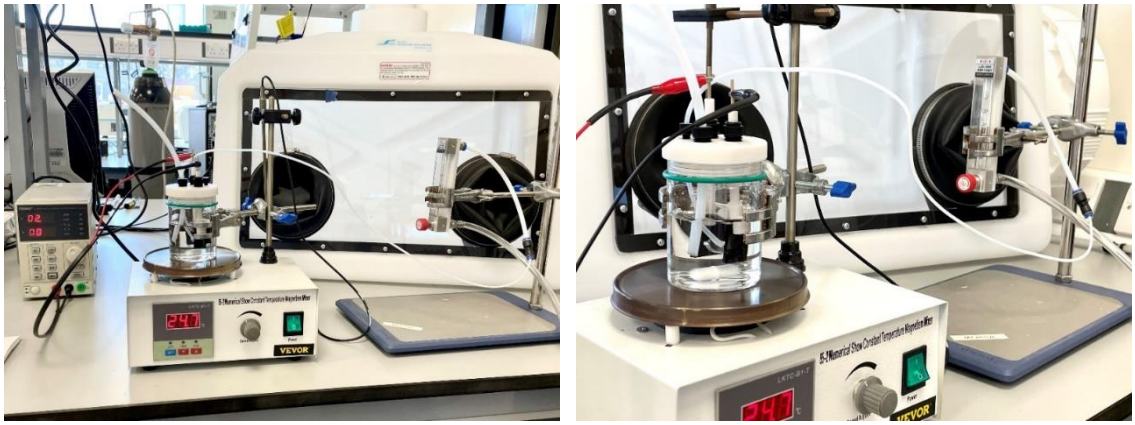

Figure 1.1. The experimental setup of electrochemical degradation.

(4) Electrochemical property investigation

The oxygen reduction reaction (ORR) process was investigated using cyclic voltammetry (CV), and the charge transfer resistance of the synthesised cathodes were compared using electrochemical impedance spectroscopy (EIS). The activity and selectivity for the $2e^-$ oxygen reduction process was evaluated using rotating ring-disk electrode (RRDE) techniques.

(5) Elucidation of pollutant degradation mechanisms in heterogeneous EF processes

Metal leaching during degradation reactions was measured to determine the contribution of the homogeneous reaction. The generation and effect of reactive radicals were identified by radical scavenger experiments and electron-spin resonance (ESR) spectroscopy. Using probe reagents, the generated hydrogen peroxide and hydroxyl radicals were quantitatively measured.

(6) Evaluate the durability and recyclability of cathodes

Cyclic experiments were conducted by collecting and washing the used cathode and then

employing it for subsequent repeated runs under identical experimental conditions. The electrocatalytic stability and recyclability of the FeNi-CA and CuCo-CA cathodes were evaluated through the degradation efficiency of target pollutants over the reused cathode. The long-term stability of the cathode materials was tested in a continuous stirred tank reactor (CSTR).

(7) Clarify the degradation intermediates and pathways

The primary degradation intermediates of the target pollutants in the electro-Fenton systems were identified using liquid chromatography-mass spectrometry (LCMS). Based on the detected intermediates, and referring to the degradation processes reported in other studies, possible oxidation pathways of the target pollutants by radical attack are proposed.

(8) Assess the acute toxicity of PS-NP degradation products

The acute toxicity of PS-NP degradation intermediates formed during the electrochemical process was assessed using the toxicity estimation software tool (T.E.S.T.) to ensure post-treatment water safety.

1.4 Thesis framework and outline

This thesis follows a publication-based format and incorporates two published journal papers and one submitted paper. Chapter 1 is a general introduction to the research background, aims, content of this thesis. Chapter 2 is a literature review that summarises and analyses existing research in this area. Chapters 3-5 comprise three papers that have been either published or submitted for publication, aligning with the objectives of this research project. Chapter 6 provides a narrative discussion about the critical links between the work, summarises the key findings of the research, discusses the limitations encountered, and offers recommendations for future research.

The framework of the research content in Chapter 3-5 is shown in Fig. 1.2.

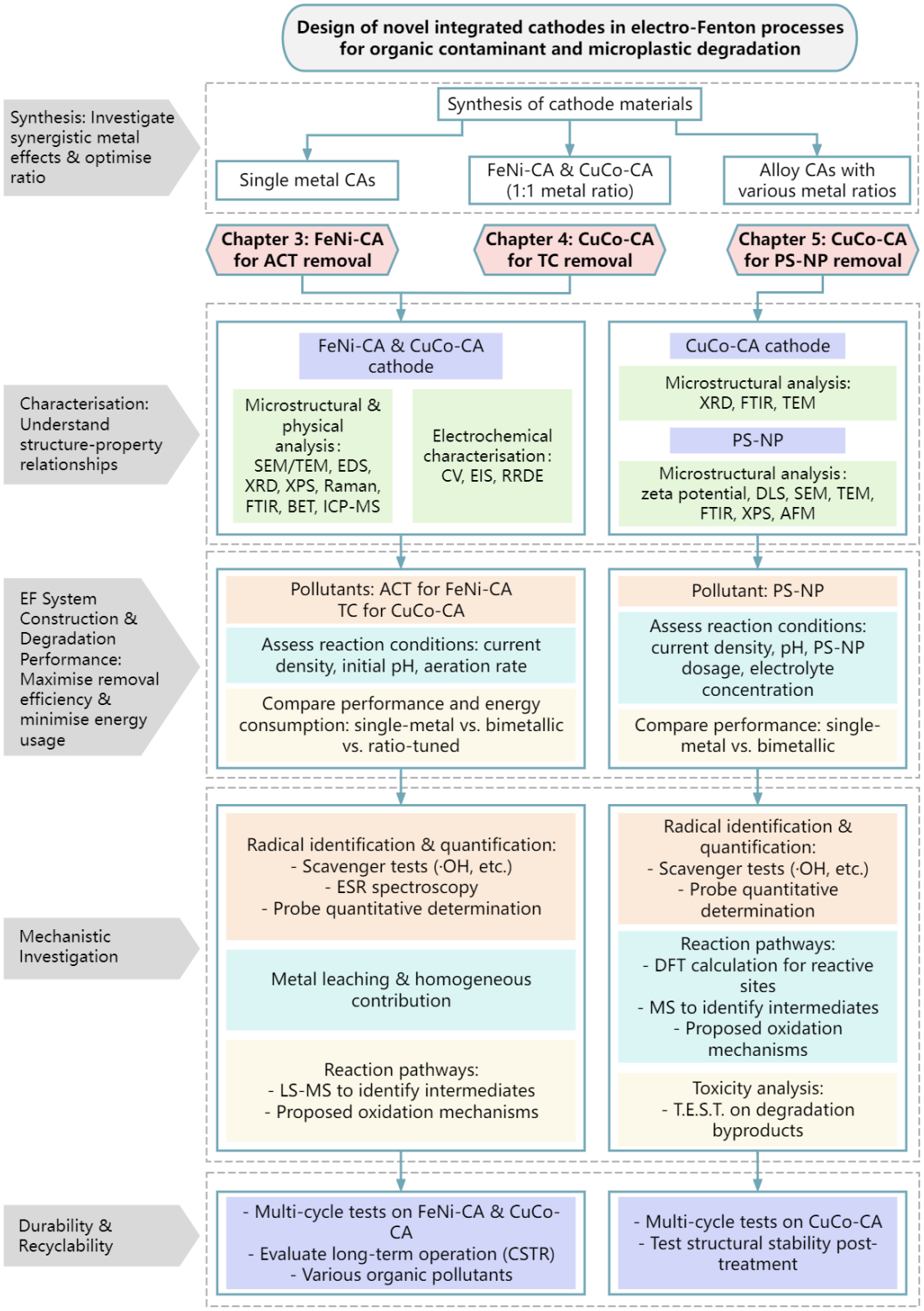

Figure 1.2. The framework of research content in three studies.

The outlines of each research work in this thesis are as follows:

Chapter 3: Publication #1 (published) [13]

A novel cathode, iron-nickel alloy carbon aerogel (FeNi-CA), was successfully synthesised and utilised as the cathode in a heterogeneous electro-Fenton process for acetaminophen (ACT) degradation. A comprehensive investigation of structural features, electrochemical properties, degradation performance, mechanisms and pathways were conducted, offering valuable insights for developing novel heterogeneous EF systems and enhancing the efficiency of micropollutant decomposition.

Chapter 4: Publication #2 (published) [14]

Building on the study of the FeNi-CA cathode, the second publication developed a CuCo carbon aerogel (CuCo-CA) cathode to target tetracycline (TC), a commonly used antibiotic and representative micropollutant. This study addressed the potential metal leaching issues from the FeNi-CA cathode, investigated the degradation performance in a continuous stirred tank reactor, and explored the synergistic effect of Cu and Co on microstructure, electrochemical activity, and TC degradation efficacy. Additionally, the broad applicability of the CuCo-CA cathode was examined by evaluating its degradation efficiency with various organic contaminants including antibiotics, analgesics, organic acid, and dye.

Chapter 5: Publication #3 (submitted)

CuCo-CA exhibited superior catalytic performance and lower metal dissolution than FeNi-CA in the EF system for pharmaceutically active compounds (PhACs) degradation. The third study expanded the application of CuCo-CA to tackle emerging micro/nano-plastic pollution, focusing on the degradation of polystyrene nanoplastics (PS-NP). This research examined the physical deformation and chemical composition changes of PS-NPs during electrochemical oxidation treatment and elucidated the underlying oxidation mechanisms. Furthermore, the degradation intermediates and pathways of PS-NPs within the optimised EF process were systematically analysed.

1.5 References

[1] R. Ahmed, A.K. Hamid, S.A. Krebsbach, J. He, D. Wang, Critical review of microplastics removal from the environment, Chemosphere 293 (2022) 133557. https://doi.org/10.1016/j.chemosphere.2022.133557.

[2] Z. Chen, X. Liu, W. Wei, H. Chen, B.-J. Ni, Removal of microplastics and nanoplastics from urban waters: Separation and degradation, Water Research 221 (2022) 118820. https://doi.org/10.1016/j.watres.2022.118820.

[3] D.B. Miklos, C. Remy, M. Jekel, K.G. Linden, J.E. Drewes, U. Hübner, Evaluation of advanced oxidation processes for water and wastewater treatment – A critical review, Water Research 139 (2018) 118–131. https://doi.org/10.1016/j.watres.2018.03.042.

[4] M. Priyadarshini, I. Das, M.M. Ghangrekar, L. Blaney, Advanced oxidation processes: Performance, advantages, and scale-up of emerging technologies, Journal of Environmental Management 316 (2022) 115295. https://doi.org/10.1016/j.jenvman.2022.115295.

[5] P.H. Allé, P. Garcia-Muñoz, K. Adouby, N. Keller, D. Robert, Efficient photocatalytic mineralization of polymethylmethacrylate and polystyrene nanoplastics by TiO2/β-SiC alveolar foams, Environ Chem Lett 19 (2021) 1803–1808. https://doi.org/10.1007/s10311-020-01099-2.

[6] F. Miao, Y. Liu, M. Gao, X. Yu, P. Xiao, M. Wang, S. Wang, X. Wang, Degradation of polyvinyl chloride microplastics via an electro-Fenton-like system with a TiO2/graphite cathode, Journal of Hazardous Materials 399 (2020) 123023. https://doi.org/10.1016/j.jhazmat.2020.123023.

[7] Z. Ning, X. Duan, Y. Li, X. Zhao, L. Chang, Degradation of polyvinyl chloride microplastics via electrochemical oxidation with a CeO2–PbO2 anode, Journal of Cleaner Production (2023) 139668. https://doi.org/10.1016/j.jclepro.2023.139668.

[8] K.M. Nair, V. Kumaravel, S.C. Pillai, Carbonaceous cathode materials for electro-Fenton technology: Mechanism, kinetics, recent advances, opportunities and challenges, Chemosphere 269 (2021). https://doi.org/10.1016/j.chemosphere.2020.129325.

[9] M. Ghasemi, A. Khataee, P. Gholami, R.D.C. Soltani, A. Hassani, Y. Orooji, In-situ electro-generation and activation of hydrogen peroxide using a CuFeNLDH-CNTs modified graphite cathode for degradation of cefazolin, Journal of Environmental Management 267 (2020) 110629. https://doi.org/10.1016/j.jenvman.2020.110629.

[10] Q. Liu, S. Cao, Y. Qiu, Effect of carbonization temperature on bimetallic FeCo-N/C nanofiber electrocatalysts for oxygen reduction reaction in sulfuric acid solution, International Journal of Hydrogen Energy 42 (2017) 29274–29282. https://doi.org/10.1016/j.ijhydene.2017.10.069.

[11] Y. Liu, Z. Yang, J. Wang, Fenton-like degradation of sulfamethoxazole in Cu0/Zn0-air system over a broad pH range: Performance, kinetics and mechanism, Chemical Engineering Journal 403 (2021) 126320. https://doi.org/10.1016/j.cej.2020.126320.

[12] Y. Zou, H. Qi, Z. Sun, In-situ catalytic degradation of sulfamethoxazole with efficient CuCo–O@CNTs/NF cathode in a neutral electro-Fenton-like system, Chemosphere 296 (2022) 134072. https://doi.org/10.1016/j.chemosphere.2022.134072.

[13] Q. Ye, T.N. Hunter, H. Xu, D. Harbottle, G.M. Kale, M.R. Tillotson, Synergistic effect of Fe and Ni on carbon aerogel for enhanced oxygen reduction and H2O2 activation in electro-Fenton process, Separation and Purification Technology 353 (2025) 128436. https://doi.org/10.1016/j.seppur.2024.128436.

[14] Q. Ye, T.N. Hunter, H. Xu, D. Harbottle, G.M. Kale, M.R. Tillotson, CuCo carbon

aerogel as a bifunctional cathode for Electro-Fenton processes: Unveiling synergistic effects and catalytic mechanisms, Separation and Purification Technology 361 (2025) 131597. https://doi.org/10.1016/j.seppur.2025.131597.

2 Literature review

2.1 Environmental challenges and remediation technologies for microcontaminants

Nowadays, wastewater treatment has evolved significantly from basic physical processes to advanced chemical and biological methods to address emerging contaminants. Initially, treatment focused on removing suspended solids through sedimentation and filtration to improve water clarity and reduce gross pollutants. The introduction of biological treatment, such as activated sludge and trickling filters, enhanced the removal of organic matter and nitrogenous compounds, reducing oxygen demand in receiving waters [1]. Chemical treatment later emerged to tackle phosphorus pollution, primarily through coagulation and precipitation [2]. Regulatory frameworks such as the Urban Wastewater Treatment Directive (91/271/EEC) [3] and the Water Framework Directive (2000/60/EC) [4] have driven improvements in nutrient removal and water quality standards. However, as wastewater treatment has progressed, it has become evident that conventional methods are insufficient for addressing newly recognised contaminants, particularly those that are persistent and bioaccumulative in aquatic environments.

In the area of environmental science, the persistent presence of microcontaminants poses significant challenges because of their detrimental effects on human health and the ecological environment. These contaminants, comprising pharmaceutical residues (such as analgesics and antibiotics) and micro/nano-plastics, are recalcitrant and can evade traditional water treatment processes. Given their resistance to conventional treatment techniques, there is a growing emphasis on developing innovative and sustainable technologies capable of degrading these contaminants at a molecular level.

2.1.1 Environmental crisis of pharmaceutical residues

Over the past few decades, advancements in medical science have significantly boosted the production and use of pharmaceutical products. Around three thousand compounds are utilised as pharmaceuticals, with annual production volumes surpassing hundreds of tons [5]. Among these, anti-inflammatory drugs, antibiotics, and analgesics are the most commonly used worldwide.

Non-steroidal anti-inflammatory drugs (NSAIDs) and analgesics represent some of the

most significant groups of pharmaceutical products globally, characterised by various chemical structures and similar therapeutic effects. These groups have an estimated annual production of hundreds of tons [6]. A substantial quantity of anti-inflammatory drugs is prescribed for human use, yet their over-the-counter sales vastly exceed prescription numbers [7]. It is estimated that around 30 million people use NSAIDs daily worldwide [8]. Globally, effluents are monitored to assess the concentrations of these drugs and their metabolites, with numerous studies indicating that both NSAIDs and analgesics are frequently detected in aquatic environments [9].

Among the pharmaceutical compounds detected in wastewater, antibiotics are particularly concerning due to their persistence, partial metabolism, and easy dispersal through ecosystems [10]. The antibiotics most frequently identified in wastewater include fluoroquinolones, tetracyclines, sulphonamides, quinolones, and nitroimidazoles (Table 2.1) [11]. Antibiotic resistance in microorganisms is intensifying and becoming more prevalent, posing a significant threat to human morbidity and mortality in the future [12]. Antibiotics have been detected in rivers globally, including Spain, Italy, South Korea, China, France, the United States, etc [13].

Table 2.1. Class and chemical structure of antibiotics.

Class	Example compound	Chemical structure
Fluoroquinolones	Ciprofloxacin	$C_{17}H_{18}FN_3O_3$
	Norfloxacin	$C_{16}H_{18}FN_3O_3$
Tetracyclines	Tetracycline	$C_{22}H_{24}N_2O_8$
	Minocycline	$C_{23}H_{27}N_3O_7$
Sulphonamides	Sulfamethoxazole	$C_{10}H_{13}N_3O_3S$
	Sulfadiazine	$C_{10}H_{10}N_4O_2S$
Quinolones	Nalidixic acid	$C_{12}H_{12}N_2O_3$
	Oxolinic acid	$C_{13}H_{11}NO_5$
Nitroimidazoles	Metronidazole	$C_6H_9N_3O_3$
	Tinidazole	$C_8H_{13}N_3O_4S$

Nowadays, the use of pharmaceuticals to diagnose and treat illness has markedly increased. This has led to larger quantities of these chemicals being released into untreated

water bodies through sewage overflows, livestock farming, stormwater runoff, aquaculture activities, and landfill leachate [14]. For example, the widespread use of antibiotics has led to their presence in water, soil, and sediments, with concentrations ranging from 463 ng L^{-1} to 31 mg L^{-1} [15]. Furthermore, these pharmaceutical by-products often enter waterbodies or sewage systems in their original form or as metabolites [16]. Although conventional treatment methods are available, their removal efficiencies for pharmaceutical compounds vary widely, ranging from 10% to 60%, depending largely on multiple factors [17]. These methods are generally inadequate for eliminating pharmaceutical residues in typical wastewater treatment plants (WWTPs), resulting in inefficiently treated or directly discharged pharmaceutical residues into the environment [18]. Pharmaceutical metabolites or partially degraded drugs/metabolites can pose greater environmental risks than the original drug, as they may exhibit higher pharmacological activity or increased mobility within the environment [19].

2.1.2 Treatment technologies for pharmaceutical residues

Research has demonstrated that a combination of diverse treatment techniques is essential for effectively mitigating pharmaceutically active compounds (PhACs) in effluent. Effective reduction is typically achieved by integrating multiple processes, such as combining biological treatment with subsequent adsorption or chemical oxidation, coupling physicochemical processes with chemical oxidation, and pairing biological methods with physical separation. During these sequences, pharmaceuticals are typically separated, chemically modified, or oxidised [14].

As shown in Fig. 2.1 [20], in traditional WWTPs, processes like flocculation, sedimentation, coagulation, and trickling filters are primarily intended to eliminate suspended and dissolved solids, and biologically degrade organic compounds from wastewater [21]. However, despite these processes, pharmaceuticals show varying degrees of resistance to conventional treatment methods; even secondary treatment units often fail to eliminate them [22]. Secondary treatments such as constructed wetlands, eco-bio reactors, extended aeration, membrane bioreactors, and sequencing batch reactors typically achieve pharmaceutical removal efficiencies ranging from 18-65% [23]. Nevertheless, hybrid treatments that combine biological and physicochemical processes have been shown to enhance pharmaceutical reduction significantly. Consequently, advanced on-site treatment methods are increasingly considered the most effective

approach for eliminating pharmaceutical effluents from hospital settings.

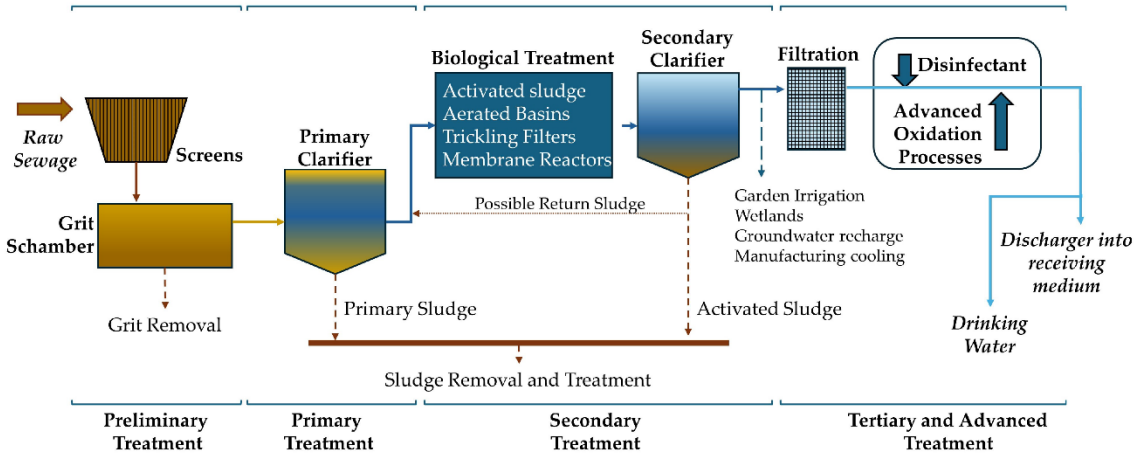

Figure 2.1. Wastewater treatment plant stages, from preliminary to advanced treatment processes.

For the removal of PhACs, advanced treatment strategies encompass a diverse array of methods, which can be implemented independently or incorporated with other biological or chemical methods. These include constructed microalgal treatment [24], constructed wetlands [25], membrane treatment [26], adsorption [27], advanced oxidation processes (AOPs) [28], and hybrid treatments [29]. Among these, AOPs have been a competitive alternative to existing technologies due to their broad applicability and high processing efficiency in degrading PhACs [14]. Currently, AOPs have demonstrated outstanding efficiency in breaking down organic pollutants in water systems by producing various reactive oxygen species (ROS), including hydroxyl radicals (·OH, E^0 = 2.7 V vs. normal hydrogen electrode [NHE]) [30]. Due to their strong oxidising properties, hydroxyl radicals can oxidise most organic pollutants almost non-selectively [31]. AOPs, either as standalone treatments or in combination with other techniques, can enhance the degradation of various pharmaceuticals in water [32]. Integrating AOPs with biological treatments offers multiple advantages, although certain complex chemicals remain challenging to degrade. AOPs can be implemented pre, post, or together with biological processes. They typically demonstrate high removal efficiencies (80-90%), which can increase up to 90% when AOPs are combined with other methods such as Fenton's reaction, coagulation, ultraviolet radiation, nanofiltration, ozonation, and electrocatalytic oxidation [33]. Research indicates that modern WWTPs and water management systems incorporating AOPs are highly effective. The electro-Fenton process, in particular, addresses the limitations of the traditional Fenton process by electrochemically

generating H_2O_2 under controlled *in situ* conditions [34].

2.1.3 Occurrence and crisis of micro/nano plastic pollution

The remarkable properties of plastics, such as high chemical and biological resistance, easy moulding, and low cost, have rendered these materials ubiquitous across the globe [35]. Commonly utilised in everyday items, plastics have significantly enhanced our quality of life and have become fundamental to the global "throwaway culture" economy. In 2021, worldwide plastic production approached nearly 390 million tonnes, with projections indicating a potential doubling over the next two decades [36].

Although the economic and daily life benefits of plastics are undeniable, the production and inadequate management of plastic waste pose a critical environmental challenge. For example, 13 million tons of plastic enter rivers and oceans worldwide each year—potentially leading to a projected accumulation of 250 million tons of plastic in aquatic environments by 2025 [37]. The lifespan of plastic products varies widely, from as brief as a single day to over fifty years, after which they are disposed of [37]. This situation significantly strains ecosystems globally, as these plastic materials are barely degradable and can persist for decades or even centuries [38].

In the classification of plastic debris, particles ranging from 1 μm to 5 mm are typically designated as microplastic (MPs), whereas those smaller than 1 μm are referred to as nanoplastics (NPs) [39]. The gradual degradation of gross plastic waste through natural physical/biological/chemical processes leads to the emergence of MP/NP. MPs and NPs have been identified in virtually all ecosystems, including continental and oceanic waters, soils, sediments, and commercial bottled water [40]. Their presence in aquatic environments such as rivers, oceans, and wastewater systems has been extensively documented in the literature [41,42]. Upon entering these environments, these plastic particulates can be ingested by various organisms, particularly those in aquatic settings, across various trophic levels. This ingestion facilitates the entry of MPs and NPs into the food chain, culminating in their ultimate consumption by humans [43]. Compelling evidence highlights the toxicity of MPs and NPs to aquatic organisms. Molecular simulations have elucidated that NPs can readily penetrate the lipid membranes of cells, causing structural alterations, reducing molecular diffusion, and significantly impacting cellular functions [44]. Furthermore, the presence of NPs in the brains of organisms

suggests their capability to traverse the blood-brain barrier. The influence of microplastics and nanoplastics on human health remains largely elusive. However, extensive research has been conducted to evaluate potential contamination pathways and their subsequent health consequences [45,46]. Human exposure to MPs and NPs is increasingly recognised as a significant health risk. Routes through which MP/NP can enter the human body include inhalation, ingestion, and direct skin contact, with potential sources being air, drinking water, and through the food chain [47]. Exposure to MP/NP has been associated with a range of adverse health outcomes, including disruption of immune function, cytotoxicity, disturbance in energy and metabolism, oxidative stress, neurotoxicity, and potential links to neurodegenerative diseases [48]. Generally, the toxicity of MPs and NPs appears to be size-dependent, with smaller particles exhibiting greater toxicity than larger ones [49].

Extensive research has been conducted on the environmental fate and occurrence of MPs and NPs, particularly within natural water bodies and wastewater treatment plants (WWTPs) [50]. In natural waters, polypropylene (PP), polyethylene (PE), and polystyrene (PS) are predominantly identified [51], while the most frequently detected polymers include polyethylene terephthalate (PET), polyester (PES), polyamide (PA), and PE in the influent and effluent of WWTPs [52]. Fig. 2.2 illustrates the occurrence of nano and microplastics in WWTPs [53]. It shows that WWTPs make significant contributions to the discharge of MPs and NPs into aquatic environments, despite conventional WWTPs being capable of removing more than 90% of MPs from sewage [54]. Furthermore, approximately 50-85% of MPs are accumulated in sewage sludge, commonly employed as biofertilisers. This retention raises substantial concerns regarding soil contamination [55]. Consequently, the release of MPs from WWTPs has garnered growing attention in the environmental science, protection, and political community.

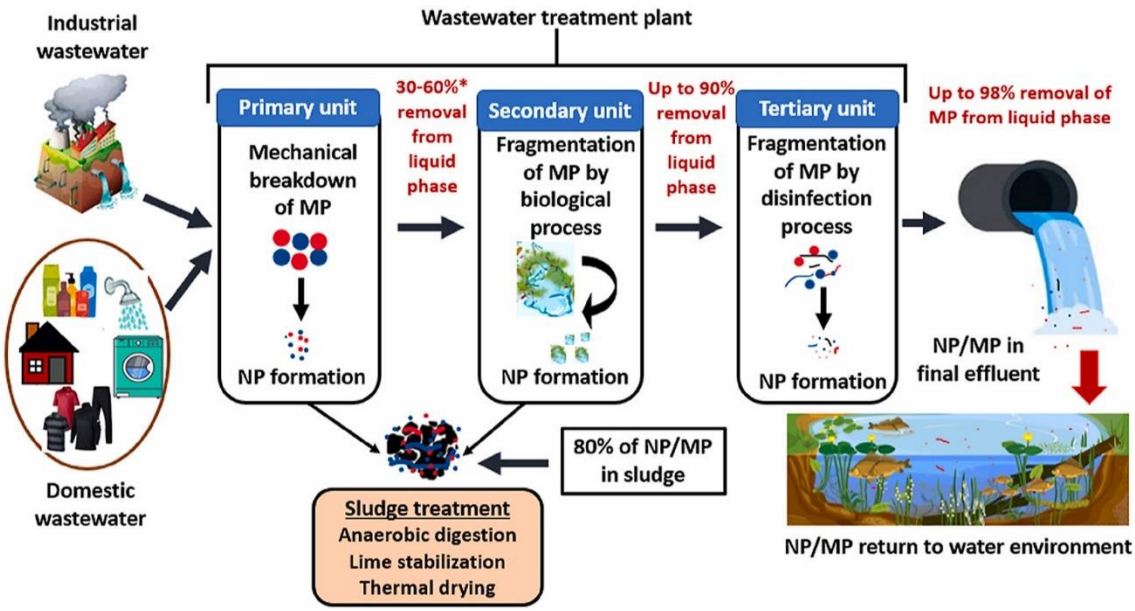

Figure 2.2. Occurrence of nano and microplastics in wastewater treatment plants.

To date, WWTPs have not implemented specific treatment technologies exclusively for removing plastic pollution from wastewater, beyond the conventional methods already in use, such as skimming, mesh screening, grit removal chambers, sedimentation, membrane bioreactors, and advanced filtration [56]. Moreover, only a few researchers have endeavoured to develop treatment technologies specifically targeting MPs and NPs. These efforts have primarily focused on evaluating MPs and NPs in wastewater, emphasising their removal performance [53,57]. Consequently, there is an ongoing demand for novel and effective treatment techniques that can address plastic pollution in wastewater effluents.

2.1.4 Separation and degradation technologies for micro/nano plastic

In previous research, the initial strategy for addressing microplastics (MPs) in liquid matrices involved separation techniques. Several methods for MP separation have been proven effective, such as filtration, sieving, and the use of activated carbon, among others [58,59]. Techniques such as filtration and sieving are predominantly utilised as pre-treatment steps to facilitate the quantification of MPs. Despite the potential of these methods, there are relatively few studies that explore their application in engineered processes specifically designed for the efficient separation of MPs.

The coagulation-flocculation/flotation (C-F/F) process is one of the most prevalent engineered separation techniques for MPs. This method relies on the solid-liquid

separation mechanism, with its efficiency primarily determined by the density differences between the fluid and the solid particles [60]. Density separation has been utilised at the laboratory scale; however, there is a notable absence of scale-up strategies in the published research, possibly due to the substantial treatment costs associated with electrolyte addition [61]. Furthermore, the effectiveness of density separation is not guaranteed as the density of MPs may change over time because of microbial colonisation on their surfaces, which can call into question the efficacy of various electrolytes used in this process [62]. In the context of chemical coagulation-flocculation, numerous coagulants have been extensively researched for the elimination of organic and inorganic pollutants [63]. Nevertheless, a limited selection of agents such as $AlCl_3$, $FeCl_3$, and specific polymers has been developed for MP separation, requiring high dosages to achieve satisfactory removal efficiencies [64].

The removal of MPs from water has been achieved through two main approaches: chemical digestion (CD) and biological digestion (BD) [65]. BD has predominantly been demonstrated at the lab scale, involving density-based separation within a matrix containing elevated electrolyte concentrations. This includes a necessity for an additional process to degrade MPs [66]. The most commonly reported CD method is wet oxidation, wherein organic compounds are decomposed under elevated temperature and pressure conditions with the aid of an oxidising agent [67]. In these processes, a low oxidant concentration is typically employed, along with either an alkaline or an acidic solution, to prevent the degradation or alteration of MPs. This is because the CD process has often been used as a pre-treatment step in experimental studies aimed at quantifying MPs in environmental samples [65]. To date, no research has explicitly explored CD or comparable methods explicitly for the removal or degradation of MPs.

Biological degradation and advanced oxidation processes (AOPs) are two technologies presently employed for the decomposition of microplastics (MPs). These processes facilitate the breakdown of the chemical bonds within polymer MPs into smaller molecular fragments. These fragments can subsequently be transformed into valuable products or potentially fully mineralised into CO_2 and H_2O [68]. The cleavage of the polymer chains occurs randomly and may target any monomer unit within the polymer, ultimately leading to the conversion of MPs into accessible organic or inorganic products.

Researchers have discovered that while MPs exhibit prolonged stability in natural settings, specific microorganisms are capable of degrading them [69]. Owing to their robust adaptability, these microorganisms can thrive in nearly any environment and possess the capability to break down various organic pollutants, including MPs [70]. Recent studies have explored the application of bacteria for the biodegradation of microplastics [71]. The primary emphasis of this research has been on the use of pure bacterial strains to mediate the microbial degradation of MPs under controlled laboratory settings. These strains are predominantly isolated from sources such as wastewater, sediment, and sludge. In addition to bacteria, fungi have demonstrated the capability to break down and metabolise MPs [72]. Over the past few decades, novel fungal species with enhanced MP degradation abilities have been identified. While these microorganisms exhibit varying levels of MP decomposition efficiency, a minimum period of 21 days is typically required to achieve satisfactory results in biodecomposition.

Recently, AOPs, as highly efficient chemical elimination processes, have demonstrated remarkable efficacy in degrading various organic pollutants in water through the generation of reactive radicals. These include the sulphate radical ($\cdot SO_4^-$, E^0 = 3.1 V vs. NHE) utilised in sulphate radical-based AOPs (SR-AOPs) and the hydroxyl radical ($\cdot OH$, E^0 = 2.7 V vs. NHE) employed in Fenton and Fenton-like reactions [73]. Studies have shown that the Fenton process can effectively convert plastic pollutants into valuable intermediates, and SR-AOPs are considered a comprehensive system for degrading a broad range of persistent organic pollutants in complex water environments [74,75]. It has been reported that SR-AOPs exhibit exceptional catalytic degradation capabilities, particularly for decomposing cosmetic microplastics primarily composed of polyethylene [76]. The oxidation process of microplastics is likely enhanced by their high redox potentials, directly inducing the decomposition process [77]. This results in the breaking of polymer chains, the production of valuable by-products, or even the complete mineralisation of microplastics. However, in contrast to more established methods for microplastic (MP) removal, the use of AOPs for degrading MPs represents a relatively new advancement [78].

2.2 Introduction to electro-Fenton processes

2.2.1 Overview of advanced oxidation processes (AOPs)

AOPs were initially introduced for treating potable water in the 1980s [79], characterised

by the production of ·OH radicals in quantities sufficient to facilitate water decontamination. The ·OH radicals are strongly oxidising species and are capable of degrading micropollutants non-selectively at a rate constant of 10^8-10^{10} $M^{-1}s^{-1}$ [80], ultimately resulting in the production of CO_2, H_2O, and various inorganic ions as final degradation products. Subsequently, the scope of AOPs broadened to encompass oxidation mechanisms involving sulphate radicals ($\cdot SO_4^-$). Unlike traditional oxidants such as chlorine and ozone, which address both decontamination and disinfection needs, AOPs are utilised specifically for targeting and eliminating organic and inorganic pollutants from water and wastewater systems [80].

As shown in Fig. 2.3, different types of AOPs rely on the *in situ* generation of ·OH species through diverse mechanisms, including chemical, sonochemical, photochemical, or electrochemical methods [81]. This diversity enables the selection of an appropriate AOP based on the specific characteristics of the target water or wastewater and the precise requirements of the treatment process. Among the earliest and most widely utilised chemical AOPs is the Fenton method, which employs a combination of H_2O_2 and soluble Fe(II) salts, commonly referred to as Fenton's reagent, to decompose stubborn micropollutants. The practicality and efficiency of this process can be greatly enhanced by integrating the Fenton technique with electrochemical reactions, leading to the development of electrochemical advanced oxidation processes (EAOPs) [82]. EAOPs represent emerging and environmentally friendly technologies that utilise electrons as a clean reagent, thereby minimising or significantly reducing the need for chemical inputs. Compared to the traditional Fenton process, the electro-Fenton method avoids the storage and transfer of H_2O_2 by producing H_2O_2 on site in the electrochemical cell. Furthermore, ·OH radicals are generated either directly via water oxidation at an anode with a high O_2 evolution overvoltage [82], or indirectly in the solution *via* electrochemically generated Fenton's reagent from electrode reactions [83].

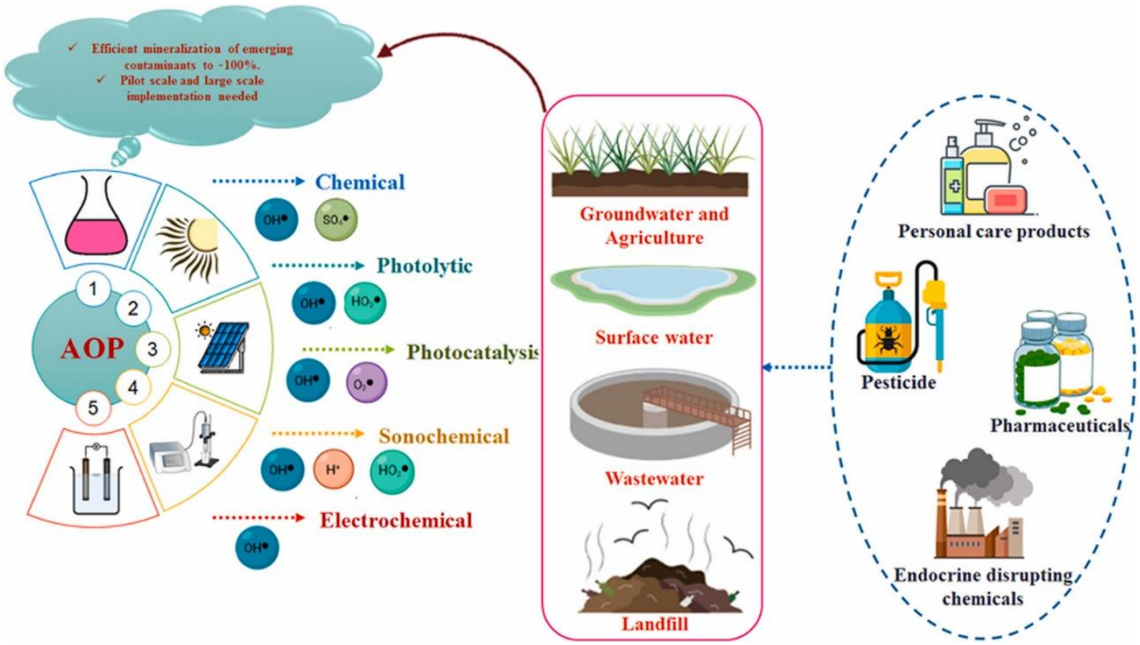

Figure 2.3. Mineralisation of emerging contaminants by advanced oxidation processes.

2.2.2 Principles of electro-Fenton (EF) reaction

EF technology is one of the most effective and eco-friendly methods for the treatment of wastewater contaminated with organic matter. Developed and widely utilised by notable research groups such as those led by Brillas and Oturan [83,84], this technology operates through a series of steps (Fig. 2.4 [85]): i) the *in situ* electro-generation of H_2O_2 through the two-electron oxygen reduction reaction (ORR), which is influenced by the applied current intensity and the level of dissolved oxygen (Eq. 2.1) [86]; ii) the production of ·OH radicals through the Fenton reaction, which occurs between Fe^{2+} ions and electro-generated H_2O_2 (Eq. 2.2); iii) the enhancement of physisorbed ·OH radical formation on the electrode surface, particularly when using advanced materials like boron-doped diamond (BDD) as the anode, as detailed in Eq. 2.3 and Eq. 2.4 [87]; iv) the regeneration of Fe^{3+}/Fe^{2+} redox cycle through direct reduction at the cathode (Eq. 2.5) [88].

$$O_2 + 2H^+ + 2e^- \rightarrow H_2O_2 \quad (2.1)$$

$$Fe^{2+} + H_2O_2 + H^+ \rightarrow Fe^{3+} + H_2O + \cdot OH \quad (2.2)$$

$$BDD + H_2O \rightarrow BDD(\cdot OH) + H^+ + e^- \quad (2.3)$$

$$BDD(\cdot OH) + organic\ compounds \rightarrow BDD + oxidised\ products \quad (2.4)$$

$$Fe^{3+} + e^- \rightarrow Fe^{2+} \quad (2.5)$$

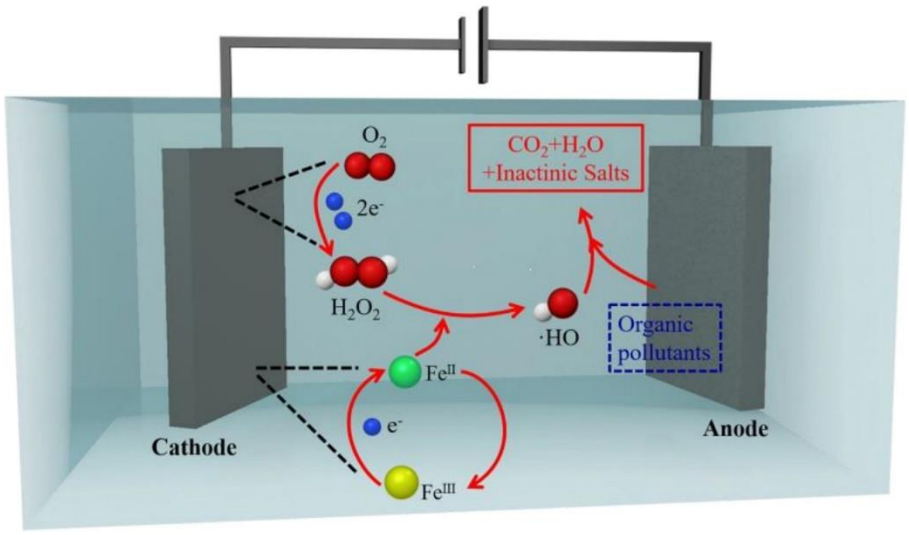

Figure 2.4. Mechanistic diagram of a hetero-EF process.

However, the above reactions predominantly occur in homogeneous solutions, which necessitate an optimal pH of around 3 and the presence of Fe^{2+} ions, which subsequently need to be removed *via* precipitation, leading to the generation of undesired iron sludge. To date, EAOPs have been mainly explored on a laboratory scale, with limited progress toward pilot or large-scale implementation [83]. Brillas *et al.* highlighted that the gap between experimental research and real-world applications is often due to technical, environmental, and economic challenges. These challenges could be addressed through several strategic modifications [89]: enhancing the design of electrochemical cells or reactors; developing advanced electrodes with superior electrocatalytic properties; improving mass transfer efficiency within the system; designing more effective catalysts; optimising operational parameters such as applied voltage or current intensity, operational pH, temperature, and catalyst dosage; and enhancing process modelling to predict pollutant behaviour.

To address the limitations associated with homogeneous EAOPs, recent research has shown that heterogeneous catalysts offer superior performance in breaking down organic contaminants compared to their homogeneous counterparts [90]. In heterogeneous Fenton systems, iron species are immobilised within solid catalysts, facilitating the activation of H_2O_2 to generate surface-bound radicals [91]. These processes are effective across neutral or even alkaline conditions, where surface-attached ·OH radicals are produced through the interaction between H_2O_2 and surface iron species (≡Fe(II)) (Eq. 2.6), significantly contributing to the degradation of pollutants [92]. The heterogeneous approach offers

additional advantages, such as the ability to operate over a wider pH range, potentially eliminating the need for effluent neutralisation; it minimises the generation of iron hydroxide sludge and the complications associated with its disposal; and the catalysts are easier to handle, can be efficiently recovered, and offer reusability potential.

$$\equiv Fe(II)+H_2O_2+H^+ \rightarrow \equiv Fe(III)+H_2O+\cdot OH \quad (2.6)$$

The described reaction mechanisms underscore the necessity for an effective catalyst in both the electrochemical reduction of oxygen to produce H_2O_2 and its subsequent activation to generate ·OH radicals in heterogeneous electro-Fenton processes [93]. Traditionally, separate catalysts have been used for each of these processes. However, recent research indicates that certain Fe or alloy particles embedded within carbon matrices exhibit remarkable catalytic properties for both the $2e^-$ oxygen reduction and heterogeneous Fenton reactions, suggesting their potential as dual-function catalysts for direct reactive radical generation from O_2. Additionally, emerging studies highlight the efficacy of metal-free carbon materials and transition single-atom catalysts, which have also demonstrated significant promise as bifunctional catalysts [94].

2.2.3 Role of EF systems in microcontaminant degradation

There is growing research interest in novel EF methods aimed at enhancing the removal of persistent, low-concentration, and challenging contaminants in water, especially pharmaceutical substances such as non-steroidal anti-inflammatory drugs (NSAIDs) and antibiotics. Table 2.2 summarises several studies on heterogeneous EF systems for pharmaceutical compound degradation in water [95]. These studies utilise catalysts such as pyrite, chalcopyrite, and nano-Fe_2O_3 with different anodes and cathodes like boron-doped diamond/carbon-felt (BDD/CF) and Pt sheet/graphite felt (GF). Operational conditions typically include a supporting electrolyte concentration, pH levels ranging from 3 to 7, and varying current intensities and airflow rates. The removal efficiencies for these pharmaceuticals are high, often reaching 100%, with total organic carbon (TOC) decay rates also being significant, indicating substantial degradation of the compounds. For instance, the antibiotics tetracycline and sulfamethazine show almost complete removal in relatively short times under specific operational conditions. These results underscore the effectiveness of electro-Fenton processes in removing contaminants from water, highlighting those conditions such as pH, catalyst type, and operational settings play crucial roles in determining efficiency.

The mineralisation routes of these substances are influenced by the molecular configuration of the target contaminant and the applied operating parameters, yet similar oxidation steps are observed in the degradation and mineralisation processes facilitated by EF and EF-like methods. Specifically, hydroxylation reactions on side chains are initiated by ·OH radical attack, leading to the formation of hydroxylated cyclic hydrocarbons through the cleavage of various bonds such as C-S, N-N, C=C, N=N, C-C, C-N, and S-N. For example, the C=C bond in the tetracycline molecule (Fig. 2.5 [96]) is particularly susceptible to hydroxyl radical attacks, yielding primary intermediates. Subsequent reactions (including hydroxylation, deamination, dechlorination, decarboxylation, desulfonation, and demethylation), along with ring-opening processes, result in the production of short-chain carboxylic acids, which are the precursors to the complete mineralisation into CO_2, H_2O, and inorganic ions [95].

Table 2.2. Studies on removal of common pharmaceutical products using heterogeneous electro-Fenton systems.

(TOC: total organic carbon, BDD: boron-doped diamond, CF: carbon felt, GF: graphite felt, MSWCNTs: magnetic single walled carbon nanotubes, AFR: air flow rate, GO: graphene oxide, PTFE: polytetrafluoroethylene.)

Pharmaceutical (Concentration)	Catalyst (Concentration)	Anode /Cathode	Operational Conditions	Removal and TOC Decay	References
Sulfamethazine (0.2 mM)	Pyrite (2 g/L)	BDD/CF	0.05 M Na_2SO_4, pH:3, AFR: 1 L/min, I = 300 mA	100% removal (40 min)	[97]
Tetracycline (0.2 mM)	Pyrite (2 g/L)	BDD/CF	0.05 M Na_2SO_4, pH:3, AFR: 1 L/min, I = 300 mA	100% removal (20 min) 96% TOC decay (480 min)	[87]
Tetracycline (0.2 mM)	Chalcopyrite (1 g/L)	BDD/CF	0.05 M Na_2SO_4, pH:5.94, AFR: 0.6 L/min, I = 300	100% removal (7 min) 85% TOC decay (120 min)	[98]

			mA		
Cephalexin (50 mg/L)	Chalcopyrite (1 g/L)	IrO_2/air diffusion cathode	0.05 M Na_2SO_4, pH:3, AFR: 0.6 L/min, I = 125 mA	94% removal (15 min) 44% TOC decay (300 min)	[99]
Amoxicillin (20 mg/L)	Nano–Fe_3O_4 (1 g/L)	Pt sheet/GF	0.01 M Na_2SO_4, pH:3, AFR: 1 L/min, I = 300 mA	98.2% removal (60 min)	[100]
Diclofenac (140 mg/L)	Fe_2O_3–modified chitosan (20 g/L)	BDD/CF	0.01 M Na_2SO_4, pH:6, AFR: 1 L/min, I = 300 mA	95% removal (120 min) 74.4% TOC decay (8 h)	[101]
Sulfamethizole (25 mg/L)	$FeCl_3$–modified perlite (n.a.)	BDD/CF	0.01 M Na_2SO_4, pH:6, AFR: 1 L/min, I = 300 mA	100% removal (15 min) 65% TOC decay (120 min)	[102]
Enoxacin (0.25 mM)	Fe_2O_3–modified kaolin (1.7 g/L)	BDD/CF	0.05 M Na_2SO_4, pH:3, AFR: 1 L/min, I = 300 mA	100% removal (15 min) 98% TOC decay (420 min)	[103]
Diclofenac (10 mg/L)	MSWCNTs–$FeCl_2$ (80 mg/L)	Ti–RuO_2/GF	0.05 M Na_2SO_4, pH:5, AFR: 1 mL/min, d = 20 mA/cm^2	97.8% removal (120 min) 71% TOC decay (120 min)	[104]
Gentamicin (20 mg/L)	Cu–Fe–NLDH (1.25 g/L)	Pt sheet/graphite plate	0.05 M Na_2SO_4, pH:6, AFR: 10 L/h, I = 400 mA	91.3% removal (100 min)	[105]
Nafcillin (36 mg/L)	Fe/Cu bimetallic nanoparticles (1 g/L)	BDD/carbon–PTFE air	0.05 M Na_2SO_4, pH:7, d = 5 mA/cm^2	100% removal (7 min)	[106]

		diffusion			
Chloramphenicol (80 mg/L)	Fe_3O_4–GO (0.5 g/L)	Pt gauze/CF	0.05 M Na_2SO_4, pH:3, AFR: 10 L/h, I = 300 mA	100% removal (45 min) 86% TOC decay (300 min)	[107]
Metronidazole (80 mg/L)	Fe_3O_4–GO (0.5 g/L)	Pt gauze/CF	0.05 M Na_2SO_4, pH:3, AFR: 10 L/h, I = 300 mA	100% removal (15 min) 73% TOC decay (300 min)	[107]
Propranolol/acebutolol (200 ng/mL each)	Fe–C (119 mg/L)	BDD/air diffusion cathode	0.05 M Na_2SO_4, pH:7, d = 75 mA/cm^2	100% removal (15 min)	[108]
Diclofenac (50 mg/L)	Pyrite (8 g/L)	Pt mesh/air diffusion cathode	0.05 M Na_2SO_4, pH:7, AFR: 0.4 L/min, d = 31.84 mA/cm^2	97.8% removal (8 min) 85% TOC decay (180 min)	[109]
Gemfibrozil (10 mg/L)	nano-ZVI@C–N (0.2 g/L)	Ti–IrO_2/air diffusion cathode	0.05 M Na_2SO_4, pH:6, AFR: 1 L/min, I = 300 mA	95% removal (60 min)	[110]

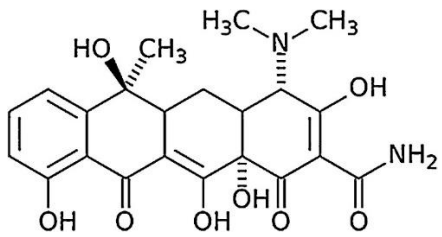

Figure 2.5. Structure of tetracycline molecule.

The application of electrochemical methods for decomposing MPs/NPs in water samples is still in its infancy, with a summary of studies listed in Table 2.3. The electrooxidation (EO) method represents a promising approach for addressing water pollution caused by MPs/NPs. Research has demonstrated the effectiveness of EO in treating synthetic

monodispersed MP suspensions [111]. This process, utilising a boron-doped diamond (BDD) anode, has proven to be a viable technology in treating water contaminated with MPs. Employing 0.03 M sodium sulphate as a supporting electrolyte and maintaining a current of 9 A over a 6-hour electrolysis period achieved a substantial MP degradation efficiency of 89%. Although the EO approach offers potential for MP degradation in real wastewater environments, further investigation is required to address potential challenges such as anode fouling and interactions with other contaminants. Another electrocatalytic oxidation method featuring a CeO_2-modified PbO_2 anode (CeO_2-PbO_2) was developed for degrading polyvinyl chloride microplastics (PVC-MPs) [112]. The CeO_2-PbO_2 anode demonstrated enhanced electrocatalytic performance compared to a pure PbO_2 anode, achieving a higher PVC-MP weight loss rate of 38.67% after 6 hours of treatment, in contrast to 22.11% observed with the pure PbO_2 anode. During the process (Fig. 2.6), ·OH radicals attack and disrupt the long-chain of PVC structure. The resulting small molecules undergo additional oxidation or cleavage at C=C and C-C bonds while chlorine atoms are removed from the polymer and its intermediates, thus facilitating the breakdown of molecular structure. Despite the improved efficiency, the weight loss rate indicates that the PVC-MP degradation rate using this method is relatively slow. There is a need to further optimise the electrochemical method to improve its performance. Furthermore, an electrooxidation-H_2O_2 system has been introduced for MP and NP degradation, employing a BDD anode and a carbon-felt cathode [113]. This setup not only generates reactive oxygen species, including ·OH and $\cdot SO_4^-$, at the BDD anode but also produces ·OH through O_2 reduction at the cathode, along with $\cdot SO_4^-$ formation through direct or indirect reactions with *in situ* generated H_2O_2. These species collectively enhance the effective degradation of MPs/NPs. Compared to traditional electrooxidation processes, the electrooxidation-H_2O_2 approach demonstrates a 2.6-fold improvement in the degradation rate of polystyrene (PS) NPs.

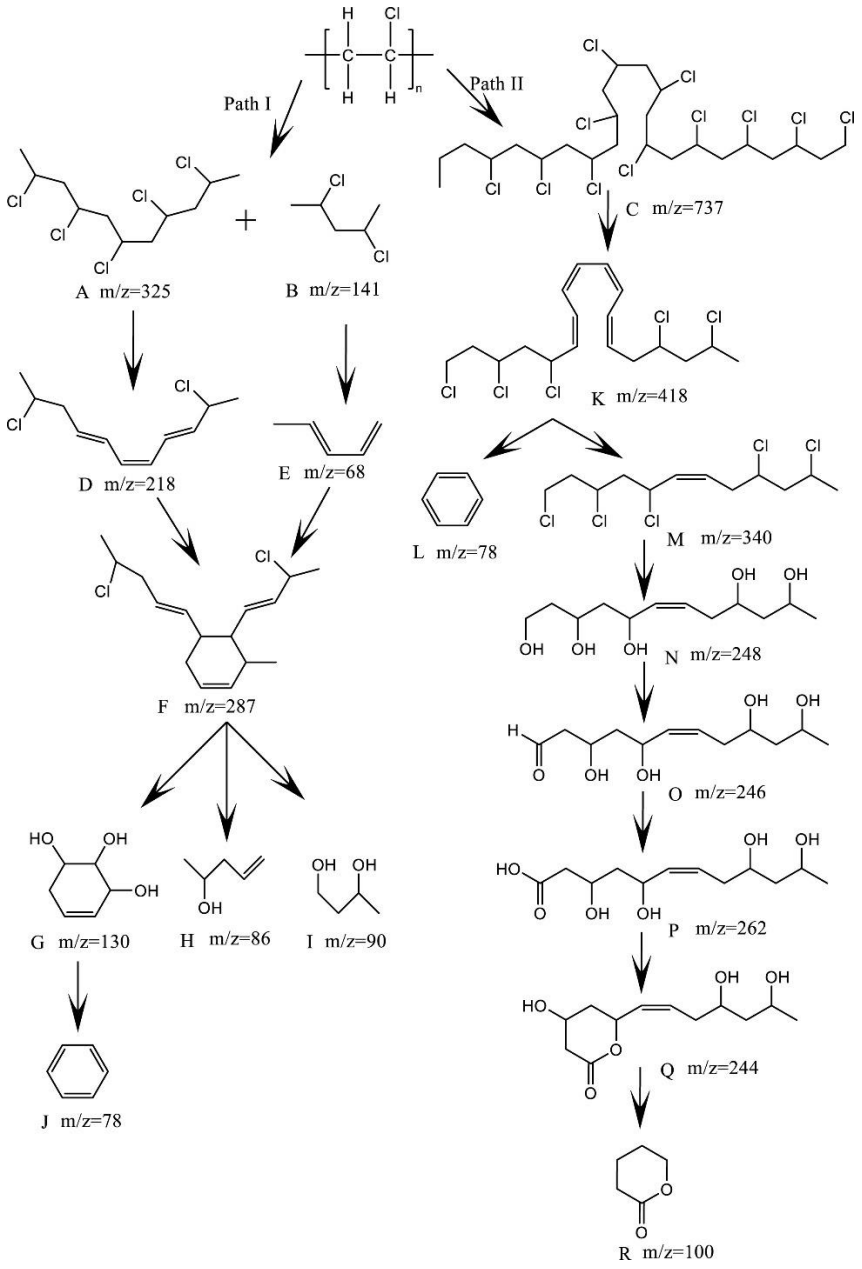

Figure 2.6. Possible degradation pathways of PVC-MPs in electrocatalytic oxidation within CeO_2-PbO_2 anode.

In addition to the EO method, one study explored the decomposition of PVC MP using an electro-Fenton-like process equipped with a TiO_2/graphite cathode [114]. This system demonstrated considerable efficacy in decomposing PVC MPs through ·OH oxidation and cathodic reduction dichlorination. Within a 6-hour reaction period, dichlorination efficiency reached 75%, and the weight loss of PVC was recorded at 56%. The dichlorination of PVC predominantly occurred *via* direct reduction driven by the applied cathode potential, while generated ·OH radicals led to the oxidation and fragmentation of the PVC backbone. However, it remains unclear whether this method is applicable to

other classes of MPs, and the reaction efficiency requires further enhancement. Another study investigated a remediation approach for polystyrene microplastics, incorporating sodium dodecyl sulphate (SDS) to improve reaction efficacy within an electrochemical advanced oxidation process using a BDD anode [115]. This EAOP approach succeeded in removing over 40% of MPs at a current density of 30 mA/cm^2, within a high MP dosage of 2 g/L, demonstrating significant efficiency improvement with SDS compared to BDD electrolysis alone. The addition of SDS substantially increased the degradation rate of MPs in 72 hours of EAOP operation, achieving 1.35-2.29 times increase relative to BDD electrolysis alone. The SDS-enhanced EAOP also resulted in a more noticeable change in particle size, morphology, and functional groups of MP particles. Post-reaction analysis revealed the formation of various alkyl-cleavage and oxidation products, indicative of the potent oxidative attack by oxidants, such as persulfate, on the MPs.

Table 2.3. Summary of some relevant studies on electrochemical methods for plastics decomposition.

Plastic	Technique	Functional materials	Critical parameters	Performance	Year	Reference
100 mg/L PS MPs	Electrochemical oxidation	BDD as anode	0.03 M Na_2SO_4; Current 9 A; 6h	Weight loss 89%	2021	[111]
100 mg/L PVC MPs	Electron-Fenton like system	TiO_2/graphite as cathode	Na_2SO_4 electrolyte; -0.7 V vs. Ag/AgCl; 6h; 100°C	Weight loss 56%; dichlorination rate 75%	2020	[114]
100 mg/L PVC MPs	Electrochemical oxidation	CeO_2-PbO_2 as anode	40 mA/cm^2; 0.05 M Na_2SO_4; 6h; 100°C	Weight loss 38.7%	2023	[112]
2 g/L PS MPs + 500 mg/L sodium dodecyl sulfate (SDS)	Electrochemical + surfactant	BDD-anode Pt-cathode	30 mA/cm^2; 0.2 M Na_2SO_4; 72h; 25°C	Weight loss 40%	2022	[115]

25 mg/L PS-NPs	Photoelectro-Fenton microreactor	MOF-derived porous α-Fe_2O_3 film	$[H_2O_2]$ = 0.5 mol/L, $[Na_2SO_4]$ = 0.05 mol/L, pH = 2, 1.2 V bias and 120 mW/cm^2 solar irradiation.	Over 80%	2023	[116]
1g/L Polyethylene (150 μm) or polyethylene terephthalate (250 μm)	Electrolysis	Titanium grids coated with Pt (cathode) or mixed Ti/Ru/Ir oxides (anode)	10 mA/cm^2; 750h	About 70% weight loss	2023	[117]

2.2.4 Advantages and challenges

Compared to traditional water treatment methods, electro-Fenton processes offer several distinct advantages [118]. These processes eliminate contaminants either through direct application of electrical potential or current, or *via* the *in-situ* generation of chemical reagents. These approaches may reduce some of the financial burdens, health risks, and environmental impacts associated with the transportation, storage, and disposal of chemical reagents or waste sludge. EF treatments provide versatile design options that can address a wide range of pollutants, including the mineralisation of recalcitrant organic contaminants into harmless CO_2 and H_2O. Additionally, the rapid kinetics of these reactions enable the use of compact, modular reactor designs [119]. Operations can be extensively automated, allowing precise control over the reaction rates and treatment levels. Moreover, electrode materials can be tailored to selectively target specific contaminants, thus enhancing efficiency, reducing energy consumption, and facilitating the recovery of resources.

Current research efforts have largely focused on developing novel wastewater treatment methods to eliminate pharmaceuticals from synthetic wastewater in batch systems, with limited emphasis on EF system scale-up for practical electrochemical applications. There is a necessity to develop heterogeneous-based EF processes in continuous flow systems

to facilitate real-world water treatment scalability. Substantial effort has been invested in creating innovative solid iron-based materials or iron-functionalised catalysts. However, further research is required to assess their performance at near-neutral pH conditions to ensure greater stability while preserving their capability to catalyse the Fenton reaction and generate reactive radicals [95]. Economic evaluations are critical for the broader adoption of EF technology, as challenges such as high energy consumption, slow degradation rates, reactor scalability issues, and catalyst reusability contribute to elevated operating costs in this emerging research area. Future investigations should address engineering and technical optimisation of reactor designs, flow dynamics, and primary treatment effectiveness [120]. Additionally, exploring cost-effective strategies such as utilising affordable reagents and electrode materials, enhancing the generation and utilisation of hydroxyl radicals, and minimising sludge production, could significantly lower operational expenses, thus enhancing the feasibility of EF technology for wastewater treatment.

To summary, in terms of the decomposition of MPs/NPs using electrochemical technologies, the currently reported electrochemical techniques necessitate integration with other technologies or reagents, such as UV irradiation [116] or surfactants [115] to enhance degradation efficiency. Some systems require stringent operational conditions, such as high temperatures [114] and current densities [112, 115], which entail increased costs and energy consumption. Furthermore, most of these techniques involve long reaction times [115, 117], thus there is a need to further improve reaction efficiency. Additionally, the universality of the developed technologies warrants further investigation, including assessing the effectiveness of the reaction systems in removing various types and sizes of MP/NP contaminants. Lastly, the degradation pathways and the environmental impact of degradation intermediates should be identified to ensure the safety of treated water.

2.3 Selective oxygen reduction reaction in heterogeneous EF processes

The design of cathode materials is critical for the practical application of EF technology in the treatment of micropollutants in water. In the heterogeneous EF process, enhancing *in situ* H_2O_2 production requires the development of optimised cathode materials with superior two-electron oxygen reduction reaction ($2e^-$ ORR) catalytic performance. This process overcomes the limitations of traditional Fenton technologies, which require

offsite production, transportation, and storage of H_2O_2. Ideal cathode materials should also exhibit high catalytic activity for *in situ* activation of H_2O_2 to enhance the production efficiency of reactive oxygen species. Additionally, the cathodes should possess excellent structural properties, such as high stability, superior electrical conductivity, a large surface area, and adaptability to a wide pH range, fulfilling requirements of industrial applications.

2.3.1 Mechanisms of ORR

Hydrogen peroxide (H_2O_2) is recognised as a versatile and eco-friendly reagent for various remediation applications. In a heterogeneous electro-Fenton (EF) system, H_2O_2 is generated *via* the selective oxygen reduction reaction (ORR), which proceeds through two distinct pathways: (i) the two-electron reduction pathway, serving as the primary reaction (Eq. 2.7, 2.9, 2.11), and (ii) the four-electron reduction pathway, acting as a competing reaction (Eq. 2.8, 2.10). The corresponding reaction equations for selective ORR through varying pathways and pH conditions are presented as follows, where RHE represents the reversible hydrogen electrode [121]:

In acidic conditions (pH < 7):

$$O_2+2H^++2e^-\rightarrow H_2O_2,\ E^0=0.70\ V\ vs.\ RHE \quad (2.7)$$

$$O_2+4H^++4e^-\rightarrow H_2O,\ E^0=1.23\ V\ vs.\ RHE \quad (2.8)$$

In basic conditions (7 < pH < 11.7):

$$O_2+H_2O+2e^-\rightarrow H_2O_2+2OH^-,\ E^0=0.70\ V\ vs.\ RHE \quad (2.9)$$

$$O_2+H_2O+4e^-\rightarrow 4OH^-,\ E^0=1.23\ V\ vs.\ RHE \quad (2.10)$$

At pH > 11.7

$$O_2+H_2O+2e^-\rightarrow HO_2^-+2OH^-,\ E^0=0.76\ V\ vs.\ RHE \quad (2.11)$$

The two-electron ORR for H_2O_2 production occurs in two sequential steps involving proton-coupled electron transfer and the formation of the HOO^* intermediate on active catalytic sites. Initially, an O_2 molecule adsorbs onto the active sites of the catalyst, where it interacts with a proton (H^+) and undergoes electron transfer, resulting in the formation of the HOO^* intermediate (Eq. 2.12, * represents the active sites of the electrocatalysts). In the subsequent step, generated HOO^* combines with an additional H^+, completing the two-electron pathway and yielding H_2O_2 (Eq. 2.13). Since the $2e^-$ ORR mechanism relies on HOO^* as the intermediate product, the selective single-electron reduction of HOO^* facilitates the targeted generation of H_2O_2 while suppressing further reduction to H_2O.

Further, the cleavage of the O-O bond in H_2O_2 *via* a proton-coupled electron transfer generates $^*OH$ and H_2O, resulting in the generation of highly reactive ·OH on the catalyst's active sites (Eq. 2.14) [122].

$$O_2 + H^+ + {}^* + e^- \rightarrow HOO^* \quad (2.12)$$

$$HOO^* + H^+ + e^- \rightarrow {}^* + H_2O_2 \quad (2.13)$$

$$H_2O_2 + {}^* + H^+ + e^- \rightarrow {}^*OH + H_2O \quad (2.14)$$

2.3.2 Carbon-based cathodes in EF processes for H_2O_2 generation

One primary approach to enhance the performance of the $2e^-$ pathway in ORR involves developing and modifying cathode materials, as demonstrated in Fig. 2.7 [121]. This focus not only facilitates efficient H_2O_2 production but also considers factors such as current efficiency and energy consumption. Ideally, catalysts optimised for the $2e^-$ ORR should exhibit excellent electrical conductivity, durability, and acid corrosion resistance. Carbon-based electrocatalysts have gained growing attention for ORR owing to their exceptional stability, tuneable surface properties, controllable porosity, and low cost [123]. The electrocatalytic performance of these materials can be improved by tailoring their surface chemical characteristics and structural features.

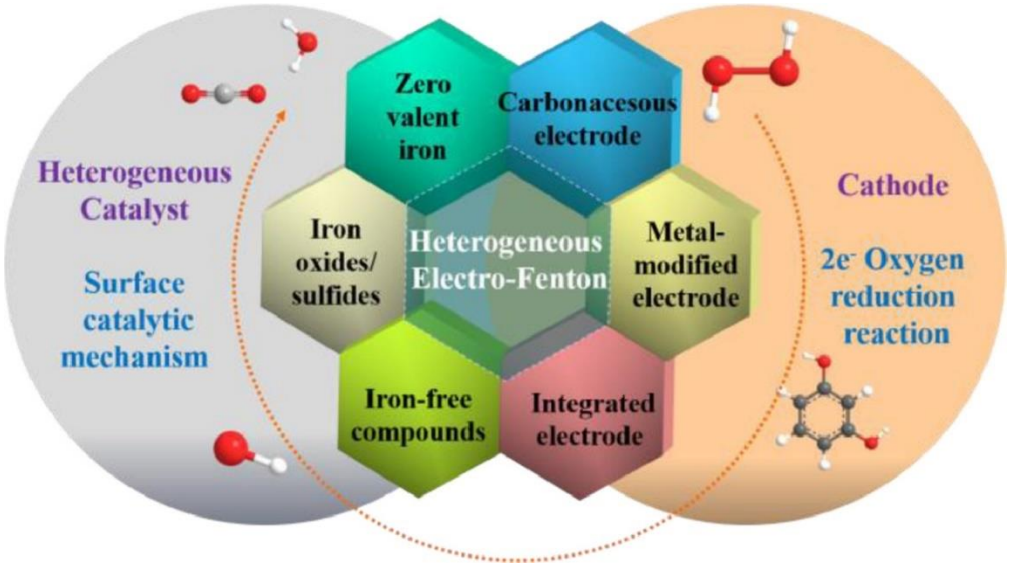

Figure 2.7. Cathode and heterogeneous catalysts for the heterogeneous electro-Fenton system.

The most commonly used carbon-based cathodes are commercially available materials such as carbon felt (CF), carbon nanotubes (CNTs), and activated carbon fibre (ACF). CNTs have gained great attention for $2e^-$ ORR because of their exceptional features,

including a large surface area, remarkable mechanical durability, chemical stability, and superior electrical conductivity. Additionally, their high adsorption capacity makes them ideal candidates for eliminating organic pollutants [124]. CF is widely recognised as one of the most efficient materials for addressing persistent organic pollutants, attributed to its stable physicochemical characteristics and cost-effectiveness [125]. ACF, a prominent nanoporous carbon material, exhibits superior conductivity, surface area, adsorption capacity, and catalytic performance. The transformation of ACF's 2D planar structure into a quasi-3D electrode, driven by its larger surface area, enhances diffusion-limited currents, facilitating more efficient H_2O_2 generation [126].

The limited catalytic efficiency of carbonaceous cathodes often necessitates applying a high potential during the ORR process to generate H_2O_2, which compromises overall production efficiency [127]. The catalytic properties of carbon materials are primarily attributed to the electronic alterations in their sp^2-sp^2 conjugated linkages or π-orbital electron delocalisation within their graphitic structures [121]. Incorporating heteroatoms such as oxygen (O), nitrogen (N), boron (B), sulphur (S), or fluorine (F) into metal-free carbon frameworks alters the local electronic distribution, creating partially charged functional groups. These changes enhance the adsorption of oxygenated intermediates and promote selective H_2O_2 production [128]. Additionally, well-designed heteroatom doping can improve structural parameters, such as hydrophilicity, pore distribution, and surface area, thereby elevating the electrocatalytic performance of the cathode materials [85]. For example, the role of oxygen-containing functional groups, similar to the effect of nitrogen doping, increases H_2O_2 generation. When carbon nanotubes underwent treatment with concentrated nitric acid, the selectivity for H_2O_2 increased significantly from 60% to 90% [129]. A strong linear relationship was identified between the oxygen content and both the activity and selectivity for H_2O_2 generation. The carbon atoms located near oxygen functional groups such as -COOH and C-O-C were identified as the active sites facilitating the ORR process.

In addition to heteroatom doping, many studies also reported the design of electrocatalysts with enhanced activity and selectivity for the $2e^-$ ORR through the incorporation of transition metals. Materials based on transitional metals include single-atom catalysts (SACs), metal sulphides, and metal oxides. Compared to noble materials, these transition metal-based materials offer benefits such as cost-effectiveness,

environmental compatibility, and abundant availability. Furthermore, the inclusion of transition metals can optimise adsorbate binding, thereby improving both activity and selectivity for H_2O_2 production [130]. For example, Barros *et al* [131] synthesised Fe_3O_4/graphene and Fe_3O_4/Printex carbon catalysts by incorporating nanoscale Fe_3O_4 particles on the carbon matrix. The results showed that Fe_3O_4/graphene demonstrated superior catalytic performance for the ORR, characterised by increased current density, a more positive onset potential, and remarkable durability. In contrast, Fe_3O_4/Printex showed greater selectivity in the electro-generation of H_2O_2. Single-atom catalysts, a burgeoning area in the field of catalysis, feature catalytically active metals dispersed at the atomic scale. Sun *et al* [132] explored H_2O_2 electrochemical production using M-N-C materials (M = Cu, Mn, Ni, Fe, and Co), revealing that Co-N-C catalysts exhibit exceptional H_2O_2 productivity. The binding energy of the HO* intermediate on Co-N-C was found to be near the peak of a volcano plot, indicating a highly favourable two-electron ORR pathway.

2.4 Bifunctional electro-Fenton cathodes for *in-situ* ·OH generation

Despite advancements in on-site H_2O_2 production through EF and ORR processes, several challenges remain to be addressed, such as secondary pollution associated with Fenton catalysts and the requirement for two distinct catalysts: one selectively reducing oxygen to H_2O_2 and the other functioning as a Fenton-like catalyst to convert H_2O_2 into hydroxyl radicals. Recent efforts have focused on developing dual-functional materials capable of both electrochemical oxygen reduction to H_2O_2 and Fenton catalysis. The strategies for designing dual-functional catalysts for the electrochemical production of H_2O_2 and its subsequent activation to generate ·OH radicals include: (1) metal composite catalysts without carbon; (2) metal-free carbon catalysts; (3) metal/carbon composite catalysts.

2.4.1 Metal composite catalysts without carbon

There are limited studies reporting the fabrication of metal composite catalysts without carbon to catalyse the synthesis and activation of H_2O_2. Within metal composite catalysts, the generation and activation of H_2O_2 can take place either on the same or on distinct metal active sites. Adjusting the proportion of different metal components can impact the catalytic behaviour. For instance, Ross *et al* [133] explored trimetallic thiospinel with a compositionally optimised formula ($CuCo_{2-x}Ni_xS_4$, $0 \leq x \leq 1.2$) as an effective dual-function catalyst. Transition metal sulphides, such as $CuCo_2S_4$, have demonstrated activity in the

$2e^-$ ORR. The partial replacement of Co with Ni in $CuCo_2S_4$ was employed to enhance its ORR efficiency. Interestingly, the study highlighted that an acid treatment process was essential for producing ·OH species, as the leached Cu^+ ions activated H_2O_2 to generate ·OH.

2.4.2 Metal-free carbonous catalysts

While heterogeneous catalysts with trapped or bonded metals can effectively reduce metal ion loss and enhance stability compared to homogeneous Fenton processes, developing metal-free carbonaceous catalysts for heterogeneous EF systems eliminates the risk of metal ion leaching under acidic conditions. As a result, there is growing interest in creating carbon-based, metal-free catalysts for such applications. Previous research has shown that carbon-based materials like carbon black, activated carbon, and graphite can catalyse the generation and activation of H_2O_2 to produce ·OH radicals [134]. However, their catalytic performance is often not as good as metal-containing catalysts. To enhance the activity of carbon catalysts, extensive studies have focused on catalyst modification and investigating the reaction mechanisms [135].

Qin *et al* [136] synthesised oxygen-doping carbon nanotubes by treating them at temperatures between 40 and 100 °C for one hour and utilising them for phenol degradation under neutral pH conditions. The production of H_2O_2 was found to increase linearly with the proportion of sp^3–C bonds, while phenol degradation rates also showed a positive correlation with the proportion of –C=O groups on the surfaces of the nanotube. Similarly, boron-doped graphene has been employed as a bifunctional catalyst for heterogeneous EF technology. Positively charged B atoms ($–BC_3$) acted as active sites to break the O–O bond in H_2O_2, whereas electrophilic B sites (e.g., $–BC_2O$, $–BCO_2$) located at edges and defect regions, served as active sites for O_2 adsorption and H_2O_2 production.

In general, several factors have been found to impact the catalytic performance of carbon-based materials [94]: (1) a larger surface area provides more space for active catalytic sites; (2) high electrical conductivity facilitated the efficiency of electron transfer; (3) incorporating heteroatoms like B, N, and O or introducing structural defects greatly influenced catalytic activity. However, the specific role of various doping or defect configurations remains controversial; and (4) proper porosity affected H_2O_2 selectivity and mass transfer. For instance, Iglesias *et al* [137] demonstrated that micropores reduced

the retention time of H_2O_2, improving H_2O_2 selectivity by preventing further reduction to water.

2.4.3 Metal/carbon composite catalysts

In metal nanoparticle-supported catalysts, many active sites may not be accessible to reactants like O_2 or H_2O_2 in heterogeneous EF processes, thereby constraining their catalytic performance. Recent advancements suggest that single-atom catalysts, where metal nanoparticles are dispersed into isolated atomic metal sites, have exhibited markedly enhanced catalytic efficiency [138]. For instance, Song *et al* [139] integrated Fe atoms into defect-enriched graphene sheets and demonstrated that these Fe atoms were predominantly anchored at pyridinic–N sites. The interaction between Fe–N and Fe–O coordination significantly enhanced both the selectivity for H_2O_2 generation and the removal of organic contaminants, even under extreme pH conditions (pH<4 or pH>10). The possible mechanism for chloramphenicol (CAP) removal with the Fe/N-DG cathode is illustrated in Fig. 2.8 [139].

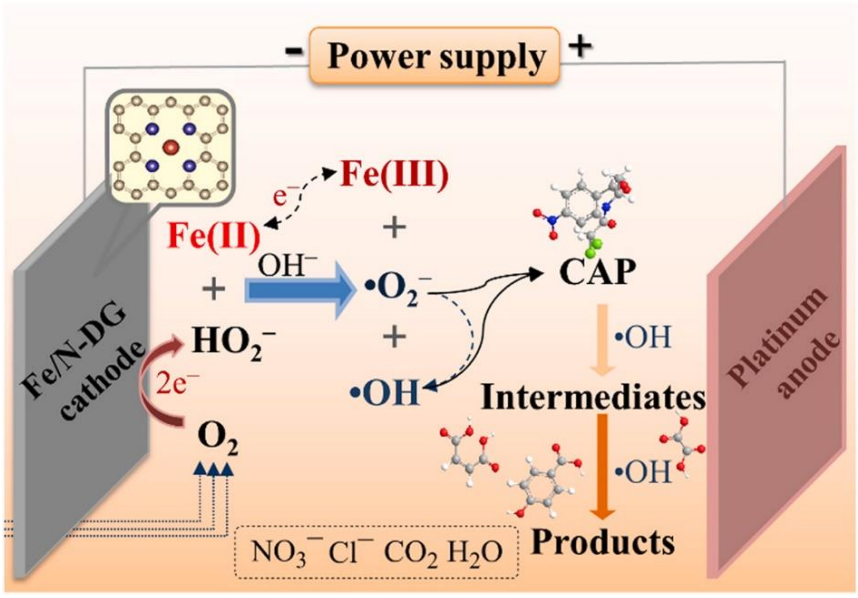

Figure 2.8. Schematic illustration of *in situ* H_2O_2 production and CAP removal on atomically dispersed Fe/N-DG cathodes under alkaline conditions.

Copper has been recognised as a key iron-free catalyst in heterogeneous electro-Fenton systems. The reaction rate of Cu^+ with H_2O_2 (1.0×10^4 $M^{-1}s^{-1}$) was significantly faster than that of Fe^{2+} (76 $M^{-1}s^{-1}$) [140]. Additionally, Cu^{2+} reduction to Cu^+ was more efficient compared to the reduction from Fe^{3+} to Fe^{2+}, due to the lower standard redox potential of the Cu^{2+}/Cu^+ couple (E = 0.16 V) than Fe^{3+}/Fe^{2+} couple (E = 0.77 V) [141]. Under neutral

pH conditions, Cu^{2+} may exist as $[Cu(H_2O)_6]^{2+}$, which allows Cu-based catalysts to demonstrate superior pH stability and catalytic performance [142]. Recent research highlighted that nitrogen-doped carbon-supported copper (Cu/N-C) functions as a bifunctional catalyst, enabling both H_2O_2 production and ·OH generation simultaneously [143]. By optimising pyrolysis temperature, it was shown that increasing the graphitic N and pyrrolic N content enhanced electron transfer and improved the adsorption of OHH^*, thereby boosting H_2O_2 selectivity. The composite structure also promoted better dispersion of Cu active sites and improved the catalyst's inherent conductivity. In summary, the combined effect of defect-rich N-doped carbon and dispersed copper significantly enhanced the $2e^-$ ORR, achieving a peak current density of 14.05 mA/cm^2.

Catalysts incorporating two or three metals with varying valence states, such as Fe, Ce, Co, Cu, La, Ni, Mo, and Mn, have shown remarkable activity and stability as dual-functional catalysts [94]. The incorporation of alloy nanoparticles or multi-metal composites into the carbon matrix is a widely employed strategy. For instance, previous research demonstrated that loading Ce and Fe on graphite felt enhanced the chemical absorption of O_2 through the presence of CeO_2, which facilitated H_2O_2 generation. Additionally, the presence of Fe(II)/Fe(III) and Ce(III)/Ce(IV) redox pairs improved interfacial electron transfer, boosting both H_2O_2 synthesis and activation [144].

Similarly, Xie *et al* [145] synthesised oxidised carbon felt modified with $LaCoO_3$ perovskite doped with Cu. While Cu doping reduced H_2O_2 synthesis efficiency on carbon felt, it significantly increased overall ·OH production. This improvement was attributed to the redox pairs Co(II)/Co(III) and Cu(I)/Cu(II), which enhanced radical generation. Furthermore, the introduction of Cu in $LaCoO_3$ increased oxygen vacancies, which promoted the adsorption of O species and enhanced the conversion of H_2O_2 into ·OH. The interaction between oxygen vacancies and O_2 also facilitated the reduction of absorbed O_2 to produce $\cdot O_2^-$, a reactive oxygen species for degrading pollutants. Li *et al* prepared an electrode containing Fe and Mn oxides coated with a carbon layer, in which the carbon component contributed to H_2O_2 production, while the metal oxides were primarily responsible for ·OH generation [146]. The addition of Mn significantly improved Fe^{3+}/Fe^{2+} regeneration by transferring electrons to Fe, accelerating the Fenton cycle.

An innovative method for fabricating bimetallic catalysts involves anchoring metal-based

layered double hydroxides (LDHs) onto carbon supports. LDHs are ionic compounds characterised by a layered configuration, where metallic cations are coordinated with hydroxyl groups in an octahedral arrangement. These structures offer a uniform distribution of metal sites for catalytic activity [94]. Ganiyu *et al* [147] successfully synthesised CoFe LDHs on carbon felt. In an acidic solution with low pH, a portion of Fe^{2+}/Co^{2+} ions leached from the catalyst, contributing to homogeneous Fenton reactions. At neutral pH, the catalyst demonstrated excellent stability, maintaining performance over seven reaction cycles through surface-catalysed processes.

In summary, bimetallic and trimetallic carbon composite catalysts outperform monometallic Fe/carbon catalysts by enhancing performance through several mechanisms: (1) other metal species, in addition to Fe, activate H_2O_2 to produce ·OH; (2) redox couples formed by additional metals promote Fe(III) reduction to Fe(II), driving Fenton mechanisms; and (3) introducing metals like Cu creates oxygen vacancies, which aid in reducing adsorbed O_2 to form $\cdot O_2^-$. The coexistence of two or more distinct metal species can effectively regulate the activity of individual metals, thereby enhancing bifunctional catalytic performance for electrosynthesis and *in situ* activation of H_2O_2.

2.5 The potential of alloy carbon aerogels as cathodes

2.5.1 Properties and synthesis of carbon aerogels

Since the early 1990s, carbon aerogels (CAs) have emerged as versatile materials with applications in areas such as water treatment [148], gas storage and separation [149], CO_2 reduction [150], catalysts and catalytic supports [151], and adsorption [152]. Their exceptional performance can be attributed to key properties, including a large surface area, good electrical conductivity, low density, diverse pore sizes, excellent corrosion resistance, and customisable surface chemistry. While traditionally utilised for adsorption and catalysis, CAs have more recently been investigated as cathode materials for electro-Fenton reactions [153].

CAs are commonly synthesised using wet chemical methods or sol-gel approaches, with precursors like melamine-formaldehyde (MF), phenol-formaldehyde (PF), resorcinol-formaldehyde (RF), and polymers such as polystyrenes and polyacrylonitriles [127]. Fig. 2.9 provides an overview of the CA synthesis process, which includes sol-gel formation,

ageing/solvent exchange, drying, and carbonisation [154]. During the gelation phase, crosslinking or polymerisation occurs, resulting in the formation of the gel structure. A critical step in aerogel production is drying the gel without causing dimensional shrinkage or structural collapse. The three primary drying techniques used are freeze-drying, ambient pressure drying, and supercritical drying. Although ambient drying is more cost-effective, it often leads to structural damage. Before drying under ambient conditions, acetone can be used as the exchange solvent to thoroughly replace any water remaining in the carbon structure because of its lower surface tension, which reduces shrinkage of the gel. The final step, carbonisation, involves heating the aerogel in a nitrogen or argon atmosphere at temperatures ranging from 600 ℃ to 2500 ℃ for 3 to 10 hours. This process removes oxygen and hydrogen groups, leaving a highly carbon-enriched network [155].

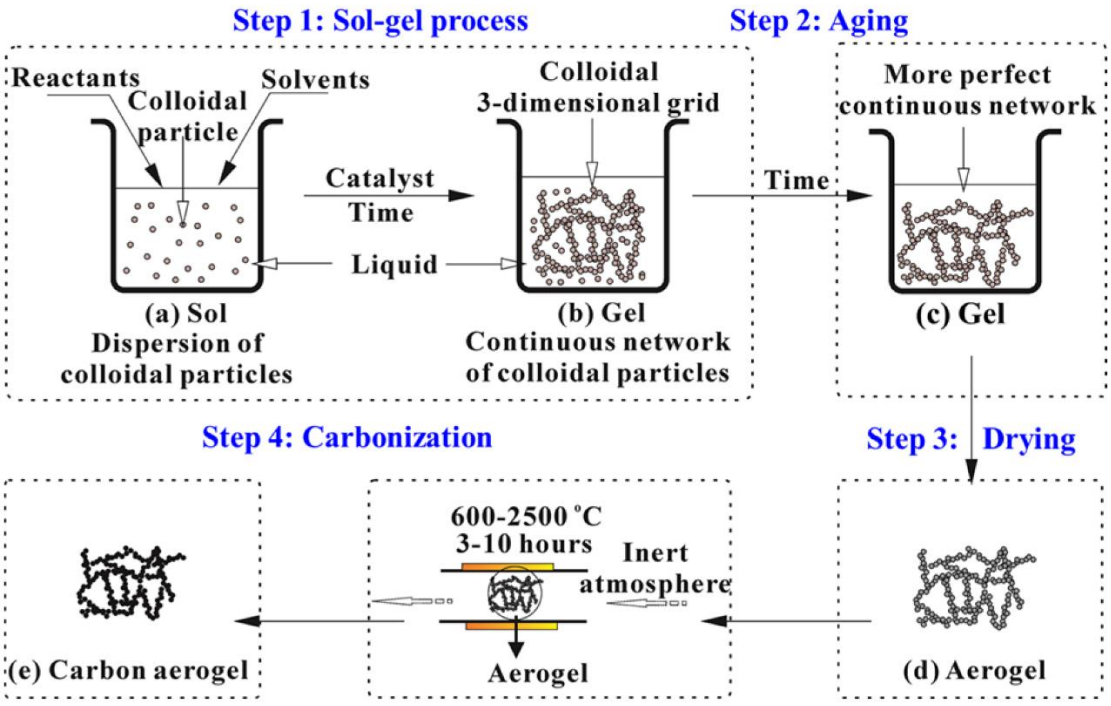

Figure 2.9. Schematic of carbon aerogel synthesis process.

2.5.2 Development of transitional metal-based carbon aerogels

Most studies have focused on CAs incorporated with iron or other transition metals (TMs) and their oxides as cathodes in heterogeneous EF systems [156]. To synthesise Fe/TMs-doped CA, metal precursors are introduced into the uniform solution prior to the formation of the sol. The integration of CAs with Fe dopants significantly enhances the performance of cathode materials in heterogeneous EF processes. For example, a mesoporous Fe_3O_4 carbon composite with an ordered structure was introduced onto CA

for degrading dimethyl phthalate (DMP) [157]. The presence of uniformly dispersed Fe_3O_4 particles significantly increased the number of catalytic sites and reduced resistance to mass transfer, achieving 95% removal of DMP within 120 minutes. In a recent advancement, a sulphide iron-based CA (FeSCA), containing Fe_3O_4 and $FeS{\cdot}FeS_2$, was employed as a heterogeneous EF cathode [158]. This system achieved 99% degradation of DMP and 3-chlorophenol (3-CP) within 240 minutes. The inclusion of sulphur promoted Fe(II)/Fe(III) regeneration and its even distribution enhanced the formation of –COOH groups, improving the selectivity of the $2e^-$ ORR.

In addition to single-metal doping, alloyed carbon aerogels have been utilised as effective catalysts for water treatment. A MOF(2Fe/Co)/CA cathode material, characterised by a large surface area and excellent catalytic properties, was developed and applied in a solar photo-electro-Fenton (SPEF) system [156]. This setup enabled consistent on-site H_2O_2 generation through the ORR, achieving an electron transfer number (n) of 2.5 in the applied potential range. The metal-organic framework (MOF) provided active sites that enhanced ORR activity, boosting H_2O_2 production. Furthermore, the photoinduced electrons (e^-) from MOF(2Fe/Co) facilitated the *in-situ* decomposition of H_2O_2, producing ·OH radicals for contaminant degradation.

2.5.3 Comparative analysis

In summary, carbon aerogels play a dual role in catalysis, serving as both highly active catalysts and as supports for metal or metal oxide catalysts. When used as catalysts, their three-dimensional network structure provides abundant active sites, while their strong adsorption capacity concentrates pollutants, enhancing catalytic efficiency. Furthermore, their excellent conductivity facilitates faster mass transfer, boosting overall reaction rates. As a result, carbon aerogels are widely employed as photocatalysts and electrocatalysts in environmental applications. As catalyst supports, carbon aerogels fulfil all essential criteria. Their unique composition and structural features can be tailored at the molecular level during the sol-gel synthesis process, offering flexibility in design. Moreover, their precursors exhibit a strong affinity for various catalysts, simplifying the process of catalyst loading and integration.

The impact of transition metal doping on carbon aerogels (CAs) remains underexplored. Most current research has concentrated on incorporating iron and its oxides into CAs to

enhance their catalytic performance. Subsequently, Fe-modified CAs have demonstrated exceptional efficiency as cathodes for both heterogeneous EF processes and photo-assisted heterogeneous EF reactions. Other transitional metals (such as Cu, Co, and Ni) should be further studied as potential catalytic components and applied to water treatment. Bimetallic-modified carbon aerogels have shown great potential as cathode materials for solar photo-electro-Fenton processes. The application of alloy carbon aerogels as bifunctional cathodes for heterogeneous EF systems and the synergistic and interactive mechanisms between metals and carbon aerogels should be further investigated.

2.6 Conclusions and research gaps

2.6.1 Conclusions

Pharmaceutical products, such as pain relievers and antibiotics, along with micro/nano plastics, in aquatic environments present serious challenges owing to their ecotoxicity and impacts on human health. Heterogeneous electro-Fenton (HEF) is among the most promising advanced oxidation processes (AOPs), showing significant potential for treating persistent organic pollutants in wastewater due to its broad pH adaptability and reusability. Substantial progress has been made in HEF research in recent years, particularly in developing heterogeneous catalysts. Transition metal-based carbon materials, as the most widely used and effective catalysts, have demonstrated outstanding performance in the electrosynthesis and the activation of H_2O_2 to produce various reactive oxygen species in the EF process.

By summarising recent advancements in micropollutants (pharmaceutical active compounds and micro/nano plastics) identification and treatment technologies, the principles and applications of electro-Fenton processes, selective oxygen reduction reaction and bifunctional electro-Fenton cathodes, and the potential of alloy carbon aerogels as cathode materials, the following conclusions may be drawn:

(i) Conventional wastewater treatment processes have limited ability to degrade pharmaceutical residues, including analgesics and antibiotics. Electro-Fenton systems demonstrate promising results for removing diverse organic contaminants, including pharmaceuticals, pesticides, and industrial byproducts.

(ii) The separation of micro/nano plastics has been extensively studied, but their degradation methods are still in their infancy, especially electrochemical methods.

Studies have shown that biological treatments are capable of degrading plastic particles to different degrees, however long treatment times are generally necessary to obtain effective performance in biodegradation.

(iii) The electrochemical methods reported to date often need to be combined with additional technologies or reagents, such as ultraviolet light or surfactants, to improve the degradation efficiency of micro/nano plastics. Other reported systems demand strict operating conditions, including elevated temperatures and high current densities, which increase costs and energy consumption.

(iv) The development of cathode materials plays a vital role in enabling the use of EF technology for treating micropollutants in water. In heterogeneous EF systems, achieving efficient *in situ* H_2O_2 generation necessitates the design of cathode materials with selective catalytic activity for $2e^-$ ORR. Optimal cathode materials should also demonstrate high catalytic efficiency for the activation of H_2O_2, thereby boosting the generation of reactive oxygen species.

(v) Various carbon-based materials, such as carbon felt, carbon aerogel, carbon nanotubes, and activated carbon fibre, are utilised in electrode fabrication to improve electrocatalytic performance. Among these, carbon aerogels stand out as an excellent option for electrode design due to their unique three-dimensional network structure, superior electrical conductivity, high surface area, and capability to serve as metal-supporting materials.

(vi) To date, the synergistic effects of transitional metals on structural features, electrochemical characteristics, and catalytic efficiency of carbon aerogel have not been comprehensively studied. Furthermore, the utilisation of bimetallic carbon aerogels as dual-function electrode materials for water purification requires further exploration and investigation.

2.6.2 Research gaps

Electro-Fenton (EF) technologies have been extensively explored for their application in removing microcontaminants. These advanced oxidation processes utilise electrochemical systems to generate hydroxyl radicals, providing a potent mechanism for breaking down complex pollutants and plastics. While considerable progress has been made in heterogeneous EF technologies for microcontaminant removal, several critical research gaps remain that hinder the full-scale adoption and optimisation of these technologies:

(i) Catalyst stability and durability: The stability and recyclability of catalysts, particularly transition metal-based and carbon-supported materials, are still concerns due to leaching and deactivation over time. Long-term studies are required to evaluate the performance of heterogeneous catalysts in continuous flow systems.

(ii) Adaptability across pH ranges: EF systems are typically limited to acidic conditions (pH $\leq$ 4), which hinders their applicability in neutral or alkaline wastewater treatment scenarios. Developing catalysts or processes that are effective in a broader pH range is an ongoing challenge.

(iii) Energy optimisation**:** High energy consumption remains a critical barrier; thus, more efficient and less intensive strategies should be explored to reduce energy demand without compromising degradation efficiency.

(iv) Mechanistic understanding: While mechanisms for radical generation and pollutant oxidation are generally understood, the detailed reaction pathways for specific contaminants and their by-products require further investigation. In particular there is a need to reduce or eliminate overall eco-toxicity in these systems.

(v) New technology development: Heterogeneous electro-Fenton application for micro/nano plastics degradation is still in its infancy. Dual-function catalysts for electro-reduction of oxygen to H_2O_2 and Fenton catalysis show great potential for plastic decontamination.

(vi) Environmental impact: Most research focuses on breaking down plastics into smaller fragments rather than complete mineralisation. Toxicological assessments of degradation intermediates and final products are often neglected, leaving potential environmental and health risks.

2.7 References

[1] M.& E. Inc., G. Tchobanoglous, H. Stensel, R. Tsuchihashi, F. Burton, Wastewater Engineering: Treatment and Resource Recovery, 5th Edition, 2014. https://www.mheducation.com/highered/product/Wastewater-Engineering-Treatment-and-Resource-Recovery-Metcalf-and-Eddy.html#mh-ecomm-he-product-accordion-1788683433-heading-mh-ecomm-accordion-list-5537edd483.

[2] L. Trotochaud, B.T. Hawkins, B.R. Stoner, Non-biological methods for phosphorus and nitrogen removal from wastewater: A gap analysis of reinvented-toilet technologies with respect to ISO 30500, Gates Open Res 3 (2020) 559. https://doi.org/10.12688/gatesopenres.12931.2.

[3] Council Directive 91/271/EEC of 21 May 1991 concerning urban waste-water treatment, 1991. http://data.europa.eu/eli/dir/1991/271/oj/eng.

[4] Directive 2000/60/EC of the European Parliament and of the Council of 23 October 2000 establishing a framework for Community action in the field of water policy, 2000. http://data.europa.eu/eli/dir/2000/60/oj/eng.

[5] P. Grenni, V. Ancona, A. Barra Caracciolo, Ecological effects of antibiotics on natural ecosystems: A review, Microchemical Journal 136 (2018) 25–39. https://doi.org/10.1016/j.microc.2017.02.006.

[6] S. Comber, M. Gardner, P. Sörme, D. Leverett, B. Ellor, Active pharmaceutical ingredients entering the aquatic environment from wastewater treatment works: A cause for concern?, Science of The Total Environment 613–614 (2018) 538–547. https://doi.org/10.1016/j.scitotenv.2017.09.101.

[7] T. Ternes, Pharmaceuticals and Metabolites as Contaminants of the Aquatic Environment, in: Pharmaceuticals and Care Products in the Environment, American Chemical Society, 2001: pp. 39–54. https://doi.org/10.1021/bk-2001-0791.ch002.

[8] P. Montuori, S.Z. Shojaeian, F. Pennino, D. D'Angelo, M. Sorrentino, S. Di Sarno, R. Nubi, A. Nardo, M. Triassi, Consumer awareness and knowledge regarding use of non-steroidal anti-inflammatory drugs (NSAIDs) in a metropolitan area, Front. Pharmacol. 15 (2024). https://doi.org/10.3389/fphar.2024.1362632.

[9] K. Świacka, A. Michnowska, J. Maculewicz, M. Caban, K. Smolarz, Toxic effects of NSAIDs in non-target species: A review from the perspective of the aquatic environment, Environmental Pollution 273 (2021) 115891. https://doi.org/10.1016/j.envpol.2020.115891.

[10] A. Mukhtar, M. Manzoor, I. Gul, R. Zafar, H.I. Jamil, A.K. Niazi, M.A. Ali, T.J. Park, M. Arshad, Phytotoxicity of different antibiotics to rice and stress alleviation upon application of organic amendments, Chemosphere 258 (2020) 127353. https://doi.org/10.1016/j.chemosphere.2020.127353.

[11] M. Ortúzar, M. Esterhuizen, D.R. Olicón-Hernández, J. González-López, E. Aranda, Pharmaceutical Pollution in Aquatic Environments: A Concise Review of Environmental Impacts and Bioremediation Systems, Front. Microbiol. 13 (2022). https://doi.org/10.3389/fmicb.2022.869332.

[12] K. Bondarczuk, Z. Piotrowska-Seget, Microbial diversity and antibiotic resistance in a final effluent-receiving lake, Science of The Total Environment 650 (2019) 2951–2961. https://doi.org/10.1016/j.scitotenv.2018.10.050.

[13] M. Bilal, S. Mehmood, T. Rasheed, H.M.N. Iqbal, Antibiotics traces in the aquatic environment: persistence and adverse environmental impact, Current Opinion in Environmental Science & Health 13 (2020) 68–74. https://doi.org/10.1016/j.coesh.2019.11.005.

[14] A. Husain Khan, H. Abdul Aziz, P. Palaniandy, M. Naushad, E. Cevik, S. Zahmatkesh,

Pharmaceutical residues in the ecosystem: Antibiotic resistance, health impacts, and removal techniques, Chemosphere 339 (2023) 139647. https://doi.org/10.1016/j.chemosphere.2023.139647.
[15] L. Riaz, T. Mahmood, A. Khalid, A. Rashid, M.B. Ahmed Siddique, A. Kamal, M.S. Coyne, Fluoroquinolones (FQs) in the environment: A review on their abundance, sorption and toxicity in soil, Chemosphere 191 (2018) 704–720. https://doi.org/10.1016/j.chemosphere.2017.10.092.
[16] S. Aydin, M.E. Aydin, A. Ulvi, H. Kilic, Antibiotics in hospital effluents: occurrence, contribution to urban wastewater, removal in a wastewater treatment plant, and environmental risk assessment, Environ Sci Pollut Res 26 (2019) 544–558. https://doi.org/10.1007/s11356-018-3563-0.
[17] P. Verlicchi, M. Al Aukidy, E. Zambello, Occurrence of pharmaceutical compounds in urban wastewater: Removal, mass load and environmental risk after a secondary treatment—A review, Science of The Total Environment 429 (2012) 123–155. https://doi.org/10.1016/j.scitotenv.2012.04.028.
[18] K. Kümmerer, Antibiotics in the aquatic environment – A review – Part I, Chemosphere 75 (2009) 417–434. https://doi.org/10.1016/j.chemosphere.2008.11.086.
[19] M.D. Celiz, J. Tso, D.S. Aga, Pharmaceutical metabolites in the environment: Analytical challenges and ecological risks, Environmental Toxicology and Chemistry 28 (2009) 2473–2484. https://doi.org/10.1897/09-173.1.
[20] J. Fernandes, P.J. Ramísio, H. Puga, A Comprehensive Review on Various Phases of Wastewater Technologies: Trends and Future Perspectives, Eng 5 (2024) 2633–2661. https://doi.org/10.3390/eng5040138.
[21] A.H. Khan, H.A. Rudayni, A.A. Chaudhary, M. Imran, S. Vambol, Modern use of modified Sequencing Batch Reactor in wastewater Treatment, Ecological Questions 33 (2022) 99–110. https://doi.org/10.12775/EQ.2022.033.
[22] D. Saidulu, B. Gupta, A.K. Gupta, P.S. Ghosal, A review on occurrences, eco-toxic effects, and remediation of emerging contaminants from wastewater: Special emphasis on biological treatment based hybrid systems, Journal of Environmental Chemical Engineering 9 (2021) 105282. https://doi.org/10.1016/j.jece.2021.105282.
[23] A.H. Khan, N.A. Khan, S. Ahmed, A. Dhingra, C.P. Singh, S.U. Khan, A.A. Mohammadi, F. Changani, M. Yousefi, S. Alam, S. Vambol, V. Vambol, A. Khursheed, I. Ali, Application of advanced oxidation processes followed by different treatment technologies for hospital wastewater treatment, Journal of Cleaner Production 269 (2020) 122411. https://doi.org/10.1016/j.jclepro.2020.122411.
[24] S.N. Tolboom, D. Carrillo-Nieves, M. de Jesús Rostro-Alanis, R. de la Cruz Quiroz, D. Barceló, H.M.N. Iqbal, R. Parra-Saldivar, Algal-based removal strategies for hazardous contaminants from the environment – A review, Science of The Total Environment 665 (2019) 358–366. https://doi.org/10.1016/j.scitotenv.2019.02.129.
[25] A. Catteau, A. Bado-Nilles, R. Beaudouin, S. Joachim, O. Palluel, C. Turiès, C. Galet, A. Geffard, J.-M. Porcher, An active biomonitoring approach using three-spined stickleback (*Gasterosteus aculeatus, L.*) to assess the efficiency of a constructed wetland as tertiary treatment of wastewater, Ecological Indicators 114 (2020) 106238. https://doi.org/10.1016/j.ecolind.2020.106238.
[26] M.A. Gulamhussein, B. Saini, A. Dey, Removal of pharmaceutical contaminants through membrane bioreactor, Materials Today: Proceedings 77 (2023) 260–268. https://doi.org/10.1016/j.matpr.2022.11.299.
[27] M. Varga, M. ELAbadsa, E. Tatár, V.G. Mihucz, Removal of selected pharmaceuticals from aqueous matrices with activated carbon under batch conditions,

Microchemical Journal 148 (2019) 661–672. https://doi.org/10.1016/j.microc.2019.05.038.

[28] R.Y. Krishnan, S. Manikandan, R. Subbaiya, M. Biruntha, M. Govarthanan, N. Karmegam, Removal of emerging micropollutants originating from pharmaceuticals and personal care products (PPCPs) in water and wastewater by advanced oxidation processes: A review, Environmental Technology & Innovation 23 (2021) 101757. https://doi.org/10.1016/j.eti.2021.101757.

[29] S.T.H. Alsalihy, A.N. Ahmed, G.H.A. Salih, M.J. M-Ridha, O.A.A. Falahi, Removal of pharmaceutical and personal care products (PhPCPs) using different low-cost materials as substrates in the vertical, horizontal, and hybrid flow systems of constructed wetland – A review, Environmental Technology & Innovation 35 (2024) 103647. https://doi.org/10.1016/j.eti.2024.103647.

[30] E. Guinea, C. Arias, P.L. Cabot, J.A. Garrido, R.M. Rodríguez, F. Centellas, E. Brillas, Mineralization of salicylic acid in acidic aqueous medium by electrochemical advanced oxidation processes using platinum and boron-doped diamond as anode and cathodically generated hydrogen peroxide, Water Research 42 (2008) 499–511. https://doi.org/10.1016/j.watres.2007.07.046.

[31] A.D. Bokare, W. Choi, Review of iron-free Fenton-like systems for activating H2O2 in advanced oxidation processes, Journal of Hazardous Materials 275 (2014) 121–135. https://doi.org/10.1016/j.jhazmat.2014.04.054.

[32] B.S. Rathi, P.S. Kumar, Application of adsorption process for effective removal of emerging contaminants from water and wastewater, Environmental Pollution 280 (2021) 116995. https://doi.org/10.1016/j.envpol.2021.116995.

[33] S.F. Ahmed, M. Mofijur, S. Nuzhat, A.T. Chowdhury, N. Rafa, Md.A. Uddin, A. Inayat, T.M.I. Mahlia, H.C. Ong, W.Y. Chia, P.L. Show, Recent developments in physical, biological, chemical, and hybrid treatment techniques for removing emerging contaminants from wastewater, Journal of Hazardous Materials 416 (2021) 125912. https://doi.org/10.1016/j.jhazmat.2021.125912.

[34] A. Mirzaei, Z. Chen, F. Haghighat, L. Yerushalmi, Removal of pharmaceuticals from water by homo/heterogonous Fenton-type processes – A review, Chemosphere 174 (2017) 665–688. https://doi.org/10.1016/j.chemosphere.2017.02.019.

[35] D. Ortiz, M. Munoz, J. Nieto-Sandoval, C. Romera-Castillo, Z.M. de Pedro, J.A. Casas, Insights into the degradation of microplastics by Fenton oxidation: From surface modification to mineralization, Chemosphere 309 (2022) 136809. https://doi.org/10.1016/j.chemosphere.2022.136809.

[36] C. Di Luca, J. Garcia, D. Ortiz, M. Munoz, J. Carbajo, Z.M. De Pedro, J.A. Casas, Mineralization of polystyrene nanoplastics in water by photo-Fenton oxidation, Journal of Environmental Chemical Engineering 11 (2023) 110755. https://doi.org/10.1016/j.jece.2023.110755.

[37] M. Enfrin, L.F. Dumée, J. Lee, Nano/microplastics in water and wastewater treatment processes – Origin, impact and potential solutions, Water Research 161 (2019) 621–638. https://doi.org/10.1016/j.watres.2019.06.049.

[38] A. Forrest, L. Giacovazzi, S. Dunlop, J. Reisser, D. Tickler, A. Jamieson, J.J. Meeuwig, Eliminating Plastic Pollution: How a Voluntary Contribution From Industry Will Drive the Circular Plastics Economy, Front. Mar. Sci. 6 (2019). https://doi.org/10.3389/fmars.2019.00627.

[39] A.L. Andrady, The plastic in microplastics: A review, Marine Pollution Bulletin 119 (2017) 12–22. https://doi.org/10.1016/j.marpolbul.2017.01.082.

[40] K.D. Cox, G.A. Covernton, H.L. Davies, J.F. Dower, F. Juanes, S.E. Dudas, Human Consumption of Microplastics, Environ. Sci. Technol. 53 (2019) 7068–7074.

https://doi.org/10.1021/acs.est.9b01517.
[41] A.A. Horton, A. Walton, D.J. Spurgeon, E. Lahive, C. Svendsen, Microplastics in freshwater and terrestrial environments: Evaluating the current understanding to identify the knowledge gaps and future research priorities, Science of The Total Environment 586 (2017) 127–141. https://doi.org/10.1016/j.scitotenv.2017.01.190.
[42] F. Salvador Cesa, A. Turra, J. Baruque-Ramos, Synthetic fibers as microplastics in the marine environment: A review from textile perspective with a focus on domestic washings, Science of The Total Environment 598 (2017) 1116–1129. https://doi.org/10.1016/j.scitotenv.2017.04.172.
[43] M. Enfrin, J. Lee, Y. Gibert, F. Basheer, L. Kong, L.F. Dumée, Release of hazardous nanoplastic contaminants due to microplastics fragmentation under shear stress forces, Journal of Hazardous Materials 384 (2020) 121393. https://doi.org/10.1016/j.jhazmat.2019.121393.
[44] G. Rossi, J. Barnoud, L. Monticelli, Polystyrene Nanoparticles Perturb Lipid Membranes, J. Phys. Chem. Lett. 5 (2014) 241–246. https://doi.org/10.1021/jz402234c.
[45] S.N. Akanyange, X. Lyu, X. Zhao, X. Li, Y. Zhang, J.C. Crittenden, C. Anning, T. Chen, T. Jiang, H. Zhao, Does microplastic really represent a threat? A review of the atmospheric contamination sources and potential impacts, Science of The Total Environment 777 (2021) 146020. https://doi.org/10.1016/j.scitotenv.2021.146020.
[46] S. Karbalaei, P. Hanachi, T.R. Walker, M. Cole, Occurrence, sources, human health impacts and mitigation of microplastic pollution, Environ Sci Pollut Res 25 (2018) 36046–36063. https://doi.org/10.1007/s11356-018-3508-7.
[47] R. Ahmed, A.K. Hamid, S.A. Krebsbach, J. He, D. Wang, Critical review of microplastics removal from the environment, Chemosphere 293 (2022) 133557. https://doi.org/10.1016/j.chemosphere.2022.133557.
[48] X. Hu, H. Gu, Y. Wang, J. Liu, Z. Yu, Y. Li, J. Jin, X. Liu, Q. Dai, G. Wang, Succession of soil bacterial communities and network patterns in response to conventional and biodegradable microplastics: A microcosmic study in Mollisol, Journal of Hazardous Materials 436 (2022) 129218. https://doi.org/10.1016/j.jhazmat.2022.129218.
[49] Y. Chae, Y.-J. An, Effects of micro- and nanoplastics on aquatic ecosystems: Current research trends and perspectives, Marine Pollution Bulletin 124 (2017) 624–632. https://doi.org/10.1016/j.marpolbul.2017.01.070.
[50] L. Hou, D. Kumar, C.G. Yoo, I. Gitsov, E.L.-W. Majumder, Conversion and removal strategies for microplastics in wastewater treatment plants and landfills, Chemical Engineering Journal 406 (2021) 126715. https://doi.org/10.1016/j.cej.2020.126715.
[51] M. Di, J. Wang, Microplastics in surface waters and sediments of the Three Gorges Reservoir, China, Science of The Total Environment 616–617 (2018) 1620–1627. https://doi.org/10.1016/j.scitotenv.2017.10.150.
[52] J. Sun, X. Dai, Q. Wang, M.C.M. van Loosdrecht, B.-J. Ni, Microplastics in wastewater treatment plants: Detection, occurrence and removal, Water Research 152 (2019) 21–37. https://doi.org/10.1016/j.watres.2018.12.050.
[53] S. Monira, R. Roychand, F.I. Hai, M. Bhuiyan, B.R. Dhar, B.K. Pramanik, Nano and microplastics occurrence in wastewater treatment plants: A comprehensive understanding of microplastics fragmentation and their removal, Chemosphere 334 (2023) 139011. https://doi.org/10.1016/j.chemosphere.2023.139011.
[54] S. Raju, M. Carbery, A. Kuttykattil, K. Senthirajah, A. Lundmark, Z. Rogers, S. Scb, G. Evans, T. Palanisami, Improved methodology to determine the fate and transport of microplastics in a secondary wastewater treatment plant, Water Research 173

(2020) 115549. https://doi.org/10.1016/j.watres.2020.115549.
[55] C. Akarsu, H. Kumbur, K. Gökdağ, A.E. Kıdeyş, A. Sanchez-Vidal, Microplastics composition and load from three wastewater treatment plants discharging into Mersin Bay, north eastern Mediterranean Sea, Marine Pollution Bulletin 150 (2020) 110776. https://doi.org/10.1016/j.marpolbul.2019.110776.
[56] D.W. Skaf, V.L. Punzi, J.T. Rolle, K.A. Kleinberg, Removal of micron-sized microplastic particles from simulated drinking water via alum coagulation, Chemical Engineering Journal 386 (2020) 123807. https://doi.org/10.1016/j.cej.2019.123807.
[57] M. Tong, L. He, H. Rong, M. Li, H. Kim, Transport behaviors of plastic particles in saturated quartz sand without and with biochar/Fe3O4-biochar amendment, Water Research 169 (2020) 115284. https://doi.org/10.1016/j.watres.2019.115284.
[58] Z. Wang, T. Lin, W. Chen, Occurrence and removal of microplastics in an advanced drinking water treatment plant (ADWTP), Science of The Total Environment 700 (2020) 134520. https://doi.org/10.1016/j.scitotenv.2019.134520.
[59] J. Li, H. Liu, J. Paul Chen, Microplastics in freshwater systems: A review on occurrence, environmental effects, and methods for microplastics detection, Water Research 137 (2018) 362–374. https://doi.org/10.1016/j.watres.2017.12.056.
[60] C. Wang, H. Wang, J. Fu, Y. Liu, Flotation separation of waste plastics for recycling—A review, Waste Management 41 (2015) 28–38. https://doi.org/10.1016/j.wasman.2015.03.027.
[61] H.A. Nel, T. Dalu, R.J. Wasserman, J.W. Hean, Colour and size influences plastic microbead underestimation, regardless of sediment grain size, Science of The Total Environment 655 (2019) 567–570. https://doi.org/10.1016/j.scitotenv.2018.11.261.
[62] B. He, A. Goonetilleke, G.A. Ayoko, L. Rintoul, Abundance, distribution patterns, and identification of microplastics in Brisbane River sediments, Australia, Science of The Total Environment 700 (2020) 134467. https://doi.org/10.1016/j.scitotenv.2019.134467.
[63] H. Wei, B. Gao, J. Ren, A. Li, H. Yang, Coagulation/flocculation in dewatering of sludge: A review, Water Research 143 (2018) 608–631. https://doi.org/10.1016/j.watres.2018.07.029.
[64] B. Ma, W. Xue, C. Hu, H. Liu, J. Qu, L. Li, Characteristics of microplastic removal via coagulation and ultrafiltration during drinking water treatment, Chemical Engineering Journal 359 (2019) 159–167. https://doi.org/10.1016/j.cej.2018.11.155.
[65] O.M. Rodríguez-Narvaez, A. Goonetilleke, L. Perez, E.R. Bandala, Engineered technologies for the separation and degradation of microplastics in water: A review, Chemical Engineering Journal 414 (2021) 128692. https://doi.org/10.1016/j.cej.2021.128692.
[66] F.G. Acién, C. Gómez-Serrano, M.M. Morales-Amaral, J.M. Fernández-Sevilla, E. Molina-Grima, Wastewater treatment using microalgae: how realistic a contribution might it be to significant urban wastewater treatment?, Appl Microbiol Biotechnol 100 (2016) 9013–9022. https://doi.org/10.1007/s00253-016-7835-7.
[67] J.J. Rueda Márquez, I. Levchuk, M. Sillanpää, Application of Catalytic Wet Peroxide Oxidation for Industrial and Urban Wastewater Treatment: A Review, Catalysts 8 (2018) 673. https://doi.org/10.3390/catal8120673.
[68] A.B. Silva, M.F. Costa, A.C. Duarte, Biotechnology advances for dealing with environmental pollution by micro(nano)plastics: Lessons on theory and practices, Current Opinion in Environmental Science & Health 1 (2018) 30–35. https://doi.org/10.1016/j.coesh.2017.10.005.
[69] M.C. Krueger, H. Harms, D. Schlosser, Prospects for microbiological solutions to environmental pollution with plastics, Appl Microbiol Biotechnol 99 (2015) 8857–

8874. https://doi.org/10.1007/s00253-015-6879-4.
[70] A.N. Brooks, S. Turkarslan, K.D. Beer, F. Yin Lo, N.S. Baliga, Adaptation of cells to new environments, WIREs Systems Biology and Medicine 3 (2011) 544–561. https://doi.org/10.1002/wsbm.136.
[71] H. Du, Y. Xie, J. Wang, Microplastic degradation methods and corresponding degradation mechanism: Research status and future perspectives, Journal of Hazardous Materials 418 (2021) 126377. https://doi.org/10.1016/j.jhazmat.2021.126377.
[72] J. Yuan, J. Ma, Y. Sun, T. Zhou, Y. Zhao, F. Yu, Microbial degradation and other environmental aspects of microplastics/plastics, Science of The Total Environment 715 (2020) 136968. https://doi.org/10.1016/j.scitotenv.2020.136968.
[73] P. Duan, Y. Qi, S. Feng, X. Peng, W. Wang, Y. Yue, Y. Shang, Y. Li, B. Gao, X. Xu, Enhanced degradation of clothianidin in peroxymonosulfate/catalyst system via core-shell FeMn @ N-C and phosphate surrounding, Applied Catalysis B: Environmental 267 (2020) 118717. https://doi.org/10.1016/j.apcatb.2020.118717.
[74] J. Wang, H. Wang, Fenton treatment for flotation separation of polyvinyl chloride from plastic mixtures, Separation and Purification Technology 187 (2017) 415–425. https://doi.org/10.1016/j.seppur.2017.06.076.
[75] C. Wang, J. Kang, P. Liang, H. Zhang, H. Sun, M. O. Tadé, S. Wang, Ferric carbide nanocrystals encapsulated in nitrogen-doped carbon nanotubes as an outstanding environmental catalyst, Environmental Science: Nano 4 (2017) 170–179. https://doi.org/10.1039/C6EN00397D.
[76] J. Kang, L. Zhou, X. Duan, H. Sun, Z. Ao, S. Wang, Degradation of Cosmetic Microplastics via Functionalized Carbon Nanosprings, Matter 1 (2019) 745–758. https://doi.org/10.1016/j.matt.2019.06.004.
[77] P. Liu, L. Qian, H. Wang, X. Zhan, K. Lu, C. Gu, S. Gao, New Insights into the Aging Behavior of Microplastics Accelerated by Advanced Oxidation Processes, Environ. Sci. Technol. 53 (2019) 3579–3588. https://doi.org/10.1021/acs.est.9b00493.
[78] N. de O. Dos Santos, R. Busquets, L.C. Campos, Insights into the removal of microplastics and microfibres by Advanced Oxidation Processes, Science of The Total Environment 861 (2023) 160665. https://doi.org/10.1016/j.scitotenv.2022.160665.
[79] W.H. Glaze, Drinking-water treatment with ozone, Environ. Sci. Technol. 21 (1987) 224–230. https://doi.org/10.1021/es00157a001.
[80] Y. Deng, R. Zhao, Advanced Oxidation Processes (AOPs) in Wastewater Treatment, Curr Pollution Rep 1 (2015) 167–176. https://doi.org/10.1007/s40726-015-0015-z.
[81] Preethi, S.P. Shanmugavel, G. Kumar, Y.K. N, G. M, R.B. J, Recent progress in mineralization of emerging contaminants by advanced oxidation process: A review, Environmental Pollution 341 (2024) 122842. https://doi.org/10.1016/j.envpol.2023.122842.
[82] M. Panizza, G. Cerisola, Electro-Fenton degradation of synthetic dyes, Water Research 43 (2009) 339–344. https://doi.org/10.1016/j.watres.2008.10.028.
[83] E. Brillas, I. Sirés, M.A. Oturan, Electro-Fenton Process and Related Electrochemical Technologies Based on Fenton's Reaction Chemistry, Chem. Rev. 109 (2009) 6570–6631. https://doi.org/10.1021/cr900136g.
[84] M.A. Oturan, J.-J. Aaron, Advanced Oxidation Processes in Water/Wastewater Treatment: Principles and Applications. A Review, Critical Reviews in Environmental Science and Technology 44 (2014) 2577–2641. https://doi.org/10.1080/10643389.2013.829765.
[85] X. Wang, C. Xu, Y. Zhu, C. Zhou, Y. Yang, J. Miao, W. Zhou, Z. Shao, The recent

progress of cathode materials for heterogeneous electro-Fenton reactions, Surfaces and Interfaces 44 (2024) 103820. https://doi.org/10.1016/j.surfin.2023.103820.

[86] S. Ammar, M.A. Oturan, L. Labiadh, A. Guersalli, R. Abdelhedi, N. Oturan, E. Brillas, Degradation of tyrosol by a novel electro-Fenton process using pyrite as heterogeneous source of iron catalyst, Water Research 74 (2015) 77–87. https://doi.org/10.1016/j.watres.2015.02.006.

[87] N. Barhoumi, N. Oturan, S. Ammar, A. Gadri, M.A. Oturan, E. Brillas, Enhanced degradation of the antibiotic tetracycline by heterogeneous electro-Fenton with pyrite catalysis, Environ Chem Lett 15 (2017) 689–693. https://doi.org/10.1007/s10311-017-0638-y.

[88] S. Qiu, D. He, J. Ma, T. Liu, T.D. Waite, Kinetic Modeling of the Electro-Fenton Process: Quantification of Reactive Oxygen Species Generation, Electrochimica Acta 176 (2015) 51–58. https://doi.org/10.1016/j.electacta.2015.06.103.

[89] V. Poza-Nogueiras, E. Rosales, M. Pazos, M.Á. Sanromán, Current advances and trends in electro-Fenton process using heterogeneous catalysts – A review, Chemosphere 201 (2018) 399–416. https://doi.org/10.1016/j.chemosphere.2018.03.002.

[90] P.V. Nidheesh, H. Olvera-Vargas, N. Oturan, M.A. Oturan, Heterogeneous Electro-Fenton Process: Principles and Applications, in: M. Zhou, M.A. Oturan, I. Sirés (Eds.), Electro-Fenton Process: New Trends and Scale-Up, Springer, Singapore, 2018: pp. 85–110. https://doi.org/10.1007/698_2017_72.

[91] X. Hou, X. Huang, F. Jia, Z. Ai, J. Zhao, L. Zhang, Hydroxylamine Promoted Goethite Surface Fenton Degradation of Organic Pollutants, Environ. Sci. Technol. 51 (2017) 5118–5126. https://doi.org/10.1021/acs.est.6b05906.

[92] Q. Yu, L. Feng, X. Chai, X. Qiu, H. Ouyang, G. Deng, Enhanced surface Fenton degradation of BPA in soil with a high pH, Chemosphere 220 (2019) 335–343. https://doi.org/10.1016/j.chemosphere.2018.12.141.

[93] P. Su, M. Zhou, X. Lu, W. Yang, G. Ren, J. Cai, Electrochemical catalytic mechanism of N-doped graphene for enhanced H2O2 yield and in-situ degradation of organic pollutant, Applied Catalysis B: Environmental 245 (2019) 583–595. https://doi.org/10.1016/j.apcatb.2018.12.075.

[94] Y. Yao, Y. Pan, Y. Yu, Z. Yu, L. Lai, F. Liu, L. Wei, Y. Chen, Bifunctional catalysts for heterogeneous electro-Fenton processes: a review, Environ Chem Lett 20 (2022) 3837–3859. https://doi.org/10.1007/s10311-022-01453-6.

[95] J. Meijide, P.S.M. Dunlop, M. Pazos, M.A. Sanromán, Heterogeneous Electro-Fenton as “Green” Technology for Pharmaceutical Removal: A Review, Catalysts 11 (2021) 85. https://doi.org/10.3390/catal11010085.

[96] M. de Cazes, M.-P. Belleville, E. Petit, M. Llorca, S. Rodríguez-Mozaz, J. de Gunzburg, D. Barceló, J. Sanchez-Marcano, Design and optimization of an enzymatic membrane reactor for tetracycline degradation, Catalysis Today 236 (2014) 146–152. https://doi.org/10.1016/j.cattod.2014.02.051.

[97] N. Barhoumi, N. Oturan, H. Olvera-Vargas, E. Brillas, A. Gadri, S. Ammar, M.A. Oturan, Pyrite as a sustainable catalyst in electro-Fenton process for improving oxidation of sulfamethazine. Kinetics, mechanism and toxicity assessment, Water Research 94 (2016) 52–61. https://doi.org/10.1016/j.watres.2016.02.042.

[98] N. Barhoumi, H. Olvera-Vargas, N. Oturan, D. Huguenot, A. Gadri, S. Ammar, E. Brillas, M.A. Oturan, Kinetics of oxidative degradation/mineralization pathways of the antibiotic tetracycline by the novel heterogeneous electro-Fenton process with solid catalyst chalcopyrite, Applied Catalysis B: Environmental 209 (2017) 637–647. https://doi.org/10.1016/j.apcatb.2017.03.034.

[99] C. Droguett, R. Salazar, E. Brillas, I. Sirés, C. Carlesi, J.F. Marco, A. Thiam, Treatment of antibiotic cephalexin by heterogeneous electrochemical Fenton-based processes using chalcopyrite as sustainable catalyst, Science of The Total Environment 740 (2020) 140154. https://doi.org/10.1016/j.scitotenv.2020.140154.

[100] R.R. Kalantary, M. Farzadkia, M. Kermani, M. Rahmatinia, Heterogeneous electro-Fenton process by Nano-Fe3O4 for catalytic degradation of amoxicillin: Process optimization using response surface methodology, Journal of Environmental Chemical Engineering 6 (2018) 4644–4652. https://doi.org/10.1016/j.jece.2018.06.043.

[101] E. Rosales, S. Diaz, M. Pazos, M.A. Sanromán, Comprehensive strategy for the degradation of anti-inflammatory drug diclofenac by different advanced oxidation processes, Separation and Purification Technology 208 (2019) 130–141. https://doi.org/10.1016/j.seppur.2018.04.014.

[102] A. Puga, E. Rosales, M. Pazos, M.A. Sanromán, Prompt removal of antibiotic by adsorption/electro-Fenton degradation using an iron-doped perlite as heterogeneous catalyst, Process Safety and Environmental Protection 144 (2020) 100–110. https://doi.org/10.1016/j.psep.2020.07.021.

[103] A. Özcan, A. Atılır Özcan, Y. Demirci, E. Şener, Preparation of Fe2O3 modified kaolin and application in heterogeneous electro-catalytic oxidation of enoxacin, Applied Catalysis B: Environmental 200 (2017) 361–371. https://doi.org/10.1016/j.apcatb.2016.07.018.

[104] M. Sadeghi, M.H. Mehdinejad, N. Mengelizadeh, Y. Mahdavi, H. Pourzamani, Y. Hajizadeh, M.R. Zare, Degradation of diclofenac by heterogeneous electro-Fenton process using magnetic single-walled carbon nanotubes as a catalyst, Journal of Water Process Engineering 31 (2019) 100852. https://doi.org/10.1016/j.jwpe.2019.100852.

[105] M. Ghasemi, A. Khataee, P. Gholami, R.D. Cheshmeh Soltani, Template-free microspheres decorated with Cu-Fe-NLDH for catalytic removal of gentamicin in heterogeneous electro-Fenton process, Journal of Environmental Management 248 (2019) 109236. https://doi.org/10.1016/j.jenvman.2019.07.007.

[106] S. Campos, R. Salazar, N. Arancibia-Miranda, M.A. Rubio, M. Aranda, A. García, P. Sepúlveda, L.C. Espinoza, Nafcillin degradation by heterogeneous electro-Fenton process using Fe, Cu and Fe/Cu nanoparticles, Chemosphere 247 (2020) 125813. https://doi.org/10.1016/j.chemosphere.2020.125813.

[107] F. Görmez, Ö. Görmez, B. Gözmen, D. Kalderis, Degradation of chloramphenicol and metronidazole by electro-Fenton process using graphene oxide-Fe3O4 as heterogeneous catalyst, Journal of Environmental Chemical Engineering 7 (2019) 102990. https://doi.org/10.1016/j.jece.2019.102990.

[108] H. Nsubuga, C. Basheer, A. Jalilov, M.B. Haider, A.A. Al-Saadi, Droplet flow-assisted heterogeneous electro-Fenton reactor for degradation of beta-blockers: response surface optimization, and mechanism elucidation, Environ Sci Pollut Res 26 (2019) 14313–14327. https://doi.org/10.1007/s11356-019-04551-1.

[109] F. Yu, Y. Wang, H. Ma, M. Zhou, Hydrothermal synthesis of FeS2 as a highly efficient heterogeneous electro-Fenton catalyst to degrade diclofenac via molecular oxygen effects for Fe(II)/Fe(III) cycle, Separation and Purification Technology 248 (2020) 117022. https://doi.org/10.1016/j.seppur.2020.117022.

[110] Z. Ye, G.E.M. Schukraft, A. L'Hermitte, Y. Xiong, E. Brillas, C. Petit, I. Sirés, Mechanism and stability of an Fe-based 2D MOF during the photoelectro-Fenton treatment of organic micropollutants under UVA and visible light irradiation, Water Research 184 (2020) 115986. https://doi.org/10.1016/j.watres.2020.115986.

[111] M. Kiendrebeogo, M.R. Karimi Estahbanati, A. Khosravanipour Mostafazadeh,

P. Drogui, R.D. Tyagi, Treatment of microplastics in water by anodic oxidation: A case study for polystyrene, Environmental Pollution 269 (2021) 116168. https://doi.org/10.1016/j.envpol.2020.116168.

[112] Z. Ning, X. Duan, Y. Li, X. Zhao, L. Chang, Degradation of polyvinyl chloride microplastics via electrochemical oxidation with a CeO2–PbO2 anode, Journal of Cleaner Production (2023) 139668. https://doi.org/10.1016/j.jclepro.2023.139668.

[113] M. Kiendrebeogo, M.R. Karimi Estahbanati, Y. Ouarda, P. Drogui, R.D. Tyagi, Electrochemical degradation of nanoplastics in water: Analysis of the role of reactive oxygen species, Science of The Total Environment 808 (2022) 151897. https://doi.org/10.1016/j.scitotenv.2021.151897.

[114] F. Miao, Y. Liu, M. Gao, X. Yu, P. Xiao, M. Wang, S. Wang, X. Wang, Degradation of polyvinyl chloride microplastics via an electro-Fenton-like system with a TiO2/graphite cathode, Journal of Hazardous Materials 399 (2020) 123023. https://doi.org/10.1016/j.jhazmat.2020.123023.

[115] J. Lu, R. Hou, Y. Wang, L. Zhou, Y. Yuan, Surfactant-sodium dodecyl sulfate enhanced degradation of polystyrene microplastics with an energy-saving electrochemical advanced oxidation process (EAOP) strategy, Water Research 226 (2022) 119277. https://doi.org/10.1016/j.watres.2022.119277.

[116] Q. Chen, L. Wan, H. Zhou, F. Luo, L. Lei, N. Wang, Photoelectro-Fenton microreactor integrated with MOF-derived porous α-Fe2O3 film for efficient nanoplastics degradation, Journal of Water Process Engineering 56 (2023) 104343. https://doi.org/10.1016/j.jwpe.2023.104343.

[117] L. Mais, N. Melis, A. Vacca, M. Mascia, Electrochemical removal of PET and PE microplastics for wastewater treatment, Environ. Sci.: Water Res. Technol. (2023). https://doi.org/10.1039/D3EW00582H.

[118] K. Zuo, S. Garcia-Segura, G.A. Cerrón-Calle, F.-Y. Chen, X. Tian, X. Wang, X. Huang, H. Wang, P.J.J. Alvarez, J. Lou, M. Elimelech, Q. Li, Electrified water treatment: fundamentals and roles of electrode materials, Nat Rev Mater 8 (2023) 472–490. https://doi.org/10.1038/s41578-023-00564-y.

[119] P.V. Nidheesh, S.O. Ganiyu, C.A. Martínez-Huitle, E. Mousset, H. Olvera-Vargas, C. Trellu, M. Zhou, M.A. Oturan, Recent advances in electro-Fenton process and its emerging applications, Critical Reviews in Environmental Science and Technology 53 (2023) 887–913. https://doi.org/10.1080/10643389.2022.2093074.

[120] U. Razzaq, T.-B. Nguyen, M.U. Saleem, V.-R. Le, C.-W. Chen, X.-T. Bui, C.-D. Dong, Recent progress in electro-Fenton technology for the remediation of pharmaceutical compounds in aqueous environments, Science of The Total Environment 946 (2024) 174253. https://doi.org/10.1016/j.scitotenv.2024.174253.

[121] Z. Wang, M. Liu, F. Xiao, G. Postole, H. Zhao, G. Zhao, Recent advances and trends of heterogeneous electro-Fenton process for wastewater treatment-review, Chinese Chemical Letters 33 (2022) 653–662. https://doi.org/10.1016/j.cclet.2021.07.044.

[122] X. Lu, P. Su, G. Song, M. Zhou, A critical review on regulating multi-electron pathways of oxygen reduction reaction on modified carbon-catalysts for organic wastewater treatment, Chemical Engineering Journal 488 (2024) 150967. https://doi.org/10.1016/j.cej.2024.150967.

[123] Y. Liu, X. Quan, X. Fan, H. Wang, S. Chen, High-Yield Electrosynthesis of Hydrogen Peroxide from Oxygen Reduction by Hierarchically Porous Carbon, Angewandte Chemie International Edition 54 (2015) 6837–6841. https://doi.org/10.1002/anie.201502396.

[124] Z. Ai, H. Xiao, T. Mei, J. Liu, L. Zhang, K. Deng, J. Qiu, Electro-Fenton

Degradation of Rhodamine B Based on a Composite Cathode of Cu2O Nanocubes and Carbon Nanotubes, J. Phys. Chem. C 112 (2008) 11929–11935. https://doi.org/10.1021/jp803243t.

[125] M.H. Chakrabarti, N.P. Brandon, S.A. Hajimolana, F. Tariq, V. Yufit, M.A. Hashim, M.A. Hussain, C.T.J. Low, P.V. Aravind, Application of carbon materials in redox flow batteries, Journal of Power Sources 253 (2014) 150–166. https://doi.org/10.1016/j.jpowsour.2013.12.038.

[126] C. Trellu, N. Oturan, F.K. Keita, C. Fourdrin, Y. Pechaud, M.A. Oturan, Regeneration of Activated Carbon Fiber by the Electro-Fenton Process, Environ. Sci. Technol. 52 (2018) 7450–7457. https://doi.org/10.1021/acs.est.8b01554.

[127] K.M. Nair, V. Kumaravel, S.C. Pillai, Carbonaceous cathode materials for electro-Fenton technology: Mechanism, kinetics, recent advances, opportunities and challenges, Chemosphere 269 (2021). https://doi.org/10.1016/j.chemosphere.2020.129325.

[128] W.L. Oliveira, E.F. de Oliveira, W.V.F. do Carmo Batista, H.A.J.L. Mourão, M.J. Mendes Pires, R.M. Coelho, G.A. Atta Diab, I.F. Teixeira, G. Marques, V.R. Mastelaro, O.R. Nascimento, C.E. Valdés, E.A. Urquieta-Gonzalez, D.E.C. Ferreira, M.C. Pereira, J.P. de Mesquita, A metal-free catalyst based on g-C3N4 functionalized with cyamelurate-like groups: Catalytic properties and mechanism of a new heterogeneous Fenton-like catalyst, Carbon 214 (2023) 118366. https://doi.org/10.1016/j.carbon.2023.118366.

[129] Z. Lu, G. Chen, S. Siahrostami, Z. Chen, K. Liu, J. Xie, L. Liao, T. Wu, D. Lin, Y. Liu, T.F. Jaramillo, J.K. Nørskov, Y. Cui, High-efficiency oxygen reduction to hydrogen peroxide catalysed by oxidized carbon materials, Nat Catal 1 (2018) 156–162. https://doi.org/10.1038/s41929-017-0017-x.

[130] Y. Wang, G.I.N. Waterhouse, L. Shang, T. Zhang, Electrocatalytic Oxygen Reduction to Hydrogen Peroxide: From Homogeneous to Heterogeneous Electrocatalysis, Advanced Energy Materials 11 (2021) 2003323. https://doi.org/10.1002/aenm.202003323.

[131] W.R.P. Barros, Q. Wei, G. Zhang, S. Sun, M.R.V. Lanza, A.C. Tavares, Oxygen reduction to hydrogen peroxide on Fe3O4 nanoparticles supported on Printex carbon and Graphene, Electrochimica Acta 162 (2015) 263–270. https://doi.org/10.1016/j.electacta.2015.02.175.

[132] Y. Sun, L. Silvioli, N.R. Sahraie, W. Ju, J. Li, A. Zitolo, S. Li, A. Bagger, L. Arnarson, X. Wang, T. Moeller, D. Bernsmeier, J. Rossmeisl, F. Jaouen, P. Strasser, Activity–Selectivity Trends in the Electrochemical Production of Hydrogen Peroxide over Single-Site Metal–Nitrogen–Carbon Catalysts, J. Am. Chem. Soc. 141 (2019) 12372–12381. https://doi.org/10.1021/jacs.9b05576.

[133] R.D. Ross, H. Sheng, A. Parihar, J. Huang, S. Jin, Compositionally Tuned Trimetallic Thiospinel Catalysts for Enhanced Electrosynthesis of Hydrogen Peroxide and Built-In Hydroxyl Radical Generation, ACS Catal. 11 (2021) 12643–12650. https://doi.org/10.1021/acscatal.1c03349.

[134] A. Georgi, F.-D. Kopinke, Interaction of adsorption and catalytic reactions in water decontamination processes: Part I. Oxidation of organic contaminants with hydrogen peroxide catalyzed by activated carbon, Applied Catalysis B: Environmental 58 (2005) 9–18. https://doi.org/10.1016/j.apcatb.2004.11.014.

[135] C. Hu, R. Paul, Q. Dai, L. Dai, Carbon-based metal-free electrocatalysts: from oxygen reduction to multifunctional electrocatalysis, Chem. Soc. Rev. 50 (2021) 11785–11843. https://doi.org/10.1039/D1CS00219H.

[136] X. Qin, K. Zhao, X. Quan, P. Cao, S. Chen, H. Yu, Highly efficient metal-free

electro-Fenton degradation of organic contaminants on a bifunctional catalyst, Journal of Hazardous Materials 416 (2021) 125859. https://doi.org/10.1016/j.jhazmat.2021.125859.

[137] D. Iglesias, A. Giuliani, M. Melchionna, S. Marchesan, A. Criado, L. Nasi, M. Bevilacqua, C. Tavagnacco, F. Vizza, M. Prato, P. Fornasiero, N-Doped Graphitized Carbon Nanohorns as a Forefront Electrocatalyst in Highly Selective O2 Reduction to H2O2, Chem 4 (2018) 106–123. https://doi.org/10.1016/j.chempr.2017.10.013.

[138] Z.W. Chen, L.X. Chen, C.C. Yang, Q. Jiang, Atomic (single, double, and triple atoms) catalysis: frontiers, opportunities, and challenges, J. Mater. Chem. A 7 (2019) 3492–3515. https://doi.org/10.1039/C8TA11416A.

[139] X. Song, H. Zhang, Z. Bian, H. Wang, In situ electrogeneration and activation of H2O2 by atomic Fe catalysts for the efficient removal of chloramphenicol, Journal of Hazardous Materials 412 (2021) 125162. https://doi.org/10.1016/j.jhazmat.2021.125162.

[140] Y. Yang, Y. Liu, X. Fang, W. Miao, X. Chen, J. Sun, B.-J. Ni, S. Mao, Heterogeneous Electro-Fenton catalysis with HKUST-1-derived Cu@C decorated in 3D graphene network, Chemosphere 243 (2020) 125423. https://doi.org/10.1016/j.chemosphere.2019.125423.

[141] M. Jiang, Z. Xu, L. Li, M. Li, G. He, W. Zhang, Fe/Cu MOFs of Fe2+-rich and Cu-doping via in situ reduction as nanozyme for peroxidase-like catalycity enhancement, Microchim Acta 191 (2024) 1–11. https://doi.org/10.1007/s00604-024-06562-3.

[142] J.I. Nieto-Juarez, K. Pierzchła, A. Sienkiewicz, T. Kohn, Inactivation of MS2 coliphage in Fenton and Fenton-like systems: role of transition metals, hydrogen peroxide and sunlight, Environ. Sci. Technol. 44 (2010) 3351–3356. https://doi.org/10.1021/es903739f.

[143] Y. Wang, Y. Xue, C. Zhang, Copper embedded in nitrogen-doped carbon matrix derived from metal-organic frameworks for boosting peroxide production and electro-Fenton catalysis, Electrochimica Acta 368 (2021) 137643. https://doi.org/10.1016/j.electacta.2020.137643.

[144] S. Qiu, Y. Wang, J. Wan, Y. Ma, Z. Yan, S. Yang, Enhanced electro-Fenton catalytic performance with in-situ grown Ce/Fe@NPC-GF as self-standing cathode: Fabrication, influence factors and mechanism, Chemosphere 273 (2021) 130269. https://doi.org/10.1016/j.chemosphere.2021.130269.

[145] L. Xie, X. Liu, J. Chang, C. Zhang, Y. Li, H. Zhang, S. Zhan, W. Hu, Enhanced redox activity and oxygen vacancies of perovskite triggered by copper incorporation for the improvement of electro-Fenton activity, Chemical Engineering Journal 428 (2022) 131352. https://doi.org/10.1016/j.cej.2021.131352.

[146] Y. Li, C. Wang, S. Pan, X. Zhao, N. Liu, Mn doping improves in-situ H2O2 generation and activation in electro-Fenton process by Fe/Mn@CC cathode using high-temperature shock technique, Chemosphere 307 (2022) 136074. https://doi.org/10.1016/j.chemosphere.2022.136074.

[147] S.O. Ganiyu, T.X.H. Le, M. Bechelany, G. Esposito, E.D. van Hullebusch, M.A. Oturan, M. Cretin, A hierarchical CoFe-layered double hydroxide modified carbon-felt cathode for heterogeneous electro-Fenton process, J. Mater. Chem. A 5 (2017) 3655–3666. https://doi.org/10.1039/C6TA09100H.

[148] P. Hu, M. Long, X. Bai, C. Wang, C. Cai, J. Fu, B. Zhou, Y. Zhou, Monolithic cobalt-doped carbon aerogel for efficient catalytic activation of peroxymonosulfate in water, Journal of Hazardous Materials 332 (2017) 195–204. https://doi.org/10.1016/j.jhazmat.2017.03.010.

[149] J.-H. Lee, Y.-J. Heo, S.-J. Park, Effect of silica removal and steam activation on extra-porous activated carbons from rice husks for methane storage, International Journal of Hydrogen Energy 43 (2018) 22377–22384. https://doi.org/10.1016/j.ijhydene.2018.10.039.

[150] X. Xiao, Y. Xu, X. Lv, J. Xie, J. Liu, C. Yu, Electrochemical CO2 reduction on copper nanoparticles-dispersed carbon aerogels, Journal of Colloid and Interface Science 545 (2019) 1–7. https://doi.org/10.1016/j.jcis.2019.03.005.

[151] C. Moreno-Castilla, F. Carrasco-Marín, M.B. Dawidziuk, Carbon Aerogel-Supported Pt Catalysts for the Hydrogenolysis and Isomerization of n-Butane: Influence of the Carbonization Temperature of the Support and Pt Particle Size, Catalysts 2 (2012) 422–433. https://doi.org/10.3390/catal2040422.

[152] H. Bi, X. Huang, X. Wu, X. Cao, C. Tan, Z. Yin, X. Lu, L. Sun, H. Zhang, Carbon Microbelt Aerogel Prepared by Waste Paper: An Efficient and Recyclable Sorbent for Oils and Organic Solvents, Small 10 (2014) 3544–3550. https://doi.org/10.1002/smll.201303413.

[153] X. Wu, X. Yang, D. Wu, R. Fu, Feasibility study of using carbon aerogel as particle electrodes for decoloration of RBRX dye solution in a three-dimensional electrode reactor, Chemical Engineering Journal 138 (2008) 47–54. https://doi.org/10.1016/j.cej.2007.05.027.

[154] L. Zuo, Y. Zhang, L. Zhang, Y.-E. Miao, W. Fan, T. Liu, Polymer/Carbon-Based Hybrid Aerogels: Preparation, Properties and Applications, Materials 8 (2015) 6806–6848. https://doi.org/10.3390/ma8105343.

[155] S.O. Ganiyu, M. Zhou, C.A. Martínez-Huitle, Heterogeneous electro-Fenton and photoelectro-Fenton processes: A critical review of fundamental principles and application for water/wastewater treatment, Applied Catalysis B: Environmental 235 (2018) 103–129. https://doi.org/10.1016/j.apcatb.2018.04.044.

[156] H. Zhao, Y. Chen, Q. Peng, Q. Wang, G. Zhao, Catalytic activity of MOF(2Fe/Co)/carbon aerogel for improving H2O2 and OH generation in solar photo–electro–Fenton process, Applied Catalysis B: Environmental 203 (2017) 127–137. https://doi.org/10.1016/j.apcatb.2016.09.074.

[157] Y. Wang, H. Zhao, G. Zhao, Highly Ordered Mesoporous Fe3O4@Carbon Embedded Composite: High Catalytic Activity, Wide pH Range and Stability for Heterogeneous Electro-Fenton, Electroanalysis 28 (2016) 169–176. https://doi.org/10.1002/elan.201500488.

[158] Q. Tian, F. Xiao, H. Zhao, X. Fei, X. Shen, G. Postole, G. Zhao, Simultaneously accelerating the regeneration of FeII and the selectivity of 2e- oxygen reduction over sulfide iron-based carbon aerogel in electro-Fenton system, Applied Catalysis B: Environmental 272 (2020) 119039. https://doi.org/10.1016/j.apcatb.2020.119039.

3 Synergistic effect of Fe and Ni on carbon aerogel for enhanced oxygen reduction and H_2O_2 activation in electro-Fenton process

Highlights

- A novel FeNi alloy carbon aerogel cathode was developed for electro-Fenton system.
- FeNi-CA showed high activity for electro-generation and *in-situ* activation of H_2O_2.
- FeNi-CA exhibited broad pH efficacy and high reusability for ACT removal.
- Oxygen evolution reaction created favourable pH conditions for cathodic reactions.
- Anodic oxygen evolution eliminated the need for external aeration.

Graphical abstract

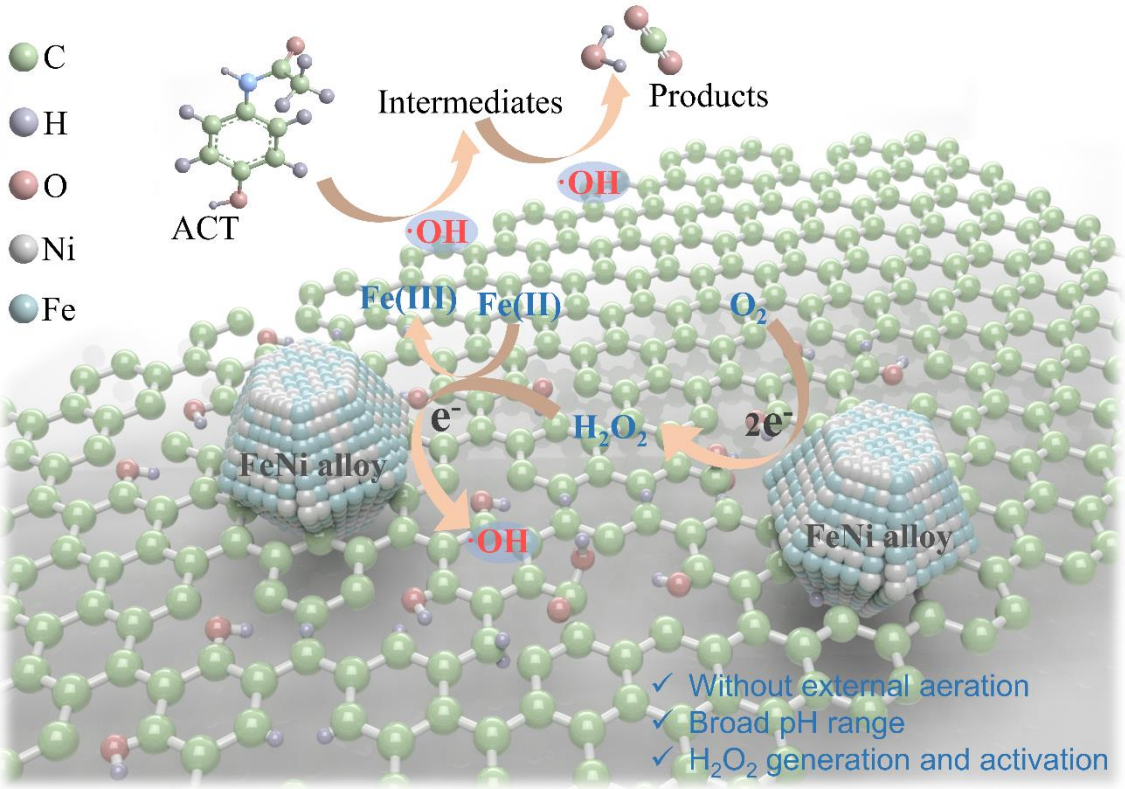

3.1 Abstract

A novel cathode, iron-nickel alloy modified carbon aerogel (FeNi-CA), was successfully synthesised and utilised as the cathode in an electro-Fenton process for acetaminophen degradation. The incorporation of Fe and Ni in the carbon matrix resulted in superior electrochemical characteristics and catalytic performance compared to Fe-CA and Ni-CA. The unique microstructure of FeNi-CA, including the presence of alloy nanoparticles, carbon defects, and abundant oxygen functional groups, enhanced $2e^-$ oxygen reduction activity and electrocatalytic performance. This enabled FeNi-CA to exhibit a dual functionality of H_2O_2 electro-generation and in situ activation. FeNi-CA demonstrated good performance over a wide pH range at a low current density of 4.44 mA/cm^2. Under optimal conditions, 99.9 % of acetaminophen was removed with a reaction rate constant (k_{obs}) of 0.054 min^{-1} through electro-sorption and oxidation processes. Importantly, a satisfactory degradation effect was achieved in the absence of external aeration. This work provides a potential wastewater treatment solution without the need for external aeration or additional chemical input by simultaneously achieving oxygen evolution reaction at the anode and oxygen reduction reaction at the cathode. Furthermore, FeNi-CA demonstrated good reusability performance with controlled metal leaching after five consecutive runs, suggesting its potential for sustained use in electro-Fenton processes over the long term.

3.2 Introduction

The presence of pharmaceutical compounds, representing the most substantial category of emerging micropollutants, has raised significant public health concerns because of their existence in various environmental compartments [1]. Acetaminophen (ACT) is one of the most commonly reported pharmaceutical products currently found in water resources [2,3], with significant adverse effects on human health, potentially leading to antibiotic resistance, endocrine disruption, and various chronic diseases [4]. Thus, ACT has emerged as a significant challenge for the treatment of domestic wastewater.

Solar photolysis, biodegradation, and conventional treatment methods such as activated sludge processes with adsorption, sedimentation, and filtration using membranes are generally inadequate for the comprehensive removal of ACT [5]. As an alternative, advanced oxidation processes (AOPs) are chemical methods that involve the

activation of certain molecules (e.g., hydrogen peroxide, ozone, persulfate), leading to the production of highly reactive radicals such as hydroxyl radicals and sulphate radicals [6]. These radicals engage in rapid and non-selective reactions with organic contaminants including ACT, ultimately breaking them down into harmless smaller molecules and achieving the purification of wastewater [7]. Nevertheless, despite significant advancements in AOPs since their formal introduction in 1987 by Glaze et al. [8], two primary challenges continue to restrict their widespread application. The first challenge associated with AOPs is the efficient activation of hydrogen peroxide (H_2O_2). In commercialised AOPs, ultraviolet light is commonly employed to produce hydroxyl radicals (·OH) by cleaving the O-O bond in H_2O_2 [9]. However, this process is highly energy-intensive. The second challenge is the sustainable production of H_2O_2. The current industrial method, known as the anthraquinone process, demands complex infrastructure and is impractical for small-scale applications [10]. Additionally, the risks related to the transportation and storage of H_2O_2 pose further obstacles to applying AOPs in remote locations and isolated communities [11].

Electro-Fenton (EF) technology, as one of the most promising AOPs, has the potential to generate H_2O_2 on-site and activate it under mild conditions. Besides, it has the advantages of a relatively simple reaction device and the elimination of the need for additional oxidants [12,13]. At the cathode in EF processes, oxygen undergoes a two-electron reduction reaction ($2e^-$ ORR), resulting in the generation of H_2O_2 as shown in Eq. 3.1 [14]. The produced H_2O_2 then reacts with an electro-Fenton catalyst, leading to the generation of highly reactive species such as ·OH [15].

$$O_2+2H^++2e^-\rightarrow H_2O_2 \qquad (3.1)$$

The key processes in EF technology involve the generation and activation of H_2O_2. The efficiency of H_2O_2 generation depends on the characteristics of the cathodic material. Carbon-based materials such as graphite felt (GF) [16,17], carbon nanotubes (CNT) [18], amorphous carbon black (CB) [19,20], and carbon aerogel (CA) [21] are commonly used in the cathodic matrix. Among them, CA is an outstanding candidate for cathode material and metal support because of its good electrical conductivity, large surface area, and corrosion resistance [22]. In recent studies, diverse approaches have been explored to enhance the electrochemical production of H_2O_2 using

modified carbon materials [23–25]. These have highlighted the significance of both the quantity and type of oxygenated surface functional groups [26]. For instance, a higher concentration of carboxyl groups leads to enhanced efficiency in generating H_2O_2 [27]. Furthermore, carbon-based materials with a higher disordered carbon ratio exhibit increased H_2O_2 production [28]. In general, carbonaceous materials with some significant features such as extensive surface area, C=C bonds, and the existence of oxygenated groups have been shown to exhibit higher catalytic activity for $2e^-$ ORR to produce H_2O_2 [26], which offers guidance for modifying carbon-based materials to enhance the yield of H_2O_2.

Due to its limited oxidation capacity, H_2O_2 alone is not active enough for the degradation of most pollutants thus highlighting the importance of the activation process for H_2O_2. In homogeneous EF processes, H_2O_2 can be activated using an externally added catalyst (Fe^{2+}) according to the Fenton reaction in Eq. 3.2. However, this presents challenges in a limited pH application range because of the formation of iron sludge [29]. In contrast, solid catalysts are employed in the heterogeneous EF processes, thus extending the pH range and addressing the limitations of homogeneous EF technology [30,31]. Among heterogeneous EF catalysts in previous studies, the applications of cathodes with assembled active Fe components hold significant importance for the electrocatalytic decomposition of contaminants. For example, a gas diffusion electrode (GDE) with the immobilisation of active Fe_3O_4 as a rotating cathode was found to be capable of decomposing H_2O_2 into ·OH [32]. Similarly, Cui et al. [33] developed a Fe_3O_4/MWCNTs/CB (carbon black) GDE, which demonstrated exceptional performance in the activation of H_2O_2. However, carbon catalysts doped with iron exhibit exceptional activity in the $4e^-$ ORR, leading to a reduced yield of H_2O_2 [34]. Therefore, enhancing the selectivity for the $2e^-$ ORR is crucial for Fe-based integrated cathodes to effectively produce ·OH radicals. Compared to monometallic Fe/carbon composite catalysts, bimetallic carbon composite catalysts possess the potential to enhance the overall efficiency of the catalysts [35]. These composites, comprising various species working synergistically, not only optimise the electronic structure but also enhance the charge-carrier density and improve conductivity [36]. Among these bimetallic materials, Fe-Ni mixture exhibits significant electrocatalytic activity [37]. The introduction of Ni is expected to enhance the $2e^-$ selectivity of Fe-based cathodes for the oxygen reduction

reaction. To the best of our knowledge, there are currently no studies on the composite of FeNi active sites and carbon aerogel as a cathode for EF system. The synergistic effects of Fe and Ni on the configuration and electrochemical characteristics of carbon aerogel (CA) have not been revealed.

$$Fe^{2+}+H_2O_2 \rightarrow Fe^{3+}+OH^- +\cdot OH \quad (3.2)$$

Furthermore, previously reported EF processes usually require oxygen/compressed air sparging to enhance H_2O_2 production [38,39]. However, the oxygen utilisation efficiency was found to be less than 0.1 % [40], indicating that a significant portion of the oxygen was not effectively utilised for H_2O_2 production and therefore caused a high cost. Hence, the development of an Electro-Fenton system that requires less oxygen or even eliminates the need for external oxygen input would be both economically advantageous and hold great promise for practical applications.

Herein, a new heterogeneous EF system was established using FeNi alloy carbon aerogel (FeNi-CA) as the cathode to achieve simultaneous generation and *in situ* activation of H_2O_2 without the need for external aeration. The microstructures and chemical compositions of the synthesised Fe-CA, Ni-CA, and FeNi-CA were analysed and compared using characterisation techniques. The synergistic effects of Fe and Ni on carbon aerogel for enhanced ORR activity and selectivity were evaluated in detail. We also assessed the performances of the EF system for the decomposition of ACT. The impacts of various reaction parameters, including initial pH, current, and aeration rate were also investigated. Furthermore, potential mechanisms of radical generation and ACT degradation pathways were proposed. The innovative process proposed in this work ensures the efficient production and immediate activation of H_2O_2 directly on the cathode surface, offering new insights for the development of novel heterogeneous EF systems and enhancing the efficiency of removing micropollutants.

3.3 Experimental section

3.3.1 Chemicals and reagents

Iron (III) acetylacetonate (AR, CAS: 14024-18-1), nickel (II) acetylacetonate (AR, CAS: 3264-82-2), iron (III) sulphate hydrate (AR, CAS: 15244-10-7) and tert-butanol (99.5%, CAS: 75-65-0) were obtained from Fluorochem Limited. Formaldehyde (37%, CAS: 50-

00-0), Nafion (5 wt%, CAS: 31175-20-9), 2,5-dihydroxybenzoic acid (99%, CAS: 490-79-9), and sodium hydroxide (≥98.0%, CAS: 1310-73-2) were purchased from Alfa Aesar. Resorcinol (99%, CAS: 108-46-3), titanium (IV) oxysulfate (≥29%, CAS: 13825-74-6), acetaminophen (≥99.0%, CAS: 103-90-2), hydrogen peroxide (30% w/w, CAS: 7722-84-1), nitric acid (69%, CAS: 7697-37-2), hydrochloric acid (37%, CAS: 7647-01-0), 2,3-dihydroxybenzoic acid (99%, CAS: 303-38-8), salicylic acid (99+%, CAS: 69-72-7), p-Benzoquinone (≥98%, CAS: 106-51-4), and 5,5-Dimethyl-1-pyrroline N-oxide (DMPO, ≥97.0%, CAS: 3317-61-1), were obtained from Sigma Aldrich. Sodium sulphate (≥99.5%, CAS: 7757-82-6), sulfuric acid (96%, CAS: 7664-93-9), nickel (II) sulphate hexahydrate (99%, CAS: 10101-97-0) and methanol (≥99.9%, CAS: 67-56-1) were purchased from Fisher Scientific. Sodium sulphite (98%, CAS: 7757-83-7) and acetone (99+%, CAS: 67-64-1) were obtained from Thermo Scientific. Sodium carbonate (AR, CAS: 497-19-8) was purchased from BioServ UK Limited. Pt and graphite sheet electrodes were purchased from Shanghai Chuxi Industrial Co., Ltd, China.

3.3.2 Cathode synthesis

The synthesis of single and alloy metal carbon aerogel cathodes in this research involved the following steps: (I) gelation phase, involving the creation and reinforcement of the gel through sol–gel and aging processes; (II) solvent exchange of water in the obtained wet gel structure with acetone; (III) drying, for the formation of the aerogel through drying the gel at room temperature and pressure; and (IV) carbonisation, the acquisition of the final aerogel through carbonisation at high temperature in a continuous flow of N_2.

Synthesis steps for the iron-nickel carbon aerogel (FeNi-CA) are similar to the method reported by Xiao et al. [41]. Firstly, 11.011 g of resorcinol was mixed with 19.64 mL of Milli-Q water. Then, 15 mL of formaldehyde (37 %) and 0.0085 g of sodium carbonate were added to the mixture under constant stirring until completely dissolved. Subsequently, the metallic precursors for FeNi-CA i.e., ferric acetylacetonate (0.5375 g) and nickel acetylacetonate (0.3721 g) respectively, were dissolved in the homogeneous solution. Since the molar ratio of Fe:Ni is 1:1 at this dosage, this cathode was also marked as $Fe_{0.5}Ni_{0.5}$-CA. After one hour of magnetic stirring, the mixture was poured into a cuboid Teflon mould. The well-sealed Teflon mould containing the precursor solution was cured in an oven using a stepped temperature profile (30 °C for 24 h, 50 °C for 24 h,

and 90 °C for 72 h) to complete the polymerisation and aging processes. An example of the obtained wet-gel in the mould is presented in Appendix B (Fig. S3.1 (a)). Subsequently, the obtained wet gel was completely immersed in acetone for 72 h to thoroughly replace the water remaining in the carbon structure, before drying under ambient conditions for one day. Acetone was chosen as the exchange solvent because of its lower surface tension to reduce the shrinkage of the gel [42]. Finally, the moulded aerogel was calcined in a tube furnace (Carbolite Gero TZF 12/38) under N_2 atmosphere with a flow rate of 0.1 L/min. The heating rate was set at 3 °C/min, starting from room temperature and reaching 950 °C, where it was maintained for 4 h. After the carbonisation procedure, the obtained FeNi-CA was cooled to ambient temperature and used as the integrated cathode in the electro-Fenton system. The obtained FeNi-CA cathode is also shown within the Appendix B (Fig. S3.1 (b)).

Similar procedures were also used to synthesise the single metal iron carbon aerogel (Fe-CA) and nickel carbon aerogel (Ni-CA), with the addition of 0.5375 g of ferric acetylacetonate and 0.3721 g of nickel acetylacetonate, respectively. The metal precursors for $Fe_{0.7}Ni_{0.3}$-CA were 0.7525 g ferric acetylacetonate and 0.2233 g nickel acetylacetonate, and for $Fe_{0.3}Ni_{0.7}$-CA were 0.3225 g ferric acetylacetonate and 0.5209 g nickel acetylacetonate. To simplify the description, FeNi-CA in this thesis refer to $Fe_{0.5}Ni_{0.5}$-CA with a metal ratio of 1:1.

3.3.3 Cathode characterisation

Nitrogen adsorption–desorption isotherms were obtained at 77K utilising a Micromeritics Tristar 3000 instrument. Before the measurement, the samples underwent degassing under vacuum at 393 K for 16 h to remove any residual moisture. The Brunauer-Emmet-Teller (BET) surface areas were calculated based on selected N_2 adsorption data within the relative pressure range of 0.05 to 0.16. Pore size distributions were determined using the Barrett–Joyner–Halenda (BJH) method [43] from the desorption branch. The morphologies of the obtained electrodes were analysed using high-resolution scanning electron microscopy (HRSEM, Carl Zeiss EVO MA15) and high-resolution transmission electron microscopy (HRTEM, FEI Titan3 Themis 300). Energy dispersive X-ray spectroscopy (EDS) mapping was conducted by operating the same equipment used for HRTEM with a HAADF detector. X-ray diffraction (XRD) tests were measured with a

D8 (Bruker) at 40 kV and 40 mA over a 2θ range of 10-80° with Cu Kα radiation. Experimental Raman spectra were recorded using a Raman microscope (Horiba Scientific LabRAM HR Evolution) with an excitation source at 514 nm (1.5 mW laser power, spot diameter is 2 μm). The surface functional groups of the cathodes were characterised using Fourier infrared diffuse reflection (FTIR, Thermo Scientific, Nicolet iS5), on powder-pressed KBr pellets. The elemental composition and chemical state were determined by X-ray photoelectron spectroscopy (XPS, ESCALAB XI^+, Thermo Scientific) using Al Kα radiation.

3.3.4 Electrochemical tests

Electrochemical experiments were performed employing a three-electrode setup. The prepared electrode served as the working electrode, with a platinum sheet serving as the counter electrode, and Ag/AgCl acted as the reference electrode. The measurements were conducted using a CHI 760E electrochemical workstation (Chenhua Instrument Co. Ltd., China). To prepare the working electrode for cyclic voltammetry (CV), grind the bulk FeNi/CA sample into powder first, and 10 mg of powder was dispersed in a solvent consisting of 1.5 mL of Milli-QTM water, 0.75 mL of ethanol, and 25 μL of 5 wt% Nafion solution. After 1 h of sonication, the resulting catalyst ink was drop-cast onto a glassy carbon electrode surface (diameter: 3 mm) at a volume of 6 μL. The electrode was left to air-dry naturally, forming a uniform catalyst film layer. CV measurements were performed separately in O_2-saturated and N_2-purged (deoxygenated) electrolytes (0.1 M Na_2SO_4 at pH = 5) with a scan rate of 10 mV/s [44]. Electrochemical impedance spectroscopy (EIS) experiments were conducted over a frequency range of 10^{-2}–10^5 Hz with 5 mV amplitude.

Oxygen reduction reaction (ORR) activity and selectivity were investigated using an AFMSRCE rotator unit (Pine Instrument Company, United States) by recording rotating ring disk electrode (RRDE) voltammograms in 0.1 M Na_2SO_4 at pH = 3. Firstly, the catalyst ink was formulated by sonicating a mixture of 10 mg catalyst powder, 1.5 mL of water, 0.75 mL of ethanol, and 25 μL of Nafion solution (5 wt%) for 1 h. Then, 12 μL of the catalyst ink was pipetted and spread onto a glassy carbon (GC) disk electrode for the RRDE test. The RRDE was composed of a GC disk (0.2475 cm^2) and a Pt ring (0.1866 cm^2). The catalyst loading density was 213 μg/cm^2. After air-drying overnight at room

temperature, the modified RRDE was used as the working electrode, equipped with Ag/AgCl reference electrode and platinum wire counter electrode. Prior to testing, the electrolyte was aerated with O_2 for 30 min. To eliminate the capacitive current of the working electrode, the baseline current was recorded under a nitrogen atmosphere at the same rotation speed (1600 rpm) and scan rate (10 mV/s) as used under oxygen condition. This baseline current was subsequently subtracted from the ORR polarisation curve [45]. The Pt ring electrode was maintained at a fixed potential of 1.3 V vs. reversible hydrogen electrode (RHE).

The determination of H_2O_2 selectivity and the corresponding electron transfer number (n) in ORR process was carried out using Eq. 3.3 and Eq. 3.4 [46]:

$$H_2O_2\ (\%) = 200 \times \frac{I_R/N}{I_D + I_R/N} \quad (3.3)$$

$$n = \frac{4I_D}{I_D + I_R/N} \quad (3.4)$$

Here, I_R represents the current at the ring electrode, I_D indicates the current at the disk electrode, and N stands for the collection efficiency (with a value of 0.37).

3.3.5 Electrochemical degradation

Electrocatalytic degradation experiments were carried out in a 150 mL single-chamber cylindrical glass cell. The fabricated carbon aerogels (working area of 4.5 cm^2) and platinum sheet (working area of 4.0 cm^2) functioned as cathode and anode, respectively. The distance between the two electrodes was kept at 2 cm. In most experiments, the DC power supply (Velleman 70–0768) was set at the optimal operative current of 20 mA for the electrocatalytic degradation process, and the relevant potential was monitored as 1.5-2.7 V. In electro-sorption (ES) experiments, the current was kept at 1 mA under 0.2 L/min N_2 atmosphere with a relevant potential of 1.3-1.5 V. The pH of the solution was adjusted with H_2SO_4 (0.1 mol/L) and NaOH (0.1 mol/L) to the desired value. Dissolved oxygen concentration and pH values were measured using HQ 40d (Hach, UK) digital multi-meter kit. The reaction was initiated by aeration with compressed air at a predetermined flow rate into the simulated wastewater, which consisted of 0.05 mol/L Na_2SO_4 and 10 mg/L ACT. Samples for analysis were collected at pre-determined intervals and then filtered using a 0.22 μm syringe filter. The concentration of ACT was quantified using high-performance liquid chromatography (HPLC), with details are

provided in the Appendix B. The electrochemical degradation of ACT was described using the pseudo-first-order kinetic model, represented using Eq. 3.5 [47]:

$$ln\,(C_0/C_t) = k_{obs}\,t \qquad (3.5)$$

where k_{obs} is the apparent reaction rate constant (min^{-1}), t is the reaction time (min), and C_0 and C_t represent the initial ACT concentration (mg/L) and ACT concentration at time t (mg/L), respectively.

Electrical energy consumptions in the electro-Fenton process were calculated according to Eq. 3.6 [48]:

$$EC_{ACT}(kWh/kg_{ACT}) = I \cdot V \cdot t/\Delta m_{ACT} \qquad (3.6)$$

where EC_{ACT} (kWh/kg_{ACT}) is the energy consumption per degraded ACT mass, I is the applied current (A), V is the average voltage (V), t is the treatment time (h), Δm_{ACT} is the ACT mass removal (g).

The synergistic effect (SE) was determined according to Eq. 3.7 [49] by evaluating the efficiency of pollutant removal in the bimetallic process against the total efficiencies of each sole process:

$$SE = \left(\frac{k_{FeNi\text{-}CA}}{k_{Fe\text{-}CA}+k_{Ni\text{-}CA}} - 1\right) * 100 \qquad (3.7)$$

where $k_{FeNi\text{-}CA}$, $k_{Fe\text{-}CA}$, and $k_{Ni\text{-}CA}$ represent the rate constants of the FeNi-CA process, Fe-CA, and Ni-CA process, respectively.

The cyclic experiments were conducted by collecting and washing the used cathode with Milli-Q™ water (Merk Millipore) and then employing it for subsequent repeated runs under identical experimental conditions. The electrocatalytic stability and recyclability of the cathodes were evaluated through the degradation efficiency of ACT over the reused cathode.

3.3.6 Analytical methods

The concentration of acetaminophen (ACT) was quantified using a high-performance liquid chromatography (HPLC) system (Agilent 1290 Infinity II) with a chromatography column (Agilent Infinity Lab Poroshell 120 EC-C18, 2.1 mm x 50 mm, 1.9 μm). The

measurement was performed at a wavelength of 254 nm, with the HPLC system maintained at a temperature of 40 °C. The mobile phase comprised Solvent (A) water with 0.1% trifluoroacetic acid and Solvent (B) acetonitrile with 0.1% trifluoroacetic acid, with the gradient being 0 min: 95%A–5%B, 5 min: 5%A–95%B, and 6 min: 95%A–5%B. The flow rate of the mobile phase was set at 0.5 mL/min and 10 μL was used as the injection volume. The degradation intermediates were determined by liquid chromatography mass spectrometry (LCMS) (Agilent 1260 Infinity II) equipped with a 3 mm × 50 mm C18 analytical column and 2.7 μm particle size (Agilent Poroshell 120 EC-C18). The mobile phase consisted of Solvent (A) 0.1% formic acid in H_2O and Solvent (B) acetonitrile with 0.1% formic acid, with a gradient elution of 0 min: 98%A–2%B, 0.5 min: 98%A–2%B, 6.5 min: 2%A–98%B, 7.5 min: 2%A–98%B, 7.6 min: 98%A–2%B, 8 min: 98%A–2%B. The signals were recorded in both positive and negative ionisation modes for a duration of 10 minutes. The chromatographic system was connected to an Agilent Infinity Lab LC/MSD XT mass spectrometer under a capillary voltage of 3000 V and drying gas of 12.0 L/min. The analyser scanned a mass range of 60–1000 m/z for full scanning at a rate of 2600 $spectrum^{-1}$. The LCMS was controlled using Agilent OpenLab CDS Chemstation Edition (rev. C.01.10 (287)).

Metal loadings on the synthesised electrodes were measured using Inductively Coupled Plasma-Mass Spectrometry (ICP-MS, Perkin Elmer Elan DRCe). Specifically, the electrodes were ground and dispersed in a beaker containing an acid mixture of HCl: HNO_3 (3:1). The solid-liquid mixture was heated slowly using a temperature-controlled hot plate until the acid was completely evaporated. It was allowed to cool down to the room temperature before adding 10 mL of nitric acid. The resulting mixture was heated to reduce the volume to 5 mL, before cooling once again to room temperature and filtered with a 0.22 μm syringe filter. The diluted metal concentrations were measured using ICP-MS.

The concentration of generated H_2O_2 was measured by colorimetric analysis of the complex formed between Ti(IV) and H_2O_2 using UV-vis (Shimadzu UV1900) at a detection wavelength of 408 nm [50]. Specifically, 1 mL aliquots at specific time intervals were extracted and added to a mixed solution containing 0.5 mL $TiOSO_4$ (0.05 M), 0.5 mL H_2SO_4 (3 M), and 3 mL H_2O. After standing for 10 min, the absorbance at a

wavelength of 408 nm was measured. The generated radicals were directly identified using Electro Spin Resonance (ESR, Bruker EMXplus EPR Spectrometer) technique with DMPO as a spin-trapping agent. The quantitative determination of hydroxyl radicals (·OH) was achieved through a probe reaction involving salicylic acid (SA) and ·OH [51]. The probe reaction was conducted by adding 0.01 M SA to oxygenated Na_2SO_4 electrolyte solution (0.05 M) prior to the experiment. At specific time intervals, 1 mL of the reaction solution was extracted for subsequent analysis via HPLC. The hydroxylated products, namely 2,3-dihydroxybenzoic acid (2,3-DHBA) and 2,5-dihydroxybenzoic acid (2,5-DHBA), were detected at a wavelength of 320 nm during HPLC analysis. The mobile phase comprised Solvent (A) water with 0.1% trifluoroacetic acid and Solvent (B) acetonitrile with 0.1% trifluoroacetic acid, with the gradient being 0 min: 95%A–5%B, 5 min: 5%A–95%B. The column temperature was kept at 40 °C and the flow rate was set as 0.5 mL/min. Under these conditions, the retention time of 2,3-DHBA and 2,5-DHBA were observed as 1.85 min and 1.7 min. The concentration of ·OH was determined by the sum of concentrations of 2,3-DHBA and 2,5-DHBA.

3.4 Results and discussion

3.4.1 Surface and structural properties

X-ray diffraction (XRD) analysis was conducted to demonstrate the composition and crystal structure of the synthesised FeNi-CA, Fe-CA and Ni-CA cathodes, as shown in Fig. 3.1 (a). Two broad XRD diffraction peaks at 23.3° for FeNi-CA and Ni-CA are observed, corresponding to the (0 0 2) reflection of the graphitic carbon [52,53]. This peak becomes sharper and shifts slightly to 25.9° in the Fe-CA cathode sample, and a small peak at 43.2° appears, which may be ascribed to amorphous carbon [34,53]. The XRD pattern of Ni-CA shows three sharp peaks at 44.5°, 51.9°, and 76.6° (2θ), which can be indexed to the three reflections of (1 1 1), (2 0 0) and (2 2 0) crystal planes of cubic Ni according to the JCPDS No. 04-0850 [54]. Besides, an obvious diffraction peak of Ni-CA at 29.5° is observed for NiC_x (JCPDS No. 45-0979) [55]. The crystalline phase of iron in Fe-CA is composed of zero valence state Fe^0 (1 1 0) and oxidation state Fe_3O_4 (JCPDS 89-0951) [56], and the minor peaks detected for Fe_3O_4 are preserved in the FeNi-CA cathode. Previous studies have shown that Fe_3O_4 has the ability to catalyse the decomposition of H_2O_2 to produce ·OH [57], which can contribute to the heterogeneous Fenton reaction. Furthermore, the XRD spectrum of FeNi-CA shows a good crystalline structure of

$FeNi_3$ as evidenced by three diffraction peaks located at 43.9°, 51.2°, and 75.2° corresponding to (1 1 1), (2 0 0), (2 2 0) crystal facets from the face-centred-cubic $FeNi_3$ phase (JCPDS, No. 65-3244) [53]. These XRD results revealed the formation of $FeNi_3$ alloy and graphitic carbon phases in the synthesised FeNi-CA cathode.

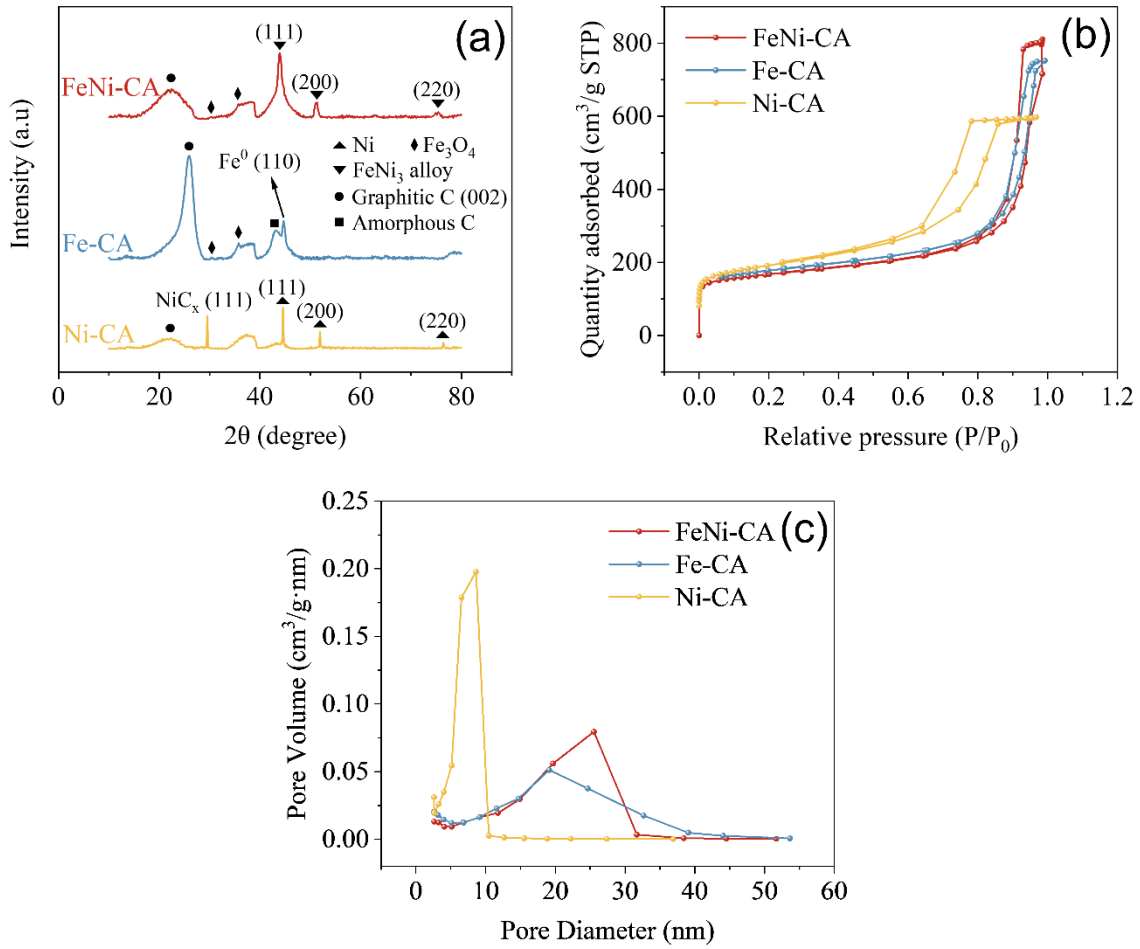

Figure 3.1. (a) XRD spectra, (b) N_2 adsorption–desorption isotherms, and (c) Pore size distribution curves of FeNi-CA, Fe-CA, and Ni-CA.

The porosity of the FeNi-CA, Fe-CA, and Ni-CA was further investigated with N_2 adsorption–desorption isotherms, as illustrated in Fig. 3.1 (b). All cathodes exhibit an isotherm categorised as IUPAC Type IV with an H1 hysteresis loop, reflecting their prominent mesoporous structures [58]. Additionally, the comparison of the pore structures between CA and FeNi-CA in Fig. S3.2 indicated that the prominent mesoporous structure of CA doesn't change after depositing FeNi alloy, while the smaller pores may be filled or covered by the FeNi alloy particles. At a low relative pressure of $P/P_0 = 0.1$, the observed adsorption suggests the existence of micropores. Conversely, at higher relative pressures, the adsorption indicates the presence of mesopores in FeNi-

CA [59]. Micropores offer abundant active sites for the oxygen reduction reaction, while meso-macro pores act as gas transfer pathways, supplying oxygen and enabling the electrolyte to permeate into the cathode interior. This dual functionality might enhance the oxygen reduction performance of FeNi-CA [60]. Pore size distributions were obtained by analysing the desorption branches of the isotherms using the BJH (Barrett–Joyner–Halenda) method [61]. As shown in Fig. 3.1 (c), Ni-CA has a saturated adsorption plateau at smaller P/P_0 and features mesopores with sizes centred at 8.6 nm, while FeNi-CA and Fe-CA have a relatively wider pore size distribution with pore diameters centred on ~20 nm and ~25 nm, respectively. The N_2 adsorption–desorption analysis yielded pore structural parameters that are presented in Table 3.1, with results indicating the single metal Ni-CA has the highest BET surface area and smallest average pore diameter amongst the three cathodes. Nevertheless, both the FeNi-CA and monometallic Fe-CA have similar pore structural parameters, and BET surface areas of around 600 m^2/g which are larger than other reported alloy carbon aerogels [34,41,62]. Such a highly porous characteristic can provide an increased number of catalytically active sites, as well as ample contact area between electrolyte and electrode for efficient electrocatalysis [63].

Table 3.1. Metal loading and porosity of FeNi-CA, Fe-CA, and Ni-CA (FeNi-CA refer to $Fe_{0.5}Ni_{0.5}$-CA with a metal ratio of 1:1).

Electrode	Metal loading [wt.%]		BET surface area (m^2/g)	Micropore area (m^2/g)	Micropore volume (cm^3/g)
	Fe	Ni			
FeNi-CA	1.15 ± 0.01	0.86 ± 0.02	589.0	350.9	0.155
Fe-CA	1.05 ± 0.04	/	609.7	351.0	0.162
Ni-CA	/	0.90 ± 0.05	665.9	301.2	0.138

The surface morphology of FeNi-CA was further examined using high-resolution scanning electron microscopy (HRSEM). The HRSEM images under 25 K magnification (Fig. 3.2 (a)) show that the synthesised FeNi-CA has a networked porous microstructure. Moreover, aggregated nanoclusters may be observed from the images under higher magnifications (Fig. 3.2 (b)). According to a previous study [64], the obtained cathode presents as a typical carbon aerogel structure, being comprised of rounded and interconnected primary clusters.

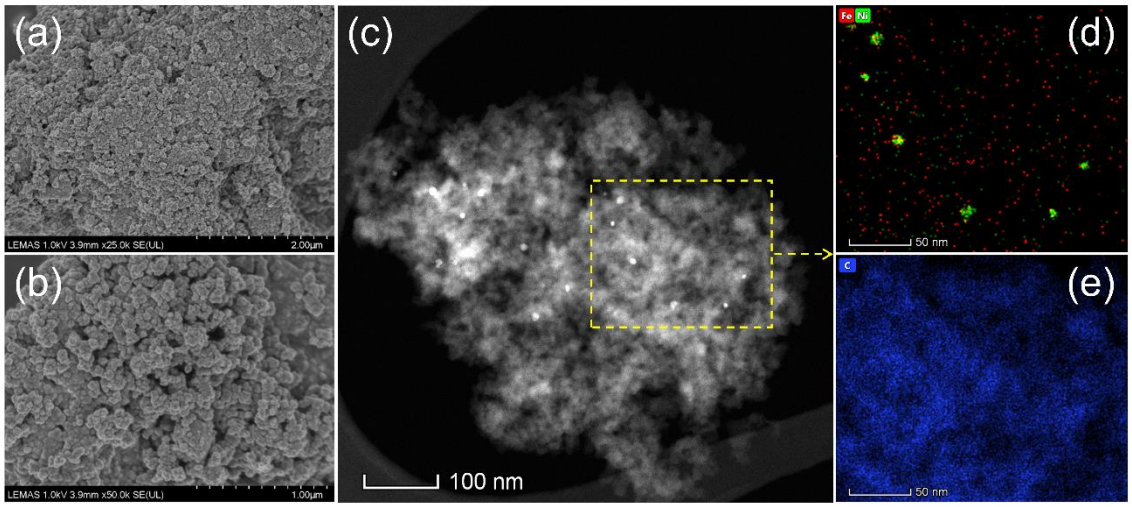

Figure 3.2. (a) and (b) HRSEM images of FeNi-CA, (c) STEM image of a FeNi-CA cluster, (d) EDS mapping of elemental Fe and Ni, and (e) EDS mapping of elemental C.

The microstructure of FeNi-CA was then characterised using high-resolution transmission electron microscopy (HRTEM) and scanning transmission electron microscopy (STEM). The STEM images in Fig. 3.2 (c) indicate nano-scale particles with a size range of 10–20 nm that are well dispersed within the carbon aerogel matrix, ensuring that they maintained high dispersion during the preparation process. Elemental C, Fe and Ni are clearly evidenced by the energy dispersive X-ray spectroscopy (EDS) mappings in Fig. 3.2 (d) and (e), as well as further images supplied in the Electronic Supplementary Materials (Appendix B, Fig. S3.3 (a)–(d)). The distribution of these elements reveals that Fe signals match Ni signals, indicating the formation of an alloy phase in the carbon aerogel structure, which is further demonstrated by the electron diffraction ring corresponding to $FeNi_3$ (1 1 1) plane with an interplanar spacing of 0.204 nm in Fig. 3.3 (a). The presence of certain transition metals (e.g., Fe, Ni, Cr) has been reported to catalyse the formation of graphite clusters during the carbonisation stage of carbon aerogel [65,66]. A detailed examination of Fig. 3.3 (b) shows partial graphitisation of the carbon phase around the alloy particles. Furthermore, the interplanar spacing of 0.253 nm depicted in Fig. 3.3 (c) confirms the presence of Fe_3O_4 within the FeNi-CA composite, which is consistent with the findings obtained from XRD analyses. Additionally, the measured interplanar spacing of 0.341 nm can be attributed to the (0 0 2) crystal plane of graphitic carbon [67]. Previous research [65] has also observed partial graphitisation of the carbon aerogel. The formation of these graphitic clusters is likely to enhance the electrochemical performance of the materials by increasing their electrical

conductivity [61].

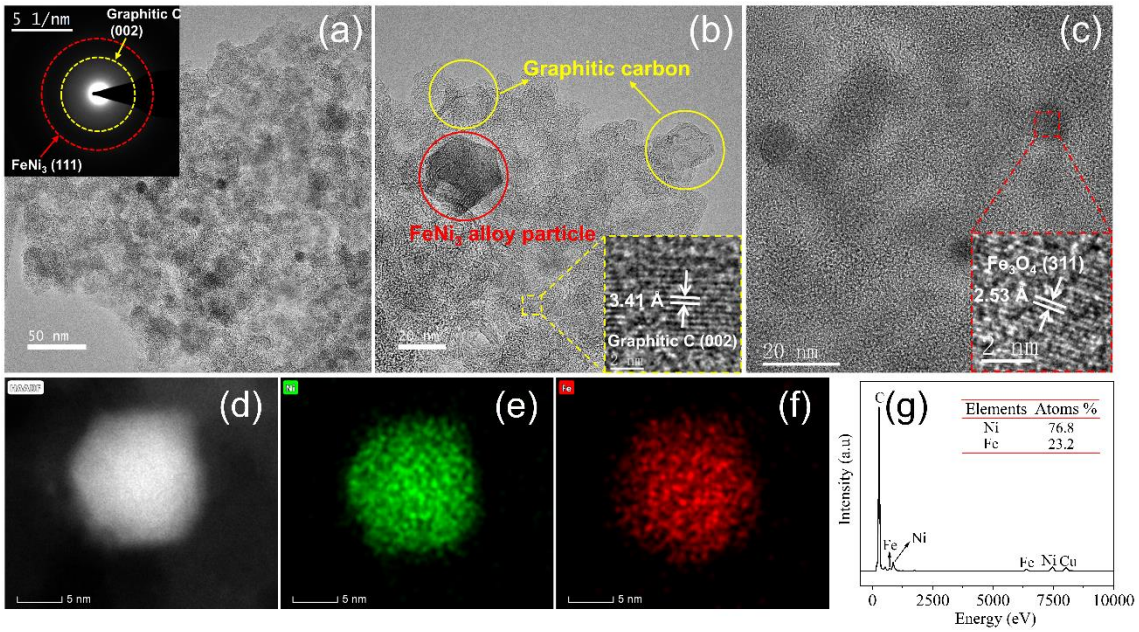

Figure 3.3. (a)–(c) HRTEM images of FeNi-CA, (d) STEM image of an individual $FeNi_3$ particle, (e) EDS mapping of elemental Ni, (f) EDS mapping of elemental Fe, (g) EDS spectra of the selected $FeNi_3$ particle.

In addition to the alloy particles, there are also free metals found in the carbon matrix that may be associated with bound ions. The atomic percentage of Fe and Ni in the selected area of Fig. S3.3 (a) (including free and alloy phases) is 43.7 % (Fe) and 56.3 % (Ni), as confirmed by the EDS spectrum (Fig. S3.3 (e)), almost in accordance with the input molar ratio during synthesis (Fe:Ni = 1:1). Furthermore, the metal loadings determined by inductively coupled plasma-mass spectrometry (ICP-MS) analysis is 1.15 wt% (Fe) and 0.86 wt% (Ni), as shown in Table 3.1.

Fig. 3.3 (d)–(f) present STEM images and element mapping taken from an individual alloy particle. These reveal that both elemental Fe and Ni distribute homogeneously in the $FeNi_3$ alloy phase. The line scanning profiles within the Appendix B (Fig. S3.4 (a)–(c) and Fig. S3.5) that were recorded from the alloy particles further confirm the uniform distribution of Fe and Ni. The molar ratio in the alloy particle was measured as 23.2 % (Fe) and 76.8 % (Ni) by the EDS spectrum (Fig. 3.3 (g)), almost consistent with the stoichiometric ratio in $FeNi_3$ alloy [53]. Previous research also found a $FeNi_3$ alloy phase in a metal–organic framework (MOF) derived three-dimensional carbonaceous matrix. The synergistic effect between Ni and Fe components was shown to play an important

role in the electrocatalysis process [68].

X-ray photoelectron spectroscopy (XPS) analysis was performed to investigate the electrode surface, providing insights into the elemental composition and surface functional groups of FeNi-CA. Results for the full spectrum, as well as Fe and Ni peaks, are presented in the Appendix B (Fig. S3.6 (a)–(c)) and identify the presence of C and O on the cathode surface within the detection limit. Due to the low metal loadings in the synthesised cathode, the high-resolution XPS spectra of the metal elements exhibit only weak signals. The C 1s XPS spectrum (Fig. 3.4 (a)) displays distinct peaks representing different carbon species. The peaks at 284.8 eV, 285.0 eV, 286.5 eV, 288.1 eV, and 291.0 eV are assigned to C–C, C defect, C-O, COOH, and π-π*, respectively [56,69]. The presence of carbon defects has been demonstrated to effectively adjust the electronic structure of the catalyst, leading to superior electrocatalytic properties [70]. Raman spectroscopy was subsequently employed to investigate the presence of carbon defects in the synthesised cathodes. As presented in Fig. 3.4 (c), all samples display characteristic D and G bands at 1350 cm^{-1} and 1590 cm^{-1}, respectively, corresponding to the disordered and graphitic phases in carbon [71]. Hence, the integrated intensity ratio of the D and G bands area indicates the degree of structural ordering and defects in the carbon framework, with a higher I_D/I_G value suggesting increased defects in disordered carbon [70]. The I_D/I_G value is approximately 3.00, 1.73, and 2.88 for the FeNi-CA, Fe-CA, and Ni-CA, respectively. These demonstrate that the incorporation of FeNi nanoalloy promotes the formation of carbon defects, aligning with the results of numerous carbon defects (39.9 % of relative abundance) presented by the C 1 s XPS spectrum.

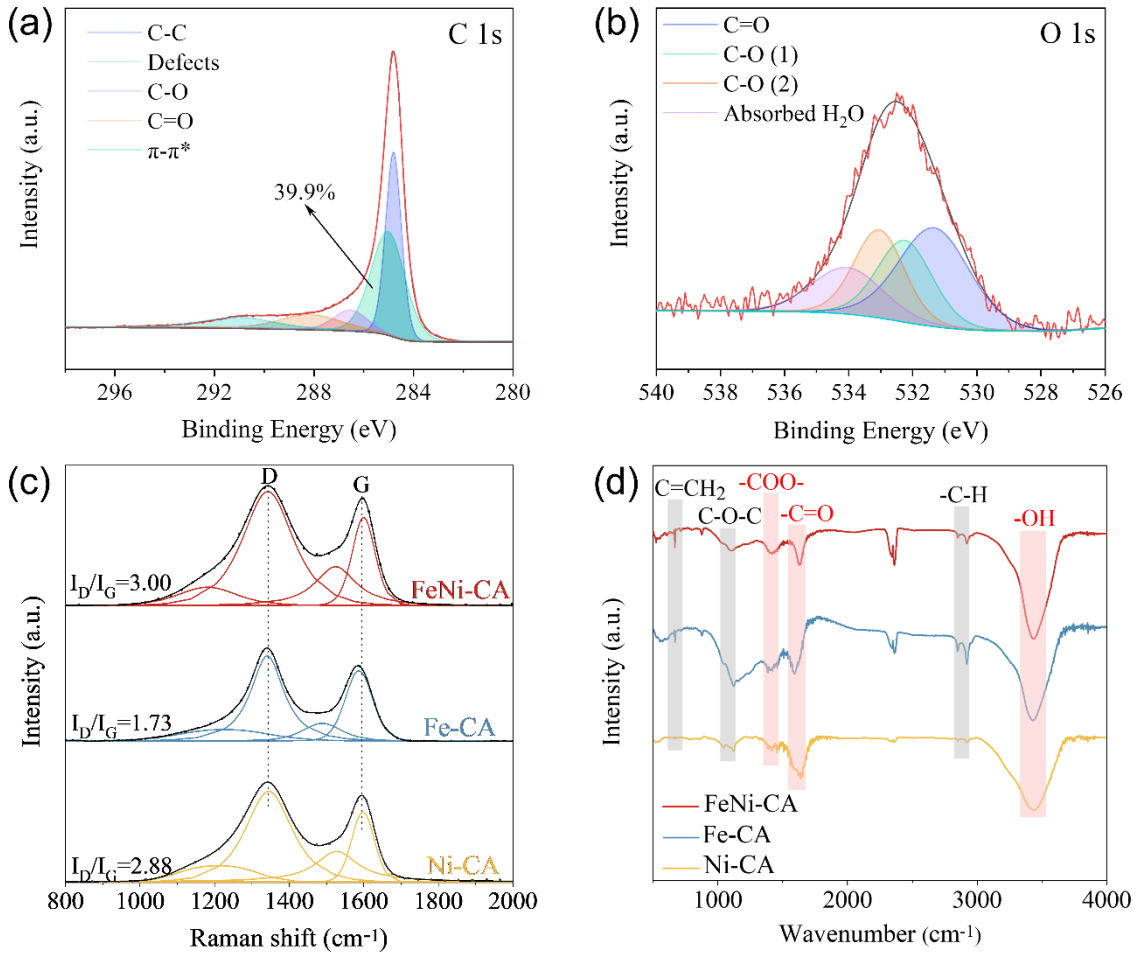

Figure 3.4. (a) C 1s XPS spectra of FeNi-CA, (b) O 1s XPS spectra of FeNi-CA (C-O (1) refers to ether and hydroxyl groups bonded to aliphatic & carbonyl shake-up and C-O (2) refers to ether and hydroxyl groups bonded to aromatics), (c) Raman spectra, and (d) FTIR spectra.

According to a previous study [72], introduced oxygen functional groups have a positive impact on the increased efficiency of H_2O_2 generation. This is because of their role in facilitating the displacement of electron density of the active site thereby enhancing interaction during O_2 adsorption [19,73]. The O 1s XPS spectra of FeNi-CA (Fig. 3.4 (b)) could be deconvoluted into four peaks associated with different oxygen groups, namely C=O at 531.3 eV, ether and hydroxyl groups bonded to aliphatic & carbonyl shake-up at 532.2 eV, ether and hydroxyl groups bonded to aromatics at 533.0 eV, and surface absorbed water at 534.0 eV [74]. Fourier transform infrared spectrometer (FTIR) analysis was also conducted to investigate functional groups and chemical bonds. The peaks observed at 3433 cm^{-1} (Fig. 3.4 (d)) may be attributed to O–H groups, stretching vibrations of −C=O bonds are observed at 1629 cm^{-1}, and peaks at 1419 cm^{-1} are

assigned to –COO- vibrations [75]. FTIR analysis also reveals the presence of oxygen functional groups on the FeNi-CA surface, which has the potential to enhance electrocatalytic ORR reactivity [28].

The combined characteristic analysis showed that FeNi-CA possesses an interconnected carbon network with a prominent mesoporous structure and high surface area. Mesopores function as pathways for gas transfer, delivering oxygen and facilitating the permeation of electrolyte into the interior of carbon materials. The nanostructured morphology of the material provides a larger number of active sites on the electrode surface, promoting enhanced catalytic activity. Additionally, the presence of $FeNi_3$ alloy, carbon defects, and abundant oxygen functional groups further enhance its structural characteristics. These unique structural features endow FeNi-CA alloys as promising candidates for electrocatalytic applications.

3.4.2 Electrochemical properties

Electrochemical testing is an efficient approach to evaluate the performance of cathodic material samples for an electro-Fenton system. To investigate the conductivity of the synthesised materials, electrochemical impedance spectroscopy (EIS) was conducted and the impedance Nyquist diagram is presented in Fig. 3.5 (a). A semi-arc in the high-frequency range was observed, representing the charge transfer resistance (R_{ct}) at the interface between the electrolyte and electrode. A larger semi-arc radius represented a greater R_{ct} [76], and the linear response in the low-frequency region corresponded to Warburg impedance reflecting ion diffusion behaviour [77]. Both Ni-CA and FeNi-CA showed smaller R_{ct} than Fe-CA, suggesting faster electron transfer rates and higher kinetics for electrochemical reactions [78]. The increased electron transfer efficiency might be due to the chemical interactions such as the electron exchange at the interface of FeNi alloy particles and the carbon matrix [41]. Cyclic voltammetry (CV) experiments were carried out to evaluate the ORR activity of the FeNi-CA cathode. No redox peaks were detected in the electrolyte saturated with N_2 when employing FeNi-CA as the working electrode (Fig. 3.5 (b)). In comparison, a distinct oxygen reduction peak emerged at −0.5 V vs. reversible hydrogen electrode (RHE) under the premise of O_2, accompanied by an increase in current response. This observation suggested the occurrence of an oxygen reduction reaction (ORR) on the surface of the electrode [79].

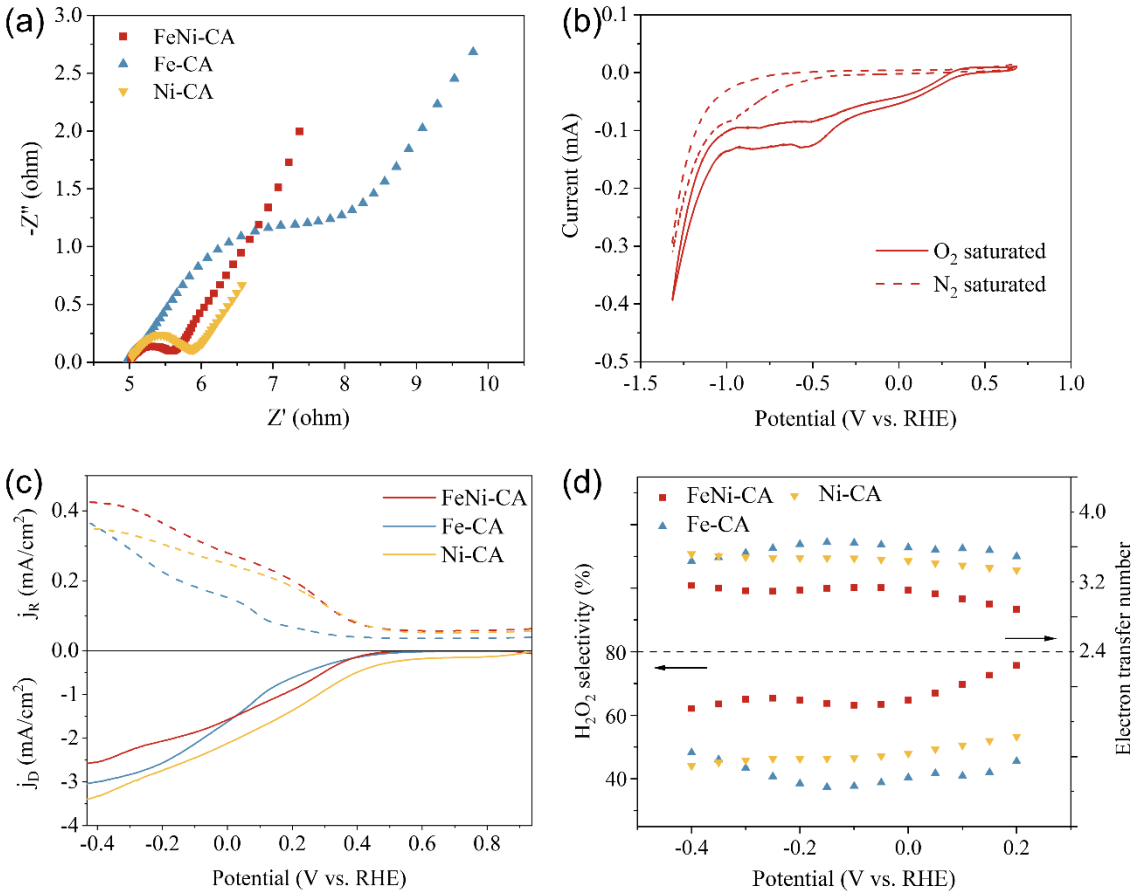

Figure 3.5. (a) EIS Nyquist plots, (b) CV curves of FeNi-CA in the presence O_2 and N_2, (c) Polarisation curves of different electrodes and simultaneous H_2O_2 oxidation currents at the ring electrode in 0.1 mol/L Na_2SO_4 at pH = 3, and (d) Calculated electron transfer number and H_2O_2 selectivity.

In addition, $2e^-$ ORR activity and selectivity of the FeNi-CA, Fe-CA, and Ni-CA electrodes were investigated using rotating ring-disk electrode (RRDE) measurements. Fig. 3.5 (c) illustrates the measurement of current resulting from oxygen reduction on the disk electrode and the quantification of generated H_2O_2 oxidation currents at 1.3 V vs. RHE on the ring electrode. The onset potential (E_{onset}) for FeNi-CA, Fe-CA, and Ni-CA were determined to be 0.421 V, 0.442 V, and 0.866 V vs. RHE, respectively. Although Ni-CA exhibited the highest ORR activity, as demonstrated by the most positive onset potential, its $2e^-$ ORR selectivity was not as high as FeNi-CA as evidenced by the smaller ring current density. The H_2O_2 selectivity and electron transfer number were calculated according to Eq. 3.3 and Eq. 3.4 in the Appendix B. In the −0.4 to 0.2 V vs. RHE range (Fig. 3.5 (d)), the H_2O_2 selectivity of the FeNi-CA catalyst was 60 %–80 %, higher than that of the monometallic Fe-CA and Ni-CA. The electron transfer number of FeNi-CA was 2.5–2.7, indicating its activity for catalysing two-electron ORR

processes from oxygen to H_2O_2. The electron transfer number results also showed the Fe-CA electrode had high activity for the $4e^-$ ORR, leading to the formation of H_2O ($O_2+4e^-+4H^+ \rightarrow H_2O$). Therefore, the incorporation of Ni increases the ORR activity and induces the conversion of $4e^-$ oxygen reduction to $2e^-$ pathways. Moreover, the synergistic effect of Fe and Ni greatly enhanced 2e ORR selectivity of pure CA (Fig. S3.7 (a)-(b)), which contributes to the improved production of H_2O_2 by over four times during the electrocatalytic reaction (Fig. S3.7 (c)).

The enhanced ORR activity observed in FeNi-CA compared to the monometallic may be primarily attributed to the alloying effect between Fe and Ni that caused lattice mismatch and electronic modification. This alloying effect has been demonstrated in other bimetallic alloys and is known to enhance catalytic performance [80]. The increased ORR activity of FeNi-CA could therefore be ascribed to (1) the presence of transition metals catalysing the partial graphitisation of the carbon aerogel to increase electrical conductivity, and the graphitic carbon further promoting the development of carbon defects. Here, the carbon defects could modify the atomic and electronic structure of the cathode, resulting in significantly improved electrocatalytic properties [26]; (2) the unique graphitic carbon structure contributed to the generation of oxygen functional groups, which played a beneficial role in enhancing the ORR electrocatalytic process; and (3) the formation of FeNi alloy facilitated efficient electron transport within the electrode, improving overall electrochemical performance [81].

3.4.3 Electro-Fenton oxidation performance

3.4.3.1 Degradation efficiency of ACT

In Section 3.4.2, the FeNi-CA cathode exhibited high ORR activity and $2e^-$ pathway selectivity, providing essential conditions for the heterogeneous electro-Fenton (EF) reaction. The electro-Fenton performances of synthesised cathodes were investigated using acetaminophen (ACT), a common analgesic agent, as the model pollutant under an initial pH of 7. Electrochemical degradation of ACT was performed within an undivided electrochemical cell, in which the fabricated carbon aerogels, platinum sheet, and 0.05 M Na_2SO_4 solution functioned as cathode, anode, and electrolyte, respectively. Samples for analysis were collected and filtered at pre-determined intervals, and then the concentration of ACT was monitored using high-performance liquid chromatography

(HPLC) to evaluate the degradation efficiency using different cathodes. Data for EF and electro-sorption (ES) degradation of ACT with the alloy and monometallic catalysts are presented in Fig. 3.6 (a), along with that for the commercial graphite sheet cathode. The degradation of ACT in electro-Fenton systems followed Pseudo-first-order kinetics, as evidenced by the high linear correlation coefficients (R^2 values are 0.998, 0.997, 0.973, and 0.992 for FeNi-CA, Fe-CA, Ni-CA, and graphite electrode, respectively) (see Fig. S3.8 (a)). The degradation of ACT using a graphite sheet as the cathode reached 43 % after 2 h (Fig. 3.6 (a)) with an apparent rate constant (k_{obs}) of 0.005 min^{-1} (see Fig. S3.8 (b)). In comparison, the ACT degradation improved with the Fe-CA and Ni-CA electrodes (both to ~45–50 %), with corresponding increases in the k_{obs}, reaching 0.009 and 0.006 min^{-1}, respectively.

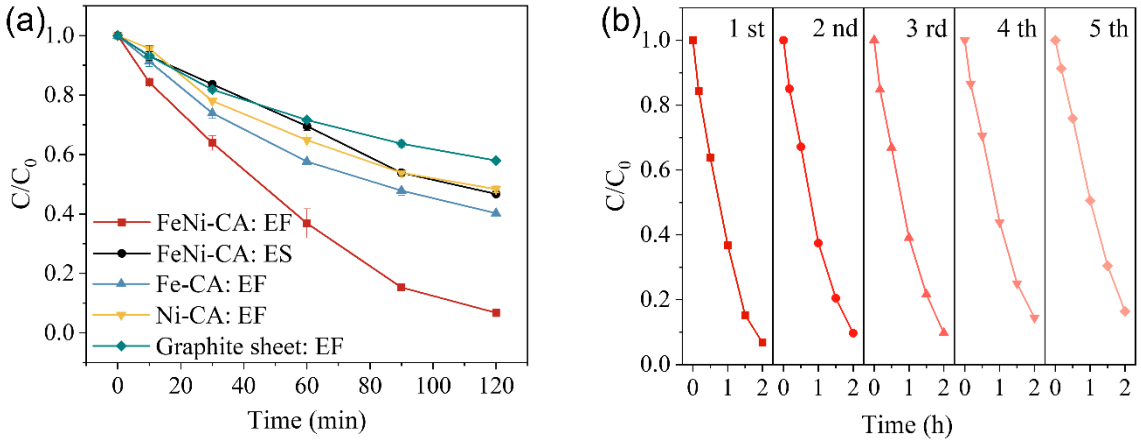

Figure 3.6. (a) ACT degradation in electro-Fenton (EF) and electro-sorption (ES) system, (b) Recycle use performance of FeNi-CA cathode in EF system. Conditions: ACT-10 mg/L, Na_2SO_4-50 mM, pH_0-7.0, 0.4 L/min compressed air and 20 mA for EF system, 0.2 L/min N_2 and 1 mA for ES system.

The electro-sorption performance was assessed at an operational current of 1 mA and 0.2 L/min N_2 atmosphere. The results showed the FeNi-CA, featuring a porous structure and high surface area, achieved 53 % electrochemical sorption capacity for ACT. In comparison to the monometallic cathodes, ACT degradation with FeNi-CA in the EF system significantly increased to 93 % within 120 min. The rate constant improved from 0.006 min^{-1} to 0.021 min^{-1} indicating enhanced reactivity of catalytic oxidative degradation. Furthermore, the electrical energy consumptions (EC) for FeNi-CA, Fe-CA, and Ni-CA based EF processes were evaluated according to Eq. 3.6, the calculation results are shown in Table 3.2. The average business electricity unit rate for the UK is 27p/kWh in 2024 [82]. The calculation results indicate that FeNi-CA based EF system has the

highest electrocatalytic performance in ACT degradation with the lowest energy consumption compared to Fe-CA and Ni-CA. Moreover, a positive synergistic effect (SE) value according to Eq. 3.7 indicates that the sole metals Fe and Ni have a beneficial synergistic effect on improving the electrocatalytic activity. To optimise the ratio of Fe and Ni components, the electrochemical performances of FeNi-CA cathodes with different metal content ($Fe_{0.5}Ni_{0.5}$-CA, $Fe_{0.7}Ni_{0.3}$-CA, and $Fe_{0.3}Ni_{0.7}$-CA) were also compared in Fig. S3.9. The results show that $Fe_{0.5}Ni_{0.5}$-CA with Fe: Ni molar ratio of 1:1 exhibited the highest efficiency on ACT degradation. In the subsequent discussion, FeNi-CA refer to $Fe_{0.5}Ni_{0.5}$-CA to simplify the description.

Table 3.2. Energy consumption and electricity cost for three EF systems (FeNi-CA refer to $Fe_{0.5}Ni_{0.5}$-CA with a metal ratio of 1:1.). Operational conditions: ACT-10 mg/L, Na_2SO_4-50 mM, pH_0-7.0.

EF system	I (A)	V (V)	t (h)	Δm_{ACT} (g)	EC_{ACT} (kWh/kg_{ACT})	Electricity cost (£/kg_{ACT})
FeNi-CA	0.02	2.455	2	1.2375×10^{-3}	79.35	21.42
Fe-CA	0.02	2.62	2	0.825×10^{-3}	127.03	34.30
Ni-CA	0.02	2.515	2	0.705×10^{-3}	142.70	38.53

The reusability of FeNi-CA was further studied under otherwise identical conditions by reusing the washed and dried cathode in subsequent runs. In this case, ACT degradation in the electro-Fenton system with FeNi-CA still reached 84 % over five consecutive runs after 120 min (Fig. 3.6 (b)), demonstrating relatively high stability and reusability of the cathode. It is noted that the degradation continues after the set time period and would still lead to more organic breakdown, with a slightly reduced reaction rate constant (Fig. S3.10 (a)–(b)). The above findings demonstrated that the incorporation of Fe and Ni with molar ratio of 1:1 on the carbon aerogel nanostructure effectively improved the performance of contaminant degradation. Here, the removal of ACT in the FeNi-CA electro-Fenton system was induced by the simultaneous effects of oxidation degradation and electro-sorption.

In general, the degradation of organic contaminants involves both direct and indirect oxidation processes. Indirect oxidation is usually triggered by the production of reactive free radicals [83]. To further investigate the role of free radicals in ACT

degradation with the FeNi-CA cathode, quenching experiments were conducted using tert-butanol (TBA) as an ·OH scavenger and p-benzoquinone (p-BQ) as a $\cdot O_2^-$ scavenger [25,29], as given in Fig. 3.7 (a) (corresponding degradation data and Pseudo-first-order fit are given within the Appendix B, Fig. S3.11). Indeed, the k_{obs} of ACT removal decreased from 0.021 min^{-1} to 0.006 min^{-1} when TBA was added to the system, indicating that ACT was eliminated through catalytic oxidation by ·OH. Additionally, about half the apparent rate constant drop was observed in the presence of p-BQ, indicating the presence of $\cdot O_2^-$. These findings suggest that O_2 undergoes an initial reduction to $\cdot O_2^-$ *via* a 1-electron pathway ($O_2+e^- \rightarrow \cdot O_2^-$) [41], followed by subsequent reduction to H_2O_2 and conversion to ·OH. It was noted that ACT was still partially degraded even after the capture of ·OH, which may be attributed to the effect of electro-sorption processes.

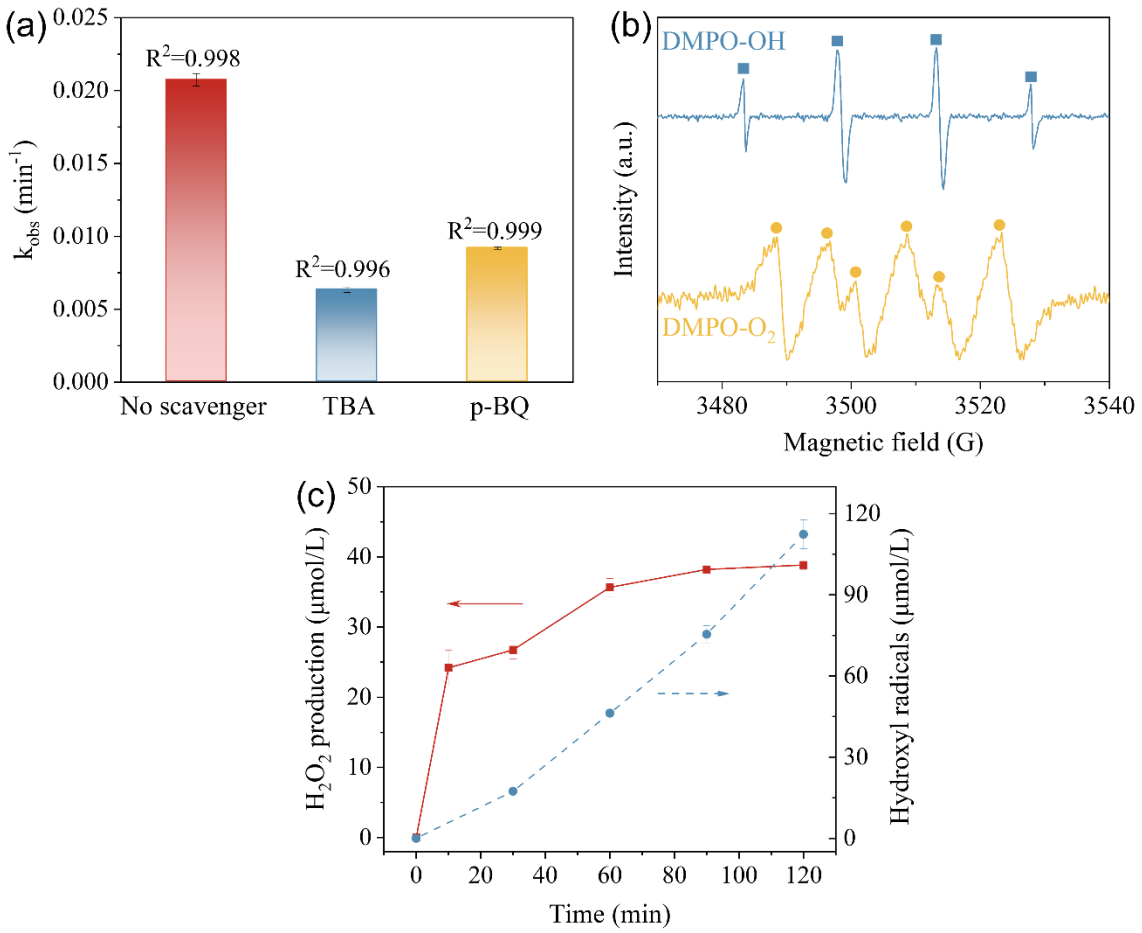

Figure 3.7. (a) The effect of radical scavengers on apparent rate constant in FeNi-CA EF system, (b) ESR spectra in FeNi-CA EF system, and (c) H_2O_2 production (red line) and hydroxyl radical generation (blue line) in FeNi-CA EF system. Conditions: ACT-10 mg/L, Na_2SO_4-50 mM, pH_0-7.0, 20 mA, without aeration, TBA-1 M, p-BQ-2 mM.

The generation of ·OH and $\cdot O_2^-$ species was further verified by electron spin resonance (ESR) spectroscopy using DMPO as the spin-trapping agent, as shown in Fig. 3.7 (b). The four-line characteristic signal with a relative intensity of 1:2:2:1 was detected as the typical spectrum of DMPO-OH spin adducts, confirming the presence of ·OH radical in the FeNi-CA EF process [84]. Additionally, the sextuplet ESR spectrum for DMPO-O_2 spin adducts proved the production of $\cdot O_2^-$ species during the reaction [85]. Overall, these results indicated that the ACT degradation in the FeNi-CA electro-Fenton system was dominated by indirect oxidation mechanisms with ·OH radicals playing a primary role. The concentration of generated ·OH radicals can be quantitatively detected through a process involving the reaction of salicylic acid (SA) with ·OH to produce 2,3-dihydroxybenzoic acid (2,3-DHBA) and 2,5-dihydroxybenzoic acid (2,5-DHBA) [86]. Thus, ·OH concentration was determined by the sum of concentrations of these two products, which can then be measured using HPLC technique. The results show that 112 μmol/L of ·OH was finally produced after 120 min reaction in the EF system using FeNi-CA as the cathode (dash blue line in Fig. 3.7 (c)).

Interestingly, the level of electro-generated H_2O_2 using FeNi-CA was quantified and found to be relatively low, measuring around 38.8 ± 0.64 μmol/L (solid red line in Fig. 3.7 (c)) after 2 h. The low concentration of H_2O_2 observed with FeNi-CA, despite its high activity and selectivity for the $2e^-$ ORR, is likely due to it undergoing rapid on-site decomposition as an intermediate to produce reactive ·OH [34]. According to other studies [87], the presence of encapsulated alloy nanoparticles in carbon materials allowed for the modulation of the local electronic environment, which in turn activated H_2O_2 through a $1e^-$ pathway, leading to the generation of ·OH. Besides, the presence of Fe_3O_4 on the surface is capable of catalysing the activation of H_2O_2 to ·OH. To explore the mechanism of H_2O_2 reduction to ·OH with FeNi-CA, ACT degradation efficiency and ·OH generation in the system containing 0.1 g/L FeNi-CA powder and 50 ppm externally supplied H_2O_2 were measured. As depicted in Fig. S3.12, 69 % of ACT removal and 89.9 μmol/L of ·OH production were observed after 2 h reaction. Therefore, it could be concluded that FeNi-CA functioned not only as an efficient cathode inducing $2e^-$ ORR but also as a heterogeneous Fenton-like catalyst for the activation of H_2O_2 to produce ·OH radicals.

3.4.3.2 Optimisation of key parameters

Optimising reaction parameters was beneficial in further enhancing degradation performance, as shown in Fig. 3.8. The influence of air flow rate on ACT degradation efficiency was investigated, and found to be insignificant (Fig. 3.8 (a)). The k_{obs} at flow rates of 0, 0.2, 0.4, and 0.6 L/min were found to be 0.015, 0.016, 0.020, and 0.015 min^{-1} (inset), respectively. These findings suggested that ACT could be efficiently removed even in the absence of external aeration, achieving ~84 % removal after 2 h. The dissolved oxygen (DO) concentration under different air flow rates before and after the reaction was also measured using a digital multi-meter kit with a luminescent dissolved oxygen probe, and the results are shown in Fig. 3.8 (b). The DO concentration in the zero-aeration system reached 16.5 mg/L after the reaction, accompanied by a change in pH from 7 to 3. The possibility of pH reduction caused by intermediate products of ACT degradation (such as organic acids) has been experimentally ruled out in Fig. S3.13, which shows that the pH dropped from 7 to about 3 in the absence of any contaminants. Besides, small bubbles were also observed around the anode during the reaction. It can be speculated that in the zero-aeration system, an oxygen evolution reaction (OER) occurred at the platinum anode, resulting in an increase in dissolved oxygen concentration and a decrease in pH (Eq. 3.8) [14,88]. Similar mechanisms of oxygen generation from OER anode without aeration have been also reported in other electrochemical systems [89–92]. The above results indicated that the oxygen generated from the anodic reaction was effectively utilised by the FeNi-CA cathode for the formation of H_2O_2. As discussed earlier, the FeNi-CA cathode had a large surface area and large pore volume, enabling enhanced adsorption, storage, and mass transfer of dissolved O_2 for electro-generation of H_2O_2 [92]. Consequently, the O_2 generated at the anode was sufficient to sustain H_2O_2 production even without external aeration, which is a more cost-effective solution compared to previously reported electrochemical H_2O_2 generation under aeration [40,93].

$$2H_2O \rightarrow 4e^- + 4H^+ + O_2 \quad E^0 = 1.23\ V \qquad (3.8)$$

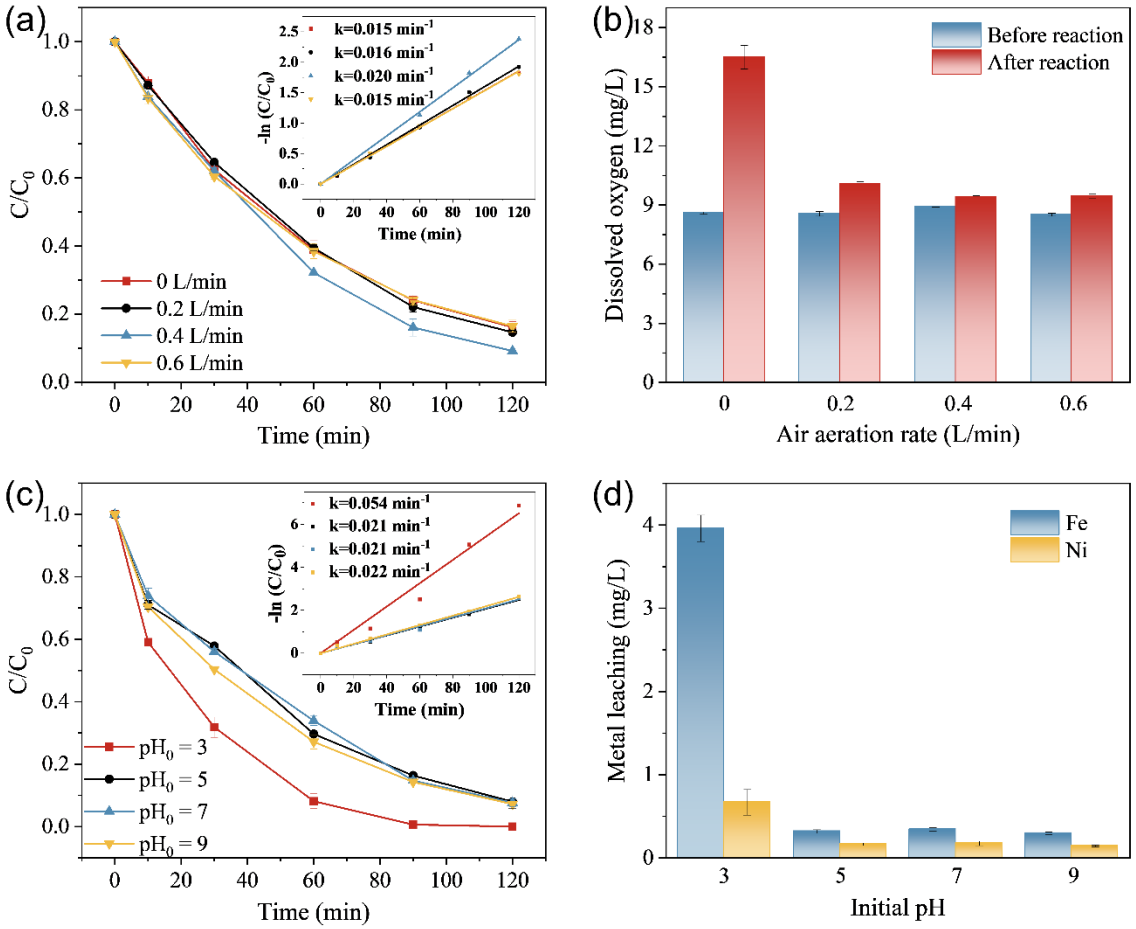

Figure 3.8. (a) The effect of air aeration rate on ACT degradation, (b) Dissolved oxygen concentrations before and after reaction under different air aeration rates, (c) The effect of initial pH on ACT degradation, and (d) Metals leaching after 120 min under different initial pH Conditions: ACT- 10 mg/L, Na_2SO_4-50 mM.

The impact of current on degradation performance was also examined due to its ability to regulate electron transfer. The degradation rate of ACT varied with current, and reaction efficiency increased to an extent with current ranging from 10 mA to 20 mA (Fig. S3.14). The electron transfer rate increased with the current values, which may be advantageous for the generation of H_2O_2 and consequent production of a greater quantity of reactive radicals [94]. However, final ACT degradation at 10 mA was slightly higher than that of 20 mA, and a decrease in ACT removal efficiency was observed at higher current conditions such as 30 mA and 40 mA. In these cases, k_{obs} decreased from 0.02 min^{-1} to 0.013 min^{-1} when the current was increased from 20 mA to 40 mA. This may be attributed to a higher four-electron reduction of oxygen reaction rate (Eq. 3.9) [95], and the occurrence of a side reaction involving hydrogen evolution ($2H^+ + 2e^- \rightarrow H_2$) [96]. These factors are unfavourable for H_2O_2 generation, leading to a decrease in the

efficiency of ACT degradation. The highest degradation efficiency of ACT was achieved at a current of 10 mA (current density of 2.2 mA/cm^2), resulting in ACT removal of 94 % within 120 min at an initial pH of 5.8.

$$O_2+2H_2O+4e^-\rightarrow 4OH^- \quad E^0=1.23\ V\ vs.\ RHE \qquad (3.9)$$

In addition to the aeration rate and current, the effect of initial pH on oxidation performance in the FeNi-CA EF process was also investigated. These results demonstrated that increasing initial pH from 3.0 to 9.0 led to a slight decrease in degradation efficiency from 99.9 % to 92.8 % after 120 min, along with a drop in the rate constant from 0.054 min^{-1} to 0.022 min^{-1} (Fig. 3.8 (c)). Considering pH is known to be a critical factor affecting metal leaching [97], the concentrations of dissolved metal ions under different initial pH conditions were also examined in Fig. 3.8 (d). Although the system at initial pH 3 exhibited the highest oxidation ability, it resulted in a release of Fe ions, as measured post-reaction. It is likely the major source of the leached metals was free metals (as observed in Fig. 3.2) rather than the alloy nanoparticles, because the carbon aerogel can provide a porous matrix that physically encapsulates the FeNi nanoparticles, thus stabilising them and reducing leaching [41,56].

Considering the leaching metals, the contribution of the homogeneous Fenton reaction (Eq. 3.2) in ACT decomposition at an initial pH of 3 was further illustrated in Fig. S3.15. The results show that although the homogeneous Fenton process appeared to have much slower kinetics possibly due to limitations in radical generation, the leached metal ions, acting as homogeneous Fenton catalysts, contributed to over 30 % of the ACT degradation at an initial pH of 3. Furthermore, a desirable degradation rate (over 90 % after 120 min) was still achieved at higher initial pH (5, 7, and 9) with controlled metal leaching levels (Fig. S3.16), thus indicating the potential of the established EF system in practical applications. It should also be noted that, even at an initial pH of 3, metal leaching significantly decreased after pre-treating the FeNi-CA cathode in the EF system in the absence of any contaminant (Fig. S3.17), effectively controlling any secondary pollution caused by released metal ions in the subsequent two runs.

The variation of pH values before and after the reaction was also recorded (Fig. S3.18). This data indicated that under all pre-reaction conditions, the pH decreased to around 3

after the degradation process where OER at the anode led to the generation of H^+ (Eq. 3.8). Conversely, the formation of H_2O_2 through the $2e^-$ reduction (Eq. 3.1) and $1e^-$ reduction pathways for ·OH radicals ($H_2O_2+e^-\rightarrow\cdot OH+OH^-$) required the involvement of H^+. Thus, the anodic oxygen evolution could be regarded as an induction stage that provided oxygen source and favourable acid condition to subsequent oxygen reduction and Fenton-like reactions.

3.4.4 Degradation mechanisms, pathways, and comparison of other EF technologies

The synergistic effect observed in the FeNi-CA system can be attributed to three key interactions and enhancements brought about by the co-presence of Fe and Ni: (1) Structural enhancement. FeNi-CA exhibits a high surface area and prominent mesoporous structure. Such a highly porous characteristic can provide more active catalytic sites, which allows for more effective interactions with the target pollutants and leads to enhanced degradation rates. Besides, mesopores serve as conduits for gas transfer, enabling the delivery of oxygen and enhancing the infiltration of electrolyte into the inner structure of carbon materials. (2) Improved electrocatalytic properties. The formation of the FeNi alloy enhances electron transport within the electrode, while the presence of transition metals catalyses the partial graphitisation of the carbon aerogel, thereby increasing its overall electrical conductivity. Additionally, the incorporation of the FeNi nanoalloy encourages the development of carbon defects. These defects play a crucial role in modifying the electronic structure of the catalyst, which in turn significantly improves its electrocatalytic properties. (3) Increased ORR activity and selectivity. The unique graphitic carbon structure facilitates the formation of oxygen functional groups, which play a beneficial role in enhancing the ORR electrocatalytic process. Additionally, the alloying of Fe and Ni leads to lattice mismatches and electronic modifications, which further improve the activity and selectivity of the ORR.

The degradation mechanism of ACT in the electro-Fenton oxidation system with FeNi-CA may be summarised as follows (Fig. 3.9): an initial current-induced oxygen evolution reaction occurs at the platinum anode, resulting in increased concentrations of dissolved oxygen and H^+ ions in the electrolyte. The generated oxygen diffuses into the cathode/electrolyte interface where it is utilised in the electro-generation of H_2O_2. The unique microstructure of the FeNi-CA cathode enables high oxygen transportation and

utilisation efficiency, thus eliminating the need for external aeration. Additionally, the OER generates H^+ ions to create a favourable pH for the two-electron ORR and subsequent activation of H_2O_2. The diffused oxygen then undergoes an initial $1e^-$ reduction pathway, forming intermediate $\cdot O_2^-$ that is then further reduced to produce H_2O_2. Subsequently, H_2O_2 undergoes conversion to ·OH radicals through a heterogeneous Fenton reaction (Eq. 3.10) [87] catalysed by multi-valence iron on surface Fe_3O_4, and a homogeneous Fenton reaction (Eq. 3.2) mainly catalysed by iron dissolution especially under acidic conditions. Finally, the target compound ACT is efficiently removed through a combination of electro-sorption processes and oxidative reactions dominated by the highly reactive ·OH radicals.

$$\equiv Fe(II)+H_2O_2+H^+ \rightarrow \equiv Fe(III)+\cdot OH+H_2O \qquad (3.10)$$

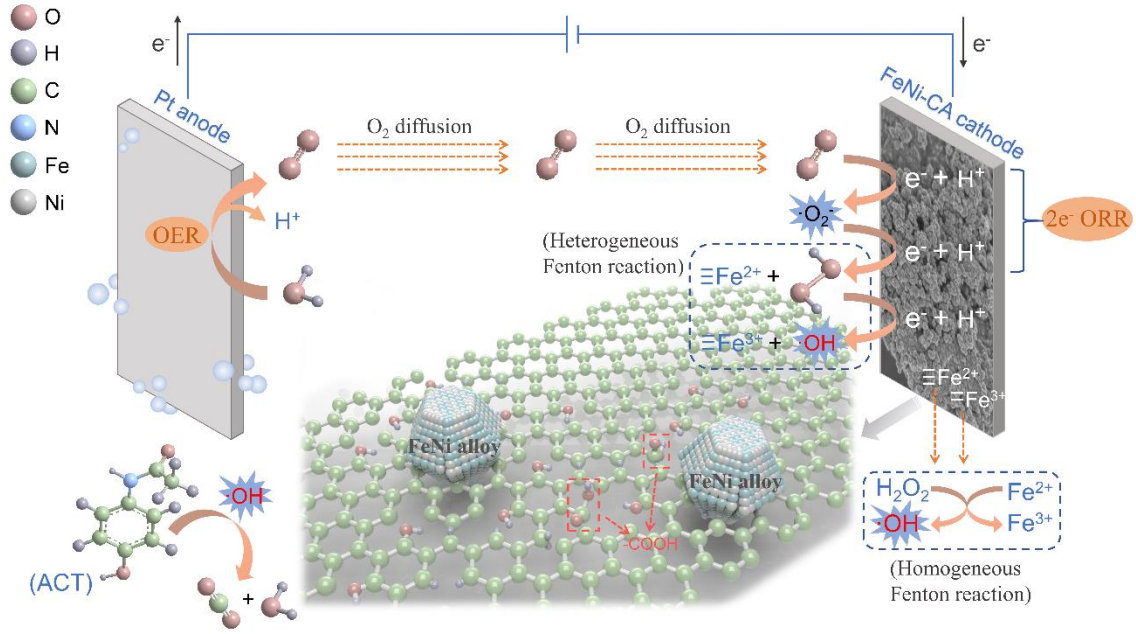

Figure 3.9. Mechanisms of radical generation and ACT degradation in FeNi-CA EF system.

The proposed system exhibited three distinctive characteristics: (1) The OER at the anode created favourable pH conditions for the oxygen reduction reaction and H_2O_2 activation at the cathode. (2) Generated oxygen via OER and the high oxygen utilisation activity of FeNi-CA eliminated the need for external aeration. (3) The synergistic effect of Fe and Ni components endowed the FeNi-CA cathode with unique structural characteristics including alloy nanoparticles, carbon defects, and abundant oxygen functional groups, thus achieving the dual functionality of $2e^-$ ORR and H_2O_2 activation.

The main degradation intermediates of ACT in the FeNi-CA electro-Fenton system were identified using LCMS (Fig. S3.19) and listed in Table S3.1. Based on the detected intermediates, and referring to ACT degradation processes reported in other studies, a possible oxidation pathway of ACT by ·OH radicals has been proposed (Fig. 3.10). ACT oxidation begins with ·OH attack on the acetyl-amino group and simultaneous hydroxylation (Route I), leading to the formation of N-(3,4-dihydroxyphenyl) formamide (P1) [98]. The detected N-(3,4-dihydroxyphenyl) acetamide (P2) and N-(2,4-dihydroxyphenyl) (P3) indicate the occurrence of hydroxylation reactions at the o- and m- positions of ACT (Route II) [99–101]. Further oxidation leads to the formation of aromatic intermediates 4-(methylamino) phenol (P4) and benzoic acid (P6), and a ring-opened product (P5) with concomitant generation of acetamide (P7) [102,103]. Subsequently, all aromatic by-products undergo further degradation, resulting in the production of aliphatic organic acids such as succinic acid (P8), 3-hydroxypropanoic acid (P10), and oxalic acid (P11) [101,104]. At the same time, ethanamine (P12) is produced by further attack of the alkyl chain of acetamide (P7) and butan-1-amine (P9) by hydroxyl radicals. At the end of the degradation process, all final by-products undergo a complete transformation to CO_2, H_2O, and inorganic ions [105].

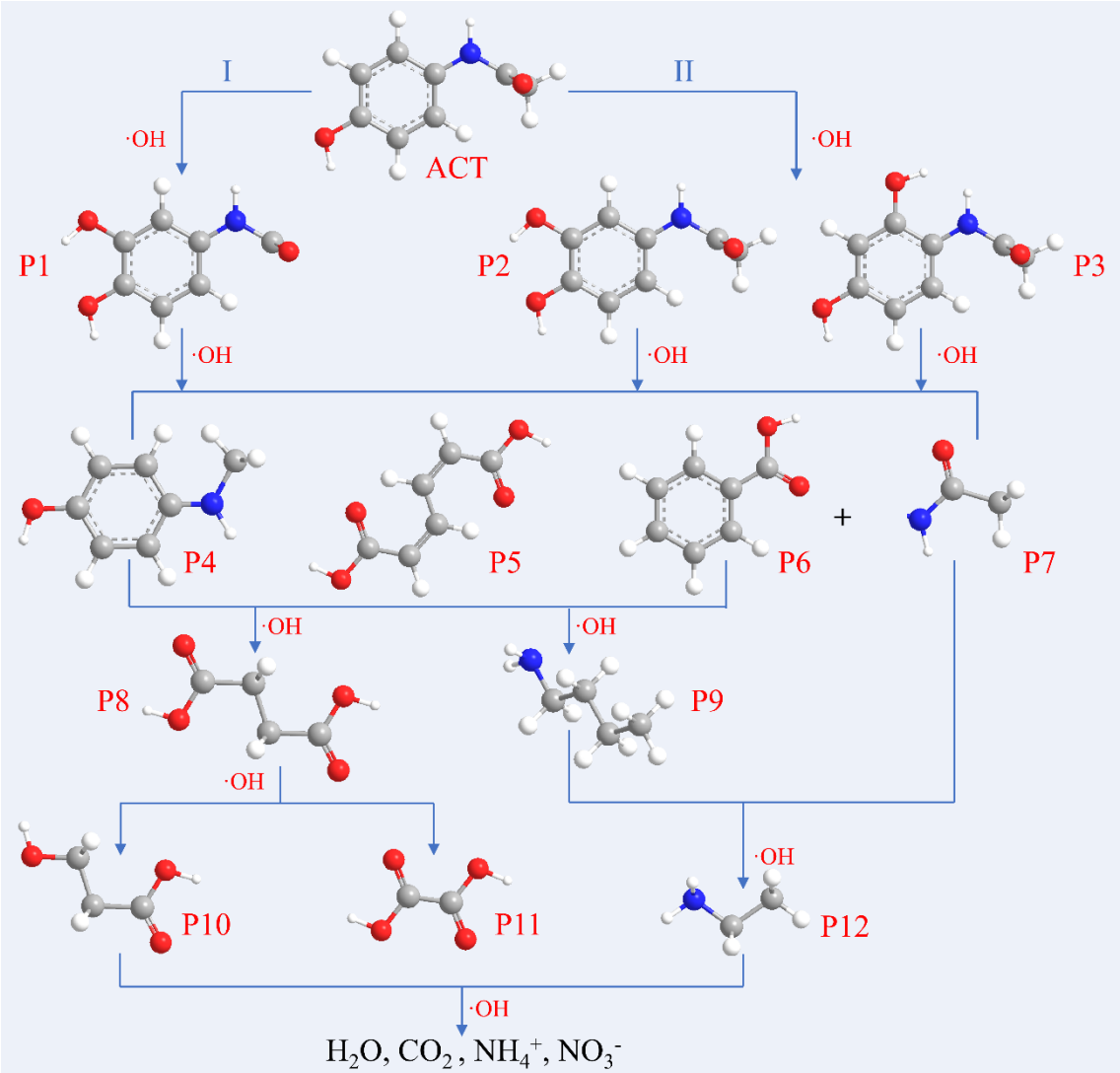

Figure 3.10. Proposed degradation pathways of ACT (grey-C atom, red-O atom, white-H atom, blue- N atom).

The removal efficiency of ACT in the proposed FeNi-CA electro-Fenton system was also compared to other reported EF and EF-based technologies, as summarised in Table 3.3. Although some of the EF-based processes listed demonstrate higher rate constants than those achieved in this study, they require additional chemical inputs such as iron catalysts and hydrogen peroxide, external air/oxygen aeration, or supplementary energy sources like solar light. This results in higher chemical and energy costs compared to our proposed FeNi-CA system, which eliminates the necessity for extra Fenton reagents or aeration. Furthermore, high current densities, such as 50 mA/cm^2, lead to increased energy consumption, raising concerns for future industrial-scale applications. The developed FeNi-CA EF system offers significant advantages in terms of reaction rate, cost-effectiveness, and environmental compatibility, positioning it as a promising advanced

oxidation process technology for wastewater treatment.

Table 3.3. Comparison with other EF and EF-based technologies for ACT removal.

Study	Electrochemical method	Experimental conditions	Current density (mA/cm^2)	C_{ACT} (mg/L)	ACT removal	k_{obs} (min^{-1})
This work	Electro-Fenton	0.05 M Na_2SO_4 at pH 3	4.44	10	99.4% within 90 min	0.054
[101]	Dynamic cross-flow electro-Fenton process coupled to anodic oxidation	[Fe^{2+}] = 0.2 mM, with 0.05 M Na_2SO_4 at pH 3 (Cathode: graphite membrane, anode: Ti/Ti_4O_7 rod)	4.42	15.1	/	0.011
[104]	Electro-Fenton	0.05 M Na_2SO_4 at pH 3, aeration rate=1 L/min (Cathode: carbon-felt, anode: Ti_4O_7 ceramic)	2.5	30.2	95% within 60 min	/
[106]	HNPs/electro-Fenton	0.01 M Na_2SO_4 at pH 5, hematite nanoparticles (HNPs) = 0.15 g/L (Cathode: carbon felt, anode: platinum sheet)	5.11	20	/	0.030
[107]	CuCoFe-LDH /electro-Fenton	0.05 M Na_2SO_4 at pH 5, CuCoFe-LDH = 0.5 g/L, 0.4 L/min air (Cathode: graphite felt, anode: dimensionally stable anode (DSA) with IrO_2 and RuO_2 coating)	10	20		0.0593
[108]	Goethite/electro-Fenton	At pH 3, goethite = 0.5 g/L (Cathode: carbon-polytetrafluoroethylene, anode: Pt)	12	100		0.0029
[109]	Electro-Fenton	122.5 µL/L H_2O_2 and 100 mg/L KCl at pH 2.75 (Cathode and anode: iron plate)	8	5.75		0.6718
[102]	Electro-Fenton	0.087 mM Fe^{2+} and 16.3 mM H_2O_2 at pH 3 (Cathode: stainless steel, anode: titanium coated RuO_2/IrO_2-coated DSA)	3.8	755	98% within 120 min	/

[105]	Electro-Fenton	0.2 mM Fe^{2+} and 0.05 M Na_2SO_4 at pH 3, oxygen aeration. (Cathode: carbon felt, counter electrode: platinum cylindrical mesh)	8.3	151	100% within 240 min	/
[110]	Solar photo electro-Fenton	0.4 mM Fe^{2+}, 0.05 M Na_2SO_4 at pH 3, (Cathode: air-diffusion electrode, anode: Pt sheet)	50	157		0.062

3.5 Conclusions

This study constructed a hetero-EF system composed of OER and ORR processes using a novel FeNi alloy carbon aerogel as a bifunctional cathode for ACT removal. The FeNi-CA exhibited a typical carbon aerogel structure with a large surface area, nano alloy particles ($FeNi_3$), carbon defects, and oxygen-functional groups, resulting in enhanced $2e^-$ ORR reactivity and selectivity. Incorporating Fe and Ni components on FeNi-CA endowed it with a fast electron transfer rate, high oxygen utilisation efficiency, and superior electrocatalytic properties. In this EF system, FeNi-CA exhibited dual functionality as an efficient cathode enabling $2e^-$ ORR and as a Fenton-like catalyst for H_2O_2 activation into ·OH radicals through proposed heterogeneous and homogeneous pathways. FeNi-CA can achieve efficient removal of ACT across a broad pH range of 3–9 while maintaining good catalytic activity after 5 consecutive cycles. Importantly, this was achieved without the requirement for external aeration, making the process significantly more industrially applicable. Optimisation of reaction parameters enabled up to 99.9 % removal of ACT through electro-Fenton oxidation and electro-sorption process after 120 min. Furthermore, ACT degradation intermediates were identified and a reasonable degradation pathway has been proposed. This research has provided valuable insights for the advancement of innovative bifunctional cathodes for electro-Fenton systems with a target of sustainable wastewater treatment. We believe this system to be highly efficient and cost-effective compared to other reported EF processes and, as such, plan further experiments with other candidate pollutants and integration into a continuous flow system.

3.6 Acknowledgements

Qian Ye receives funding from the China Scholarship Council (CSC, 202106240065)

under the Ministry of Education of P.R. China. The authors express their gratitude to the funding organisations for their support in conducting this research.

The authors extend their appreciation to the individuals at the University of Leeds who have provided technical assistance and training: Dr. Jeanine Williams (HPLC and LCMS), Ms. Karine Alves Thorne (metal loading measurements), and Dr. Ben Douglas (BET). Additionally, we would like to thank Ms. Karen Stevens, Dr. David Elliott, Mr. Morgan McGowan, and Ms. Emma Tidswell for their guidance on the safe setup and operation of the equipment.

3.7 References

[1] L.A. Pérez-Estrada, S. Malato, W. Gernjak, A. Agüera, E.M. Thurman, I. Ferrer, A.R. Fernández-Alba, Photo-fenton degradation of diclofenac: Identification of main intermediates and degradation pathway, Environmental Science and Technology 39 (2005) 8300–8306. https://doi.org/10.1021/es050794n.

[2] N. Villota, J.I. Lombraña, A. Cruz-Alcalde, M. Marcé, S. Esplugas, Kinetic study of colored species formation during paracetamol removal from water in a semicontinuous ozonation contactor, Science of The Total Environment 649 (2019) 1434–1442. https://doi.org/10.1016/j.scitotenv.2018.08.417.

[3] W.-C. Yun, K.-Y.A. Lin, W.-C. Tong, Y.-F. Lin, Y. Du, Enhanced degradation of paracetamol in water using sulfate radical-based advanced oxidation processes catalyzed by 3-dimensional Co3O4 nanoflower, Chemical Engineering Journal 373 (2019) 1329–1337. https://doi.org/10.1016/j.cej.2019.05.142.

[4] E.S. Fisher, S.C. Curry, Chapter Ten - Evaluation and treatment of acetaminophen toxicity, in: A. Ramachandran, H. Jaeschke (Eds.), Advances in Pharmacology, Academic Press, 2019: pp. 263–272. https://doi.org/10.1016/bs.apha.2018.12.004.

[5] M. Pacheco-Álvarez, R. Picos Benítez, O.M. Rodríguez-Narváez, E. Brillas, J.M. Peralta-Hernández, A critical review on paracetamol removal from different aqueous matrices by Fenton and Fenton-based processes, and their combined methods, Chemosphere 303 (2022) 134883. https://doi.org/10.1016/j.chemosphere.2022.134883.

[6] B.C. Hodges, E.L. Cates, J.-H. Kim, Challenges and prospects of advanced oxidation water treatment processes using catalytic nanomaterials, Nature Nanotech 13 (2018) 642–650. https://doi.org/10.1038/s41565-018-0216-x.

[7] C.B. Molina, E. Sanz-Santos, A. Boukhemkhem, J. Bedia, C. Belver, J.J. Rodriguez, Removal of emerging pollutants in aqueous phase by heterogeneous Fenton and photo-Fenton with Fe2O3-TiO2-clay heterostructures, Environ Sci Pollut Res 27 (2020) 38434–38445. https://doi.org/10.1007/s11356-020-09236-8.

[8] W.H. Glaze, J.-W. Kang, D.H. Chapin, The Chemistry of Water Treatment Processes Involving Ozone, Hydrogen Peroxide and Ultraviolet Radiation, Taylor & Francis (1987). https://doi.org/10.1080/01919518708552148.

[9] I.A. Katsoyiannis, S. Canonica, U. von Gunten, Efficiency and energy requirements for the transformation of organic micropollutants by ozone, O3/H2O2 and UV/H2O2, Water Research 45 (2011) 3811–3822. https://doi.org/10.1016/j.watres.2011.04.038.

[10] J.M. Campos-Martin, G. Blanco-Brieva, J.L.G. Fierro, Hydrogen Peroxide Synthesis: An Outlook beyond the Anthraquinone Process, Angewandte Chemie International Edition 45 (2006) 6962–6984. https://doi.org/10.1002/anie.200503779.

[11] J. Xu, X. Zheng, Z. Feng, Z. Lu, Z. Zhang, W. Huang, Y. Li, D. Vuckovic, Y. Li, S. Dai, G. Chen, K. Wang, H. Wang, J.K. Chen, W. Mitch, Y. Cui, Organic wastewater treatment by a single-atom catalyst and electrolytically produced H2O2, Nat Sustain 4 (2021) 233–241. https://doi.org/10.1038/s41893-020-00635-w.

[12] D. Guo, Y. Liu, H. Ji, C.-C. Wang, B. Chen, C. Shen, F. Li, Y. Wang, P. Lu, W. Liu, Silicate-enhanced heterogeneous flow-through electro-Fenton system using iron oxides under nanoconfinement, Environ. Sci. Technol. 55 (2021) 4045–4053. https://doi.org/10.1021/acs.est.1c00349.

[13] H. Qi, X. Sun, Z. Sun, Porous graphite felt electrode with catalytic defects for enhanced degradation of pollutants by electro-Fenton process, Chemical Engineering Journal 403 (2021) 126270. https://doi.org/10.1016/j.cej.2020.126270.

[14] G. Lama, J. Meijide, A. Sanromán, M. Pazos, Heterogeneous advanced oxidation processes: Current approaches for wastewater treatment, Catalysts 12 (2022) 344. https://doi.org/10.3390/catal12030344.
[15] M. Dolatabadi, T. Świergosz, S. Ahmadzadeh, Electro-Fenton approach in oxidative degradation of dimethyl phthalate - The treatment of aqueous leachate from landfills, Science of The Total Environment 772 (2021) 145323. https://doi.org/10.1016/j.scitotenv.2021.145323.
[16] D. Li, T. Zheng, Y. Liu, D. Hou, K.K. Yao, W. Zhang, H. Song, H. He, W. Shi, L. Wang, J. Ma, A novel Electro-Fenton process characterized by aeration from inside a graphite felt electrode with enhanced electrogeneration of H2O2 and cycle of Fe3+/Fe2+, Journal of Hazardous Materials 396 (2020) 122591. https://doi.org/10.1016/j.jhazmat.2020.122591.
[17] D. Li, T. Zheng, Y. Liu, D. Hou, H. He, H. Song, J. Zhang, S. Tian, W. Zhang, L. Wang, J. Ma, A cost-effective Electro-Fenton process with graphite felt electrode aeration for degradation of dimethyl phthalate: Enhanced generation of H2O2 and iron recycling that simultaneously regenerates the electrode, Chemical Engineering Journal 394 (2020) 125033. https://doi.org/10.1016/j.cej.2020.125033.
[18] R.D.C. Soltani, A. Rezaee, A.R. Khataee, H. Godini, Electrochemical generation of hydrogen peroxide using carbon black-, carbon nanotube-, and carbon black/carbon nanotube-coated gas-diffusion cathodes: effect of operational parameters and decolorization study, Res Chem Intermed 39 (2013) 4277–4286. https://doi.org/10.1007/s11164-012-0944-8.
[19] P.J.M. Cordeiro-Junior, R. Gonçalves, T.T. Guaraldo, R. da Silva Paiva, E.C. Pereira, M.R. de V. Lanza, Oxygen reduction reaction: Semi-empirical quantum mechanical and electrochemical study of Printex L6 carbon black, Carbon 156 (2020) 1–9. https://doi.org/10.1016/j.carbon.2019.09.036.
[20] M. S. Kronka, F. L. Silva, A. S. Martins, M. O. Almeida, K. M. Honório, M.R. V. Lanza, Tailoring the ORR selectivity for H2O2 electrogeneration by modification of Printex L6 carbon with 1,4-naphthoquinone: a theoretical, experimental and environmental application study, Materials Advances 1 (2020) 1318–1329. https://doi.org/10.1039/D0MA00290A.
[21] G. Gan, X. Li, S. Fan, L. Wang, M. Qin, Z. Yin, G. Chen, Carbon aerogels for environmental clean-up, European Journal of Inorganic Chemistry 2019 (2019) 3126–3141. https://doi.org/10.1002/ejic.201801512.
[22] H. Li, X. Shu, P. Tong, J. Zhang, P. An, Z. Lv, H. Tian, J. Zhang, H. Xia, Fe–Ni alloy nanoclusters anchored on carbon aerogels as high-efficiency oxygen electrocatalysts in rechargeable Zn–air batteries, Small 17 (2021) 2102002. https://doi.org/10.1002/smll.202102002.
[23] J.-M. Liu, Z.-Y. Ji, Y.-B. Shi, P. Yuan, X.-F. Guo, L.-M. Zhao, S.-M. Li, H. Li, J.-S. Yuan, Effective treatment of levofloxacin wastewater by an electro-Fenton process with hydrothermal-activated graphite felt as cathode, Environmental Pollution 266 (2020) 115348. https://doi.org/10.1016/j.envpol.2020.115348.
[24] H. Nsubuga, C. Basheer, M. Baseer Haider, An enhanced beta-blockers degradation method using copper-boron-ferrite supported graphite electrodes and continuous droplet flow-assisted electro-Fenton reactor, Separation and Purification Technology 221 (2019) 408–420. https://doi.org/10.1016/j.seppur.2019.03.095.
[25] H. Qi, X. Sun, Z. Sun, Cu-doped Fe2O3 nanoparticles/etched graphite felt as bifunctional cathode for efficient degradation of sulfamethoxazole in the heterogeneous electro-Fenton process, Chemical Engineering Journal 427 (2022)

131695. https://doi.org/10.1016/j.cej.2021.131695.
[26] E. Fajardo-Puerto, A. Elmouwahidi, E. Bailón-García, A.F. Pérez-Cadenas, F. Carrasco-Marín, From Fenton and ORR 2e−-type catalysts to bifunctional electrodes for environmental remediation using the electro-Fenton process, Catalysts 13 (2023) 674. https://doi.org/10.3390/catal13040674.
[27] P.J.M. Cordeiro-Junior, M.S. Kronka, L.A. Goulart, N.C. Veríssimo, L.H. Mascaro, M.C. dos Santos, R. Bertazzoli, M.R. de V. Lanza, Catalysis of oxygen reduction reaction for H2O2 electrogeneration: The impact of different conductive carbon matrices and their physicochemical properties, Journal of Catalysis 392 (2020) 56–68. https://doi.org/10.1016/j.jcat.2020.09.020.
[28] H. Xu, H. Guo, C. Chai, N. Li, X. Lin, W. Xu, Anodized graphite felt as an efficient cathode for in-situ hydrogen peroxide production and Electro-Fenton degradation of rhodamine B, Chemosphere 286 (2022) 131936. https://doi.org/10.1016/j.chemosphere.2021.131936.
[29] W. Yang, M. Zhou, N. Oturan, M. Bechelany, M. Cretin, M.A. Oturan, Highly efficient and stable FeIIFeIII LDH carbon felt cathode for removal of pharmaceutical ofloxacin at neutral pH, Journal of Hazardous Materials 393 (2020) 122513. https://doi.org/10.1016/j.jhazmat.2020.122513.
[30] N. Barhoumi, N. Oturan, H. Olvera-Vargas, E. Brillas, A. Gadri, S. Ammar, M.A. Oturan, Pyrite as a sustainable catalyst in electro-Fenton process for improving oxidation of sulfamethazine. Kinetics, mechanism and toxicity assessment, Water Research 94 (2016) 52–61. https://doi.org/10.1016/j.watres.2016.02.042.
[31] L. Labiadh, M.A. Oturan, M. Panizza, N.B. Hamadi, S. Ammar, Complete removal of AHPS synthetic dye from water using new electro-Fenton oxidation catalyzed by natural pyrite as heterogeneous catalyst, Journal of Hazardous Materials 297 (2015) 34–41. https://doi.org/10.1016/j.jhazmat.2015.04.062.
[32] Y. Zhang, M. Gao, S.-G. Wang, W. Zhou, Y. Sang, X.-H. Wang, Integrated electro-Fenton process enabled by a rotating Fe3O4/gas diffusion cathode for simultaneous generation and activation of H2O2, Electrochimica Acta 231 (2017) 694–704. https://doi.org/10.1016/j.electacta.2017.02.091.
[33] L. Cui, H. Huang, P. Ding, S. Zhu, W. Jing, X. Gu, Cogeneration of H2O2 and OH via a novel Fe3O4/MWCNTs composite cathode in a dual-compartment electro-Fenton membrane reactor, Separation and Purification Technology 237 (2020) 116380. https://doi.org/10.1016/j.seppur.2019.116380.
[34] X. Shen, F. Xiao, H. Zhao, Y. Chen, C. Fang, R. Xiao, W. Chu, G. Zhao, In situ-formed PdFe nanoalloy and carbon defects in cathode for synergic reduction–oxidation of chlorinated pollutants in electro-Fenton process, Environ. Sci. Technol. 54 (2020) 4564–4572. https://doi.org/10.1021/acs.est.9b05896.
[35] M. Ghasemi, A. Khataee, P. Gholami, R.D.C. Soltani, A. Hassani, Y. Orooji, In-situ electro-generation and activation of hydrogen peroxide using a CuFeNLDH-CNTs modified graphite cathode for degradation of cefazolin, Journal of Environmental Management 267 (2020) 110629. https://doi.org/10.1016/j.jenvman.2020.110629.
[36] Q. Liu, S. Cao, Y. Qiu, Effect of carbonization temperature on bimetallic FeCo-N/C nanofiber electrocatalysts for oxygen reduction reaction in sulfuric acid solution, International Journal of Hydrogen Energy 42 (2017) 29274–29282. https://doi.org/10.1016/j.ijhydene.2017.10.069.
[37] S. Sajjadi, A. Hasanzadeh, A. Khataee, Two-electron oxygen reduction on NiFe alloy enclosed carbonic nanolayers derived from NiFe-metal-organic frameworks, Journal of Electroanalytical Chemistry 840 (2019) 449–455.

https://doi.org/10.1016/j.jelechem.2019.04.025.
[38] M. Zarei, D. Salari, A. Niaei, A. Khataee, Peroxi-coagulation degradation of C.I. Basic Yellow 2 based on carbon-PTFE and carbon nanotube-PTFE electrodes as cathode, Electrochimica Acta 54 (2009) 6651–6660. https://doi.org/10.1016/j.electacta.2009.06.060.
[39] L. Zhou, Z. Hu, C. Zhang, Z. Bi, T. Jin, M. Zhou, Electrogeneration of hydrogen peroxide for electro-Fenton system by oxygen reduction using chemically modified graphite felt cathode, Separation and Purification Technology 111 (2013) 131–136. https://doi.org/10.1016/j.seppur.2013.03.038.
[40] F. Yu, M. Zhou, L. Zhou, R. Peng, A novel electro-Fenton process with H2O2 generation in a rotating disk reactor for organic pollutant degradation, Environ. Sci. Technol. Lett. 1 (2014) 320–324. https://doi.org/10.1021/ez500178p.
[41] F. Xiao, Z. Wang, J. Fan, T. Majima, H. Zhao, G. Zhao, Selective electrocatalytic reduction of oxygen to hydroxyl radicals via 3-electron pathway with FeCo alloy encapsulated carbon aerogel for fast and complete removing pollutants, Angewandte Chemie International Edition 60 (2021) 10375–10383. https://doi.org/10.1002/anie.202101804.
[42] Q. Abbas, M. Mirzaeian, M.A. Abdelkareem, A. Al Makky, A. Yadav, A.G. Olabi, Structural tuneability and electrochemical energy storage applications of resorcinol-formaldehyde-based carbon aerogels, International Journal of Energy Research 46 (2022) 5478–5502. https://doi.org/10.1002/er.7556.
[43] R. Bardestani, G.S. Patience, S. Kaliaguine, Experimental methods in chemical engineering: specific surface area and pore size distribution measurements—BET, BJH, and DFT, The Canadian Journal of Chemical Engineering 97 (2019) 2781–2791. https://doi.org/10.1002/cjce.23632.
[44] C. Tanggarnjanavalukul, N. Phattharasupakun, J. Wutthiprom, P. Kidkhunthod, M. Sawangphruk, Charge storage mechanisms of birnessite-type MnO2 nanosheets in Na2SO4 electrolytes with different pH values: In situ electrochemical X-ray absorption spectroscopy investigation, Electrochimica Acta 273 (2018) 17–25. https://doi.org/10.1016/j.electacta.2018.04.022.
[45] X. Shen, F. Xiao, H. Zhao, Y. Chen, C. Fang, R. Xiao, W. Chu, G. Zhao, In situ-formed PdFe nanoalloy and carbon defects in cathode for synergic reduction–oxidation of chlorinated pollutants in electro-Fenton process, Environ. Sci. Technol. 54 (2020) 4564–4572. https://doi.org/10.1021/acs.est.9b05896.
[46] Y. Zhao, F. Wang, P. Wei, G. Yu, S. Cui, J. Liu, Cobalt and iron oxides co-supported on carbon nanotubes as an efficient bifunctional catalyst for enhanced electrocatalytic activity in oxygen reduction and oxygen evolution reactions, ChemistrySelect 3 (2018) 207–213. https://doi.org/10.1002/slct.201702231.
[47] Y. Zhu, F. Deng, S. Qiu, F. Ma, Y. Zheng, L. Gao, A self-sufficient electro-Fenton system with enhanced oxygen transfer for decontamination of pharmaceutical wastewater, Chemical Engineering Journal 429 (2022) 132176. https://doi.org/10.1016/j.cej.2021.132176.
[48] E. Rosales, S. Diaz, M. Pazos, M.A. Sanromán, Comprehensive strategy for the degradation of anti-inflammatory drug diclofenac by different advanced oxidation processes, Separation and Purification Technology 208 (2019) 130–141. https://doi.org/10.1016/j.seppur.2018.04.014.
[49] Z. Hajalifard, M. Mousazadeh, S. Khademi, N. Khademi, M.H. Jamadi, M. Sillanpää, The efficacious of AOP-based processes in concert with electrocoagulation in abatement of CECs from water/wastewater, Npj Clean Water 6 (2023) 1–25.

https://doi.org/10.1038/s41545-023-00239-9.
[50] G. Daniel, Y. Zhang, S. Lanzalaco, F. Brombin, T. Kosmala, G. Granozzi, A. Wang, E. Brillas, I. Sirés, C. Durante, Chitosan-derived nitrogen-doped carbon electrocatalyst for a sustainable upgrade of oxygen reduction to hydrogen peroxide in UV-assisted electro-Fenton water treatment, ACS Sustainable Chem. Eng. 8 (2020) 14425–14440. https://doi.org/10.1021/acssuschemeng.0c04294.
[51] X. Qin, P. Cao, X. Quan, K. Zhao, S. Chen, H. Yu, Y. Su, Highly efficient hydroxyl radicals production boosted by the atomically dispersed Fe and Co sites for heterogeneous electro-Fenton oxidation, Environ. Sci. Technol. 57 (2023) 2907–2917. https://doi.org/10.1021/acs.est.2c06981.
[52] S. Bai, X. Shen, G. Zhu, Z. Xu, J. Yang, In situ growth of FeNi alloy nanoflowers on reduced graphene oxide nanosheets and their magnetic properties, CrystEngComm 14 (2012) 1432–1438. https://doi.org/10.1039/C1CE05916E.
[53] G. Fu, Z. Cui, Y. Chen, Y. Li, Y. Tang, J.B. Goodenough, Ni3Fe-N doped carbon sheets as a bifunctional electrocatalyst for air cathodes, Advanced Energy Materials 7 (2017) 1601172. https://doi.org/10.1002/aenm.201601172.
[54] J.-W. Zhang, H. Zhang, T.-Z. Ren, Z.-Y. Yuan, T.J. Bandosz, FeNi doped porous carbon as an efficient catalyst for oxygen evolution reaction, Front. Chem. Sci. Eng. 15 (2021) 279–287. https://doi.org/10.1007/s11705-020-1965-2.
[55] J. Hwang, J.-H. Jin, H. Kim, K.Y. Lee, I.-H. Yang, Fabrication of Ni2O3–NiCx core–shell nanoparticles on fluorine-doped tin oxide electrodes via oxygen feeding from SnO2 under hydrogen conditions and their electrochemical performance as supercapacitors, Colloid and Interface Science Communications 44 (2021) 100470. https://doi.org/10.1016/j.colcom.2021.100470.
[56] H. Zhao, L. Qian, Y. Chen, Q. Wang, G. Zhao, Selective catalytic two-electron O2 reduction for onsite efficient oxidation reaction in heterogeneous electro-Fenton process, Chemical Engineering Journal 332 (2018) 486–498. https://doi.org/10.1016/j.cej.2017.09.093.
[57] K. Liu, J.C.-C. Yu, H. Dong, J.C.S. Wu, M.R. Hoffmann, Degradation and mineralization of carbamazepine using an electro-Fenton reaction catalyzed by magnetite nanoparticles fixed on an electrocatalytic carbon fiber textile cathode, Environ. Sci. Technol. 52 (2018) 12667–12674. https://doi.org/10.1021/acs.est.8b03916.
[58] K.S.W. Sing, Reporting physisorption data for gas/solid systems with special reference to the determination of surface area and porosity (Recommendations 1984), Pure and Applied Chemistry 57 (1985) 603–619. https://doi.org/10.1351/pac198557040603.
[59] O. Czakkel, K. Marthi, E. Geissler, K. László, Influence of drying on the morphology of resorcinol–formaldehyde-based carbon gels, Microporous and Mesoporous Materials 86 (2005) 124–133. https://doi.org/10.1016/j.micromeso.2005.07.021.
[60] C. Chen, Y. Zhu, M. Tian, Y. Chen, Y. Yang, K. Jiang, S. Gao, Sustainable self-powered electro-Fenton degradation using N, S co-doped porous carbon catalyst fabricated with adsorption-pyrolysis-doping strategy, Nano Energy 81 (2021) 105623. https://doi.org/10.1016/j.nanoen.2020.105623.
[61] R. Bardestani, G.S. Patience, S. Kaliaguine, Experimental methods in chemical engineering: specific surface area and pore size distribution measurements—BET, BJH, and DFT, The Canadian Journal of Chemical Engineering 97 (2019) 2781–2791. https://doi.org/10.1002/cjce.23632.
[62] H. Zhao, L. Qian, X. Guan, D. Wu, G. Zhao, Continuous bulk FeCuC aerogel with

ultradispersed metal nanoparticles: An efficient 3D heterogeneous Electro-Fenton cathode over a wide range of pH 3–9, Environ. Sci. Technol. 50 (2016) 5225–5233. https://doi.org/10.1021/acs.est.6b00265.

[63] G. Fu, Z. Cui, Y. Chen, L. Xu, Y. Tang, J.B. Goodenough, Hierarchically mesoporous nickel-iron nitride as a cost-efficient and highly durable electrocatalyst for Zn-air battery, Nano Energy 39 (2017) 77–85. https://doi.org/10.1016/j.nanoen.2017.06.029.

[64] A. Abdelwahab, J. Castelo-Quibén, M. Pérez-Cadenas, F.J. Maldonado-Hódar, F. Carrasco-Marín, A.F. Pérez-Cadenas, Insight of the effect of graphitic cluster in the performance of carbon aerogels doped with nickel as electrodes for supercapacitors, Carbon 139 (2018) 888–895. https://doi.org/10.1016/j.carbon.2018.07.034.

[65] F.J. Maldonado-Hódar, C. Moreno-Castilla, J. Rivera-Utrilla, Y. Hanzawa, Y. Yamada, Catalytic graphitization of carbon aerogels by transition metals, Langmuir 16 (2000) 4367–4373. https://doi.org/10.1021/la991080r.

[66] Z. Xu, D. Cai, Z. Hu, L. Gan, A combination of porous and crystalline characters in carbon aerogels by a synergistic graphitization, Microporous and Mesoporous Materials 195 (2014) 36–42. https://doi.org/10.1016/j.micromeso.2014.04.013.

[67] B. Wang, Y. Xia, G. Wang, Y. Zhou, H. Wang, Core shell MoS2/C nanospheres embedded in foam-like carbon sheets composite with an interconnected macroporous structure as stable and high-capacity anodes for sodium ion batteries, Chemical Engineering Journal 309 (2017) 417–425. https://doi.org/10.1016/j.cej.2016.10.073.

[68] J. Ding, Q. Sun, L. Zhong, X. Wang, L. Chai, Q. Li, T.-T. Li, Y. Hu, J. Qian, S. Huang, Thermal conversion of hollow nickel-organic framework into bimetallic FeNi3 alloy embedded in carbon materials as efficient oer electrocatalyst, Electrochimica Acta 354 (2020) 136716. https://doi.org/10.1016/j.electacta.2020.136716.

[69] L. Cui, D. Wu, X. Liu, Y. Li, X. Fan, F. Zhang, G. Zhang, W. Peng, Electro-reduction induced fast metal redox cycle on Co3O4-CuO@CNTs/Copper foam cathode for enhanced Fenton-like reaction, Journal of Colloid and Interface Science 643 (2023) 613–625. https://doi.org/10.1016/j.jcis.2023.03.145.

[70] Y.J. Sa, J.H. Kim, S.H. Joo, Active edge-site-rich carbon nanocatalysts with enhanced electron transfer for efficient electrochemical hydrogen peroxide production, Angewandte Chemie International Edition 58 (2019) 1100–1105. https://doi.org/10.1002/anie.201812435.

[71] A. K. Yousef, Y. Kim, P. Bhanja, P. Mei, M. Pramanik, M.M. S. Sanad, M. M. Rashad, A. Y. El-Sayed, A. Ali Alshehri, Y. Gamaan Alghamdi, K. Ahmed Alzahrani, Y. Ide, J. Lin, Y. Yamauchi, Iron phosphide anchored nanoporous carbon as an efficient electrode for supercapacitors and the oxygen reduction reaction, RSC Advances 9 (2019) 25240–25247. https://doi.org/10.1039/C9RA04326H.

[72] H. Zhao, X. Shen, Y. Chen, S.-N. Zhang, P. Gao, X. Zhen, X.-H. Li, G. Zhao, A COOH-terminated nitrogen-doped carbon aerogel as a bulk electrode for completely selective two-electron oxygen reduction to H2O2, Chem. Commun. 55 (2019) 6173–6176. https://doi.org/10.1039/C9CC02580D.

[73] K.-H. Wu, D. Wang, X. Lu, X. Zhang, Z. Xie, Y. Liu, B.-J. Su, J.-M. Chen, D.-S. Su, W. Qi, S. Guo, Highly selective hydrogen peroxide electrosynthesis on carbon: In situ interface engineering with surfactants, Chem 6 (2020) 1443–1458. https://doi.org/10.1016/j.chempr.2020.04.002.

[74] M. Smith, L. Scudiero, J. Espinal, J.-S. McEwen, M. Garcia-Perez, Improving the deconvolution and interpretation of XPS spectra from chars by ab initio calculations, Carbon 110 (2016) 155–171. https://doi.org/10.1016/j.carbon.2016.09.012.

[75] Y. Meng, T.M. Young, P. Liu, C.I. Contescu, B. Huang, S. Wang, Ultralight carbon

aerogel from nanocellulose as a highly selective oil absorption material, Cellulose 22 (2015) 435–447. https://doi.org/10.1007/s10570-014-0519-5.

[76] H.A. Kuo, A. Ramachandran, D.I. Oyarzun, E.C. Clevenger, J.G. Santiago, M. Stadermann, P.G. Campbell, S.A. Hawks, Understanding resistances in capacitive deionization devices, Environ. Sci.: Water Res. Technol. 6 (2020) 1842–1854. https://doi.org/10.1039/D0EW00169D.

[77] M. Shi, Y. Chen, H. Wen, Y. Liu, One-step heat treatment to process semi-coke powders as an anode material with superior rate performance for Li-ion batteries, RSC Advances 8 (2018) 41207–41217. https://doi.org/10.1039/C8RA07899H.

[78] P. Chen, K. Xu, T. Zhou, Y. Tong, J. Wu, H. Cheng, X. Lu, H. Ding, C. Wu, Y. Xie, Strong-coupled cobalt borate nanosheets/graphene hybrid as electrocatalyst for water oxidation under both alkaline and neutral conditions, Angewandte Chemie International Edition 55 (2016) 2488–2492. https://doi.org/10.1002/anie.201511032.

[79] I. Diouf, O. Dia, M.B. Diedhiou, P. Drogui, A.O. Toure, S.M. Lo, M. Rumeau, C.G. Mar/Diop, Electro-generation of hydrogen peroxide using a graphite cathode from exhausted batteries: study of influential parameters on electro-Fenton process, Environmental Technology 41 (2020) 1434–1445. https://doi.org/10.1080/09593330.2018.1537309.

[80] Y. Fu, H.-Y. Yu, C. Jiang, T.-H. Zhang, R. Zhan, X. Li, J.-F. Li, J.-H. Tian, R. Yang, NiCo alloy nanoparticles decorated on N-doped carbon nanofibers as highly active and durable oxygen electrocatalyst, Advanced Functional Materials 28 (2018) 1705094. https://doi.org/10.1002/adfm.201705094.

[81] Z. Li, X. Xu, X. Lu, C. He, J. Huang, W. Sun, L. Tian, Synergistic coupling of FeNi3 alloy with graphene carbon dots for advanced oxygen evolution reaction electrocatalysis, Journal of Colloid and Interface Science 615 (2022) 273–281. https://doi.org/10.1016/j.jcis.2022.01.088.

[82] Business Electricity Rates UK, Business Electricity Prices (n.d.). https://www.businesselectricityprices.org.uk/ (accessed May 14, 2024).

[83] F.E. Titchou, H. Zazou, H. Afanga, E.G. Jamila, R. Ait Akbour, M. Hamdani, M.A. Oturan, Comparative study of the removal of direct red 23 by anodic oxidation, electro-Fenton, photo-anodic oxidation and photoelectro-Fenton in chloride and sulfate media, Environmental Research 204 (2022) 112353. https://doi.org/10.1016/j.envres.2021.112353.

[84] Q. Ye, H. Xu, Q. Wang, X. Huo, Y. Wang, X. Huang, G. Zhou, J. Lu, J. Zhang, New insights into the mechanisms of tartaric acid enhancing homogeneous and heterogeneous copper-catalyzed Fenton-like systems, Journal of Hazardous Materials 407 (2021) 124351. https://doi.org/10.1016/j.jhazmat.2020.124351.

[85] Q. Ye, H. Xu, J. Zhang, Q. Wang, P. Zhou, Y. Wang, X. Huang, X. Huo, C. Liu, J. Lu, Enhancement of peroxymonosulfate activation for antibiotics removal by nano zero valent tungsten induced Cu(II)/Cu(I) redox cycles, Chemical Engineering Journal 382 (2020) 123054. https://doi.org/10.1016/j.cej.2019.123054.

[86] X. Qin, P. Cao, X. Quan, K. Zhao, S. Chen, H. Yu, Y. Su, Highly efficient hydroxyl radicals production boosted by the atomically dispersed Fe and Co sites for heterogeneous electro-Fenton oxidation, Environ. Sci. Technol. 57 (2023) 2907–2917. https://doi.org/10.1021/acs.est.2c06981.

[87] Y. Yao, Y. Pan, Y. Yu, Z. Yu, L. Lai, F. Liu, L. Wei, Y. Chen, Bifunctional catalysts for heterogeneous electro-Fenton processes: a review, Environ Chem Lett 20 (2022) 3837–3859. https://doi.org/10.1007/s10311-022-01453-6.

[88] J. Xie, C. Zhang, T.D. Waite, Hydroxyl radicals in anodic oxidation systems:

generation, identification and quantification, Water Research 217 (2022) 118425. https://doi.org/10.1016/j.watres.2022.118425.

[89] H. Zhang, X. Wan, G. Li, F. Zhang, A Three-electrode Electro-Fenton System Supplied by Self-generated Oxygen with Automatic pH-regulation for Groundwater Remediation, Electrochimica Acta 250 (2017) 42–48. https://doi.org/10.1016/j.electacta.2017.08.040.

[90] J. Zhang, Y. Liu, J. Li, K. Wang, X. Zhao, X. Liu, Enhanced recovery of phosphorus from hypophosphite-laden wastewater via field-induced electro-Fenton coupled with anodic oxidation, Journal of Hazardous Materials 464 (2024) 132750. https://doi.org/10.1016/j.jhazmat.2023.132750.

[91] S.Y. Yang, H.W. Jeong, B. Kim, D.S. Han, W. Choi, H. Park, Electrocatalytic cogeneration of reactive oxygen species for synergistic water treatment, Chemical Engineering Journal 358 (2019) 497–503. https://doi.org/10.1016/j.cej.2018.09.192.

[92] F. Yu, M. Zhou, X. Yu, Cost-effective electro-Fenton using modified graphite felt that dramatically enhanced on H2O2 electro-generation without external aeration, Electrochimica Acta 163 (2015) 182–189. https://doi.org/10.1016/j.electacta.2015.02.166.

[93] A.R. Khataee, M. Safarpour, M. Zarei, S. Aber, Electrochemical generation of H2O2 using immobilized carbon nanotubes on graphite electrode fed with air: Investigation of operational parameters, Journal of Electroanalytical Chemistry 659 (2011) 63–68. https://doi.org/10.1016/j.jelechem.2011.05.002.

[94] F. Qiu, L. Wang, H. Li, Y. Pan, H. Song, J. Chen, Y. Fan, S. Zhang, Electrochemically enhanced activation of Co3O4/TiO2 nanotube array anode for persulfate toward high catalytic activity, low energy consumption, and long lifespan performance, Journal of Colloid and Interface Science 655 (2024) 594–610. https://doi.org/10.1016/j.jcis.2023.11.045.

[95] S. Cheng, C. Shen, H. Zheng, F. Liu, A. Li, OCNTs encapsulating Fe-Co PBA as efficient chainmail-like electrocatalyst for enhanced heterogeneous electro-Fenton reaction, Applied Catalysis B: Environmental 269 (2020) 118785. https://doi.org/10.1016/j.apcatb.2020.118785.

[96] J. Ekspong, E. Gracia-Espino, T. Wågberg, Hydrogen evolution reaction activity of heterogeneous materials: A theoretical model, J. Phys. Chem. C 124 (2020) 20911–20921. https://doi.org/10.1021/acs.jpcc.0c05243.

[97] J. He, X. Yang, B. Men, D. Wang, Interfacial mechanisms of heterogeneous Fenton reactions catalyzed by iron-based materials: A review, Journal of Environmental Sciences 39 (2016) 97–109. https://doi.org/10.1016/j.jes.2015.12.003.

[98] M. Qutob, M. A. Hussein, K. A. Alamry, M. Rafatullah, A review on the degradation of acetaminophen by advanced oxidation process: pathway, by-products, biotoxicity, and density functional theory calculation, RSC Advances 12 (2022) 18373–18396. https://doi.org/10.1039/D2RA02469A.

[99] S. Chen, P. He, P. Zhou, X. Wang, F. Xiao, Q. He, J. Li, L. Jia, H. Zhang, B. Jia, B. Tang, Development of a novel graphitic carbon nitride and multiwall carbon nanotube co-doped Ti/PbO2 anode for electrocatalytic degradation of acetaminophen, Chemosphere 271 (2021) 129830. https://doi.org/10.1016/j.chemosphere.2021.129830.

[100] Y. Gao, J. Zhou, Y. Rao, H. Ning, J. Zhang, J. Shi, N. Gao, Comparative study of degradation of ketoprofen and paracetamol by ultrasonic irradiation: Mechanism, toxicity and DBP formation, Ultrasonics Sonochemistry 82 (2022) 105906. https://doi.org/10.1016/j.ultsonch.2021.105906.

[101] H. Olvera-Vargas, J.-C. Rouch, C. Coetsier, M. Cretin, C. Causserand, Dynamic cross-flow electro-Fenton process coupled to anodic oxidation for wastewater treatment: Application to the degradation of acetaminophen, Separation and Purification Technology 203 (2018) 143–151. https://doi.org/10.1016/j.seppur.2018.03.063.

[102] M.D.G. de Luna, M.L. Veciana, C.-C. Su, M.-C. Lu, Acetaminophen degradation by electro-Fenton and photoelectro-Fenton using a double cathode electrochemical cell, Journal of Hazardous Materials 217–218 (2012) 200–207. https://doi.org/10.1016/j.jhazmat.2012.03.018.

[103] Y. Ling, G. Liao, P. Xu, L. Li, Fast mineralization of acetaminophen by highly dispersed Ag-g-C3N4 hybrid assisted photocatalytic ozonation, Separation and Purification Technology 216 (2019) 1–8. https://doi.org/10.1016/j.seppur.2019.01.057.

[104] S.O. Ganiyu, N. Oturan, S. Raffy, M. Cretin, C. Causserand, M.A. Oturan, Efficiency of plasma elaborated sub-stoichiometric titanium oxide (Ti4O7) ceramic electrode for advanced electrochemical degradation of paracetamol in different electrolyte media, Separation and Purification Technology 208 (2019) 142–152. https://doi.org/10.1016/j.seppur.2018.03.076.

[105] T.X.H. Le, T.V. Nguyen, Z. Amadou Yacouba, L. Zoungrana, F. Avril, D.L. Nguyen, E. Petit, J. Mendret, V. Bonniol, M. Bechelany, S. Lacour, G. Lesage, M. Cretin, Correlation between degradation pathway and toxicity of acetaminophen and its by-products by using the electro-Fenton process in aqueous media, Chemosphere 172 (2017) 1–9. https://doi.org/10.1016/j.chemosphere.2016.12.060.

[106] F. Ghanbari, A. Hassani, S. Wacławek, Z. Wang, G. Matyszczak, K.-Y.A. Lin, M. Dolatabadi, Insights into paracetamol degradation in aqueous solutions by ultrasound-assisted heterogeneous electro-Fenton process: Key operating parameters, mineralization and toxicity assessment, Separation and Purification Technology 266 (2021) 118533. https://doi.org/10.1016/j.seppur.2021.118533.

[107] C. Xue, Z. Cao, X. Tong, P. Yang, S. Li, X. Chen, D. Liu, W. Huang, Investigation of CuCoFe-LDH as an efficient and stable catalyst for the degradation of acetaminophen in heterogeneous electro-Fenton system: Key operating parameters, mechanisms and pathways, Journal of Environmental Management 327 (2023) 116787. https://doi.org/10.1016/j.jenvman.2022.116787.

[108] H. Öztürk, S. Barışçı, O. Turkay, Paracetamol degradation and kinetics by advanced oxidation processes (AOPs): Electro-peroxone, ozonation, goethite catalyzed electro-fenton and electro-oxidation, Environmental Engineering Research 26 (2021). https://doi.org/10.4491/eer.2018.332.

[109] S. Ahmadzadeh, M. Dolatabadi, Removal of acetaminophen from hospital wastewater using electro-Fenton process, Environ Earth Sci 77 (2018) 53. https://doi.org/10.1007/s12665-017-7203-7.

[110] L.C. Almeida, S. Garcia-Segura, N. Bocchi, E. Brillas, Solar photoelectro-Fenton degradation of paracetamol using a flow plant with a Pt/air-diffusion cell coupled with a compound parabolic collector: Process optimization by response surface methodology, Applied Catalysis B: Environmental 103 (2011) 21–30. https://doi.org/10.1016/j.apcatb.2011.01.003.

4 CuCo carbon aerogel as a bifunctional cathode for Electro-Fenton processes: Unveiling synergistic effects and catalytic mechanisms

Highlights

- Unique microstructure endows CuCo/CA with enhanced electrochemical properties.
- The synergistic effect of Cu and Co promotes electrocatalytic activity in CA.
- CuCo/CA cathode achieves simultaneous *in-situ* generation and activation of H_2O_2.
- Various organic micropollutants are degraded without a need for external aeration.
- CuCo/CA EF system has broad pH adaptability, long-term stability and recyclability.

Graphical abstract

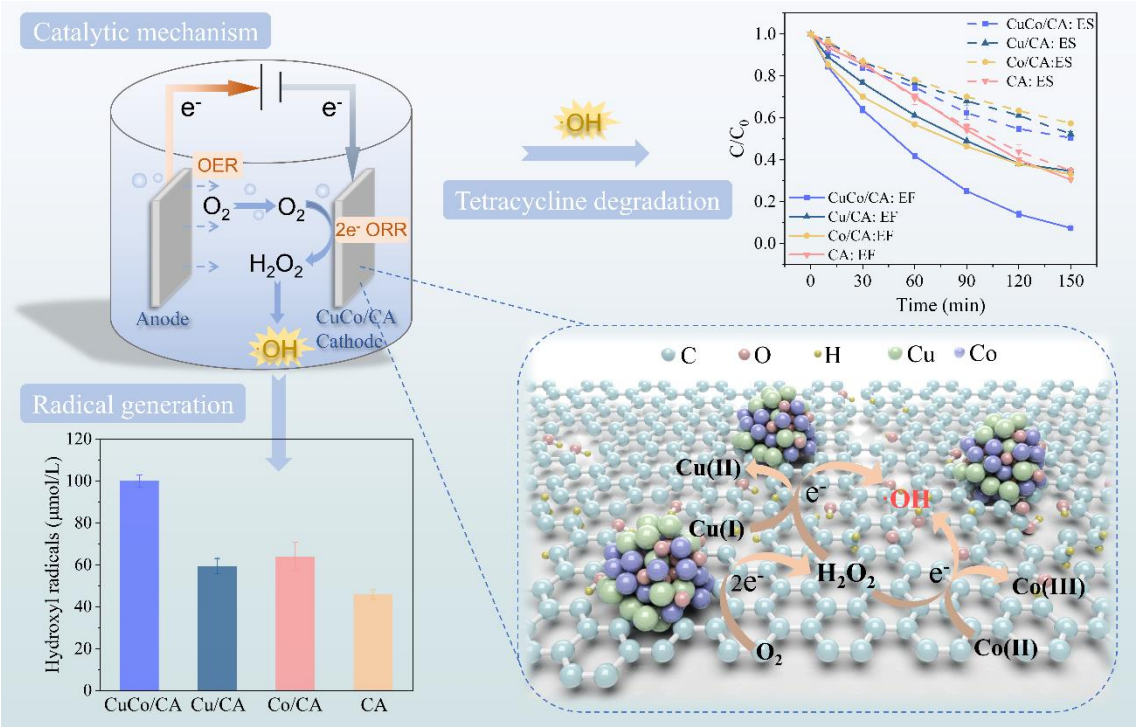

4.1 Abstract

Combining electrocatalytic oxygen reduction reaction (ORR) and heterogeneous electro-Fenton (HEF) reaction is considered a promising approach for generating reactive radicals to decompose organic micropollutants in water. A novel catalyst, copper-cobalt carbon aerogel (CuCo/CA), was successfully fabricated and directly applied as a bifunctional cathode in an HEF system. The synergistic effect of Cu and Co contributed to the development of distinctive microstructures, including abundant oxygen-containing groups, carbon defects, a large surface area and a unique porous structure. These structural features endowed CuCo/CA with rapid electron transfer capability and enhanced activity and selectivity for the two-electron ORR process. In the constructed EF system, CuCo/CA achieved its dual functionality by catalysing the electrosynthesis of hydrogen peroxide and it's *in situ* activation to generate highly reactive hydroxyl radicals. Notably, anodic oxygen evolution in the system eliminated the need for additional oxygen input, enhancing its cost-effectiveness. The system demonstrated degradation ability for a range of candidate organic pollutants, including antibiotics, analgesics, organic acid and dye. After six consecutive runs, CuCo/CA EF system achieved satisfactory TC removal and good adaptability within a broad pH range. Long-term stability and low electricity consumption highlighted the potential of CuCo/CA as an efficient and sustainable cathode in EF technology for water decontamination.

4.2 Introduction

Inefficient biodegradation of antibiotics has classified them as persistent organic pollutants (POPs) in the environment [1]. Tetracycline (TC), a commonly used antibiotic, frequently contaminates water bodies, harming plant growth, aquatic ecosystems, and microbial communities [2]. TC is frequently detected in water bodies such as surface water, drinking water and wastewater [3]. As a result, the need for effective removal methods is increasing. The Electro-Fenton (EF) process, which generates reactive hydroxyl radicals (·OH) for pollutant oxidation, is a promising advanced oxidation process (AOP) for breaking down these persistent compounds [4].

In EF systems, hydrogen peroxide (H_2O_2) is generated *in situ via* a two-electron oxygen reduction reaction (ORR, Equation 4.1) at the cathode, avoiding risks of H_2O_2 transportation and handling compared to classic Fenton system [5].

Subsequently, ·OH radicals are produced through the activation of H_2O_2 by Fe^{2+} (Equation 4.2) [6], effectively decomposing various organics via non-selective oxidation. However, homogeneous EF systems are limited by pH constraints (typically below 4) and require continuous Fe^{2+} addition [4]. Therefore, integrated cathode materials with dual functionalities, including two-electron ORR and *in situ* H_2O_2 activation, hold significant application potential. In such systems, electro-activation of H_2O_2 to ·OH depends on a one-electron redox cycle occurring at exposed active sites of the cathode, which eliminates the need for Fe^{2+} and widens applicable pH range [7].

$$O_2 + 2H^+ + 2e^- \rightarrow H_2O_2 \quad (4.1)$$

$$Fe^{2+} + H_2O_2 \rightarrow Fe^{3+} + OH^- + \cdot OH \quad (4.2)$$

Ensuring high ·OH production efficiency in the hetero-EF reaction requires a catalyst that can selectively catalyse H_2O_2 generation *via* a two-electron pathway and subsequently activates H_2O_2 to yield ·OH. Previous studies have highlighted hetero-EF activity of ·OH production in materials such as a magnetite/multiwalled carbon nanotubes [8], defective three-dimensional porous carbon [9], and carbon nanofibers [10]. However, achieving rapid electro generation of ·OH remains challenging due to the difficulty in synchronising efficient catalysis of both selective generation and activation of H_2O_2 into ·OH on a single electrocatalyst. It has been reported that a multi-component combination of transition metals with carbon composite catalysts has the potential to enhance electrochemical activity by regulating individual metal activity, thus further improving overall performance [11]. Catalysts synthesised through synergistic interaction of copper (Cu) and cobalt (Co) find extensive applications in various fields, including supercapacitors [12], Zn–air batteries [13], and electrochemical sensors [14]. Incorporation of Cu and Co species has been demonstrated to enhance electrochemical performance, such as specific capacity and cycling stability. Cu is regarded as one of the most crucial iron-free catalysts in Fenton-like systems. Copper ions (Cu^+) have a higher reaction rate ($k = 1 \times 10^4\ M^{-1}s^{-1}$) with H_2O_2 (Equation 4.3 compared to Fe^{2+} ($k = 76\ M^{-1}s^{-1}$) and can function effectively within a broad pH range [15]. Additionally, the Co^{2+}/Co^{3+} pair offers a stable redox potential, while Co^{2+} species in solution and on the surface exhibit great potential in the H_2O_2-mediated degradation of organic pollutants [16].

$$Cu^{+} + H_2O_2 \rightarrow Cu^{2+} + OH^{-} + \cdot OH \quad (4.3)$$

To enhance electrocatalytic activity, a variety of carbon-based materials are employed in electrode fabrication including carbon felt [17], carbon aerogel [18], and graphite felt (GF) [19]. Among them, carbon aerogel (CA), distinguished by its 3D network structure, good electrical conductivity, and high surface area, emerges as an outstanding candidate for electrode construction [20]. In addition, carbon aerogel may also serve as a support for metal or metal oxide catalysts. The 3D network structure of CA increases active sites of the catalysts, and its adsorption capacity raises pollutant concentrations around these sites, leading to enhanced catalytic activity [18]. So far, the synergistic effects of Cu and Co on microstructures, electrochemical properties, and catalytic performances of CA have not been systematically revealed, and application of bimetallic carbon aerogel as an efficient electrode material for water decontamination remains to be further investigated.

In this work, a CuCo carbon aerogel (CuCo/CA) was synthesised as a bifunctional cathode in a hetero-EF system. The cathode microstructure, such as surface morphology, porosity, and chemical composition of CuCo/CA was analysed and compared with those of Cu/CA, Co/CA and pure CA. The synergistic effects of Cu and Co on regulating microstructure, enhancing ORR activity and selectivity and improving electrocatalytic ability were systematically investigated. This system simultaneously generates and activates H_2O_2 *in situ* without external aeration. Reaction parameters were optimised and radical generation mechanisms were revealed using TC as a model pollutant. Recyclability of CuCo/CA was investigated in six consecutive runs while long-term stability was evaluated in a continuous stirred tank reactor (CSTR). Finally, the extensively catalytic properties were further assessed using various organic contaminants.

4.3 Experimental section

4.3.1 Chemicals and reagents

Pt sheet electrode was sourced from the Shanghai Chuxi Industrial Co., Ltd., China. Tert-butanol ($(CH_3)_3COH$, 99.5%) was procured from Fluorochem Ltd., UK. Resorcinol ($C_6H_6O_2$, 99%), titanium (IV) oxysulfate ($TiSO_5$, ≥29%), tetracycline hydrochloride (TC, $C_{22}H_{25}ClN_2O_8$, ≥99%), hydrogen peroxide (30% w/w, H_2O_2), cobalt (II) acetylacetonate ($Co(C_5H_7O_2)_2$, Analytical Reagent grade), nitric acid (HNO_3, 69%), hydrochloric acid

(HCl, 37%), 5,5-Dimethyl-1-pyrroline N-oxide (DMPO, $C_6H_{11}NO$, ⩾97.0%), and p-benzoquinone ($C_6H_4O_2$, ≥98%) were sourced from Sigma-Aldrich, *via* Merck Life Science Ltd., UK. Copper (II) acetate (Cu $(CH_3COO)_2$, 98%), formaldehyde (CH_2O, 37%), Nafion (5 wt%), sodium hydroxide (NaOH, ≥ 98%), sodium sulfite (Na_2SO_3, 98%), and acetone (C_3H_6O, ≥99+%) were acquired from Thermo Scientific, UK. Sodium sulfate (Na_2SO_4, 99.5%), sulfuric acid (H_2SO_4, 96%), and methanol (CH_3OH, ≥99.9%) were purchased from Fisher Scientific, UK. Sodium carbonate (Na_2CO_3, Analytical Reagent grade) was bought from BioServ Ltd., UK.

4.3.2 Cathode synthesis

Referring to the fabrication methodology of bimetallic carbon aerogel in our previous work [21], synthesis of CuCo/CA cathode (molar ratio of Cu:Co is 1:1) comprised of four stages: Gelation, solvent exchange, drying, and carbonisation. Fig. 4.1 illustrates the schematic diagram of synthesis process.

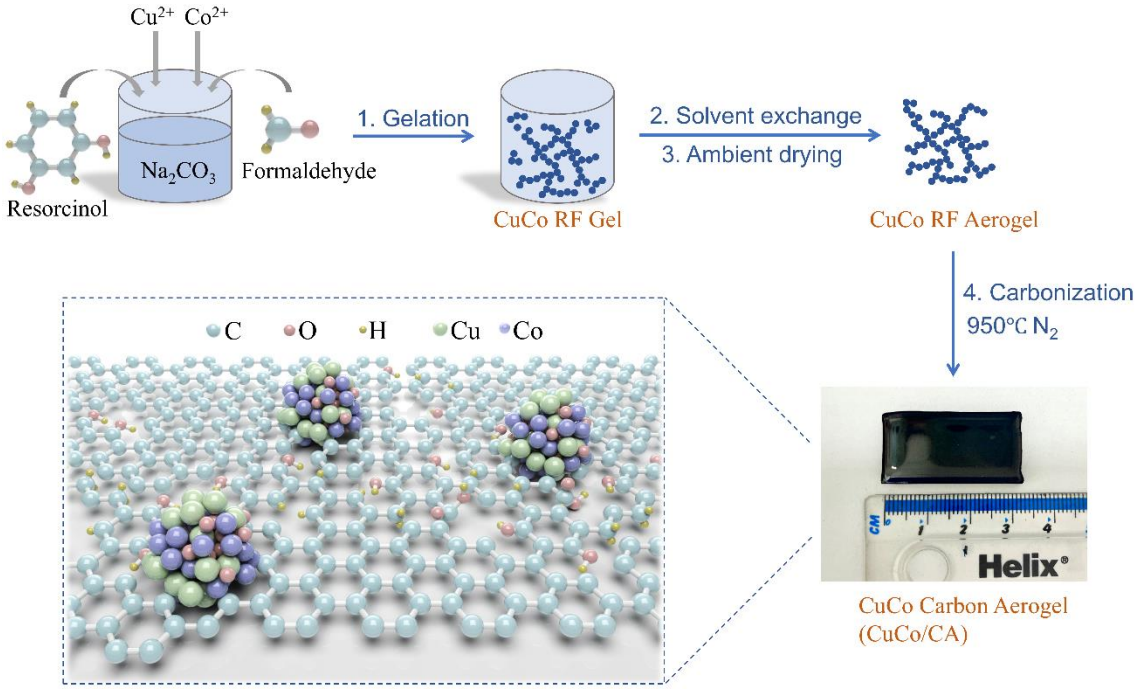

Figure 4.1. Schematic diagram showing four-stage synthesis of CuCo/CA cathode. A similar process was utilised for the synthesis of Cu/CA, Co/CA and CA.

The synthesis of the CuCo/CA cathode (molar ratio of Cu: Co is 1:1) comprised of four stages: (1) Gelation: in which 11.011 g of resorcinol was introduced to 19.64 mL of ultrapure water, followed by 15 mL of 37% formaldehyde solution and 0.0085 g of

sodium carbonate. The resulting mixture was continuously stirred until complete dissolution. Copper (II) acetate (0.2430 g) and cobalt (II) acetylacetonate (0.3703 g), as metallic precursors for CuCo/CA, were then dissolved in the well-prepared uniform solution. The resulting solution was magnetically stirred for one hour before pouring into a cuboid glass mould which was tightly clamp-sealed. The precursor solution contained in the mould was cured in an oven using a multi-step temperature profile, comprising 30 °C for 1 day, 50 °C for 1 day, and 90 °C for 3 days to enable polymerisation and aging processes. (2) Solvent exchange: the mould was removed from the oven and allowed to naturally air-cool before the resulting wet gel was extracted and fully immersed in acetone for 72 h (refresh the acetone every 24 h), ensuring thorough replacement of any residual water within the carbon structure. Acetone was selected as the exchange solvent due to its lower surface tension, aimed at minimising gel shrinkage. (3) Drying: following solvent exchange the gel was left to dry under ambient conditions for a further day, yielding an aerogel of specific dimensions and shape. (4) Carbonisation: finally, the shaped carbon aerogel was subjected to carbonisation within a tube furnace (Carbolite Gero TZF 12/38) under a flowing nitrogen atmosphere of 0.1 L/min. The furnace temperature was ramped at a rate of 3 °C/min from room temperature to 950 °C, where it was held for 4 hours. After completion of the carbonisation process the resulting CuCo/CA was allowed to cool to ambient temperature, and subsequently utilised as an integrated cathode within the electro-Fenton system.

The synthesis of Cu/CA and Co/CA went through identical stages with the addition of 0.2430 g of copper (II) acetate and 0.3703 g cobalt (II) acetylacetonate, respectively, to the precursor solution. The pure CA was prepared without the addition of metallic precursors. The metal precursor for $Cu_{0.3}Co_{0.7}$/CA are 0.1458 g copper (II) acetate and 0.5184 g cobalt (II) acetylacetonate, and for $Cu_{0.7}Co_{0.3}$/CA are 0.3402 copper (II) acetate and 0.2222 g cobalt (II) acetylacetonate.

4.3.3 Characterisation methods

X-ray diffraction (XRD) patterns were obtained using a Cu K Alpha radiation source (λ = 1.5406 Å) scanning in the 2θ range of 10° to 80° with a step size of 0.02° using a Shimadzu XRD-6100 instrument. The surface morphology information was obtained through high-resolution transmission electron microscopy (HRTEM) using a FEI Titan3

Themis 300 instrument. The energy dispersive X-ray spectroscopy (EDS) mapping was executed using the same instrument employed for HRTEM with a HAADF detector. X-ray photoelectron spectroscopy (XPS) was characterised using an ESCALAB XI^+ (Al Kα radiation) manufactured by Thermo Scientific was used to perform C1s, O1s, Cu2p and Co2p orbital spectrum scanning on the CuCo/CA sample to analyse the chemical state of the elements on the surface. Experimental Fourier Transform Infrared (FTIR) diffuse reflection spectra were recorded using a Nicolet iS5 (Thermo Scientific) on powder-pressed KBr pellets. Defects and disorder information of the cathodes were obtained using Raman microscopy (Horiba Scientific LabRAM HR Evolution) equipped with an excitation source at 514 nm (1.5 mW laser power, spot diameter of 2 μm). To investigate the surface porosity information of the synthesised cathodes, a Micromeritics Tristar 3000 instrument was used to obtain N_2 adsorption–desorption isotherms at a temperature of 77 K. Prior to conducting measurements, the samples underwent a vacuum degassing process at 393 K for 16 h to effectively eliminate any residual moisture. N_2 adsorption data acquired within the range of relative pressures from 0.05 to 0.16 kPa were selected to calculate the Brunauer-Emmet-Teller (BET) surface area. Furthermore, the assessment of pore size distributions was accomplished through the application of the Barrett-Joyner-Halenda (BJH) method [22] with data collected from the desorption branch.

4.3.4 Electrochemical property tests

Cyclic voltammetry (CV) tests were carried out using a three-electrode system utilising a CHI 760E electrochemical workstation (Chenhua Instrument Co.Ltd., China). To prep are the working electrode, the bulk CuCo/CA sample was first ground into powder. Subsequently, 10 mg of the powder was dispersed in a solvent comprising 1.5 mL of Milli-Q^{TM} water, 0.75 mL of ethanol, and 25 μL of 5 wt% Nafion solution. Following 1 h of sonication, the resulting catalyst ink (6 μL) was drop-cast onto a glassy carbon electrode surface (diameter: 3 mm) and left to air-dry naturally, forming a uniform catalyst film layer. The obtained electrodes were used as the working electrode, and platinum sheet and Ag/AgCl served as the counter and reference electrodes, respectively. The CV curve was recorded in O_2-saturated electrolyte (0.1 M Na_2SO_4 at pH = 5) with a scan rate of 10 mV/s. Before starting the test, the electrolyte was aerated with O_2 for 30 min to achieve saturation, and aeration was maintained at 0.3 L/min throughout the test.

Electrochemical impedance spectroscopy (EIS) measurements were performed employing a three-electrode system, in which the bulk synthesised samples served as the working electrode, and platinum sheet and Ag/AgCl functioned as the counter and reference electrodes, respectively. The EIS experiments were conducted using a potentiostat (Gamry, 1010E) across a frequency range of 10^{-2}-10^{-5} Hz with an amplitude of 5 mV.

Rotating ring-disk electrode (RRDE) testing was used to assess oxygen reduction reaction (ORR) activity and selectivity. RRDE voltammograms were recorded in 0.1 M Na_2SO_4 at pH 3 using an AFMSRCE rotator unit (Pine Instrument Company, United States). The preparation of catalyst ink was identical as for CV testing. 12 μL of the catalyst ink was pipetted and spread onto a glassy carbon disk electrode for the RRDE tests. The RRDE setup comprised of a glassy carbon disk (0.2475 cm^2) and a Pt ring (0.1866 cm^2) with a catalyst loading density of 213 μg/cm^2. Following overnight air-drying at room temperature, the modified RRDE was employed as the working electrode, equipped with an Ag/AgCl reference electrode and a platinum wire counter electrode. Prior to testing, the electrolyte was aerated with O_2 for 30 min. To eliminate the capacitive current of the working electrode, the background current was measured under an N_2 atmosphere using the same rotation speed (1600 rpm) and scan rate (10 mV/s) as those used under O_2, and then subtracted from the ORR polarisation curve. The Pt ring electrode was held at a constant potential of 1.3 V vs. the reversible hydrogen electrode (RHE).

4.3.5 Electrochemical degradation

Electrochemical degradations were performed within an undivided electrochemical cell (150 mL), in which the platinum sheet (4 cm^2) and synthesised carbon aerogels (CuCo/CA, Cu/CA, Co/CA and pure CA, 4.5 cm^2) were employed 2 cm away as the anode and cathode, respectively. The simulated pollutant solution comprised of 10 mg/L tetracycline (TC) and 0.05 mol/L Na_2SO_4 (as electrolyte) with Milli-Q^{TM} water (Merck Millipore), stirred with a magnetic bar at 400 rpm (25°C). For electro-Fenton (EF) systems, a DC power supply (Velleman 70–0768), configured for the operating current of the electrocatalytic reaction, was connected to the cathode and anode, and a constant current mode was used. No additional aeration was provided in most electro-Fenton

reactions, while compressed air cylinders were utilised to evaluate the impact of various aeration rates. For electro-sorption (ES) systems, 1 mA of current with a flowing nitrogen (N_2) atmosphere of 0.2 L/min was maintained during reaction, and the solution was aerated with N_2 for 20 min prior to reaction to remove any oxygen. The initial pH of the solution was adjusted to the desired value using NaOH and H_2SO_4, and pH and dissolved oxygen (DO) concentration were monitored using a digital multi-meter kit (HQ 40d, Hach, UK). Water samples were withdrawn for measurement at preset intervals using a 10 mL syringe, followed by filtration through a 0.22 μ m filter. The cathode was collected and cleaned with ultra-pure water for the reuse experiments, where its recyclability was assessed based on the decomposition efficiency of TC.

4.3.6 Analytical methods

The concentration of TC was measured using a UV–Vis spectroscopy (Shimadzu UV1900) at a detection wavelength of 357 nm [23]. The pseudo-first-order kinetic model was used to describe the removal of TC in Equation 4.4, where C_0 represents initial pollutant concentration (mg/L), C_t represents pollutant concentration at time t (mg/L), k_{obs} is apparent rate constant (min^{-1}) and t represents reaction time (min), respectively.

$$ln\,(C_0/C_t) = k_{obs}\,t \qquad (4.4)$$

The concentrations of metronidazole (MNZ) and acid orange 7 (AO7) were detected at a wavelength of 318 nm and 486 nm, respectively [24,25]. The concentration of acetaminophen (ACT) was determined using high-performance liquid chromatography (HPLC, Agilent 1290 Infinity II) at 254 nm, equipped with an Agilent Infinity Lab Poroshell 120 EC-C18 column (2.1 mm x 50 mm, 1.9 μm). The mobile phase consisted of Solvent (A) - water with 0.1% trifluoroacetic acid, and Solvent (B) - acetonitrile with 0.1% trifluoroacetic acid. The gradient elution profile was: 0 min: 95%A–5%B, 5 min: 5%A–95%B, and 6 min: 95%A–5%B. The flow rate of the mobile phase was set to 0.5 mL/min, and the injection volume was 10 μL. Salicylic acid (SA) was measured using HPLC at 320 nm wavelength using an identical mobile phase as ACT. The gradient was adjusted to, 0 min: 95%A–5%B, and 5 min: 5%A–95%B. The column temperature was maintained at 40 °C, and the flow rate was set at 0.5 mL/min.

The concentration of hydrogen peroxide (H_2O_2) generated was assessed using

colorimetric analysis. This relied on the formation of a titanium (IV) and H_2O_2 complex, with detection performed using UV-vis spectroscopy at a detection wavelength of 408 nm [26]. Specifically, 1 mL samples at specific time intervals were withdrawn from the reactor and introduced into a mixed solution comprising 0.5 mL of 0.05 M titanium oxysulfate ($TiSO_5$), 0.5 mL of 3 M sulfuric acid (H_2SO_4), and 3 mL of water. After allowing the solution to stand for 10 minutes, the absorbance was measured. Hydroxyl radicals (·OH) were quantitatively determined using a probe reaction involving salicylic acid (SA) and ·OH [27]. In this experiment, 0.01 M SA was added to 0.05 M oxygenated Na_2SO_4 electrolyte solution before reaction. At predetermined time, 1 mL of the reaction mixture was withdrawn for analysis using HPLC. The hydroxylated products, 2,3-dihydroxybenzoic acid (2,3-DHBA) and 2,5-dihydroxybenzoic acid (2,5-DHBA), were detected at 320 nm wavelength during HPLC analysis. The mobile phase consisted of water with 0.1% trifluoroacetic acid (Solvent A) and acetonitrile with 0.1% trifluoroacetic acid (Solvent B). The gradient used was, 0 min: 95%A–5%B, and 5 min: 5%A–95%B. The column temperature was maintained at 40 °C, and the flow rate was set at 0.5 mL/min. Under these experimental conditions, 2,3-DHBA and 2,5-DHBA exhibited retention times of 1.85 min and 1.7 min, respectively. The concentration of ·OH was determined by summing the concentrations of 2,3-DHBA and 2,5-DHBA.

Metal loadings on the fabricated electrodes were quantified using Inductively Coupled Plasma-Mass Spectrometry (ICP-MS, Perkin Elmer Elan DRCe). The electrode was ground up using a pestle and mortar before being dispersed in a beaker filled with a 3:1 mixture of hydrochloric acid (HCl) and nitric acid (HNO3). The resulting solid-liquid mixture was gradually heated on a temperature-controlled hot plate until complete evaporation of the acid. Subsequently, the mixture was allowed to cool to room temperature, and 10 mL of nitric acid was added. The resulting solution was once again heated to reduce its volume to 5 mL, followed by cooling to room temperature and filtration through a 0.22 μm syringe filter. The diluted metal concentration was determined using ICP-MS. The presence of radicals was directly detected using Electro Spin Resonance (ESR, Bruker EMXplus EPR Spectrometer) technique with DMPO as a spin-trapping agent. The detection of ·OH was conducted in aqueous water while the detection of $\cdot O_2^-$ was instead conducted in a methanol medium owing to the limited reactivity of $\cdot O_2^-$ radicals with DMPO and the potential interference from ·OH radicals in

aqueous environments.

4.3.7 Continuous stirred tank reactor

The operational stability of the CuCo/CA cathode was also investigated using a continuous stirred tank reactor (CSTR) over a 48-h reaction time, and the schematic diagram of the reactor is shown in Fig. 4.9 (c). The reactor comprised an undivided cylindrical-shaped glass cell, two peristaltic pumps (Watson Marlow 323S), a DC power supply, and containers for the stock feed solution and a post-reaction disposal solution. Two peristatic pumps were employed to ensure a steady flow of TC solution through the reactor. One pump was used to feed the stock solution into the reactor, and the other pump was used to collect the treated solution; the pumps were calibrated to maintain a steady reactor solution volume. The cell was equipped with a platinum sheet anode and CuCo/CA cathode with a 2 cm inter-electrode separation. A supporting electrolyte of 0.05 M Na_2SO_4 and a model contaminant solution of 10 mg/L TC were utilised. Continuous stirring of the sample solution was achieved using a magnetic stirrer and PTFE magnetic bar.

4.4 Results and discussion

4.4.1 Characterisation and electrochemical performances

Physical and chemical characterisations are typically employed to gain insights into the catalytic mechanisms and performances. The crystalline composition of CuCo/CA cathode was first analysed through X-ray diffraction (XRD) (Fig. 4.2 (a)). CuCo/CA exhibits a mixed phase comprising graphitic carbon, Co, Cu and Cu_2O. Three distinct diffraction peaks (44.2°, 51.5°, and 75.8°) corresponding to (1 1 1), (2 0 0), and (2 2 0) planes of Co indicated the incorporation of Co species into the carbon matrix [28]. The characteristic 2θ peak at ~ 23° is attributed to the crystallographic reflection of graphitic carbon [29]. Peaks at 2θ values of 36.4°, 42.3°, and 61.3° match the (1 1 1), (2 0 0) and (2 2 0) planes of Cu_2O [12], which might be beneficial to an overall enhancement of catalytic performance. Additionally, the peaks at 43.3°, 50.4° and 74.1° corresponding to Cu phase [30] confirmed the successful incorporation of elemental Cu into the carbon aerogel framework.

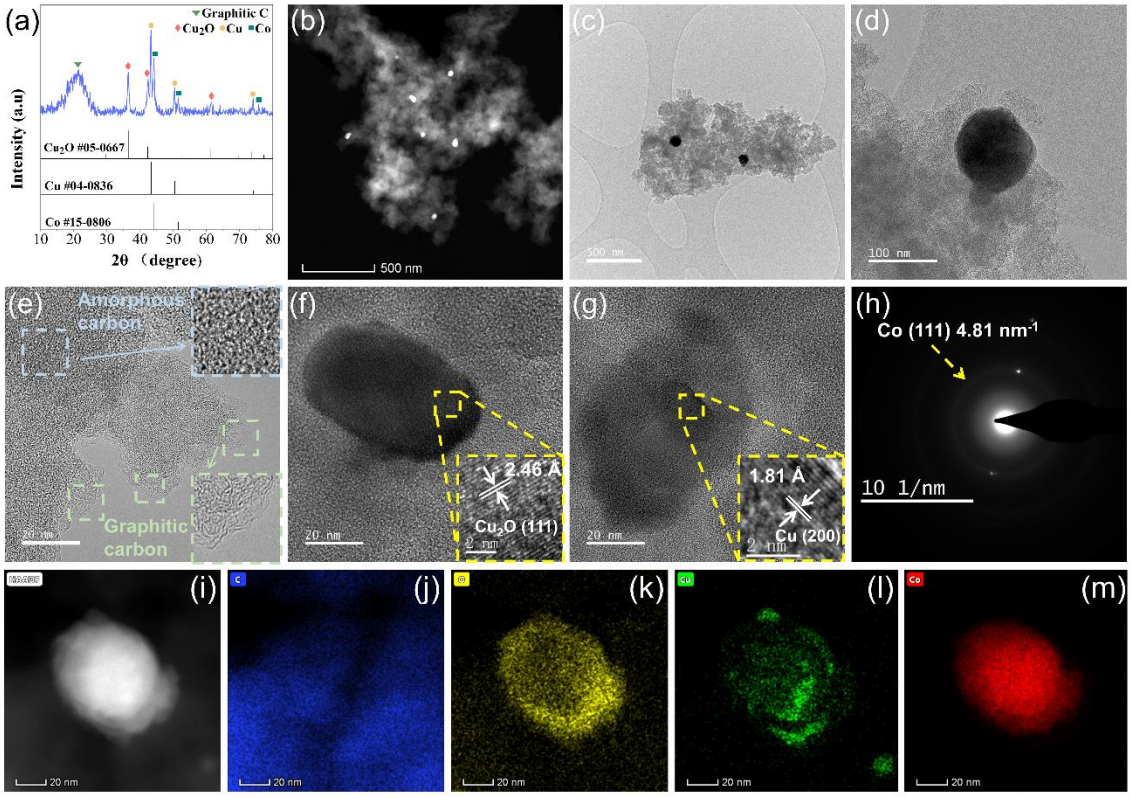

Figure 4.2. (a) XRD patterns, (b)-(g) HRTEM images, (h) Electron diffraction pattern, and (i) HAADF-STEM images of CuCo/CA cathode; EDS mapping of (j) C, (k) O, (l) Cu and (m) Co element on CuCo/CA.

High-resolution transmission electron microscopy (HRTEM) images at various magnifications are shown in Fig. 4.2 (b)-(d). They illustrate the uniform dispersion of metallic nanoparticles with a diameter of ~ 100 nm in CuCo/CA. These particles within the organic aerogel matrix promote the formation of graphite clusters during carbonisation (Fig. 4.2 (e)). Notably, partial graphitisation within carbon aerogel was previously reported when transition metals such as Fe, Ni and Co were used as doping metals, which endows the materials with good electrical conductivity and is conducive to efficient transport of electrons [31]. HRTEM images in Fig. 4.2 (f)-(h) provide clear insight into interlayer distance and electron diffraction ring. Specifically, the measured spacing of 0.246 nm and 0.181 nm respectively corresponded to Cu_2O (1 1 1) and Cu (2 0 0) planes, and the electron diffraction ring is associated with Co (1 1 1) [32], in accordance with XRD findings. Furthermore, energy dispersive X-ray spectroscopy (EDS) mappings in Fig. 4.2 (i)-(m) and Fig. S4.1 clearly show that elemental O is distributed in both carbon matrix and nanoparticles, while Cu and Co are selectively positioned in the central nanoparticle area. The distributions of elemental Cu and O on particles are

correlated, with both being predominantly located at the edges of particle (see line scanning results), possibly due to the formation of Cu_2O. In contrast, elemental Co exhibits homogeneous distribution on the nanoparticle scale.

In a previous study by Lu et al., [33] a positive correlation was observed between oxygen content and both activity and selectivity in oxygen reduction reaction (ORR), thus indicating the significance of oxygen functional groups. Fig. 4.3 (a) exhibits a Fourier-transform infrared spectroscopy (FTIR) obtained in investigation of oxygen-containing functional groups on the synthesised cathodes. Two obvious adsorption peaks at ~ 1407.8 cm^{-1} and ~ 1637.3 cm^{-1} are attributed to –COO- and −C=O bond stretches, respectively [34]. Additionally, strong adsorption peaks at 3444.2 cm^{-1} correspond to –OH vibration [35], which indicated the presence of abundant oxygen functional groups on synthesised CuCo/CA. By comparing the FTIR peak intensity between these four cathodes, the doping of Cu and Co elements on carbon aerogel is conducive to the formation of oxygen-containing functional groups, especially –COO- groups. The O 1 s high-resolution spectrum obtained from CuCo/CA using X-ray photoelectron spectroscopy (XPS) in Fig. 4.3 (b) is deconvoluted into the following bands: oxygen doubly bound to carbon (C=O) at ~ 531.2 eV, ether and hydroxyl groups bonded to aliphatic & carbonyl shake-up at 532.1 eV, ether and hydroxyl groups bonded to aromatics at 533.0 eV, and surface absorbed water at 533.9 eV [36]. According to a previous study [37], the introduction of abundant surface oxygen-containing groups has a positive impact on the electrocatalytic process of $2e^-$ ORR for the generation of H_2O_2.

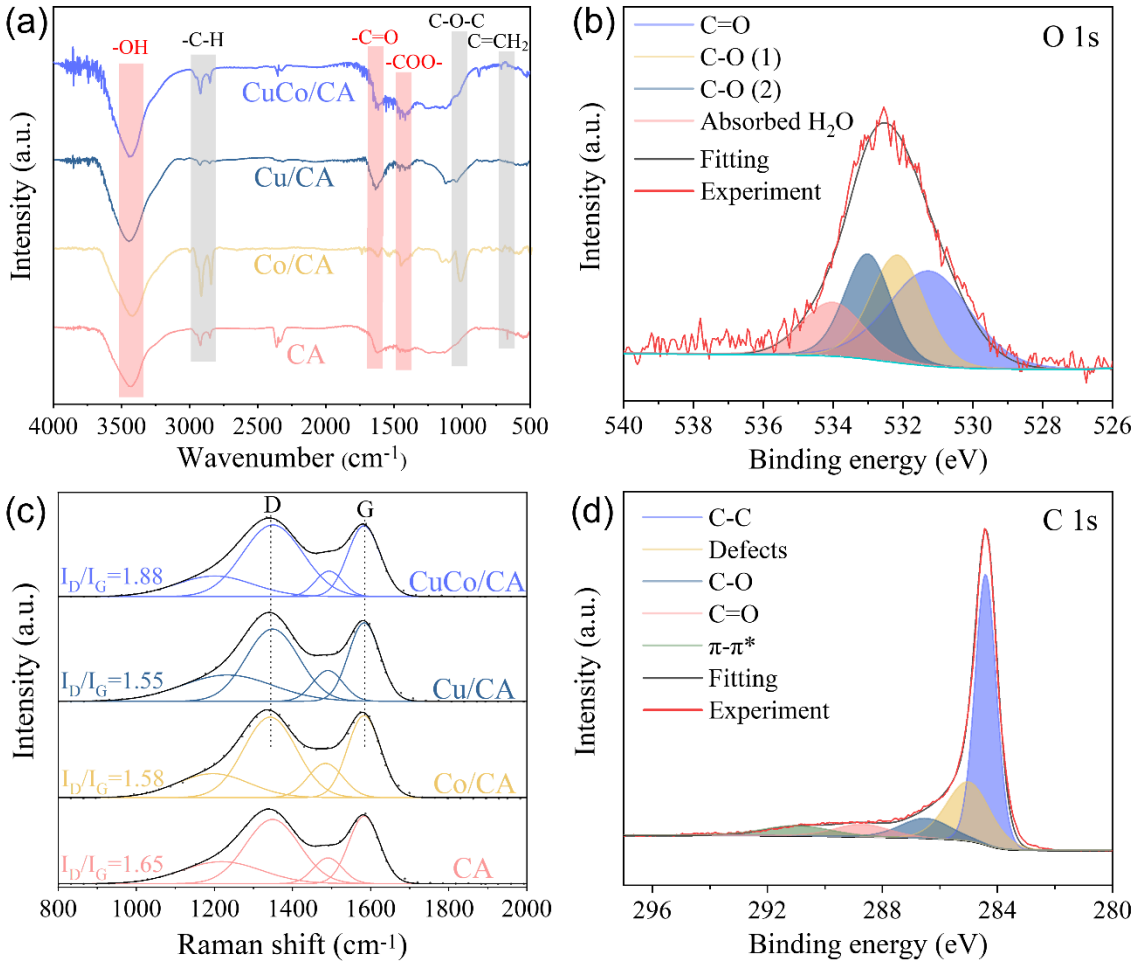

Figure 4.3. (a) FTIR spectra of various cathodes; (b) O 1 s XPS spectra of CuCo/CA (C-O (1) refers to ether and hydroxyl groups bonded to aliphatic & carbonyl shake-up and C-O (2) refers to ether and hydroxyl groups bonded to aromatics); (c) Raman spectra various cathodes and (d) C 1 s XPS spectra of CuCo/CA.

In addition to oxygen-containing functional groups, carbon defects are also regarded as active sites for catalytic two-electron ORR [33]. The defect degree of four cathodes were assessed through Raman spectroscopy in Fig. 4.3 (c). Two prominent peaks are observed at ~ 1340 cm^{-1} (D band) and ~ 1583 cm^{-1} (G band), which represent disordered structure of sp^3 hybridised carbon atoms (suggesting defect degree) and aromatic ring structure of sp^2 hybridised carbon atoms (suggesting degree of graphitisation), respectively [38]. By employing peak fitting analysis, I_D/I_G ratios calculated using the peak area are determined as: 1.88 (CuCo/CA), 1.55 (Cu/CA), 1.58 (Co/CA) and 1.65 (CA). These ratios signify that while synthesised cathodes possess abundant defect sites and structural distortions, they retain a considerable degree of graphitic structure. In comparison, the higher I_D/I_G value observed for CuCo/CA provide clear evidence that the synergistic effect of Cu and Co increases the number of carbon defects to improve ORR

activity. A similar bimetallic effect has also been found in other carbon materials [11,39]. Furthermore, deconvolution of C 1 s spectrum (Fig. 4.3 (d)) of CuCo/CA also shows a carbon defect peak at 285.4 eV [40], and the presence of C–O and C=O groups correspond to the O 1 s spectrum. These results indicated that a large number of carbon defects were formed during the carbonisation process of CuCo/CA, promoting the generation of oxygen functional groups. These groups are considered to be catalytic sites for the two-electron ORR process [41], facilitating H_2O_2 generation.

The ORR electrocatalytic activity of CuCo/CA was directly evaluated using conventional three-electrode cyclic voltammetry (CV) in oxygen-saturated 0.1 M Na_2SO_4 (pH = 5) electrolyte solution. As illustrated in Fig. 4.4 (a), a distinct peak at approximately −0.57 V vs. reversible hydrogen electrode (RHE) is observed due to the reduction of O_2, reflecting the catalytic activity of the CuCo/CA cathode for oxygen reduction [42]. The bulk metallic content of CuCo/CA was determined using inductively coupled plasma mass spectrometry (ICP-MS) with copper (Cu) and cobalt (Co) loadings at 1.00 wt% and 0.94 wt%, respectively (Table 4.1). Due to low metal loadings, elemental Cu and Co are not observed in the full XPS spectrum, whilst obvious signals for C and O are detected (Fig. S4.2 (a)). In the high-resolution XPS spectrum of Cu 2p (Fig. 4.4 (b)), two sub-peaks of Cu 2p 3/2 and Cu 2p 1/2 at 932.7 eV and 952.2 eV correspond to Cu(I) [43], further verifying the presence of Cu_2O in the CuCo/CA cathode and consistent with XRD results. Fig. S4.2 (b) shows the high-resolution XPS spectrum of Co 2p, and two peaks emerge at 780.1 eV and 795.5 eV, corresponding to Co 2p3/2 and Co 2p1/2 spin–orbit peaks, respectively [44]. According to a previous study [45], Cu(I) species are regarded as a Fenton-like catalyst and have been applied in H_2O_2 activation to generate ·OH radicals, as shown in Equation 4.3. Additionally, it has been widely reported that Co^{2+}/Co^{3+} redox couples play a crucial role in enhancing the Fenton-like reaction by facilitating the *in situ* activation of H_2O_2 to generate hydroxyl radicals ($Co^{2+} + H_2O_2 \rightarrow Co^{3+} + \cdot OH + OH^-$) [46–51]. The presence of catalytically active metal components thus endows CuCo/CA cathode with another important role as an integrated Fenton-like catalyst to induce radical generation.

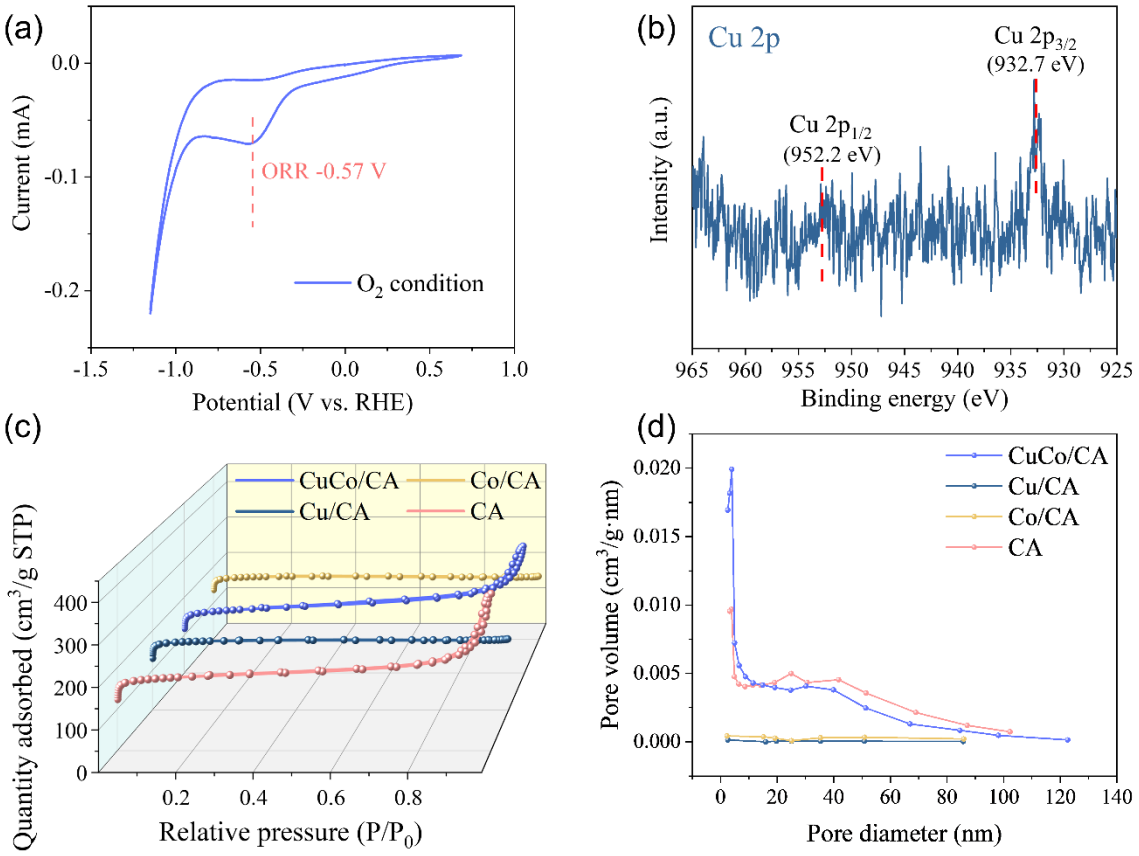

Figure 4.4. (a) CV curve of CuCo/CA in the presence of O_2; (b) Cu 2p XPS spectrum of CuCo/CA; (c) N_2 adsorption–desorption isotherms and (d) Pore size distribution curves of various cathodes.

Table 4.1. Porosity and metal loadings of synthesised cathodes.

Electrode	BET surface area (m^2/g)	t-Plot micropore area (m^2/g)	t-Plot micropore volume (cm^3/g)	BJH adsorption cumulative volume (cm^3/g)	ICP [wt.%]	
					Cu	Co
CA	601.4	480.3	0.223	0.343	/	/
Cu/CA	583.8	531.5	0.248	0.009	0.93±0.02	/
Co/CA	576.6	533.7	0.249	0.002		0.91+0.04
CuCo/CA	574.2	453.1	0.209	0.296	1.00±0.03	0.94±0.04

Pore structure properties of the synthesised cathodes were analysed by N_2 adsorption–desorption tests as shown in Fig. 4.4 (c)-(d), and Table. 4.1. The synthesised cathodes possess a BET surface area of 574 ~ 601 m^2/g, surpassing some other reported carbon aerogels [52,53]. The relatively high specific surface area not only exposes abundant

active sites on the surface but also imparts strong adsorption forces between cathodes and pollutant compounds. Pure CA exhibits the highest adsorption pore volume of 0.343 cm^3/g, it is therefore speculated that the porous characteristics mainly originate from the carbon skeleton, and the abundant nanoparticles occupy adsorption sites and pore channels.

Cu/CA and Co/CA curve (Fig. 4.4 (c)) exhibits IUPAC Type I isotherm behaviour, with a rapid increase in gas adsorption capacity in relatively low-pressure region, which indicated a typical microporous structure [54]. Negligible adsorption pore capacity was observed for Cu/CA and Co/CA within the detected range of 2.6-157.9 nm, as shown in Fig. 4.4 (d). This is because nitrogen, as the adsorbate gas, is limited by its molecular size, making it unable to easily penetrate extremely small pores. Consequently, micropores (smaller than 2 nm) cannot be accurately detected. The curves for pure CA and CuCo/CA exhibit an isotherm of IV featuring H3-type hysteresis loops, reflecting their prominent mesoporous structure [55]. These observations are consistent with narrow mesopore size distributions for CA and CuCo/CA, centred at 2.6 nm and 4.0 nm respectively. In addition, a rapid increase in gas adsorption within low relative pressure region is observed for both CA and CuCo/CA, indicating the coexistence of a micropore structure. Micropores provide a number of active sites for the process of oxygen reduction, whereas meso-macro pores serve as channels for oxygen transport, facilitating oxygen supply and allowing electrolyte to infiltrate the interior of the cathode [56]. The combination of two roles greatly improves catalyst's oxygen reduction performance [57].

A previous investigation found that pore structures of electrode materials also had an effect on electrochemical performance [58]. Electrochemical impedance spectroscopy (EIS) Nyquist plots of four cathodes all exhibit an incomplete semicircle in the high-frequency range and a straight line in the low-frequency range (Fig. 4.5 (a)). The charge transfer resistance (R_{ct}) of each cathode was qualitatively compared by analysing the radius of the semicircle in the Nyquist plots. The CuCo/CA electrode exhibited the smallest semicircle radius, indicating the lowest charge transfer resistance and enhanced electron transfer kinetics, while Cu/CA showed the largest semicircle radius, reflecting its relatively inferior electrochemical performance. These results suggest that the synergistic effect of Cu and Co resulted in a reduction of charge transfer resistance of

carbon aerogel, indicating a more efficient electron transfer process between the electrode–electrolyte interface [59].

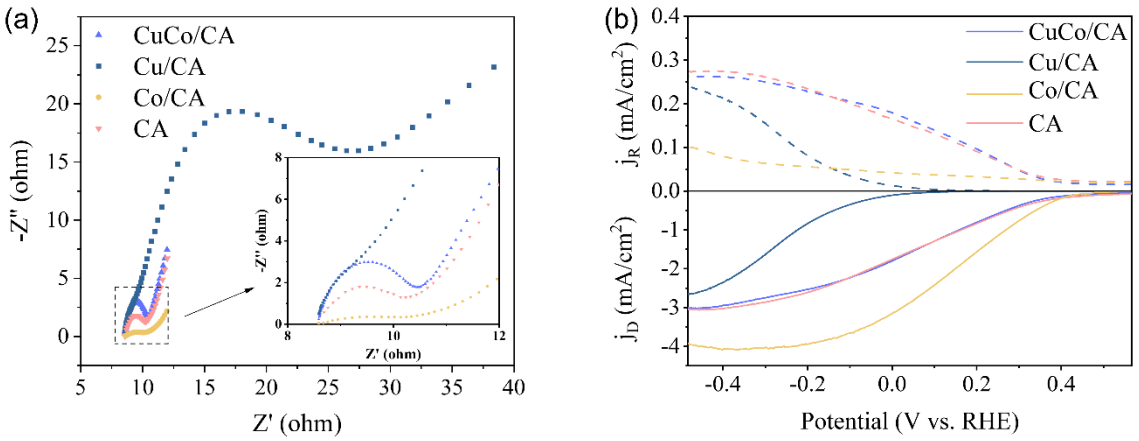

Figure 4.5. (a) EIS Nyquist plots; (b) Polarisation curves of different electrodes at 1600 rpm and simultaneous H_2O_2 oxidation currents at the ring electrode in 0.1 mol/L Na_2SO_4 at pH = 3.

To further investigate the synergistic effect of Cu and Co on ORR activity and selectivity, a rotating ring-disk electrode was used to evaluate ORR performance at 1600 rpm. Fig. 4.5 (b) shows oxygen reduction currents observed on the disk electrode and the corresponding H_2O_2 oxidation currents measured at 1.3 V on the ring electrode. Linear sweep voltammetry (LSV) outcome reveals that CuCo/CA and pure CA have very similar ORR performance, which may be due to their similar porosity characteristics. The ORR half-wave potential ($E_{1/2}$) of CuCo/CA, Cu/CA, Co/CA and pure CA were measured as 0.056 V, −0.265 V, 0.144 V and 0.047 V (vs. RHE), respectively. The results show that addition of Co to Cu/CA increased ORR activity, reflected by a 321 mV positive shift in the half-wave potential [60]. Co/CA exhibits the highest ORR activity due to the most positive half-wave potential; however, it has the lowest 2 e^- ORR selectivity due to the lowest ring current density tested. On the other hand, the incorporation of Cu enhances the selectivity for 2e^- ORR, as the ring current exhibits significant increases for CuCo/CA electrode compared to Co/CA. The enhanced ORR properties are attributed to the fact that the synergistic effect of Cu and Co enables carbon aerogel to form a unique microstructure during the synthesis process, with abundant carbon defects and oxygen functional groups. The synergistic effect of the two metals offsets the shortcomings of the single metal. Overall, CuCo/CA has outstanding performance in both ORR activity and selectivity, so it can catalyse the heterogeneous electro-Fenton system to potentially achieve the highest pollutant removal efficiency.

4.4.2 Hetero electro-Fenton performance

4.4.2.1 Degradation performance and radical generation

Utilising tetracycline (TC) as a candidate pollutant, enabled the performance of different heterogeneous electro-Fenton systems to be evaluated. As depicted in Fig. S4.3 (a), pseudo-first-order kinetic plots for TC removal were observed for the synthesised cathodes under neutral pH conditions. The corresponding kinetic rate constant in the CuCo/CA EF system was 0.988 h^{-1}, which was 2.16, 2.06 and 2.21 times as fast as Cu/CA (0.457h^{-1}), Co/CA (0.481 h^{-1}) and pure CA (0.447 h^{-1}), respectively (Fig. S4.3 (b)). The electro-sorption (ES) of these porous cathodes was further investigated at an operating current of 1 mA and under an N_2 atmosphere, where oxidative degradation could not contribute to TC removal. As shown in Fig. 4.6 (a) (dashed lines), pure CA electrode (characterised by distinctive porous structure and highest surface area) exhibited the highest adsorption capability of 65%. In contrast, the ES capacity of CuCo/CA electrode almost reached 50% after 2.5 h, potentially due to its smaller specific surface area [61]. Notably, TC degradation employing CuCo/CA electrode increased significantly up to 93% (Fig. 4.6 (a)-solid lines) after 2.5 h. This was indicative of high reactivity for both adsorption and oxidative degradation pathways in the CuCo/CA EF system. In comparison, TC removal rate with pure CA, Co/CA and Cu/CA in EF systems was 70%, 67% and 65%, respectively, which demonstrated TC removal using these cathodes was mainly ascribed to their high electro-sorption capacities. Since the synergistic effect of Cu and Co transition metals on carbon aerogel greatly enhances the catalytic performance, the impact of Cu/Co metal ratio was further investigated, as shown in Fig. S4.4. The $Cu_{0.5}Co_{0.5}$/CA electrode, with an optimal Cu/Co ratio of 1.0, achieved the highest TC removal efficiency of 90%. Within 150 min, the TC removal efficiencies for $Cu_{0.3}Co_{0.7}$/CA and $Cu_{0.7}Co_{0.3}$/CA electrodes were 60.6% and 68%, respectively.

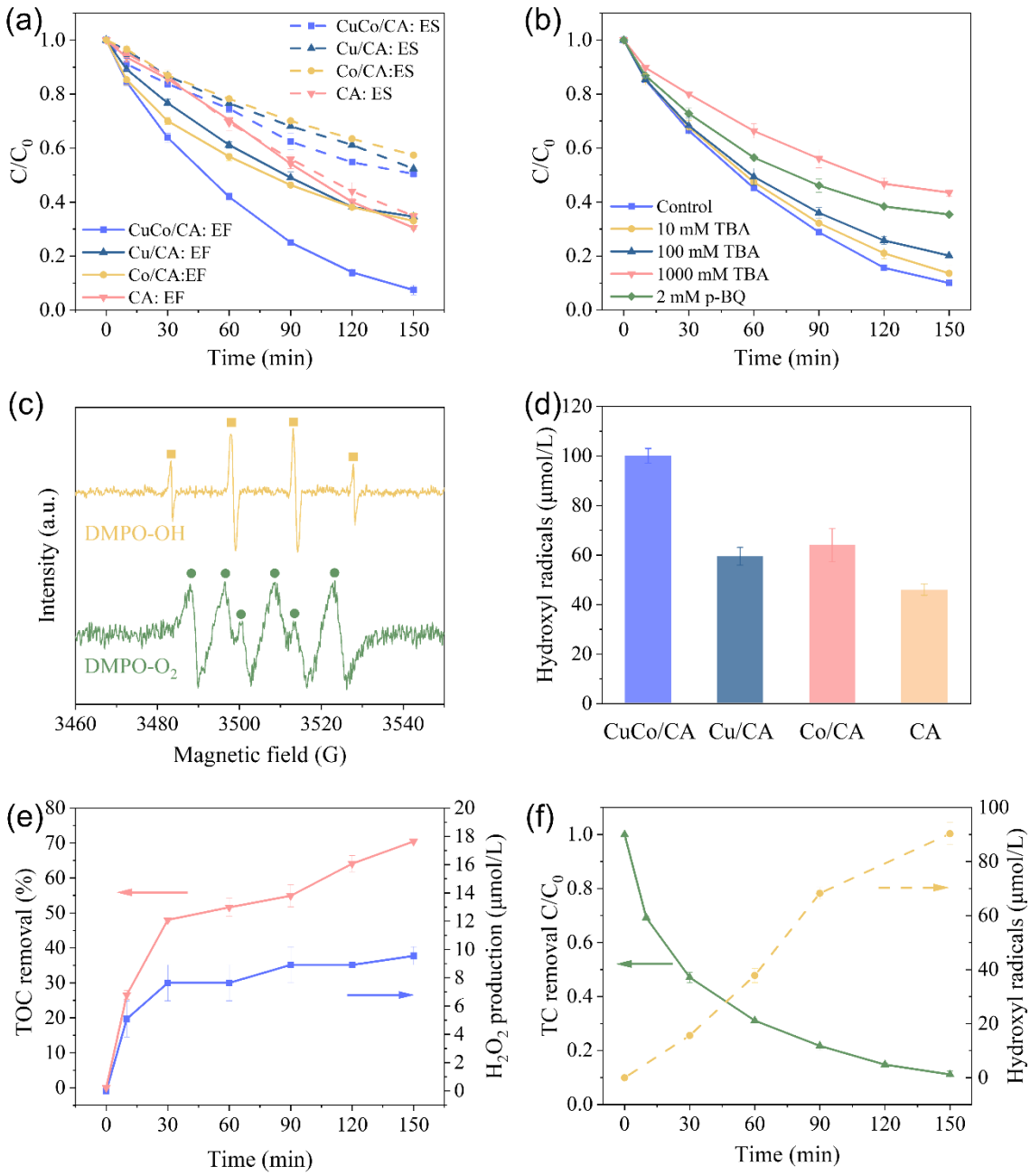

Figure 4.6. (a) TC removal in electro-sorption (ES) and electro-Fenton (EF) systems; (b) Effect of radical scavengers on TC degradation in CuCo/CA EF system; (c) ESR spectra for CuCo/CA EF system; (d) Production of hydroxyl radical after 150 min; (e) TOC removal (left) and H_2O_2 production (right) in CuCo/CA EF system. Conditions: pH_0 7.0, Na_2SO_4 50 mM, TC 10 mg/L, salicylic acid 0.01 M, no external aeration and 20 mA for EF systems, 0.2 L/min N_2 and 1 mA for ES systems. (f) TC removal (left) and hydroxyl radical generation (right) in the presence of CuCo/CA powder (0.2 g/L) and externally supplied H_2O_2 (50 ppm).

Moreover, electricity consumptions of EF processes based on CuCo/CA, Cu/CA, Co/CA and pure CA cathodes were evaluated according to Equation 4.5 [62].

$$EC_{TC}(kWh/kg_{TC}) = I \cdot V \cdot t / \Delta m_{TC} \quad (4.5)$$

where EC_{TC} (kWh/kg_{TC}) is electricity consumption per kg TC degradation, I is current (A), V is average voltage (V), t is reaction time (h), Δm_{TC} is TC mass loss (g). The average commercial electricity price in the UK is £0.27 /kWh in 2024 [63]. As shown in Table 4.2, the CuCo/CA-based EF system demonstrates exceptional electrocatalytic efficiency for TC degradation, achieving the least electricity consumption. Importantly, the energy consumption for degrading each kilogram of TC in the CuCo/CA EF system requires only approximately one-fifth of that for previously reported electro-Fenton systems [64], indicating the practical application potential of this process.

Table 4.2. Electricity consumption and cost in various EF systems. Conditions: pH_0-7.0, Na_2SO_4-50 mM, TC-10 mg/L, 20 mA.

EF system	I (A)	$V_{average}$ (V)	t (h)	Δm_{TC} (g)	EC_{TC} (kWh/kg_{TC})	Electricity cost (£/kg_{TC})
CuCo-CA	0.02	2.375	2.5	1.3875×10^{-3}	85.59	23.11
Cu-CA	0.02	2.642	2.5	0.981×10^{-3}	134.66	36.36
Co-CA	0.02	2.471	2.5	1.005×10^{-3}	122.94	33.19
CA	0.02	2.495	2.5	1.0425×10^{-3}	119.66	32.31

To further elucidate reactive species involved in the oxidative degradation of TC in a CuCo/CA EF system, tert-butanol (TBA) was used as a ·OH radical scavenger. TBA was chosen because of its high rate constant with ·OH radical ($k = 6.0 \times 10^8$ $M^{-1}s^{-1}$) [65]. The results in Fig. 4.6 (b) show that the TC degradation rate gradually decreased with increasing TBA dosage. The reaction rate constant decreased from 0.847 h^{-1} to 0.364 h^{-1} with the addition of 1 M TBA into the system (Fig. S4.5), demonstrating the key role of ·OH radicals in the oxidative degradation of TC. P-benzoquinone (p-BQ) has also been used as a $\cdot O_2^-$ radical scavenger with a high rate constant with $\cdot O_2^-$ ($k = 0.9$–1.0×10^9 $M^{-1}s^{-1}$) [66]. Our results showed that addition of p-BQ led to a drop in TC degradation rate from 87% to 65%. These results suggest that O_2 initially undergoes reduction to an $\cdot O_2^-$ radical intermediate *via* a one-electron pathway, which is then followed by further reduction to H_2O_2, and subsequently ·OH [53]. Furthermore, electron spin resonance (ESR) spectroscopy was used with DMPO as a spin-trapping agent to

directly prove the generation of ·OH and $\cdot O_2^-$ radicals in the CuCo/CA EF process. As shown in Fig. 4.6 (c), the characteristic peak with intensity ratio of 1:2:2:1 corresponding to DMPO-·OH adduct was observed in an EF system utilising CuCo/CA as the cathode, thereby confirming the generation of ·OH species [45]. The sextuplet ESR signal of DMPO-$\cdot O_2^-$ spin adduct was also detected [67], which is consistent with the results of quenching experiments. The effective degradation of TC in CuCo/CA EF system was primarily induced by an indirect oxidation process in the presence of O_2, which is dominated by ·OH species. Under the attack of ·OH radicals, a total organic carbon (TOC) removal efficiency of 70.46% after 2.5 h was achieved under optimal operating conditions (Fig. 4.6 (e), left axis), demonstrating the system's ability to effectively break down the pollutants into mineralised products.

The concentration of electro-generated ·OH was also quantified using the probe reaction of salicylic acid and ·OH [68]. As shown in Fig. 4.6 (d), the accumulated concentration of ·OH in CuCo/CA EF system was determined to be 100.1 μ mol/L after 150 min without external aeration. In comparison, the production of ·OH in EF systems using Cu/CA, Co/CA and pure CA cathode reached 59.3 μ mol/L, 63.9 μ mol/L and 45.9 μ mol/L, respectively. This result further indicates that the removal of TC with Cu/CA, Co/CA and pure CA is mainly through electro-sorption processes. Table S4.1 summarises ·OH production rate in various electro-Fenton systems [69–75], showing that the CuCo/CA based EF system has a stronger ability to generate ·OH radicals than these previously reported EF systems, indicating that the proposed system has great application prospects in oxidative degradation of organic contaminants.

Previous studies have indicated that H_2O_2 can be electro-generated *via* two-electron ORR pathways on carbon-based materials [76]. However, the concentration of accumulated H_2O_2 over CuCo/CA was negligible, measured at 8.9 μmol/L within 2 h (Fig. 4.6 (e), right axis). Such an observation may be attributed to its rapid on-site decomposition into reactive ·OH intermediates [52]. Additionally, in an undivided electro-Fenton system, the generated H_2O_2 can undergo chemical or electrochemical decomposition via disproportionation ($H_2O_2 \rightarrow H_2O+1/2O_2$) and reduction at the cathode ($H_2O_2+2e^- \rightarrow 2OH^-$) [77]. The plateau indicates that a steady-state balance is reached between H_2O_2 generation and its consumption or decomposition, which highlighted the

system's efficiency in maintaining active hydroxyl radical generation for pollutant degradation. Similar research findings also suggest that alloy particles encapsulated within carbon matrix enable modulation of local electronic environment, facilitating the activation of H_2O_2 via a $1e^-$ pathway to generate OH radicals [78]. To investigate whether CuCo/CA participated in the activation process of H_2O_2, TC degradation and ·OH generation efficiency were measured in a system comprised of CuCo/CA powder and externally added H_2O_2. Fig. 4.6 (f) shows that TC removal reached 89% and 90 μ mol/L of ·OH radical was generated at 150 min reaction time, in the presence of 50 ppm H_2O_2 and 0.2 g/L CuCo/CA nanoparticles. Hence, it could be inferred that the CuCo/CA cathode can not only induce $2e^-$ electrochemical process of oxygen reduction to produce H_2O_2, but also catalyse *in situ* activation of H_2O_2 to generate ·OH species further leading to TC degradation.

4.4.2.2 Optimisation of operational conditions

In addition to inherent characteristics of the electrode, reaction conditions such as current density, pH value and aeration rate play a crucial role in the degradation efficiency of contaminants in EF systems. Fig. 4.7 (a) shows that the increase in current density accelerated electron transfer rate in ORR process, however, excessive current and cathode potential led to side reactions such as hydrogen evolution ($2H^+ + 2e^- \rightarrow H_2$) and four-electron reduction of oxygen as shown in Equation 4.6 [79]. Within 150 min, TC removal reached its highest level of 90% at a current of 20 mA. However, continuing to increase current to 30 mA and 40 mA led to a reduction in TC degradation, dropping to 82% and 74%, respectively. This change might be due to occurrence of side reactions utilising part of the electrical energy. Acidic pH conditions, especially pH of 3, were more conducive to TC degradation in the CuCo/CA EF system (Fig. 4.7 (b)). This is because the generation of H_2O_2 and ·OH required participation of H^+, as depicted in Equations 4.1, 4.7, respectively. The highest first-order reaction rate constant of 1.08 h^{-1} was obtained under pH 3 condition, while TC degradation still reached 82%, 88% and 86% under pH conditions of 5, 7 and 9, respectively. These results demonstrated that the electro-Fenton system with CuCo/CA cathode has good adaptability to a wide range of pH conditions.

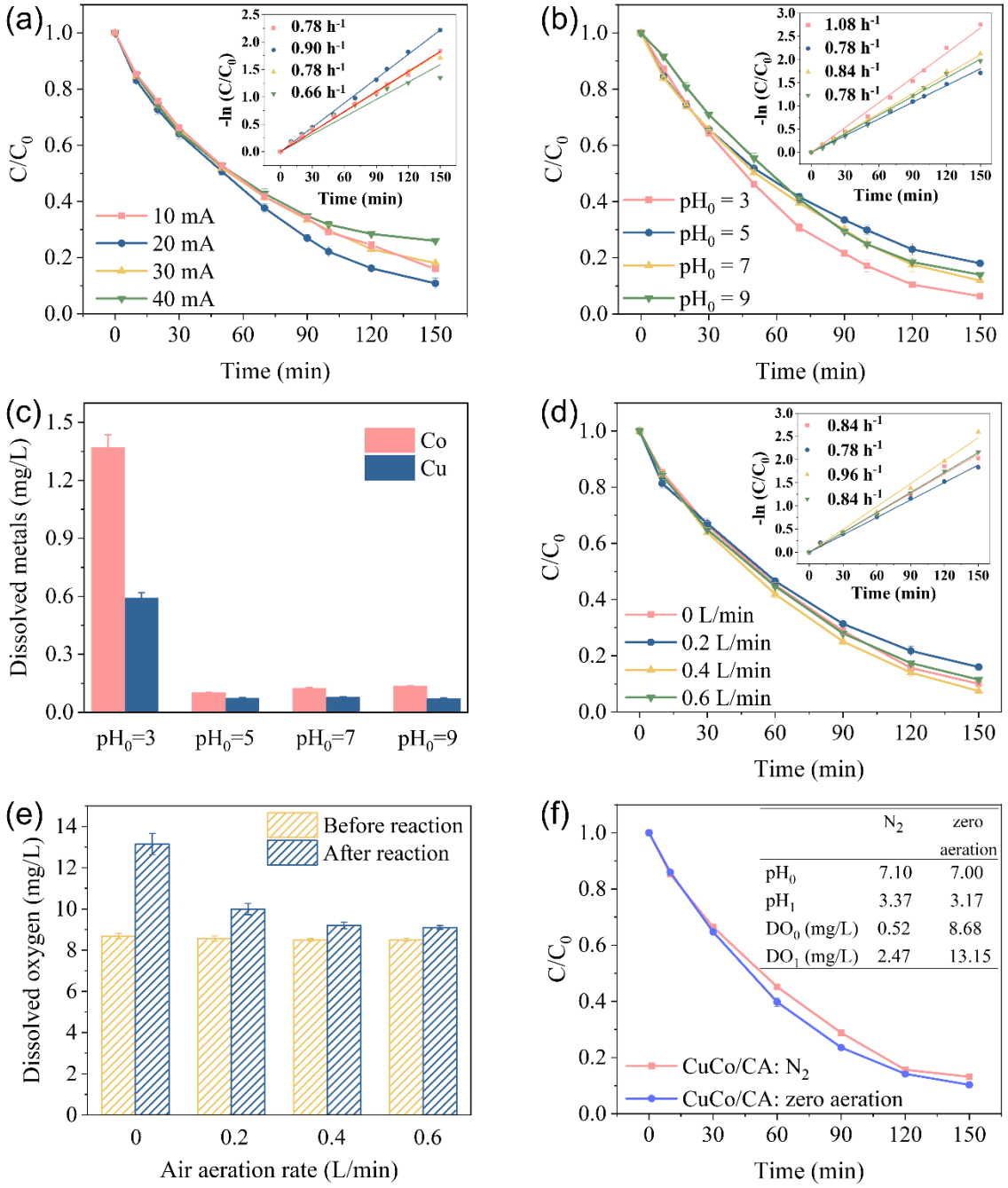

Figure 4.7. Impact of (a) current (the corresponding voltage ranges are: 10 mA: 1.65–2.30 V, 20 mA: 2.00–2.75 V, 30 mA: 2.42–3.02 V, 40 mA: 2.74–3.51 V) and (b) initial pH in CuCo/CA EF system; (c) Metal leaching after 2.5 h reaction in CuCo/CA EF system; (d) Impact of airflow rate in CuCo/CA EF system; (e) Concentration of dissolved oxygen in CuCo/CA EF system; (f) Degradation of TC under an N_2 atmosphere and zero aeration. Inserted graphs are pseudo-first-order kinetic models with rate constants. Conditions: Na_2SO_4 = 50 mM, ACT = 10 mg/L, 200 mL/min N_2 for N_2 experiment.

Furthermore, the amount of leached copper ions and cobalt ions at various pH values were recorded in Fig. 4.7 (c), as well as further information in Fig. S4.6. Although strong acidic condition (pH 3) did lead to a notable release of Co ions initially, assessed as 1.37 ppm

after 2.5 h reaction, results in Fig. S4.7 indicated that dissolution of metal ions significantly reduced in the second and third rounds of recycling runs. In the third run, leaching of Co and Cu ions after 150 min reaction time reduced to 0.21 ppm and 0.26 ppm, respectively. Under other pH conditions (such as pH 5, 7 and 9), dissolution of metal ions was also negligible whilst achieving considerable degradation performance (Fig. 4.7 (c)).

$$O_2+2H_2O+4e^- \rightarrow 4OH^- \quad E^0=1.23\ V\ vs.\ RHE \tag{4.6}$$

$$H_2O_2+e^-+H^+ \rightarrow \cdot OH+H_2O \tag{4.7}$$

The impact of airflow rate on TC removal efficiency was further examined and found to be negligible (Fig. 4.7 (d)). The observed rate constants (inset) at airflow rates of 0, 0.2, 0.4 and 0.6 L/min were measured as 0.84, 0.78, 0.96 and 0.84 h^{-1}, respectively. The results indicated that TC can be effectively eliminated even without external aeration, achieving approximately 90% decomposition within 2.5 h reaction time. The dissolved oxygen (DO) was measured before and after treatment under various air flow rates, as shown in Fig. 4.7 (e). Interestingly, following EF reaction, DO concentration in the system without external aeration increased from 8.68 mg/L to 13.15 mg/L, while pH decreased from 7.0 to 3.17 (Fig. 4.7 (f)). As shown by Equation 4.8 [80], oxygen evolution reaction (OER) occurring near the anode could provide sufficient oxygen for the non-aerated system to complete electro-Fenton process, which led to efficient degradation of TC even without external aeration. Similar oxygen generation mechanisms from OER anode, even in the absence of aeration, have been reported in other electrochemical systems as well [81]. In addition, continuously generated H^+ ions caused a drop in pH value; the pH dropped from 7.0 to 3.2 after 2.5 h reaction time and remained more or less stable at around 3.2 (see Fig. S4.8). The subsequent formation of H_2O_2 and ·OH radicals *via* $2e^-$ and $1e^-$ reduction pathways required the involvement of H^+ ions. Consequently, maintaining a constant H^+ ion concentration was conducive to the generation of H_2O_2 and ·OH radicals.

$$2H_2O \rightarrow 4e^-+4H^++O_2 \tag{4.8}$$

In order to investigate OER activity and oxygen transfer efficiency at the solid–liquid interface i.e., between electrolyte and electrode, a heterogeneous electro-Fenton TC degradation experiment was carried out under a nitrogen (N_2) atmosphere. The reactor was aerated with N_2 for 20 min to strip out as much dissolved oxygen as possible. DO concentration before reaction (DO_0) was 0.52 mg/L and increased to 2.47 mg/L after

reaction (DO_1), while the solution pH decreased from 7.10 to 3.37 (Fig. 4.7 (f)), demonstrating that OER still occurred under an N_2 atmosphere. This system was still able to achieve similar TC degradation to the zero-aeration system, which was around 90% removal after 150 min reaction time. These results indicate that once O_2 is generated near the anode it may be transferred through the solution and, at the solid–liquid interface, undergo a reduction process at the cathode even at low DO levels. The CuCo/CA cathode, characterised by its substantial surface area and pore volumes, facilitated the adsorption, storage and mass transfer of dissolved O_2, thus promoting efficient utilisation of O_2 and electro-generation of H_2O_2 [82]. As a result, the oxygen produced at the anode proved adequate for sustaining H_2O_2 generation without the need for external aeration. This approach may be more cost-effective in comparison with previous electrochemical H_2O_2 generation methods requiring external aeration [4,68,83,84].

In summary, the synergistic effect of Cu and Co within CuCo/CA EF system can be ascribed to following aspects: (1) Structural improvements. CuCo/CA features a large surface area and a structure with coexistence of micropores and mesopores, offering a number of active sites to promote more efficient interactions with contaminant molecules and leading to improved oxygen reduction reaction. The mesopores also function as gas transport channels, enhancing oxygen transport and promoting electrolyte penetration into the carbon matrix. (2) Enhanced electrocatalytic activity. Cu and Co are embedded in carbon aerogel, catalysing the graphitisation process of carbon matrix and leading to faster electron transfer. Furthermore, the introduction of CuCo alloy induces formation of carbon defects, which modify electronic structure and greatly boost its electrocatalytic performance. (3) Enhanced selectivity and activity of oxygen reduction. Presence of graphitic carbon promotes the generation of oxygen-containing group, which aid in oxygen reduction process. Moreover, the co-existence of Cu and Co results in lattice distortion and electronic environment adjustment that further enhance both selectivity and activity of ORR.

Based on above findings, the mechanisms for oxygen species production and TC degradation are illustrated in Fig. 4.8. Initially, oxygen evolution and accumulation take place near the anode, which are induced by an electric current effect. The produced oxygen subsequently diffuses to interface of electrolyte and cathode, where it goes

through a $2e^-$ reduction pathway to produce H_2O_2. The excellent pore structure of CuCo/CA electrode achieves efficient oxygen transport and utilisation and eliminates the need for additional oxygen input to produce H_2O_2. Moreover, H^+ ions produced through oxygen evolution process establish an advantageous pH condition for $2e^-$ oxygen reduction and *in situ* H_2O_2 activation. Catalytically active Cu^+ and Co^{2+} on CuCo/CA cathode catalyse H_2O_2 activation on-site to produce highly oxidative ·OH radicals, thus enabling oxidative degradation of organic contaminants in water. Then, Cu^{2+} and Co^{3+} can subsequently be reduced back to Cu^+ and Co^{2+} at the cathode, completing the redox cycle. This cycle promotes continuous activation of H_2O_2 and enhances the overall efficiency of the electro-Fenton system.

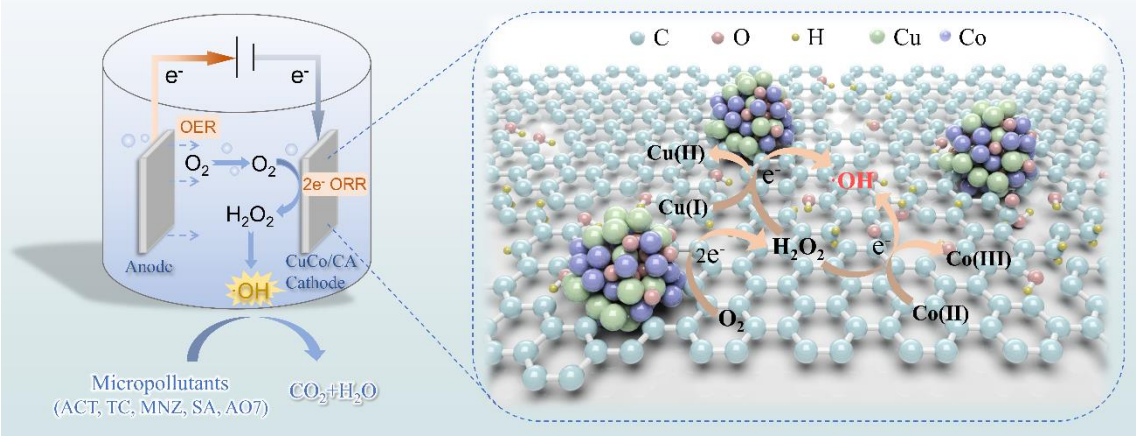

Figure 4.8. Schematic of mechanisms for radical generation in CuCo/CA EF system.

4.4.3 Recyclability, stability, and broad applicability of CuCo/CA

In order to evaluate recyclability of the CuCo/CA cathode, six consecutive electro-Fenton TC degradation experiments were conducted. The results are shown in Fig. 4.9 (a), in which the overall difference in TC degradation rates was very small. After six runs, the CuCo/CA electro-Fenton system achieved 84% TC removal within 150 min with a slight drop in the reaction rate constant (see Fig. S4.9). These results suggest that CuCo/CA, as an integrated electrode, could maintain stability during electro-Fenton process and retain good performance. The stability of the CuCo/CA cathode was further investigated in Fig. 4.9 (b) using a continuous stirred tank reactor (CSTR, Fig. 4.9 (c)) for a 48-h experiment under different flow velocities and initial TC concentrations. The results show that the CuCo/CA EF system with a slower flow rate and a lower TC concentration achieved higher removal performance due to longer hydraulic retention time. The electrocatalytic performance of CuCo/CA in all three systems was relatively stable over 48 h reaction

time, despite a slightly reduced TC removal rate towards the end. This consistency in performance may due to the corrosion-resistant property of carbon-based aerogel material, with bimetallic particles well protected by outer carbon [53].

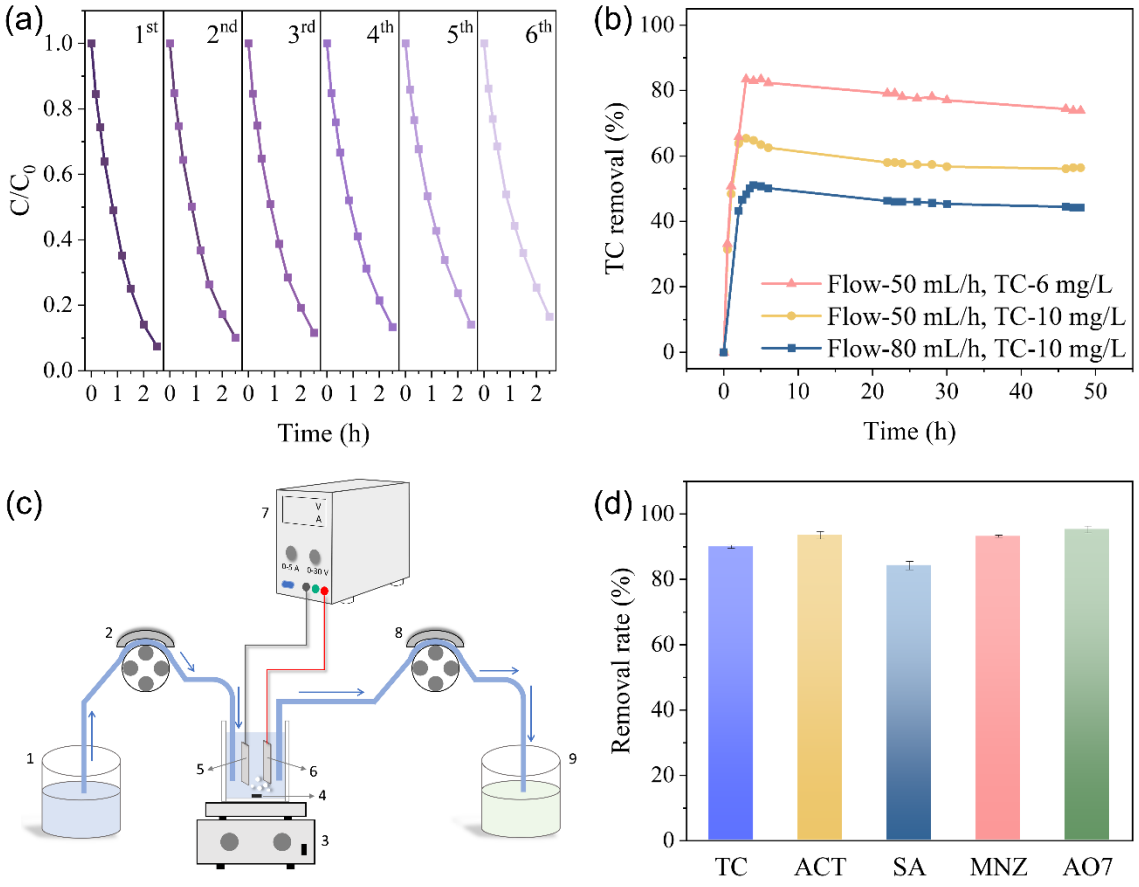

Figure 4.9. (a) TC degradation in 6 consecutive CuCo/CA EF system runs; (b) TC removal during 48 h continuous stirred CuCo/CA EF system runs at varying fluid flow velocity; (c) Schematic diagram of the continuously stirred electro-Fenton reaction system: 1- Feed TC stock solution, 2 and 8 peristaltic pump, 3 − magnetic stirrer, 4 − PTFE stirrer bar, 5 − CuCo/CA cathode, 6 − platinum anode, 7 − DC power supply, 9 − post-reactor flow; and (d) The removal rate of various micropollutants in CuCo/CA EF system after 150 min. Conditions: pollutant = 10 mg/L, Na_2SO_4 = 50 mM, pH_0 = 7.0, 20 mA, zero aeration.

Further, the broad applicability of the CuCo/CA cathode was evaluated by investigating its degradation efficiency with various organic contaminants including antibiotics, analgesic, organic acid, and dye. Results in Fig. 4.9 (d) and Fig. S4.10 (a) show that the removal rates of tetracycline (TC), acetaminophen (ACT), metronidazole (MNZ), salicylic acid (SA) and acid orange 7 (AO7) were 90%, 94%, 93%, 84% and 95%, respectively, after 2.5 h reaction time. Pseudo-first-order plots were observed for all contaminant removal experiments, shown in Fig. S4.10 (b). The CuCo/CA EF system exhibited the highest apparent rate constant for MNZ removal, which was 1.12 h^{-1} (Fig.

S4.10 (c)). This performance highlights the relatively wide applicability of CuCo/CA electrodes in an EF system for oxidative decomposition of various organic pollutants in water.

The above results indicate that CuCo/CA not only possessed high oxygen reduction catalytic activity but also exhibited long-term stability and recyclability. It demonstrates the desired removal efficiency for various organic pollutants, suggesting significant practical applications for water environmental remediation.

4.5 Conclusions

In this study, we have reported a novel electro-Fenton approach for selective $2e^-$ ORR and activation of *in situ* generated H_2O_2 using an integrated CuCo/CA cathode. The integration of Cu and Co into the carbon matrix enhanced the electro-generation of H_2O_2, conductivity, mass transfer, and oxygen reduction activity. The oxygen evolution process around the Pt anode provided advantageous pH conditions and oxygen supply for H_2O_2 production and radical generation near the cathode. As catalytically active metal components, Cu(I) and Co(II) imparted an additional role to CuCo/CA as an integrated catalyst inducing on-site H_2O_2 activation to form reactive ·OH species. Consequently, the established heterogeneous EF system exhibited promising TC removal (94%) within 2.5 h at pH 7 and a current density of 4.4 mA/cm^2. The High efficiency of CuCo/CA cathode in utilising oxygen eliminated the need for external aeration, which has greater industrial applicability compared to previously reported EF systems that require external aeration. The efficient degradation of TC primarily occurred through an indirect oxidation process dominated by ·OH radical. Importantly, ideal degradation efficiencies have been achieved over a wide pH range of 3–9, and CuCo/CA demonstrated good recyclability after six runs, and long-term stability after 48 h for continuous TC removal. Finally, the proposed technology exhibited high electrocatalytic activity towards various micropollutants. This research therefore offers an eco-friendly and sustainable approach to degrading persistent organic contaminants, presenting potential for advancing water decontamination technologies.

4.6 Acknowledgements

Qian Ye is funded by the China Scholarship Council (CSC, 202106240065) from the

Ministry of Education of P.R. China. The authors are grateful to the funders and acknowledge their support of this work. The authors wish to express their gratitude to colleagues at the University of Leeds for their invaluable assistance: Dr. Jeanine Williams (HPLC), Ms. Karine Alves Thorne (metal loading analysis), and Dr. Ben Douglas (BET measurement). Special thanks are also due to Dr. David Elliott, Mr. Morgan McGowan, and Ms. Emma Tidswell for their guidance on laboratory equipment and technical support.

4.7 References

[1] A.K. Sarmah, M.T. Meyer, A.B.A. Boxall, A global perspective on the use, sales, exposure pathways, occurrence, fate and effects of veterinary antibiotics (VAs) in the environment, Chemosphere 65 (2006) 725–759. https://doi.org/10.1016/j.chemosphere.2006.03.026.

[2] D. Qiao, Z. Li, J. Duan, X. He, Adsorption and photocatalytic degradation mechanism of magnetic graphene oxide/ZnO nanocomposites for tetracycline contaminants, Chemical Engineering Journal 400 (2020) 125952. https://doi.org/10.1016/j.cej.2020.125952.

[3] M. Zhang, Y.-S. Liu, J.-L. Zhao, W.-R. Liu, L.-Y. He, J.-N. Zhang, J. Chen, L.-K. He, Q.-Q. Zhang, G.-G. Ying, Occurrence, fate and mass loadings of antibiotics in two swine wastewater treatment systems, Science of The Total Environment 639 (2018) 1421–1431. https://doi.org/10.1016/j.scitotenv.2018.05.230.

[4] P. Dong, X. Chen, M. Guo, Z. Wu, H. Wang, F. Lin, J. Zhang, S. Wang, C. Zhao, H. Sun, Heterogeneous electro-Fenton catalysis with self-supporting CFP@MnO2-Fe3O4/C cathode for shale gas fracturing flowback wastewater, Journal of Hazardous Materials 412 (2021) 125208. https://doi.org/10.1016/j.jhazmat.2021.125208.

[5] F. Sopaj, N. Oturan, J. Pinson, F. Podvorica, M.A. Oturan, Effect of the anode materials on the efficiency of the electro-Fenton process for the mineralization of the antibiotic sulfamethazine, Applied Catalysis B: Environmental 199 (2016) 331–341. https://doi.org/10.1016/j.apcatb.2016.06.035.

[6] E. Mousset, L. Frunzo, G. Esposito, E.D. van Hullebusch, N. Oturan, M.A. Oturan, A complete phenol oxidation pathway obtained during electro-Fenton treatment and validated by a kinetic model study, Applied Catalysis B: Environmental 180 (2016) 189–198. https://doi.org/10.1016/j.apcatb.2015.06.014.

[7] Y. Zhu, F. Deng, S. Qiu, F. Ma, Y. Zheng, L. Gao, A self-sufficient electro-Fenton system with enhanced oxygen transfer for decontamination of pharmaceutical wastewater, Chemical Engineering Journal 429 (2022) 132176. https://doi.org/10.1016/j.cej.2021.132176.

[8] L. Cui, H. Huang, P. Ding, S. Zhu, W. Jing, X. Gu, Cogeneration of H2O2 and OH via a novel Fe3O4/MWCNTs composite cathode in a dual-compartment electro-Fenton membrane reactor, Separation and Purification Technology 237 (2020) 116380. https://doi.org/10.1016/j.seppur.2019.116380.

[9] P. Cao, X. Quan, K. Zhao, S. Chen, H. Yu, Y. Su, High-Efficiency Electrocatalysis of Molecular Oxygen toward Hydroxyl Radicals Enabled by an Atomically Dispersed Iron Catalyst, Environ. Sci. Technol. 54 (2020) 12662–12672. https://doi.org/10.1021/acs.est.0c03614.

[10] K. Liu, J.C.-C. Yu, H. Dong, J.C.S. Wu, M.R. Hoffmann, Degradation and mineralization of carbamazepine using an electro-Fenton reaction catalyzed by magnetite nanoparticles fixed on an electrocatalytic carbon fiber textile cathode, Environ. Sci. Technol. 52 (2018) 12667–12674. https://doi.org/10.1021/acs.est.8b03916.

[11] L. Cui, Z. Li, Q. Li, M. Chen, W. Jing, X. Gu, Cu/CuFe2O4 integrated graphite felt as a stable bifunctional cathode for high-performance heterogeneous electro-Fenton oxidation, Chemical Engineering Journal 420 (2021) 127666. https://doi.org/10.1016/j.cej.2020.127666.

[12] C. Jin, Y. Cui, G. Zhang, W. Luo, Y. Liu, Y. Sun, Z. Tian, W. Zheng, Synthesis of copper-cobalt hybrid oxide microflowers as electrode material for supercapacitors,

Chemical Engineering Journal 343 (2018) 331–339. https://doi.org/10.1016/j.cej.2018.02.117.

[13] M. Huo, B. Wang, C. Zhang, S. Ding, H. Yuan, Z. Liang, J. Qi, M. Chen, Y. Xu, W. Zhang, H. Zheng, R. Cao, 2D Metal–Organic Framework Derived CuCo Alloy Nanoparticles Encapsulated by Nitrogen-Doped Carbonaceous Nanoleaves for Efficient Bifunctional Oxygen Electrocatalyst and Zinc–Air Batteries, Chemistry – A European Journal 25 (2019) 12780–12788. https://doi.org/10.1002/chem.201902389.

[14] X. Feng, X. Yin, X. Bo, L. Guo, An ultrasensitive luteolin sensor based on MOFs derived CuCo coated nitrogen-doped porous carbon polyhedron, Sensors and Actuators B: Chemical 281 (2019) 730–738. https://doi.org/10.1016/j.snb.2018.11.010.

[15] Y. Liu, Z. Yang, J. Wang, Fenton-like degradation of sulfamethoxazole in Cu0/Zn0-air system over a broad pH range: Performance, kinetics and mechanism, Chemical Engineering Journal 403 (2021) 126320. https://doi.org/10.1016/j.cej.2020.126320.

[16] Y. Zou, H. Qi, Z. Sun, In-situ catalytic degradation of sulfamethoxazole with efficient CuCo–O@CNTs/NF cathode in a neutral electro-Fenton-like system, Chemosphere 296 (2022) 134072. https://doi.org/10.1016/j.chemosphere.2022.134072.

[17] H. Afanga, H. Zazou, F.E. Titchou, J.E. Gaayda, F. Sopaj, R.A. Akbour, M. Hamdani, Electrochemical oxidation of Naphthol Blue Black with different supporting electrolytes using a BDD /carbon felt cell, Journal of Environmental Chemical Engineering 9 (2021) 104498. https://doi.org/10.1016/j.jece.2020.104498.

[18] G. Gan, X. Li, S. Fan, L. Wang, M. Qin, Z. Yin, G. Chen, Carbon aerogels for environmental clean-up, European Journal of Inorganic Chemistry 2019 (2019) 3126–3141. https://doi.org/10.1002/ejic.201801512.

[19] D. Li, T. Zheng, Y. Liu, D. Hou, K.K. Yao, W. Zhang, H. Song, H. He, W. Shi, L. Wang, J. Ma, A novel Electro-Fenton process characterized by aeration from inside a graphite felt electrode with enhanced electrogeneration of H2O2 and cycle of Fe3+/Fe2+, Journal of Hazardous Materials 396 (2020) 122591. https://doi.org/10.1016/j.jhazmat.2020.122591.

[20] H. Zhao, L. Qian, Y. Chen, Q. Wang, G. Zhao, Selective catalytic two-electron O2 reduction for onsite efficient oxidation reaction in heterogeneous electro-Fenton process, Chemical Engineering Journal 332 (2018) 486–498. https://doi.org/10.1016/j.cej.2017.09.093.

[21] Q. Ye, T.N. Hunter, H. Xu, D. Harbottle, G.M. Kale, M.R. Tillotson, Synergistic effect of Fe and Ni on carbon aerogel for enhanced oxygen reduction and H2O2 activation in electro-Fenton process, Separation and Purification Technology 353 (2025) 128436. https://doi.org/10.1016/j.seppur.2024.128436.

[22] R. Bardestani, G.S. Patience, S. Kaliaguine, Experimental methods in chemical engineering: specific surface area and pore size distribution measurements—BET, BJH, and DFT, The Canadian Journal of Chemical Engineering 97 (2019) 2781–2791. https://doi.org/10.1002/cjce.23632.

[23] C. Yin, Y. Liu, X. Kang, X. Li, Synergistic degradation of tetracycline by CDs decorated g-C3N4 under LED light irradiation combined with the persulfate-based advanced oxidation process, Applied Catalysis A: General 636 (2022) 118571. https://doi.org/10.1016/j.apcata.2022.118571.

[24] X. Chen, W. Wang, H. Xiao, C. Hong, F. Zhu, Y. Yao, Z. Xue, Accelerated TiO2 photocatalytic degradation of Acid Orange 7 under visible light mediated by peroxymonosulfate, Chemical Engineering Journal 193–194 (2012) 290–295. https://doi.org/10.1016/j.cej.2012.04.033.

[25] J. Wang, J. Deng, E. Du, H. Guo, Reevaluation of radical-induced differentiation in UV-based advanced oxidation processes (UV/hydrogen peroxide, UV/peroxydisulfate, and UV/chlorine) for metronidazole removal: Kinetics, mechanism, toxicity variation, and DFT studies, Separation and Purification Technology 301 (2022) 121905. https://doi.org/10.1016/j.seppur.2022.121905.

[26] G. Daniel, Y. Zhang, S. Lanzalaco, F. Brombin, T. Kosmala, G. Granozzi, A. Wang, E. Brillas, I. Sirés, C. Durante, Chitosan-derived nitrogen-doped carbon electrocatalyst for a sustainable upgrade of oxygen reduction to hydrogen peroxide in UV-assisted electro-Fenton water treatment, ACS Sustainable Chem. Eng. 8 (2020) 14425–14440. https://doi.org/10.1021/acssuschemeng.0c04294.

[27] X. Qin, P. Cao, X. Quan, K. Zhao, S. Chen, H. Yu, Y. Su, Highly efficient hydroxyl radicals production boosted by the atomically dispersed Fe and Co sites for heterogeneous electro-Fenton oxidation, Environ. Sci. Technol. 57 (2023) 2907–2917. https://doi.org/10.1021/acs.est.2c06981.

[28] N.A. Barakat, M. El-Newehy, S.S. Al-Deyab, H.Y. Kim, Cobalt/copper-decorated carbon nanofibers as novel non-precious electrocatalyst for methanol electrooxidation, Nanoscale Res Lett 9 (2014) 2. https://doi.org/10.1186/1556-276X-9-2.

[29] L.M. Pastrana-Martínez, A.M. Regadera-Macías, S. Morales-Torres, F.J. Maldonado-Hódar, Revisiting the influence of metals on resorcinol-formaldehyde carbon gels: Physicochemical properties, transformations and synergism between phases, Inorganica Chimica Acta 535 (2022) 120850. https://doi.org/10.1016/j.ica.2022.120850.

[30] K. Xiao, X. Qi, Z. Bao, X. Wang, L. Zhong, K. Fang, M. Lin, Y. Sun, CuFe, CuCo and CuNi nanoparticles as catalysts for higher alcohol synthesis from syngas: a comparative study, Catal. Sci. Technol. 3 (2013) 1591–1602. https://doi.org/10.1039/C3CY00063J.

[31] F.J. Maldonado-Hódar, C. Moreno-Castilla, J. Rivera-Utrilla, Y. Hanzawa, Y. Yamada, Catalytic graphitization of carbon aerogels by transition metals, Langmuir 16 (2000) 4367–4373. https://doi.org/10.1021/la991080r.

[32] L. Shang, X. Lv, H. Shen, Z. Shao, G. Zheng, Selective carbon dioxide electroreduction to ethylene and ethanol by core-shell copper/cuprous oxide, Journal of Colloid and Interface Science 552 (2019) 426–431. https://doi.org/10.1016/j.jcis.2019.05.073.

[33] Z. Lu, G. Chen, S. Siahrostami, Z. Chen, K. Liu, J. Xie, L. Liao, T. Wu, D. Lin, Y. Liu, T.F. Jaramillo, J.K. Nørskov, Y. Cui, High-efficiency oxygen reduction to hydrogen peroxide catalysed by oxidized carbon materials, Nat Catal 1 (2018) 156–162. https://doi.org/10.1038/s41929-017-0017-x.

[34] M. Mohsenpour, S. Motahari, F. Tajabadi, M. Najafi, Preparation and application of sunlight absorbing ultra-black carbon aerogel/graphene oxide membrane for solar steam generation systems, RSC Advances 10 (2020) 41780–41790. https://doi.org/10.1039/D0RA07522A.

[35] Y. Ping, Y. Zhang, Y. Gong, B. Cao, Q. Fu, C. Pan, Edge-riched graphene nanoribbon for high capacity electrode materials, Electrochimica Acta 250 (2017) 84–90. https://doi.org/10.1016/j.electacta.2017.08.051.

[36] M. Smith, L. Scudiero, J. Espinal, J.-S. McEwen, M. Garcia-Perez, Improving the deconvolution and interpretation of XPS spectra from chars by ab initio calculations, Carbon 110 (2016) 155–171. https://doi.org/10.1016/j.carbon.2016.09.012.

[37] H. Zhao, X. Shen, Y. Chen, S.-N. Zhang, P. Gao, X. Zhen, X.-H. Li, G. Zhao, A

COOH-terminated nitrogen-doped carbon aerogel as a bulk electrode for completely selective two-electron oxygen reduction to H2O2, Chem. Commun. 55 (2019) 6173–6176. https://doi.org/10.1039/C9CC02580D.

[38] S. Wang, L. Zhang, Z. Xia, A. Roy, D.W. Chang, J. Baek, L. Dai, BCN Graphene as Efficient Metal-Free Electrocatalyst for the Oxygen Reduction Reaction, Angew Chem Int Ed 51 (2012) 4209–4212. https://doi.org/10.1002/anie.201109257.

[39] X. Sun, H. Qi, Z. Sun, Bifunctional nickel foam composite cathode co-modified with CoFe@NC and CNTs for electrocatalytic degradation of atrazine over wide pH range, Chemosphere 286 (2022) 131972. https://doi.org/10.1016/j.chemosphere.2021.131972.

[40] M.J. Pinzón C., J.M. de Aquino, R.G. Freitas, G.A. Pereira, L.M. Da Silva, H. Zanin, A comprehensive study about the influence of pore structures of carbon-based electrode materials on the charge-storage processes of water-in-salt based supercapacitors, Journal of Energy Storage 62 (2023) 106858. https://doi.org/10.1016/j.est.2023.106858.

[41] Y.J. Sa, J.H. Kim, S.H. Joo, Active Edge-Site-Rich Carbon Nanocatalysts with Enhanced Electron Transfer for Efficient Electrochemical Hydrogen Peroxide Production, Angewandte Chemie International Edition 58 (2019) 1100–1105. https://doi.org/10.1002/anie.201812435.

[42] J. Zhang, X. Song, P. Li, S. Wang, Z. Wu, X. Liu, An Iron-Based Catalyst with Multiple Active Components Synergetically Improved Electrochemical Performance for Oxygen Reduction Reaction, Catalysts 8 (2018) 243. https://doi.org/10.3390/catal8060243.

[43] P. Cao, K. Zhao, X. Quan, S. Chen, H. Yu, Efficient and stable heterogeneous electro-Fenton system using iron oxides embedded in Cu, N co-doped hollow porous carbon as functional electrocatalyst, Separation and Purification Technology 238 (2020) 116424. https://doi.org/10.1016/j.seppur.2019.116424.

[44] K. Jiao, Z. Kang, B. Wang, S. Jiao, Y. Jiang, Z. Hu, Applying Co3O4@nanoporous Carbon to Nonenzymatic Glucose Biofuel Cell and Biosensor, Electroanalysis 30 (2018) 525–532. https://doi.org/10.1002/elan.201700719.

[45] Q. Ye, H. Xu, Q. Wang, X. Huo, Y. Wang, X. Huang, G. Zhou, J. Lu, J. Zhang, New insights into the mechanisms of tartaric acid enhancing homogeneous and heterogeneous copper-catalyzed Fenton-like systems, Journal of Hazardous Materials 407 (2021) 124351. https://doi.org/10.1016/j.jhazmat.2020.124351.

[46] Y. Wu, T. She, Y. Wang, Z. Xu, T. Huang, Q. Ji, H. Song, S. Yang, S. Li, S. Yan, L. Zhang, H. He, Enhancing cationic superexchange interaction via adjustive lattice distortion in cobalt-based perovskite for improved Fenton-like decontamination, Applied Catalysis B: Environmental 343 (2024) 123569. https://doi.org/10.1016/j.apcatb.2023.123569.

[47] Y. Gao, W. Zhu, J. Liu, P. Lin, J. Zhang, T. Huang, K. Liu, Mesoporous sulfur-doped CoFe2O4 as a new Fenton catalyst for the highly efficient pollutants removal, Applied Catalysis B: Environmental 295 (2021) 120273. https://doi.org/10.1016/j.apcatb.2021.120273.

[48] S.K. Ling, S. Wang, Y. Peng, Oxidative degradation of dyes in water using Co2+/H2O2 and Co2+/peroxymonosulfate, Journal of Hazardous Materials 178 (2010) 385–389. https://doi.org/10.1016/j.jhazmat.2010.01.091.

[49] T. She, Y. Wu, Q. Ji, Z. Xu, Y. Wang, H. Chu, Y. Liu, H. Song, S. Yang, S. Li, L. Zhang, H. He, Passivating surface states of graphitic carbon nitride for improved photocatalytic Fenton-like decontamination, Separation and Purification Technology

329 (2024) 125193. https://doi.org/10.1016/j.seppur.2023.125193.
[50] L. Wei, K. Zhou, H. Li, P. Yang, B. Liu, Cobalt based bimetallic catalysts for heterogeneous electro-Fenton adapting to vary pH for HEDP and MIT degradation, Environmental Technology 0 (n.d.) 1–12. https://doi.org/10.1080/09593330.2024.2356226.
[51] Y. Li, M. Yan, H. Lin, S. Wang, X. Duan, X.-L. Wu, Electrochemical generation of H*-•OH redox pair for rapid removal of refractory nitro-organic micropollutants, Applied Catalysis B: Environment and Energy 361 (2025) 124663. https://doi.org/10.1016/j.apcatb.2024.124663.
[52] X. Shen, F. Xiao, H. Zhao, Y. Chen, C. Fang, R. Xiao, W. Chu, G. Zhao, In situ-formed PdFe nanoalloy and carbon defects in cathode for synergic reduction–oxidation of chlorinated pollutants in electro-Fenton process, Environ. Sci. Technol. 54 (2020) 4564–4572. https://doi.org/10.1021/acs.est.9b05896.
[53] F. Xiao, Z. Wang, J. Fan, T. Majima, H. Zhao, G. Zhao, Selective electrocatalytic reduction of oxygen to hydroxyl radicals via 3-electron pathway with FeCo alloy encapsulated carbon aerogel for fast and complete removing pollutants, Angewandte Chemie International Edition 60 (2021) 10375–10383. https://doi.org/10.1002/anie.202101804.
[54] Z. Xu, F. Zhang, W. Lin, H. Zhang, Polymer network-derived nitrogen/sulphur co-doped three-dimensionally interconnected hierarchically porous carbon for oxygen reduction, lithium-ion battery, and supercapacitor, RSC Adv. 9 (2019) 36570–36577. https://doi.org/10.1039/C9RA07619K.
[55] J. Lu, W. Hao, X. Wu, X. Shen, S. Cui, W. Shi, Electronic Modulation of the 3D Architectured Ni/Fe Oxyhydroxide Anchored N-Doped Carbon Aerogel with Much Improved OER Activity, Gels 9 (2023) 190. https://doi.org/10.3390/gels9030190.
[56] L. Yang, J. Shui, L. Du, Y. Shao, J. Liu, L. Dai, Z. Hu, Carbon-Based Metal-Free ORR Electrocatalysts for Fuel Cells: Past, Present, and Future, Advanced Materials 31 (2019) 1804799. https://doi.org/10.1002/adma.201804799.
[57] C. Chen, Y. Zhu, M. Tian, Y. Chen, Y. Yang, K. Jiang, S. Gao, Sustainable self-powered electro-Fenton degradation using N, S co-doped porous carbon catalyst fabricated with adsorption-pyrolysis-doping strategy, Nano Energy 81 (2021) 105623. https://doi.org/10.1016/j.nanoen.2020.105623.
[58] L. Wang, Y. Zhou, J. Qiu, Influence of pore structures on the electrochemical performance of asphaltene-based ordered mesoporous carbons, Microporous and Mesoporous Materials 174 (2013) 67–73. https://doi.org/10.1016/j.micromeso.2013.02.024.
[59] Y. Chen, S. Ji, S. Zhao, W. Chen, J. Dong, W.-C. Cheong, R. Shen, X. Wen, L. Zheng, A.I. Rykov, S. Cai, H. Tang, Z. Zhuang, C. Chen, Q. Peng, D. Wang, Y. Li, Enhanced oxygen reduction with single-atomic-site iron catalysts for a zinc-air battery and hydrogen-air fuel cell, Nat Commun 9 (2018) 5422. https://doi.org/10.1038/s41467-018-07850-2.
[60] L. Yan, Y. Liu, J. Hou, High-Efficiency Oxygen Reduction Reaction Revived from Walnut Shell, Molecules 28 (2023) 2072. https://doi.org/10.3390/molecules28052072.
[61] A. Lissaneddine, M.-N. Pons, F. Aziz, N. Ouazzani, L. Mandi, E. Mousset, A critical review on the electrosorption of organic compounds in aqueous effluent – Influencing factors and engineering considerations, Environmental Research 204 (2022) 112128. https://doi.org/10.1016/j.envres.2021.112128.
[62] E. Rosales, S. Diaz, M. Pazos, M.A. Sanromán, Comprehensive strategy for the

degradation of anti-inflammatory drug diclofenac by different advanced oxidation processes, Separation and Purification Technology 208 (2019) 130–141. https://doi.org/10.1016/j.seppur.2018.04.014.

[63] Business Electricity Rates UK, Business Electricity Prices (n.d.). https://www.businesselectricityprices.org.uk/ (accessed May 14, 2024).

[64] S. Han, Z. Wang, X. Pi, C. Wu, X. Wang, Y. Wang, X. Liu, H. Zhao, Promotion of tetracycline degradation by electro-Fenton: Controlling the reaction zone by N-doped modified activated carbon cathode, Journal of Cleaner Production 370 (2022) 133524. https://doi.org/10.1016/j.jclepro.2022.133524.

[65] A. Khan, Z. Liao, Y. Liu, A. Jawad, J. Ifthikar, Z. Chen, Synergistic degradation of phenols using peroxymonosulfate activated by CuO-Co3O4@MnO2 nanocatalyst, Journal of Hazardous Materials 329 (2017) 262–271. https://doi.org/10.1016/j.jhazmat.2017.01.029.

[66] C. Qi, X. Liu, J. Ma, C. Lin, X. Li, H. Zhang, Activation of peroxymonosulfate by base: Implications for the degradation of organic pollutants, Chemosphere 151 (2016) 280–288. https://doi.org/10.1016/j.chemosphere.2016.02.089.

[67] Q. Ye, H. Xu, J. Zhang, Q. Wang, P. Zhou, Y. Wang, X. Huang, X. Huo, C. Liu, J. Lu, Enhancement of peroxymonosulfate activation for antibiotics removal by nano zero valent tungsten induced Cu(II)/Cu(I) redox cycles, Chemical Engineering Journal 382 (2020) 123054. https://doi.org/10.1016/j.cej.2019.123054.

[68] X. Qin, P. Cao, X. Quan, K. Zhao, S. Chen, H. Yu, Y. Su, Highly efficient hydroxyl radicals production boosted by the atomically dispersed Fe and Co sites for heterogeneous electro-Fenton oxidation, Environ. Sci. Technol. 57 (2023) 2907–2917. https://doi.org/10.1021/acs.est.2c06981.

[69] J. Deng, J. Lu, Q. Yan, J. Pan, Basic research on chemical mechanical polishing of single-crystal SiC—Electro–Fenton: Reaction mechanism and modelling of hydroxyl radical generation using condition response modelling, Journal of Environmental Chemical Engineering 9 (2021) 104954. https://doi.org/10.1016/j.jece.2020.104954.

[70] D. Kubo, Y. Kawase, Hydroxyl radical generation in electro-Fenton process with in situ electro-chemical production of Fenton reagents by gas-diffusion-electrode cathode and sacrificial iron anode, Journal of Cleaner Production 203 (2018) 685–695. https://doi.org/10.1016/j.jclepro.2018.08.231.

[71] T. Yatagai, Y. Ohkawa, D. Kubo, Y. Kawase, Hydroxyl radical generation in electro-Fenton process with a gas-diffusion electrode: Linkages with electro-chemical generation of hydrogen peroxide and iron redox cycle, Journal of Environmental Science and Health, Part A 52 (2017) 74–83. https://doi.org/10.1080/10934529.2016.1229935.

[72] S. Qiu, D. He, J. Ma, T. Liu, T.D. Waite, Kinetic Modeling of the Electro-Fenton Process: Quantification of Reactive Oxygen Species Generation, Electrochimica Acta 176 (2015) 51–58. https://doi.org/10.1016/j.electacta.2015.06.103.

[73] T. Luo, H. Feng, L. Tang, Y. Lu, W. Tang, S. Chen, J. Yu, Q. Xie, X. Ouyang, Z. Chen, Efficient degradation of tetracycline by heterogeneous electro-Fenton process using Cu-doped Fe@Fe2O3: Mechanism and degradation pathway, Chemical Engineering Journal 382 (2020) 122970. https://doi.org/10.1016/j.cej.2019.122970.

[74] X. Zhou, D. Xu, Y. Chen, Y. Hu, Enhanced degradation of triclosan in heterogeneous E-Fenton process with MOF-derived hierarchical Mn/Fe@PC modified cathode, Chemical Engineering Journal 384 (2020) 123324. https://doi.org/10.1016/j.cej.2019.123324.

[75] Y. Chai, P. Qin, Z. Wu, M. Bai, W. Li, J. Pan, R. Cao, A. Chen, D. Jin, C. Peng, A

coupled system of flow-through electro-Fenton and electrosorption processes for the efficient treatment of high-salinity organic wastewater, Separation and Purification Technology 267 (2021) 118683. https://doi.org/10.1016/j.seppur.2021.118683.

[76] H. Qi, X. Sun, Z. Sun, Porous graphite felt electrode with catalytic defects for enhanced degradation of pollutants by electro-Fenton process, Chemical Engineering Journal 403 (2021) 126270. https://doi.org/10.1016/j.cej.2020.126270.

[77] E. Brillas, I. Sirés, M.A. Oturan, Electro-Fenton Process and Related Electrochemical Technologies Based on Fenton's Reaction Chemistry, Chem. Rev. 109 (2009) 6570–6631. https://doi.org/10.1021/cr900136g.

[78] Y. Yao, Y. Pan, Y. Yu, Z. Yu, L. Lai, F. Liu, L. Wei, Y. Chen, Bifunctional catalysts for heterogeneous electro-Fenton processes: a review, Environ Chem Lett 20 (2022) 3837–3859. https://doi.org/10.1007/s10311-022-01453-6.

[79] G. Xia, Y. Lu, H. Xu, Electrogeneration of hydrogen peroxide for electro-Fenton via oxygen reduction using polyacrylonitrile-based carbon fiber brush cathode, Electrochimica Acta 158 (2015) 390–396. https://doi.org/10.1016/j.electacta.2015.01.102.

[80] G. Lama, J. Meijide, A. Sanromán, M. Pazos, Heterogeneous advanced oxidation processes: Current approaches for wastewater treatment, Catalysts 12 (2022) 344. https://doi.org/10.3390/catal12030344.

[81] J. Zhang, Y. Liu, J. Li, K. Wang, X. Zhao, X. Liu, Enhanced recovery of phosphorus from hypophosphite-laden wastewater via field-induced electro-Fenton coupled with anodic oxidation, Journal of Hazardous Materials 464 (2024) 132750. https://doi.org/10.1016/j.jhazmat.2023.132750.

[82] F. Yu, M. Zhou, X. Yu, Cost-effective electro-Fenton using modified graphite felt that dramatically enhanced on H2O2 electro-generation without external aeration, Electrochimica Acta 163 (2015) 182–189. https://doi.org/10.1016/j.electacta.2015.02.166.

[83] C. Kuang, Y. Xu, W. Lai, G. Xie, Z. Pan, L. Zheng, M.P. Talawar, J. Ling, S. Ye, X. Zhou, Novel electrodes for cathode electro-Fenton oxidation coupled with anodic oxidation system for advanced treatment of livestock wastewater, Electrochimica Acta 321 (2019) 134605. https://doi.org/10.1016/j.electacta.2019.134605.

[84] M. Yu, H. Dong, K. Liu, Y. Zheng, M.R. Hoffmann, W. Liu, Porous carbon monoliths for electrochemical removal of aqueous herbicides by "one-stop" catalysis of oxygen reduction and H2O2 activation, Journal of Hazardous Materials 414 (2021) 125592. https://doi.org/10.1016/j.jhazmat.2021.125592.

5 Advanced polystyrene nanoplastic remediation through electro-Fenton process: degradation mechanisms and pathways

Highlights

- An electro-Fenton process for nanoplastic treatment under mild conditions is proposed.
- Polystyrene decomposition pathways in an EF system are revealed for the first time.
- A comprehensive methodology is developed to characterise polystyrene degradation.
- Combine experiments and DFT calculations to identify reaction sites and pathways.
- The acute toxicity of polystyrene degradation products is significantly reduced.

Graphical abstract

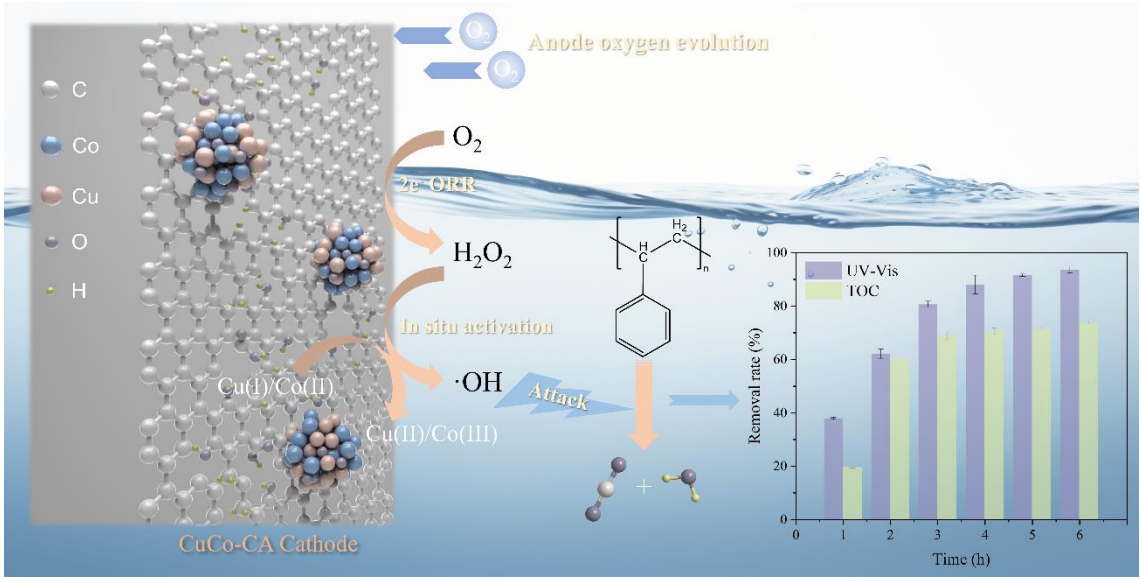

5.1 Abstract

Nanoplastics are increasingly recognised as emerging pollutants posing significant ecological risks, and necessitate development of effective remediation strategies. Heterogeneous electro-Fenton (EF) processes have demonstrated excellent capabilities in degrading various persistent organic contaminants. In this study, we propose a novel approach for the degradation of polystyrene nanoplastics (PS-NPs) by incorporating a novel copper-cobalt carbon aerogel (CuCo-CA) as a bifunctional cathode. The bifunctional capability of CuCo-CA for H_2O_2 electro-synthesis and *in situ* activation induced the efficient generation of hydroxyl radicals for the oxidative decomposition of PS-NPs. After optimising pH condition, current intensity, initial PS-NP dosage, and electrolyte concentration, a PS-NP removal efficiency of 94.8% using UV-vis spectroscopy, and total organic carbon removal of 73.7% were achieved after 6 hours. The CuCo-CA cathode maintained an excellent degradation rate and preserved active functional groups after five consecutive cycles. A comprehensive methodology was developed to characterise the changes in morphology, particle size, elemental composition, and functional groups of PS-NPs before and after electro-Fenton treatment. Density functional theory (DFT) calculations were used to identify reactive sites on polystyrene molecules. In combination with mass spectrometry analysis of intermediates, the degradation pathways of PS-NPs were proposed. Post-treatment analysis identified various chain-break and oxidation products, attributed to aggressive oxidative attack by hydroxyl radicals. Toxicity assessments revealed that the final products were less harmful compared to the initial PS molecules. Overall, this study provides valuable insights into optimising electro-Fenton technology for the efficient degradation of nanoplastics.

5.2 Introduction

Microplastics (MPs, 1 μm ~ 5 mm) and nanoplastics (NPs, < 1 μm) are defined as small particles less than 5 mm in diameter originating from raw plastic materials such as microbeads found in cosmetics and soaps. They are environmentally concerning due to their wide-ranging occurrence, small size and resistant chemical properties [1]. These characteristics facilitate the entry of MPs/NPs into animal and human bodies *via* food chains, affecting both aquatic life and human health through inhalation, ingestion, or direct contact [2]. Approximately 1.5 million tons of MPs/NPs are estimated to be released into aquatic environments annually [3], prompting a need for innovative

treatment solutions to tackle MP and NP pollution effectively.

Research on MP/NP separation in water primarily involves methods like filtration, sieving, and activated carbon, often used as pre-treatment to quantify MP/NP [4]. Techniques like coagulation-flocculation/flotation, and more novel approaches such as magnetic and electrostatic separation, alongside pressurised fluid extraction show promise to address MP/NP pollution [5–7]. However, these separation processes only achieve phase transfer of plastic particles. In contrast, decomposition techniques such as biological degradation and advanced oxidation processes (AOPs) facilitate the breakdown of chemical bonds within the MP/NP polymeric chain into smaller fragments, or potentially mineralise to CO_2 and H_2O [8,9]. Such degradation processes are therefore more conducive to alleviating the crisis of environmental plastic pollution. Researchers have discovered that while MPs/NPs exhibit prolonged stability in natural settings, specific microorganisms such as bacteria and fungi are capable of degrading them [10]. However, most reported biodegradation methods struggle to achieve the desired effects due to severe operating conditions and long treatment times required.

Recently, AOPs have demonstrated outstanding efficacy in degrading persistent organic contaminants in aqueous matrices through the generation of various reactive oxygen species (ROS), such as the hydroxyl radical (·OH) [11]. In the field of AOPs, several studies have reported the photodegradation of MPs using semiconductor materials such as TiO_2-based nanomaterials as photocatalysts [12–14]. However, the recyclability of these catalysts poses a challenge due to their suspension in water, which can lead to secondary pollution and restrict large-scale application. Electrochemical advanced oxidation processes (EAOPs), with the assistance of electron and fixed electrode materials, present a promising solution to these challenges. This approach addresses issues related to the shedding, dissolution, and agglomeration of unstable catalysts, and minimises the use of chemical reagents, thereby facilitating the expansion of wastewater treatment applications on a plant scale.

The application of EAOPs for the removal/degradation of MPs/NPs in aquatic environments is still in its infancy, with early-stage studies indicating potential yet highlighting the need for further development. Electrooxidation (EO) processes

employing boron-doped diamond (BDD) anodes and electrochemical oxidation systems featuring modified anodes, such as CeO_2-PbO_2, have shown higher degradation efficiencies for specific types of MPs [15,16]. Additionally, an electrooxidation-H_2O_2 system incorporating a BDD anode and carbon-felt cathode has been developed, significantly enhancing the degradation rate of polystyrene nanoparticles [17]. Despite these advancements, challenges such as anode fouling, slow degradation rates for certain plastics, and the need for system optimisation highlight the complexity of scaling these technologies for broader environmental applications.

Electro-Fenton (EF) process, one of the most effective and eco-friendly emerging technologies, is extensively utilised for the treatment of wastewater contaminated with organic compounds [18]. Although significant progress has been made in treating organic pollutants using EF processes, the application of these techniques for the removal of nanoplastics has been scarcely reported. Limited studies have explored the mitigation of MP/NP pollution using EF or EF coupled with other techniques, such as the decomposition of PVC MPs using an electro-Fenton-like system equipped with a TiO_2/graphite cathode [19], and the effective decomposition of PS-NPs in a photoelectron-Fenton microreactor integrated with a MOF-derived porous α-Fe_2O_3 film [20]. Undoubtedly, the development of these methods offers highly advantageous degradation pathways for MPs and NPs. However, the reported EF system requires stringent reaction conditions, such as elevated temperatures of up to 100℃, to achieve a reduction in the weight loss of MPs. Additionally, the inclusion of irradiation in the photoelectron-Fenton process implies additional energy consumption and operational costs. Consequently, there is an urgent need for highly efficient, cost-effective, and sustainable remediation technologies to remove micro/nano plastics from aquatic environments.

Polystyrene (PS) was selected as representative nano-sized plastic particles because it is extensively utilised in foam products, cosmetics, and capacitor dielectrics, leading to its pervasive presence in aquatic environments [2]. Currently, no studies have explored the treatment of PS using electro-Fenton processes, and the oxidative degradation mechanisms and environmental impact of intermediates also remain unclear. In this study, an electro-Fenton system with copper-cobalt carbon aerogel (CuCo-CA) as an integrated

cathode was proposed to explore the degradation performance, process, and mechanisms of polystyrene nanoplastics (PS-NPs). The specific objectives of this research were to: (i) develop and optimise an electro-Fenton process for the degradation of PS nanoplastics without reliance on external aeration; (ii) investigate the physical deformation and chemical composition alterations of PS-NPs during the electrochemical oxidation treatment; (iii) elucidate the underlying oxidation mechanisms and analyse the degradation intermediates and pathways of PS-NPs in the optimised EF process.

5.3 Experimental section

5.3.1 Chemicals and reagents

Polystyrene nanoparticles (spheres, 120 nm, 2.5 wt%), which were sourced from Jiangsu Zhichuan Technology Co., Ltd (Jiangsu, China), had a mildly anionic surface charge due to the presence of sodium dodecyl benzene sulfonate. The platinum electrode was obtained from Shanghai Chuxi Industrial Co., Ltd., China. Cobalt (III) acetylacetonate ($C_{15}H_{21}CoO_6$, analytical reagent grade) was sourced from Fluorochem Ltd., UK. Resorcinol ($C_6H_6O_2$, 99%) and salicylic acid ($C_7H_6O_3$, 99+%) were obtained from Sigma-Aldrich, through Merck Life Science Ltd., UK. Copper (II) acetate ($Cu(CH_3COO)_2$, 98%), formaldehyde (CH_2O, 37%), sodium hydroxide (NaOH, ≥98%), sodium sulphite (Na_2SO_3, 98%), and acetone (C_3H_6O, ≥99+%) were purchased from Thermo Scientific, UK. Sodium sulphate (Na_2SO_4, 99.5%) and sulfuric acid (H_2SO_4, 96%) were purchased from Fisher Scientific, UK. Sodium carbonate (Na_2CO_3, analytical reagent grade) was sourced from BioServ Ltd., UK.

5.3.2 Cathode synthesis

Based on our previously reported work [21], the fabrication of the CuCo-CA cathode (Cu: Co molar ratio of 1:1) involved four sequential steps: (1) Gelation: Resorcinol (11.011g) was dissolved in 19.64 mL of ultrapure water, followed by the addition of 15 mL of 37% formaldehyde solution and 0.0085 g of sodium carbonate under continuous stirring. Subsequently, 0.1215 g of copper (II) acetate and 0.1852 g of cobalt (II) acetylacetonate, serving as metallic precursors, were added to the homogeneous solution. The mixture was stirred magnetically for one hour before being poured into a glass mould that was tightly sealed. The polymerisation and aging processes were conducted by curing the precursor in an oven using a stepwise temperature program: 30 ℃ for 24 hours, 50 ℃ for another

24 hours, and finally 90 ℃ for 72 hours. (2) Solvent exchange: After cooling, the wet gel was removed from the mould and immersed in acetone for 72 hours to replace any residual water. The acetone was replaced with fresh solvent each day. (3) Drying: following solvent exchange, the gel was air-dried under ambient conditions for 24 hours, resulting in an aerogel with a defined shape and size. (4) Carbonisation: the dried aerogel was placed in a tube furnace (Carbolite Gero TZF 12/38) under a nitrogen flow of 0.1 L/min. The furnace temperature was ramped at 3 ℃/min to 950 ℃ and maintained for 4 hours. After cooling to room temperature, the resulting CuCo-CA cathode was ready for use as a cathode in the electro-Fenton system.

The synthesis of Cu-CA and Co-CA followed the same procedure, except that only 0.1215 g of copper (II) acetate or 0.1852 g of cobalt (II) acetylacetonate were used as precursor, respectively. In contrast, pure CA was prepared without adding any metallic precursors.

5.3.3 Electro-Fenton system construction

The prepared CuCo carbon aerogel (CuCo-CA) was employed as a functional cathode material in the electro-Fenton system to degrade polystyrene nanoplastics. Degradation experiments for PS-NPs were conducted in a single-chamber cylindrical glass reactor at atmospheric pressure and ambient temperature, and a magnetic stirrer was used to evenly disperse the polystyrene nanoparticles. The cell consisted of a CuCo-CA cathode with an area of 4.5 cm^2 and a platinum sheet anode (4 cm^2), placed 2 cm apart. A DC power source (Velleman 70–0768) was adjusted to deliver an optimal current of 20 mA in most degradation processes, with the voltage ranging between 1.87 V and 2.6 V. To investigate the effect of different pH values, the initial pH of the electrolyte was controlled using 0.1 M H_2SO_4 and 0.1 M NaOH to attain the desired level. The pH was measured using an HQ 40d (Hach, UK) digital multi-meter kit. The reaction was initiated by introducing current into the electrolyte solution containing 0.05 M Na_2SO_4 and 20 mg/L of PS. Samples were taken at specified intervals for analysis without filtration.

5.3.4 Characterisation methods

5.3.4.1 Polystyrene nanoplastics

The structural and size information of the polystyrene particles before and after electro-Fenton treatment were obtained using a high-resolution transmission electron microscope

(HRTEM, FEI Titan3 Themis 300). A droplet of the aqueous suspension was applied onto a copper grid coated with a holey carbon film. Prior to any microscopic observation, the grids were hydrophilised through plasma treatment using a plasma cleaner (Henniker HPT-100). The surface morphological properties of PS-NPs were observed using a scanning electron microscope (SEM, Zeiss Evo 15). SEM images were acquired by depositing 10 μL of the PS sample onto an aluminium stub, which was covered with a silicon wafer and coated with a 5 nm layer of gold. The particle recognition and statistical size analysis were performed via Image J software (National Institutes of Health, USA). The size distribution and surface potential of nanoplastics within the pH range 3~9 were assessed on a Malvern Zetasizer ZS dynamic light-scattering (DLS) analyser (Malvern Instruments Ltd., UK).

The chemical states of carbon and oxygen were analysed using a Thermo Scientific K-Alpha X-ray photoelectron spectrometer (XPS). XPS analysis, including survey and high-resolution spectra, was conducted using an Al Kα radiation source operated at 10 mA and 15 kV, with a base pressure maintained at 2×10^{-9} mbar. The survey spectra were captured with an analyser pass energy of 150 eV and an energy step size of 1.0 eV, while the high-resolution C 1s and O 1s spectra were collected at a pass energy of 50 eV with a step size of 0.1 eV. Energy calibration was conducted using the C 1s peak of aliphatic carbon at 284.8 eV. The proportion of each component was determined by calculating the integrated area of each peak obtained from the fitting results. To further investigate the functional groups of the plastic particles, Fourier transform infrared spectroscopy (FTIR) analysis was carried out on both fresh and treated PS nanoplastics using a PerkinElmer Spectrum Two FTIR Spectrometer. Topographic images of PS-NPs particle arrangement and aggregation were obtained using an atomic force microscope (AFM, Bruker Innova), by dropping the particle suspension on a silicon wafer and then then allowing it to dry naturally.

5.3.4.2 CuCo-CA cathode

To investigate any structural or compositional changes to the CuCo-CA cathode before and after recycling experiments, TEM, FTIR, and X-ray diffraction (XRD) analysis were conducted. XRD analysis was carried out using a Shimadzu XRD-6100 instrument with Cu Kα radiation (λ = 1.5406 Å), scanning over a 2θ range of 10° to 80° with a step size of 0.02°. FTIR spectra over a wavelength range of 500-4000 cm^{-1} were acquired using a

Nicolet iS5 spectrometer (Thermo Scientific) with KBr pellets.

5.3.5 Analytical methods

The determination of PS-NPs was conducted based on established methods from previous studies [22–24]. The concentration of PS nanoplastics was quantified using a UV-vis spectrometer (Shimadzu UV1900) at 201 nm. A calibration curve plotting absorbance versus concentration for PS nanoplastics was constructed across a concentration range of 0-20 mg/L, resulting in a correlation coefficient (R^2) of 0.9993 (Fig. S5.1). The degradation of PS-NPs was modelled using a pseudo-first-order kinetic equation (Eq. 5.1), where C_0 denotes the initial PS-NPs concentration (mg/L), C_t represents the PS-NPs concentration at time t (mg/L), k_{obs} is the apparent rate constant (h^{-1}), and t is the reaction time (h).

$$ln\,(C_0/C_t) = k_{obs}\,t \qquad (5.1)$$

Total organic carbon (TOC) content in aqueous suspensions over the treatment period was evaluated using an Analytik Jena Multi NC2100 combustion analyser. The measurements were performed on unfiltered samples, with 5 mL of the suspension collected at designated time intervals. TOC analysis does not directly quantify polymer concentrations in suspensions, but it provides insights into the conversion of organic carbon within PS polymer into CO_2 during electrochemical oxidation. Specifically, the residual organic carbon in the suspension accounts for both the degradation intermediates resulting from partial decomposition of PS nanoplastic, and the remaining PS in the suspension.

The quantitative determination of hydroxyl radicals (·OH) was carried out using a probe reaction with salicylic acid (SA) [25]. In this experiment, 0.01 M SA was added to a 0.05 M oxygenated Na_2SO_4 electrolyte solution. At specific time intervals, 1 mL of the reaction solution was collected and analysed *via* high-performance liquid chromatography (HPLC, Agilent 1290 Infinity II). Hydroxylated products, including 2,3-dihydroxybenzoic acid (2,3-DHBA) and 2,5-dihydroxybenzoic acid (2,5-DHBA), were detected at a wavelength of 320 nm. The mobile phase consisted of water containing 0.1% trifluoroacetic acid (Solvent A) and acetonitrile containing 0.1% trifluoroacetic acid (Solvent B). A gradient elution was applied: 0 min (95%A–5%B) to 5 min (5%A–95%B). The HPLC analysis

was carried out with the column set at 40 °C and a flow rate of 0.5 mL/min. Under these experimental parameters, 2,3-DHBA and 2,5-DHBA exhibited retention times of 1.85 min and 1.7 min, respectively. The concentration of ·OH was calculated as the sum of the concentrations of 2,3-DHBA and 2,5-DHBA.

The analysis of polystyrene and its degraded solutions was conducted in both positive and negative ion modes by direct injection (5 µl) into a Bruker Impact II mass spectrometer with a VIP-HESI (Vacuum Insulated Probe Heated Electrospray Ionisation) ion source and a scanning mass range from m/z 50 to m/z 3000. A mixture of 50% acetonitrile and 50% water in 0.1% formic acid was used as a buffer to introduce the sample into the mass spectrometer. The experimental parameters included a capillary voltage of 4500 V for positive mode and 3500 V for negative mode, desolvation temperature of 260 °C, and desolvation gas flow of 10 L min^{-1}. Acute toxicity, measured as the 96-hour lethal concentration for 50% mortality (LC50) in fathead minnow, as well as the Tetrahymena pyriformis IGC_{50} of styrene and degradation intermediates, were assessed using the Toxicity Estimation Software Tool (TEST, version 5.1.2). The consensus method, based on quantitative structure–activity relationship (QSAR) modelling, was applied for these estimations.

5.3.6 Theoretical calculation

The density functional theory (DFT) computational calculations were carried out using the Gaussian 09 program package [26]. The B3LYP [27] density functional method with the D3(BJ) dispersion correction was employed to carry out all computations. The 6-31G(d) basis set was used for the atoms in geometry optimisations applying the PCM mode with water as the solvent. Vibrational frequency analyses at the same level of theory were performed to characterise stationary points as local minima without any imaginary frequencies.

The Fukui function [28], which is commonly applied to predict reactive sites for electrophilic (f^+), nucleophilic (f^-), and radical attacks (f^0), was utilised in this study. The condensed Fukui function was based on the natural charges of each atom (NPA). The Fukui function is defined as:

$$f(r) = \left(\frac{\partial^2 E}{\partial N.\partial v(r)}\right) = \left[\frac{\partial \mu}{\partial v(r)}\right]_N = \left[\frac{\partial \rho(r)}{\partial N}\right]_{V(r)} \quad (5.2)$$

Where $\rho(r)$ is the electron density at point *r* in space, and *N* is the number of electrons in the system. The constant *v* in the partial derivative in external potential. In the condensed version of the Fukui function, atomic population numbers represent the electron density distribution around each atom. The condensed Fukui function can be calculated for three cases:

Nucleophilic attack: $f_A^+ = q_N^A - q_{N+1}^A$ (5.3)

Electrophilic attack: $f_A^- = q_{N-1}^A - q_N^A$ (5.4)

Radical attack: $f_A^0 = (q_{N-1}^A - q_{N+1}^A)/2$ (5.5)

where q^A represents the atomic charge population of atom *A* in the corresponding state. The Fukui function provides valuable insight into the reactive sites of a molecule, with larger condensed Fukui function (CFF) values typically indicating more reactive regions. In this study, as the primary attacking species was ·OH, the CFF for radical attack was used to analyse the regioselectivity in PS-NP degradation.

5.4 Results and discussion

5.4.1 Analysis of polystyrene nanoplastic degradation performance in EF systems

5.4.1.1 Monitoring degradation performance using UV-vis and TOC analysis

To monitor the concentration of polystyrene nanoplastics (PS-NPs) during the reaction and calculate the degradation rate, the absorbance of the extracted water sample at 201nm was measured using UV-vis technology, and the concentration corresponding to the absorbance was obtained using the calibration curve. The reduction in concentration served as an indicator for assessing the degradation progress of PS-NPs, and the efficiency of different electro-Fenton (EF) systems using CuCo-CA, Cu-CA, Co-CA, and pure CA as cathodes. As shown in Fig. 5.1(a), the EF process in the presence of the CuCo-CA cathode achieved the highest PS-NPs removal, reaching 93.6% within 6 h, which may be attributed to enhanced generation of reactive species. The white reaction suspension of PS-NPs became clear and transparent following treatment with the CuCo-CA electro-Fenton system (Fig. S5.2). In contrast, pure CA, without any transition metal loading, achieved 79.0% removal that may be associated with the absence of catalytic metal sites. Additionally, Fig. S5.3 and Fig. 5.1(b) present the pseudo-first-order kinetic fitting and

rate constants for the different systems: 0.491 h^{-1} for CuCo-CA, 0.290 h^{-1} for Cu-CA, 0.426 h^{-1} for Co-CA, and 0.233 h^{-1} for pure CA. These highlight the synergistic effect of the Cu and Co bimetallic components on promoting PS-NP decomposition through electro-Fenton mechanisms. TOC analysis was used as an independent quantitative verification for complete PS-NPs breakdown. Although TOC removal percentage was lower than that observed using UV-vis removal, it reached 73.7% after 6 h in CuCo-CA system (Fig. 5.1(c)). This suggests that a substantial proportion of the PS nanoparticles were gradually degraded and mineralised into CO_2 and H_2O through electrochemical oxidation, while a small portion remained in the reaction solution as intermediate breakdown products.

Electro-Fenton systems typically induce oxidative degradation of organic pollutants by generating hydroxyl radicals (·OH, E_0 = 2.7 V versus normal hydrogen electrode [NHE]) as reactive oxygen species. Previous research by the current authors [29] demonstrated that ·OH serves as the dominant free radical in the EF process using a FeNi-CA cathode. Therefore, the concentration of ·OH generated in the CuCo/CA EF system over the reaction time was quantitatively analysed using salicylic acid as a probe reagent. As shown in Fig. 5.1(d), after initiating the electro-Fenton reaction, ·OH radicals were continuously generated and gradually accumulated, reaching a maximum concentration of 175.3 μmol/L after 6 hours. To further explore the role of ·OH species in the decomposition of PS-NPs in the CuCo-CA EF system, a quenching test was conducted using tert-butanol (TBA) as a scavenger for ·OH [30]. As shown in Fig. 5.1(a), the presence of TBA led to a decrease in PS-NP removal from 93.6% to 20.7% after 6 hours, highlighting the significant role of ·OH radicals in the degradation process.

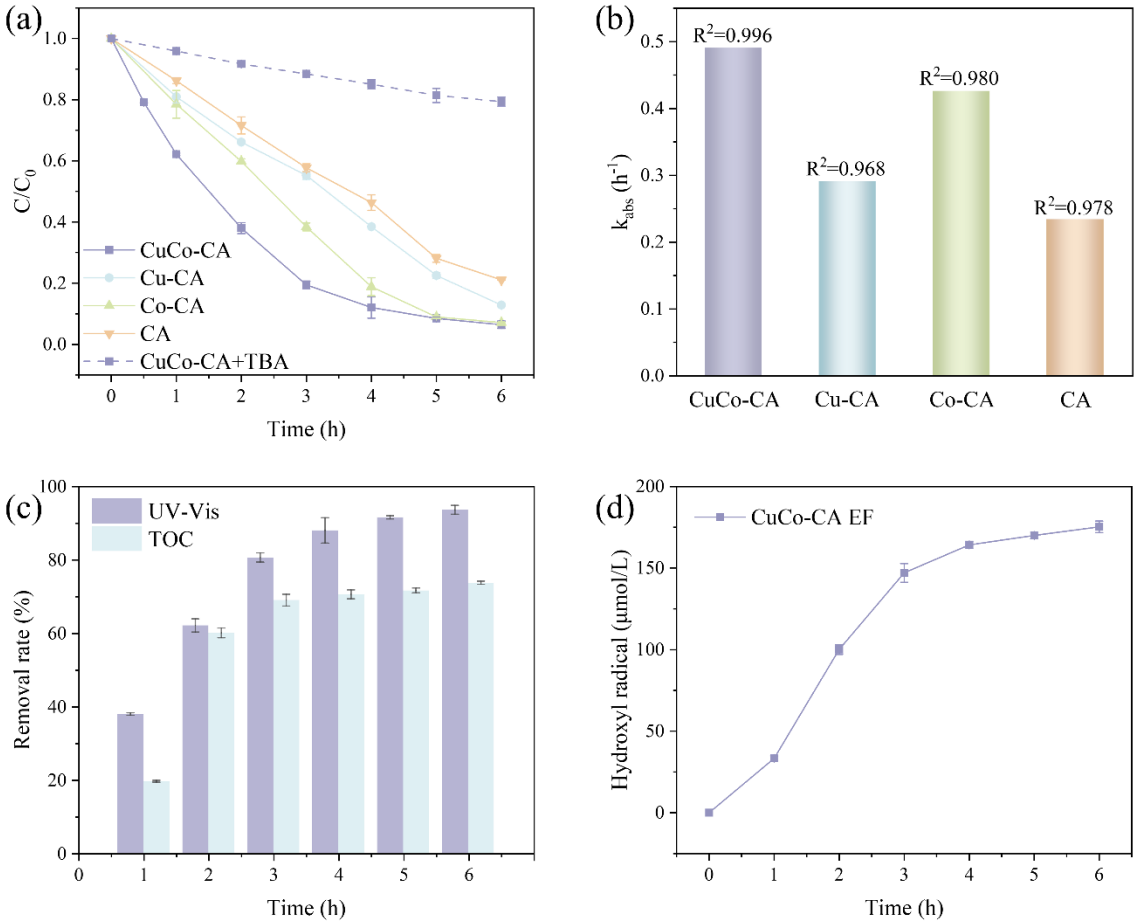

Figure 5.1. (a) UV-vis removal of PS-NPs in electro-Fenton systems using different cathodes, and impact of TBA; (b) Reaction rate constants of the pseudo-first-order kinetic model; (c) UV-vis and TOC removal of PS-NPs in the CuCo-CA EF system; and (d) Generation of hydroxyl radicals in the CuCo-CA EF system. Conditions: [PS-NPs] = 20 mg/L, pH 7.0, applied current 20 mA, [Na_2SO_4] = 0.05 mol/L, [salicylic acid] = 0.01M, [TBA] = 1M, no aeration.

5.4.1.2 Optimisation of operational parameters

To optimise reaction conditions in the CuCo-CA EF system, operational parameters (i.e., initial pH, current, PS-NP concentration, and electrolyte concentration) affecting the removal of PS-NP were further investigated in Fig. 5.2. The pseudo-first-order kinetic fitting and reaction rate constant under each parameter were shown in Fig. S5.4 and Fig. 5.3, respectively. The pH condition played a vital role in influencing the efficacy of the heterogeneous electro-Fenton system, as it impacts the speciation of pollutants and electrochemical reactions. In acidic solutions, the increased availability of protons facilitated the conversion of dissolved oxygen into H_2O_2 *via* a two-electron pathway, as described by Eq. 5.6 [31]. Although a high decrease in apparent UV-vis absorbance was observed at pH 3, this was mainly attributed to the effect of electrosorption rather than

actual oxidative degradation (Fig. 5.2(a)). At other pH values, the contribution of electrosorption to the degradation rate was almost negligible. Moreover, the increase in pH helped to reduce the oxidation potential of ·OH radicals, thereby lowering the threshold for ·OH generation [32]. This may explain the 80% removal rate observed under pH 9 conditions. Overall, in the initial pH range of 3 to 9, removal efficiencies ranged from 69% to 94% for the CuCo-CA EF system over six hours. The optimal operational pH condition for PS-NP removal in the CuCo-CA EF system was pH 7, and the peak reaction rate constant (0.491 h^{-1}) was attained at pH 7.0, as shown in Fig. 5.3.

Cathode: $O_2+2H^++2e^- \rightarrow H_2O_2$ (5.6)

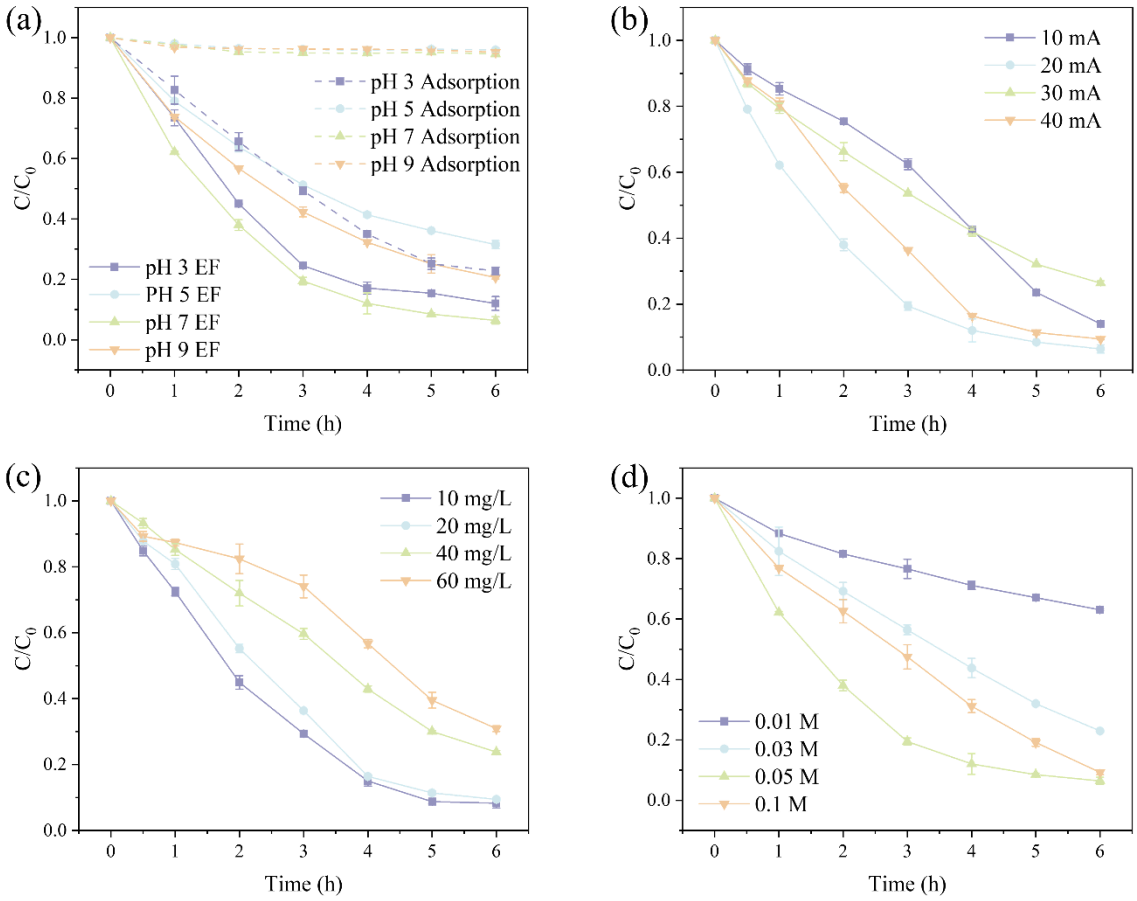

Figure 5.2. Impact of (a) initial pH value; (b) current; (c) initial concentration of PS-NP; and (d) Na_2SO_4 concentration on PS-NPs removal in the CuCo-CA EF system.

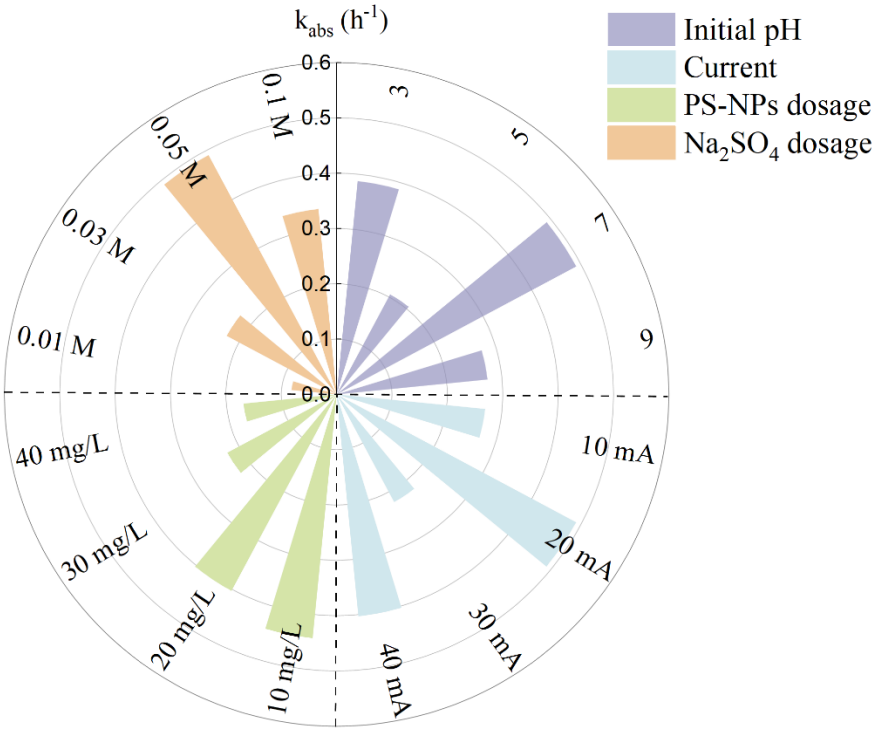

Figure 5.3. Reaction rate constant comparison under various conditions.

The efficacy of EF systems was significantly influenced by the applied current density, which drove electron transfer and correlated with the rate of H_2O_2 production. A higher current density increased the quantity of ·OH radicals both in solution and physisorbed on the electrodes [31], thus the PS-NP removal rate after 6 h improved from 85% to 94% as current rose from 10 mA to 20 mA (Fig. 5.2(b)). However, a drop in reaction rate was observed when applied current was increased to 30 mA and 40 mA, since high applied current densities enhanced the rate of side reactions including cathodic hydrogen evolution (Eq. 5.7) and parasitic reactions involving ·OH radicals (Eq. 5.8) [33]. Therefore, the optimal applied current in the CuCo-CA EF system for PS-NP removal was 20 mA to achieve relatively high current efficiency and low energy consumption.

$$2H^+ + 2e^- \rightarrow H_2 \quad (5.7)$$

$$2 \cdot OH \rightarrow O_2 + 2H^+ + 2e^- \quad (5.8)$$

As shown in Fig. 5.2(c), overall degradation efficiency showed a slight difference between the initial PS-NP concentrations of 10 mg/L and 20 mg/L, with over 90% PS-NP removal observed under these conditions. Additional increases in PS-NP concentration beyond a particular threshold of 20 mg/L led to a decrease in removal rates, although, it would be expected that similar removal end-points may be achieved over longer time

periods than studied. This phenomenon may be attributed to the fact that under specific reaction conditions, a finite amount of ·OH radicals is generated per unit time. When the pollutant concentration increased, the available ·OH radicals became insufficient to effectively degrade the elevated levels of pollutant, resulting in a decrease in pollutant removal efficiency. This observation has been noted by other researchers [34,35].

Sodium sulphate (Na_2SO_4) is widely used as an electrolyte in EF processes due to its high ionic strength and minimal interference in aqueous solution [31], and its concentration plays a critical role in reaction efficiency. Low electrolyte concentrations may not provide sufficient conductivity, while high concentrations can lead to electrode corrosion and reduce the reaction time of Fenton reagents [36]. The removal rate of polystyrene particles increased from 37.0% at 0.01 M Na_2SO_4 to 93.6% at an optimal concentration of 0.05M Na_2SO_4 (Fig. 5.2(d)), and the reaction rate constant improved from 0.082 h^{-1} to 0.491 h^{-1} (Fig. 5.3). However, when Na_2SO_4 dosage was further increased to 0.1 M removal efficiency significantly decreased, likely due to SO_4^{2-} ions consuming radicals (Eq. 5.9 and Eq. 5.10) [31].

$$\cdot OH + SO_4^{2-} \rightarrow OH^- + \cdot SO_4^- \quad (5.9)$$

$$\cdot SO_4^- + e^- \rightarrow SO_4^{2-} \quad (5.10)$$

5.4.1.3 Reusability and stability of the CuCo-CA cathode

The recycling performance of the cathode material helps determine the economic benefit of the treatment process. After cleaning and drying, the CuCo-CA cathode was applied to the EF system for five consecutive runs, and the degradation of PS-NPs under identical reaction parameters is shown in Fig. 5.4(a). The results indicated a slight decline in PS-NP removal efficiency after five consecutive cycles and 6 h reaction time. The reusability performance of the CuCo-CA cathode was greatly influenced by its structural characteristics; hence, the microstructural features of the CuCo-CA cathode were further investigated. As shown in the TEM images (Fig. 5.4(d)~(e)), uniformly distributed CuCo nanoparticles formed within the carbon matrix, where the presence of transition metals catalysed the formation of graphitic carbon, thereby enhancing conductivity and facilitating electron transfer. Fig. 5.4(b)~(c) show the lattice structure and functional group changes of the cathode before and after reuse. XRD spectra revealed that catalytically active Cu(I) species were oxidised to Cu(II) during the reaction, thus

activating hydrogen peroxide to produce ·OH radicals (Eq. 5.11) [37]. However, the catalytic activity of Cu(II) was much lower than that of Cu(I), limiting ·OH species production and reducing PS-NP degradation efficiency. FTIR analysis showed oxygen functional groups such as -OH and -COO- groups remained after reuse, which played a crucial role in the electrosynthesis process of H_2O_2 [38], indicating that the cathode retains its electrocatalytic activity for ORR. Consequently, the degradation efficiency still reached 78.7% after five consecutive runs. The CuCo-CA cathode therefore demonstrated significant structural stability and recyclability during the oxidative degradation of PS-NPs, highlighting its potential for application in water purification to address nanoplastic contamination.

$$Cu(I)+H_2O_2 \rightarrow Cu(II)+ \cdot OH+OH^- \qquad (5.11)$$

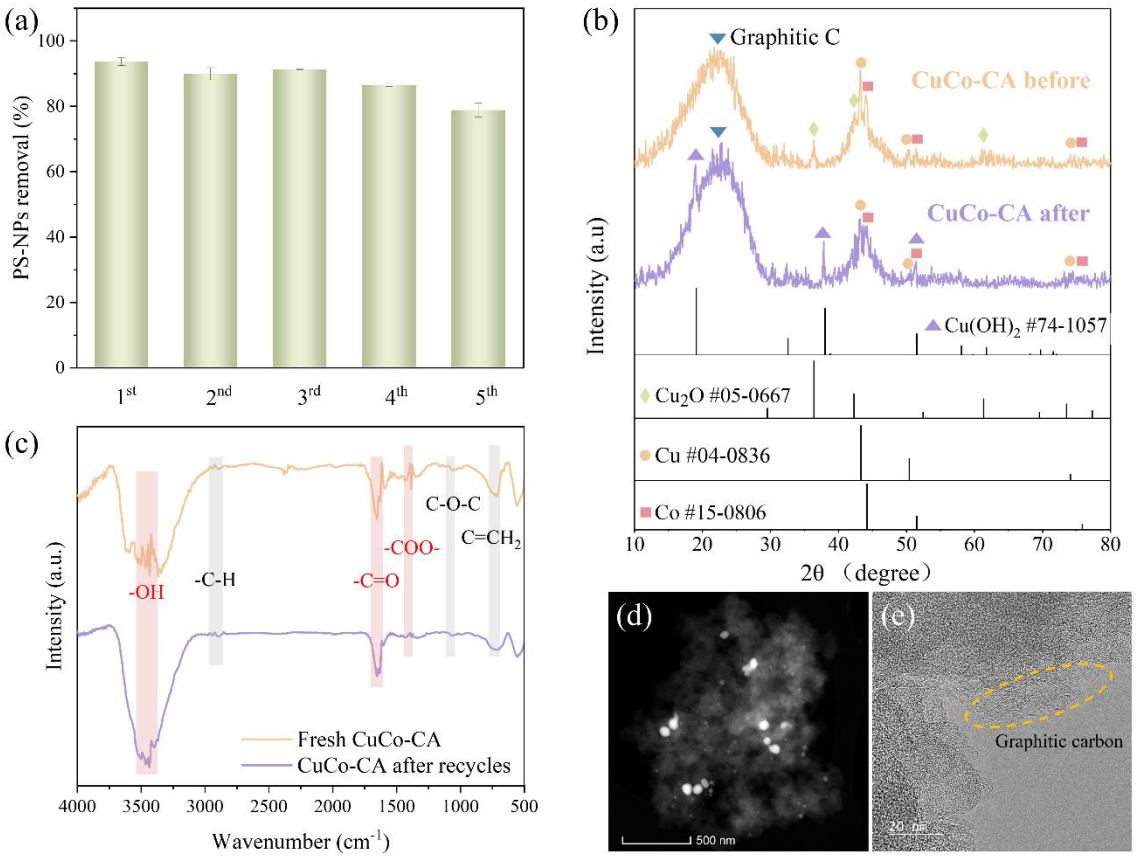

Figure 5.4. (a) Recycling performance of the CuCo-CA cathode on PS-NP removal; (b) XRD spectrum and (c) FTIR spectrum of the CuCo-CA cathode before and after recycling; (d) and (e) HRTEM images of the original CuCo-CA cathode. Conditions: [PS-NP] = 20 mg/L, pH 7.0, applied current = 20 mA, [Na_2SO_4] = 0.05 mol/L, no aeration.

5.4.2 Investigation of structural and compositional changes to PS-NPs

5.4.2.1 Zeta potential, SEM/TEM imaging and Dynamic Light Scattering Analysis

Zeta potential measurements were conducted across varying pH levels to gain insights into PS-NP dispersion stability. As shown in Fig. 5.5(a), the zeta potential of the nanoparticles generally varied between -15 mV and -40 mV with increasing pH. The negative charge observed on PS-NPs across the entire pH range may be attributed to the anionic charge derived from sodium dodecyl benzene sulfonate present on the nanoparticles, which was added to control the particle size during synthesis and to prevent agglomeration during storage. A zeta potential value of approximately -30 mV at pH 7 suggests the NPs are electrostatically stable and well-dispersed as colloids [23]. Dynamic light scattering (DLS) was applied to measure the size distribution of PS-NPs before and after treatment in the CuCo-CA EF process, Fig. 5.5(b). The intensity-based particle size distribution of PS-NPs before the reaction, measured at pH 7 and 25℃, indicated a particle size of approximately 120 nm, consistent with the size observed in SEM imaging (Fig. 5.5(c)). While the intensity of the pre-reaction peak centred at around 120 nm diminished after treatment, the DLS measurements indicated the emergence of larger particles, as well as a broadening of the distribution post-treatment. This phenomenon may be attributed to PS particle aggregation, which could be influenced by changes in pH during the reaction (e.g., pH decreased from 7.0 to 3.2 after 6 h degradation) and modifications to the surface functional groups of the polymer nanobeads during reaction. It is also clear, therefore, that complete degradation of the NPs is not achieved (as inferred from TOC analysis), with residual NPs being unstable in their partially degraded state.

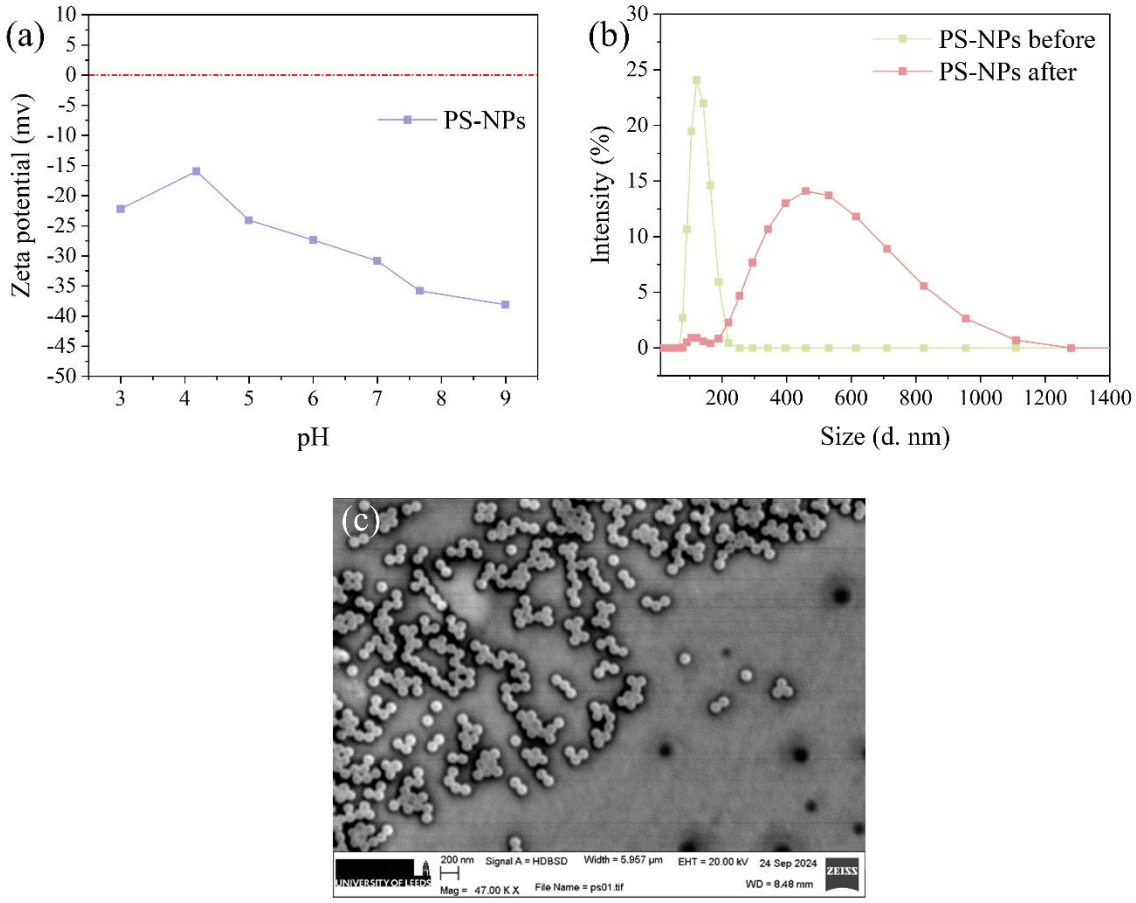

Figure 5.5. (a) Zeta potential under different pH conditions of original PS-NPs; (b) Dynamic light-scattering size distribution of PS-NPs before and after EF reaction; and (c) SEM images of original PS-NPs. Conditions: [PS-NPs] = 20 mg/L, pH 7.0, Applied current = 20 mA, [Na_2SO_4] = 0.05 mol/L, no aeration.

Transmission electron microscope (TEM) is an intuitive technique for visually assessing particle alterations during oxidative treatment, allowing for a quantitative analysis through statistical evaluation of nanoparticle size distribution. Fig. 5.6(a1)~(a2) indicates that the fresh PS nanoparticles exhibited a smooth, spherical morphology with distinct edges and a uniform particle size distribution. The mean diameter of the fresh PS nanoparticles was 118.6 nm, which aligned with the size distribution results from DLS analysis. The fading of particle boundaries and the presence of polymeric fragments were observed following electrochemical treatment, Fig. 5.6(b1) and Fig. 5.6(c)~(f). It may be inferred that new surface functional groups formed as a result of polymer chain breakdown during the radical attack, leading to a loss of spherical definition and particle agglomeration due to surface adhesion [39]. Additionally, a particle size reduction was clearly evidenced through statistical analysis of mean diameter, Fig. 5.6(b2). Critically,

the TEM therefore suggests electrochemical treatment results in evolving surface degradation that breakdowns the PS from the outside in. It is also noted that in the focal resolution of the TEM, it was not possible to observe the larger particle clusters measured from the DLS, while it is emphasised that the TEM images post-treatment only captures the small overall fraction of particles that remain. It is still assumed the great majority of particles are fully degraded and removed from the system.

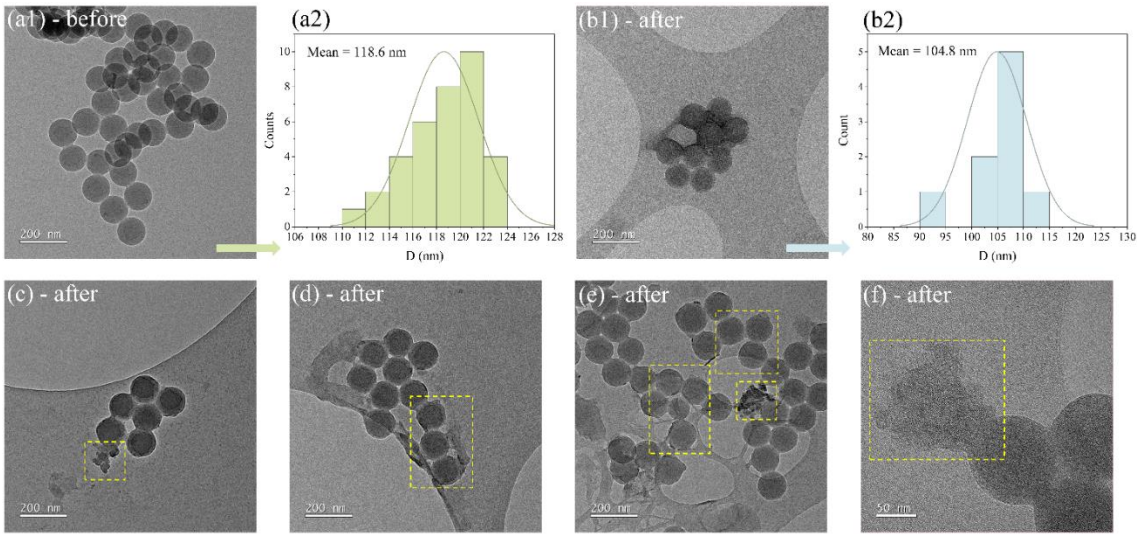

Figure 5.6. (a1) and (a2) HRTEM images and size distribution of PS-NPs before reaction; (b1) ~ (f) HRTEM images and size distribution of PS-NPs post-reaction. Conditions: [PS-NPs] = 20 mg/L, pH 7.0, applied current = 20 mA, [Na_2SO_4] = 0.05 mol/L, no aeration.

5.4.2.2 XPS, FTIR, and AFM Analysis

The structural and functional group changes to the polystyrene nanoplastics (PS-NP) during CuCo-CA EF system treatment were characterised using Fourier Transform Infrared Spectroscopy (FTIR, Fig. 5.7(a)). The aromatic C-H stretch vibrations at 3060 and 3026 cm^{-1}, along with the $–CH_2$ asymmetric stretch vibration at 2924 cm^{-1}, represent typical absorption bands of polystyrene [40]. The characteristic absorption bands of the benzene ring were observed at 1601 and 1493 cm^{-1}, which may be associated with the stretching modes of C=C bonds [41]. The spectral bands at around 697 cm^{-1}, 756 cm^{-1}, 906 cm^{-1}, and 1028 cm^{-1} were indicative of C-H out-of-plane vibrations, suggesting the presence of a single substituent on the aromatic benzene ring and confirming the characteristic phenyl ring structure of polystyrene [42]. The distinct functional groups of PS (i.e., cyclic C-H and C=C bonds) remained stable after EF treatment. However, oxidative degradation is known to induce changes in surface functional groups, particularly in the carbonyl region (1650-1850 cm^{-1}) [43], which were observed in the

zoomed spectra, Fig. 5.7(a). The FTIR results demonstrated the incorporation of carbonyl groups such as carboxylic acids, aldehydes, esters and ketones onto the PS-NP surface because of electrochemical oxidation processes.

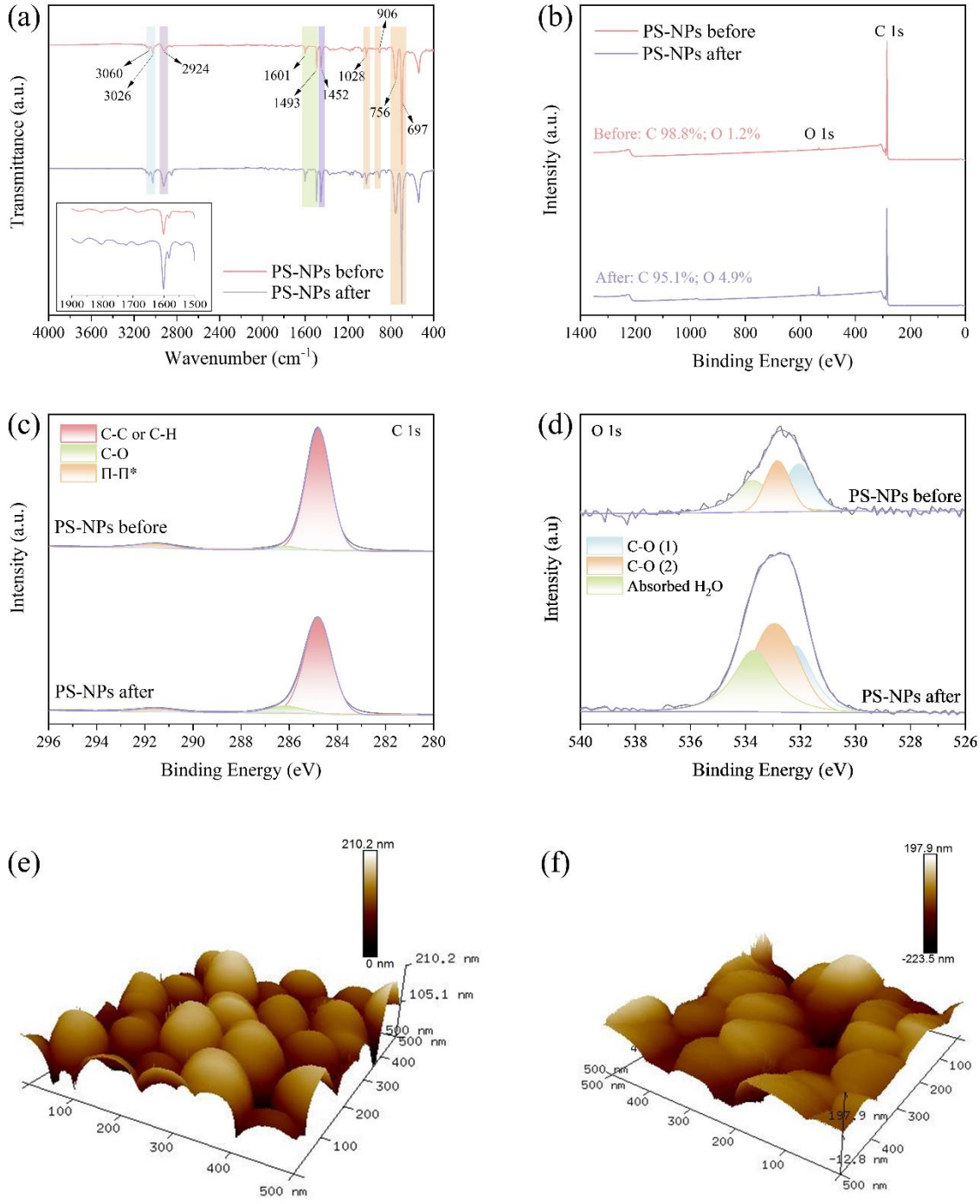

Figure 5.7. (a) FTIR spectra; (b) XPS full spectra; (c) C1s XPS spectra; (d) O1s XPS spectra of PS-NP pre- and post-reaction (C-O (1) refers to ether and hydroxyl groups bonded to aliphatic & carbonyl shake-up and C-O (2) refers to ether and hydroxyl groups bonded to aromatics); (e) AFM topographic image of PS-NP pre-reaction; and (f) AFM topographic image of PS-NPs post-reaction. Conditions: [PS-NPs] = 20 mg/L; pH 7.0;

applied current = 20 mA; [Na_2SO_4] = 0.05 mol/L; no aeration.

Fig. 5.7(b) presents the x-ray photoelectron spectrometer (XPS) survey spectra of the original PS-NP and PS nanoplastics with the EF process after 6 h. The original PS-NPs exhibited C 1s and O 1s peaks, with atomic percentages of 98.8% and 1.2%, respectively. In contrast, after 6 hours of electrochemical oxidation, the oxygen content in the PS-NPs increased to 4.9%. This rise in the O/C ratio might be attributed to rapid oxidation on the surface under attack from free radicals [44]. Additionally, the C 1s peaks in Fig. 5.7(c) were deconvoluted into three main components, corresponding to C-C/C-H (284.8 eV), C-OH/C-O-C (286.14 eV), and π-π^* bonding (291.5 eV) [45,46]. Following EF treatment with the CuCo-CA cathode, there was a notable increase in the C-OH/C-O-C content, while the peak area of C-C/C-H decreased after oxidation. The π-π^* intensity, a signature feature of phenyl rings, showed a slight reduction following 6 hours of EF treatment. This decline could be caused by either the cleavage of phenyl rings or the release of small phenyl-containing molecules from the polystyrene structure. [44]. In the O 1s spectra of PS-NPs, Fig. 5.7(d), peaks corresponding to ether and hydroxyl groups bonded to aliphatic & carbonyl shake-up (C-O (1), 532.26 eV), ether and hydroxyl groups bonded to aromatics (C-O (2), 533.01 eV), and surface absorbed water (533.85 eV) [47] were observed in both pre- and post-reaction samples. The increased intensity of oxygen atoms and oxygen-containing functional groups on the PS-NP surface indicated oxidation had occurred during treatment.

Topographic images of PS-NP pre- and post-treatment were obtained using atomic force microscopy (AFM), Fig. 5.7(e)~(f). The initial particle image showed a relatively organised arrangement of spherical nanoparticles with a consistent height, and the surface profile reflected well-separated nanoparticles with clear boundaries. In comparison, the boundaries between post-reaction PS-NP particles were less distinct (some overlapping or fusion was observed) and the surface appeared more uneven, suggesting surface erosion and enhanced aggregation post-reaction. Combined with the results from XPS, it is speculated that changes in surface properties, for example, the introduction of oxygen-containing functional groups, might have enhanced inter-particle interactions resulting in aggregation.

The above analyses characterised the physical deformation and chemical compositional changes in PS nanoparticles. The electro-Fenton treatment accelerated the formation of plastic fragments, and a reduction in particle size. The attack of hydroxyl radicals led to the opening of the benzene ring, and the volatilisation of small phenyl group containing molecules on the main polystyrene chain. At the same time, the incorporation of carbonyl groups was enhanced, which was manifested as an increase in the oxidation degree on the polystyrene surface.

5.4.3 Mechanisms of electrochemical degradation of PS-NPs

5.4.3.1 DFT calculation and PS-NP degradation pathways

To further investigate the structural changes of the PS molecules during degradation in the CuCo-CA EF system, DFT (density functional theory) calculations were conducted. Sites with higher f^- and f^0 values exhibit greater reactivity, as they are more susceptible to being attacked by electrophiles and reactive radicals, respectively [48,49]. Accordingly, three styrene monomers were used to analyse the highest occupied molecular orbital (HOMO), and the lowest unoccupied molecular orbital (LUMO) distributions, and to calculate the Fukui index (f^- and f^0 values) based on the natural population analysis (NPA) charge distribution of PS molecules, Fig. 5.8(a), Fig. S5.5, and Table. S5.1. It was observed that the HOMO was primarily localised around the carbon atoms of the benzene ring, where the electron density is relatively high, making these sites more susceptible to oxidation reactions [50].

For further elucidation of the degradation pattern of PS, optimised PS structures and corresponding reactive sites were labelled with atoms showing relatively high f^- and f^0 values circled in red, Fig. 5.8(b). First, several reactive sites were observed on the benzene ring of each monomer, indicating that the carbon atoms in the aromatic ring are preferentially attacked. This finding aligned with previously reported observations that hydroxyl radicals preferentially target aromatic rings and double bonds over alkanes [43]. Second, carbon atoms on the main chain connecting the benzene rings were also reactive for substitution reactions because the connected hydrogen atoms have a relatively high f^- value.

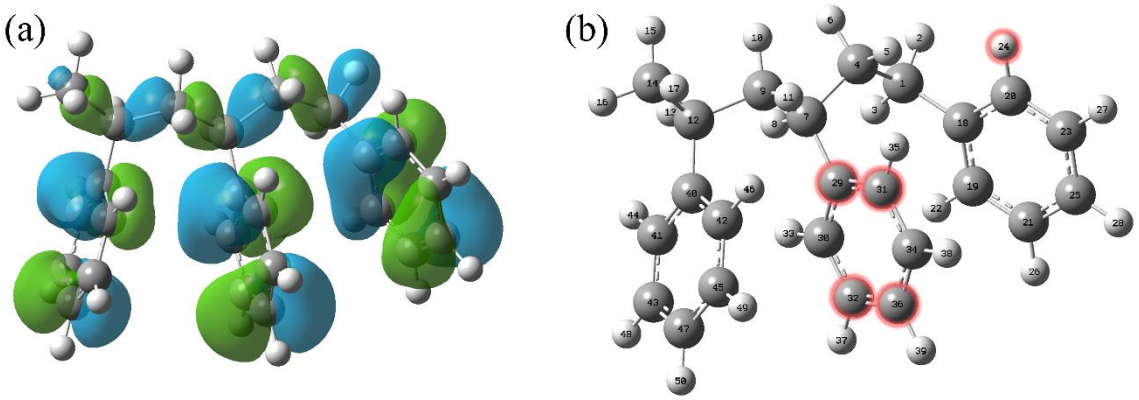

Figure 5.8. (a) HOMO distribution map of the polystyrene molecule; (b) Chemical structure and reactive sites on the polystyrene molecule.

To clarify the degradation pathway of PS in the CuCo-CA EF reaction, intermediates were analysed by direct injection into a mass spectrometer. Fig. S5.6 displays the mass spectrum of the fragmented intermediates, and Table. S5.2 lists the detected degradation products and their structural information. Based on intermediate identification and predicted reaction sites, a potential degradation pathway for PS was proposed, as shown in Fig. 5.9. Initially, for hydroxylation on the aromatic ring, atoms with high f^0 values (31C, 32C, 42C, and 43C) in PS were prone to attack by ·OH radicals, forming hydroxylated intermediates TP5/TP6 ($C_{17}H_{20}O_4$) [51]. The ·OH radicals further attack the polystyrene backbone, preferentially targeting hydrogen atoms along the connecting polymer chain, such as 2H with a high f^- value of 0.02543, and continue to hydroxylate carbon atoms connected to the benzene ring, forming two isomers TP7/TP8 ($C_8H_{10}O_3$). Subsequent oxidation of these intermediates at the benzene and phenethyl positions leads to the formation of acetophenone (TP9, C_8H_8O) and benzoic acid (TP10, $C_7H_6O_2$). Another pathway observed for TO5/TP6 involved ring-opening reactions on the benzene ring, yielding aliphatic chain compounds such as esters, aldehydes, and alcohols (PS11, TP12, TP13, TP14) [51].

Moreover, due to the electron cloud effects of the benzene ring, carbon atoms connected to the ring exhibit a particle electron-deficient state. Thus, free radicals may initially target the carbon on the polymer chain connected to the benzene ring, breaking C-C bonds in the main chain and resulting in shorter-chain polymers such as TP1/TP2 [52]. Tertiary carbon sites in TP1/TP2 were further attacked by ·OH, yielding smaller fragments of TP3/TP4 ($C_{10}H_{12}O$). Further reactions led to a breaking down of the polystyrene

backbone or aromatic ring into lower molecular weight species including TP15 and TP16, which often contained oxygenated functional groups. After 6 hours of reaction, TOC removal efficiency in the suspension reached 73.7%, Fig. 5.1(c). PS-NP may completely mineralise into CO_2 and H_2O with extended treatment time.

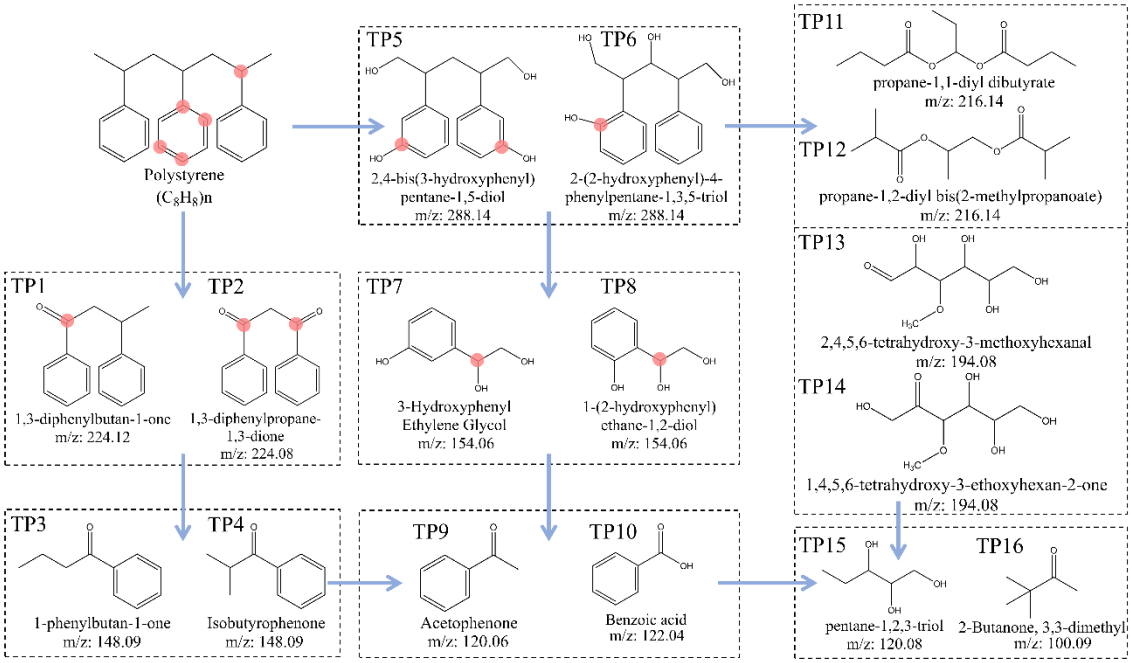

Figure 5.9. Degradation pathways of PS-NP in the CuCo-CA EF system.

5.4.3.2 Acute toxicity estimation and proposed mechanism

The acute toxicity of styrene monomers and intermediates formed during the electrochemical degradation process was assessed using the Toxicity Estimation Software Tool (T.E.S.T.), as shown in Table. S5.3 and Fig. 5.10. The fathead minnow LC_{50} (96) was calculated as 6.09 mg/L for polystyrene, an indication it is classified as a "toxic" substance (Fig. 5.10(a)) [53]. Although some intermediates (TP1, TP2, TP5, and TP11) exhibited higher toxicity than styrene, the final products, TP15 and TP16, generated after further electrochemical oxidation, showed a substantial reduction in acute toxicity and were considered "not harmful". Additionally, tetrahymena pyriformis IGC_{50} indicates the concentration of a test chemical (mg/L) causing 50% inhibition after 48 hours; the higher the IGC_{50} value, the lower the growth inhibition effect. As illustrated in Fig. 5.10(b), six intermediates were found to have higher IGC_{50} values than styrene, especially the initial degradation products TP1 and TP2. However, after ring-opening and chain-breaking reactions, growth inhibition significantly decreased. These results demonstrate that while polystyrene decomposition may initially produce more "toxic" intermediates, the reactive

oxygen species generated by the CuCo-CA EF system effectively destroy these structures, achieving greater oxidation or mineralisation and ensuring post-treatment water safety.

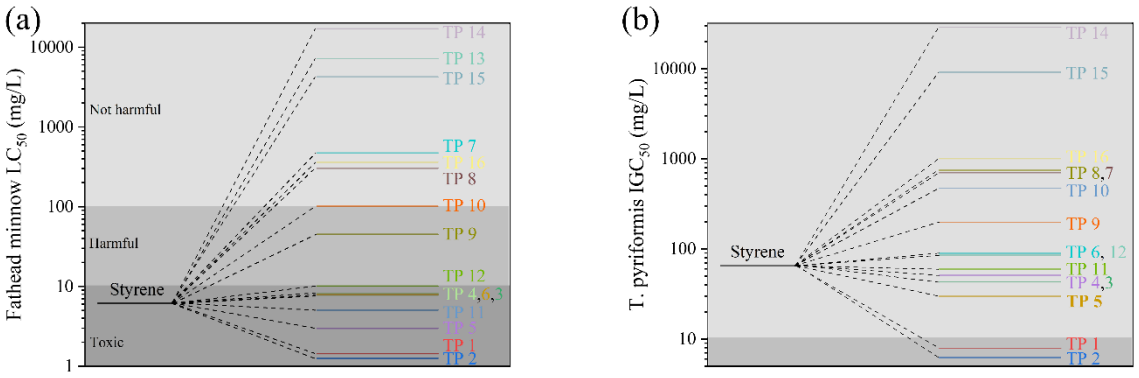

Figure 5.10. (a) and (b) Acute toxicity estimation of styrene and degradation intermediates.

Based on the above findings, the reaction mechanism of PS-NP degradation in the CuCo-CA EF system can be summarised in Fig. 5.11. Initially, oxygen evolution (Eq. 5.12) occurred near the anode, as evidenced by bubble formation, a decrease in solution pH (from 7.01 to 3.35), and an increase in dissolved oxygen concentration (from 8.75 to 13.72 mg/L) during the reaction; our previous study elaborated on this mechanism [29]. The H^+ ions produced during the reaction created a favourable pH environment for *in situ* generation and activation of H_2O_2, as shown in Eq. 5.6 and Eq. 5.11. The generated oxygen subsequently diffused to the electrolyte-cathode interface, where it underwent a two-electron reduction pathway to produce H_2O_2. Furthermore, catalytically active Cu(I) sites on the CuCo/CA cathode induced H_2O_2 *in situ* activation, generating highly reactive ·OH free radicals, thereby enabling the oxidative degradation of polystyrene nanoparticles and step-by-step mineralisation.

$$2H_2O \rightarrow 4e^- + 4H^+ + O_2 \qquad (5.12)$$

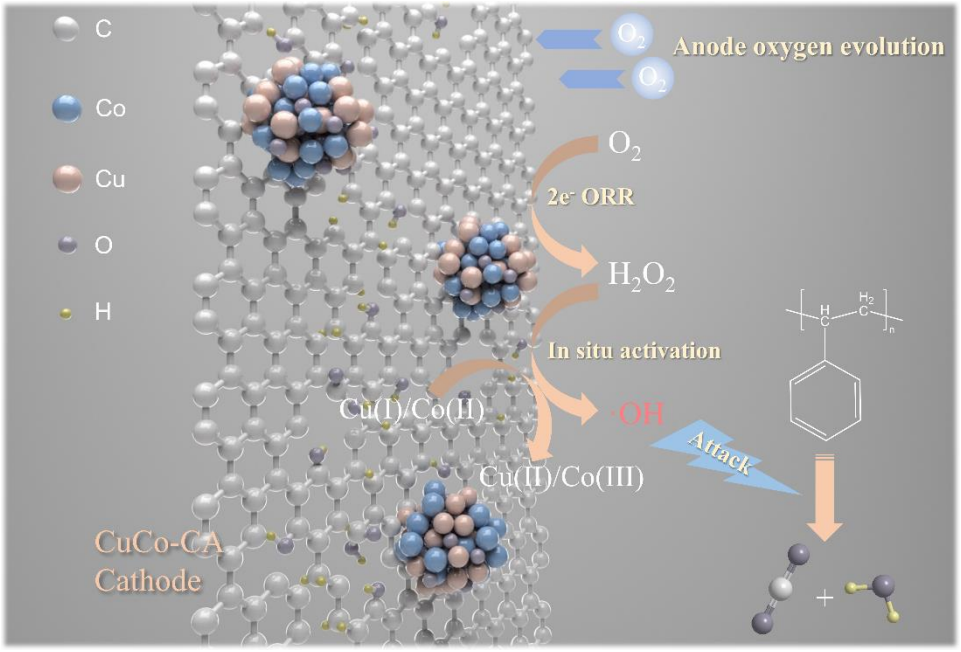

Figure 5.11. Schematic of proposed mechanism of PS-NP degradation in the CuCo-CA EF process.

5.5 Conclusion

This study proposed an advanced electro-Fenton strategy assisted by a CuCo-CA bifunctional cathode for the treatment of polystyrene nanoplastics (PS-NP), examining its degradation performance and underlying mechanisms. In this approach, reactive free radicals (·OH) were effectively produced *via* the *in situ* generation and activation of H_2O_2 without the need for external aeration, potentially making it cost-effective at scale. The CuCo-CA EF system achieved a reaction rate constant of 0.4906 h^{-1} for PS-NP removal at a current density of 4.44 mA/cm^2 and a neutral pH condition, demonstrating improved efficiency compared to EF processes using Cu-CA, Co-CA, or pure CA as the cathode. CuCo-CA exhibited good recyclability over five consecutive runs. The characterisation analysis highlighted the physical deformation and chemical composition changes of PS nanoparticles during electro-Fenton treatment. New surface functional groups were formed as a result of polymer chain fragmentation induced by the oxidative attack of radicals, leading to a loss of spherical shape, size reduction, and particle agglomeration due to surface adhesion. Hydroxyl radicals predominantly attacked the aromatic rings and the carbon atoms on the main chain connected to the benzene rings, causing the incorporation of carbonyl groups and oxidation on the polystyrene surface. After six hours of treatment, TOC removal efficiency in the suspension reached 73.7%. Reactive radicals effectively degraded potentially more toxic intermediates, gradually mineralising them

into harmless end products, thereby ensuring treated water safety. Overall, this study demonstrates that the CuCo-CA EF process is a promising technology for small-scale nanoplastic treatment in wastewater. Further research could explore its applicability to the degradation of other types of nanoplastics.

5.6 Acknowledgements

Qian Ye is funded by the China Scholarship Council (CSC, 202106240065) under the Ministry of Education of P.R. China. The authors are grateful to the funders and acknowledge their support of this work.

The authors wish to express their gratitude to colleagues at the University of Leeds who have provided laboratory apparatus, technical support and training: Mr. Stuart King (FTIR), Dr. Jeanine Williams (HPLC), Dr. Chhaya Patole (MS) and Dr. Ben Douglas (DLS). Additionally, we would like to thank Dr. David Elliott, Mr. Morgan McGowan, and Ms. Emma Tidswell for their guidance on the safe setup and operation of equipment.

5.7 References

[1] A.L. Andrady, The plastic in microplastics: A review, Marine Pollution Bulletin 119 (2017) 12–22. https://doi.org/10.1016/j.marpolbul.2017.01.082.
[2] R. Ahmed, A.K. Hamid, S.A. Krebsbach, J. He, D. Wang, Critical review of microplastics removal from the environment, Chemosphere 293 (2022) 133557. https://doi.org/10.1016/j.chemosphere.2022.133557.
[3] Y. Pico, A. Alfarhan, D. Barcelo, Nano- and microplastic analysis: Focus on their occurrence in freshwater ecosystems and remediation technologies, TrAC Trends in Analytical Chemistry 113 (2019) 409–425. https://doi.org/10.1016/j.trac.2018.08.022.
[4] L. Hou, D. Kumar, C.G. Yoo, I. Gitsov, E.L.-W. Majumder, Conversion and removal strategies for microplastics in wastewater treatment plants and landfills, Chemical Engineering Journal 406 (2021) 126715. https://doi.org/10.1016/j.cej.2020.126715.
[5] C. Wang, H. Wang, J. Fu, Y. Liu, Flotation separation of waste plastics for recycling—A review, Waste Management 41 (2015) 28–38. https://doi.org/10.1016/j.wasman.2015.03.027.
[6] O.M. Rodríguez-Narvaez, A. Goonetilleke, L. Perez, E.R. Bandala, Engineered technologies for the separation and degradation of microplastics in water: A review, Chemical Engineering Journal 414 (2021) 128692. https://doi.org/10.1016/j.cej.2021.128692.
[7] J. Grbic, B. Nguyen, E. Guo, J.B. You, D. Sinton, C.M. Rochman, Magnetic Extraction of Microplastics from Environmental Samples, Environ. Sci. Technol. Lett. 6 (2019) 68–72. https://doi.org/10.1021/acs.estlett.8b00671.
[8] A.B. Silva, M.F. Costa, A.C. Duarte, Biotechnology advances for dealing with environmental pollution by micro(nano)plastics: Lessons on theory and practices, Current Opinion in Environmental Science & Health 1 (2018) 30–35. https://doi.org/10.1016/j.coesh.2017.10.005.
[9] Z. Chen, W. Wei, X. Liu, B.-J. Ni, Emerging electrochemical techniques for identifying and removing micro/nanoplastics in urban waters, Water Research 221 (2022) 118846. https://doi.org/10.1016/j.watres.2022.118846.
[10] M.C. Krueger, H. Harms, D. Schlosser, Prospects for microbiological solutions to environmental pollution with plastics, Appl Microbiol Biotechnol 99 (2015) 8857–8874. https://doi.org/10.1007/s00253-015-6879-4.
[11] P. Duan, Y. Qi, S. Feng, X. Peng, W. Wang, Y. Yue, Y. Shang, Y. Li, B. Gao, X. Xu, Enhanced degradation of clothianidin in peroxymonosulfate/catalyst system via core-shell FeMn @ N-C and phosphate surrounding, Applied Catalysis B: Environmental 267 (2020) 118717. https://doi.org/10.1016/j.apcatb.2020.118717.
[12] X.L. García-Montelongo, A. Martínez-de la Cruz, S. Vázquez-Rodríguez, L.M. Torres-Martínez, Photo-oxidative degradation of TiO2/polypropylene films, Materials Research Bulletin 51 (2014) 56–62. https://doi.org/10.1016/j.materresbull.2013.11.040.
[13] R. Verma, S. Singh, M.K. Dalai, M. Saravanan, V.V. Agrawal, A.K. Srivastava, Photocatalytic degradation of polypropylene film using TiO2-based nanomaterials under solar irradiation, Materials & Design 133 (2017) 10–18. https://doi.org/10.1016/j.matdes.2017.07.042.
[14] S.S. Ali, I.A. Qazi, M. Arshad, Z. Khan, T.C. Voice, Ch.T. Mehmood, Photocatalytic degradation of low density polyethylene (LDPE) films using titania nanotubes, Environmental Nanotechnology, Monitoring & Management 5 (2016) 44–53.

https://doi.org/10.1016/j.enmm.2016.01.001.
[15] M. Kiendrebeogo, M.R. Karimi Estahbanati, A. Khosravanipour Mostafazadeh, P. Drogui, R.D. Tyagi, Treatment of microplastics in water by anodic oxidation: A case study for polystyrene, Environmental Pollution 269 (2021) 116168. https://doi.org/10.1016/j.envpol.2020.116168.
[16] Z. Ning, X. Duan, Y. Li, X. Zhao, L. Chang, Degradation of polyvinyl chloride microplastics via electrochemical oxidation with a CeO2–PbO2 anode, Journal of Cleaner Production (2023) 139668. https://doi.org/10.1016/j.jclepro.2023.139668.
[17] M. Kiendrebeogo, M.R. Karimi Estahbanati, Y. Ouarda, P. Drogui, R.D. Tyagi, Electrochemical degradation of nanoplastics in water: Analysis of the role of reactive oxygen species, Science of The Total Environment 808 (2022) 151897. https://doi.org/10.1016/j.scitotenv.2021.151897.
[18] Z. Wang, M. Liu, F. Xiao, G. Postole, H. Zhao, G. Zhao, Recent advances and trends of heterogeneous electro-Fenton process for wastewater treatment-review, Chinese Chemical Letters 33 (2022) 653–662. https://doi.org/10.1016/j.cclet.2021.07.044.
[19] F. Miao, Y. Liu, M. Gao, X. Yu, P. Xiao, M. Wang, S. Wang, X. Wang, Degradation of polyvinyl chloride microplastics via an electro-Fenton-like system with a TiO2/graphite cathode, Journal of Hazardous Materials 399 (2020) 123023. https://doi.org/10.1016/j.jhazmat.2020.123023.
[20] Q. Chen, L. Wan, H. Zhou, F. Luo, L. Lei, N. Wang, Photoelectro-Fenton microreactor integrated with MOF-derived porous α-Fe2O3 film for efficient nanoplastics degradation, Journal of Water Process Engineering 56 (2023) 104343. https://doi.org/10.1016/j.jwpe.2023.104343.
[21] Q. Ye, T.N. Hunter, H. Xu, D. Harbottle, G.M. Kale, M.R. Tillotson, CuCo carbon aerogel as a bifunctional cathode for Electro-Fenton processes: Unveiling synergistic effects and catalytic mechanisms, Separation and Purification Technology 361 (2025) 131597. https://doi.org/10.1016/j.seppur.2025.131597.
[22] Z. Chen, Z. Huang, J. Liu, E. Wu, Q. Zheng, L. Cui, Phase transition of Mg/Al-flocs to Mg/Al-layered double hydroxides during flocculation and polystyrene nanoplastics removal, Journal of Hazardous Materials 406 (2021) 124697. https://doi.org/10.1016/j.jhazmat.2020.124697.
[23] Z. Chen, J. Liu, C. Chen, Z. Huang, Sedimentation of nanoplastics from water with Ca/Al dual flocculants: Characterization, interface reaction, effects of pH and ion ratios, Chemosphere 252 (2020) 126450. https://doi.org/10.1016/j.chemosphere.2020.126450.
[24] G. Zhou, X. Huang, H. Xu, Q. Wang, M. Wang, Y. Wang, Q. Li, Y. Zhang, Q. Ye, J. Zhang, Removal of polystyrene nanoplastics from water by CuNi carbon material: The role of adsorption, Science of The Total Environment 820 (2022) 153190. https://doi.org/10.1016/j.scitotenv.2022.153190.
[25] X. Qin, P. Cao, X. Quan, K. Zhao, S. Chen, H. Yu, Y. Su, Highly efficient hydroxyl radicals production boosted by the atomically dispersed Fe and Co sites for heterogeneous electro-Fenton oxidation, Environ. Sci. Technol. 57 (2023) 2907–2917. https://doi.org/10.1021/acs.est.2c06981.
[26] M. Frisch, G. Trucks, H. Schlegel, G. Scuseria, M. Robb, J. Cheeseman, G. Scalmani, V. Barone, G. Petersson, H. Nakatsuji, Gaussian 09, Revision A. 02, Gaussian, Inc., Wallingford, CT, 2016, Chem. Chem. Phys. Accept. Manuscr 37 (1988) 785–789.
[27] A.D. Becke, Density-functional thermochemistry. III. The role of exact exchange, The Journal of Chemical Physics 98 (1993) 5648–5652. https://doi.org/10.1063/1.464913.

[28] R.G. Parr, W. Yang, Density functional approach to the frontier-electron theory of chemical reactivity, J. Am. Chem. Soc. 106 (1984) 4049–4050. https://doi.org/10.1021/ja00326a036.
[29] Q. Ye, T.N. Hunter, H. Xu, D. Harbottle, G.M. Kale, M.R. Tillotson, Synergistic effect of Fe and Ni on carbon aerogel for enhanced oxygen reduction and H2O2 activation in electro-Fenton process, Separation and Purification Technology 353 (2025) 128436. https://doi.org/10.1016/j.seppur.2024.128436.
[30] Q. Zhang, M. Zhou, X. Du, P. Su, W. Fu, G. Song, Highly efficient dual-cathode Electro-Fenton process without aeration at a wide pH range: Simultaneously enhancing Fe(II) regeneration and mineralization efficiency, Chemical Engineering Journal 429 (2022) 132436. https://doi.org/10.1016/j.cej.2021.132436.
[31] H. He, Z. Zhou, Electro-Fenton process for water and wastewater treatment, Critical Reviews in Environmental Science and Technology 47 (2017) 2100–2131. https://doi.org/10.1080/10643389.2017.1405673.
[32] V. Kavitha, K. Palanivelu, Destruction of cresols by Fenton oxidation process, Water Research 39 (2005) 3062–3072. https://doi.org/10.1016/j.watres.2005.05.011.
[33] B. Hou, H. Han, S. Jia, H. Zhuang, P. Xu, K. Li, Three-dimensional heterogeneous electro-Fenton oxidation of biologically pretreated coal gasification wastewater using sludge derived carbon as catalytic particle electrodes and catalyst, Journal of the Taiwan Institute of Chemical Engineers 60 (2016) 352–360. https://doi.org/10.1016/j.jtice.2015.10.032.
[34] M. Teymori, H. Khorsandi, A.A. Aghapour, S.J. Jafari, R. Maleki, Electro-Fenton method for the removal of Malachite Green: effect of operational parameters, Appl Water Sci 10 (2019) 39. https://doi.org/10.1007/s13201-019-1123-5.
[35] K. Yin, L. Hao, G. Li, CuO nanosheets incorporated scrap steel slag coupled with persulfate catalysts for high-efficient degradation of sulfonamide from water, Environmental Research 216 (2023) 114614. https://doi.org/10.1016/j.envres.2022.114614.
[36] F.C. Ruiz, P.S. Martínez, E.B. Castro, R. Humana, H.A. Peretti, A. Visintin, Effect of electrolyte concentration on the electrochemical properties of an AB5-type alloy for Ni/MH batteries, International Journal of Hydrogen Energy 38 (2013) 240–245. https://doi.org/10.1016/j.ijhydene.2012.10.007.
[37] L. Wang, J. Jiang, J. Ma, S. Pang, T. Zhang, A review on advanced oxidation processes homogeneously initiated by copper(II), Chemical Engineering Journal 427 (2022) 131721. https://doi.org/10.1016/j.cej.2021.131721.
[38] H. Zhao, X. Shen, Y. Chen, S.-N. Zhang, P. Gao, X. Zhen, X.-H. Li, G. Zhao, A COOH-terminated nitrogen-doped carbon aerogel as a bulk electrode for completely selective two-electron oxygen reduction to H2O2, Chem. Commun. 55 (2019) 6173–6176. https://doi.org/10.1039/C9CC02580D.
[39] E. Yousif, R. Haddad, Photodegradation and photostabilization of polymers, especially polystyrene: review, SpringerPlus 2 (2013) 398. https://doi.org/10.1186/2193-1801-2-398.
[40] R. Betancourt-Galindo, C. Cabrera Miranda, B.A. Puente Urbina, A. Castañeda-Facio, S. Sánchez-Valdés, J. Mata Padilla, L.A. García Cerda, Y.A. Perera, O.S. Rodríguez-Fernández, Encapsulation of Silver Nanoparticles in a Polystyrene Matrix by Miniemulsion Polymerization and Its Antimicrobial Activity, International Scholarly Research Notices 2012 (2012) 186851. https://doi.org/10.5402/2012/186851.
[41] L.P. Domínguez-Jaimes, E.I. Cedillo-González, E. Luévano-Hipólito, J.D. Acuña-

Bedoya, J.M. Hernández-López, Degradation of primary nanoplastics by photocatalysis using different anodized TiO2 structures, Journal of Hazardous Materials 413 (2021) 125452. https://doi.org/10.1016/j.jhazmat.2021.125452.

[42] D. lal S, S.J. T, R. C, Solid-phase photodegradation of polystyrene by nano TiO2 under ultraviolet radiation, Environmental Nanotechnology, Monitoring & Management 12 (2019) 100229. https://doi.org/10.1016/j.enmm.2019.100229.

[43] D. Ortiz, M. Munoz, J. Nieto-Sandoval, C. Romera-Castillo, Z.M. de Pedro, J.A. Casas, Insights into the degradation of microplastics by Fenton oxidation: From surface modification to mineralization, Chemosphere 309 (2022) 136809. https://doi.org/10.1016/j.chemosphere.2022.136809.

[44] P. Liu, L. Qian, H. Wang, X. Zhan, K. Lu, C. Gu, S. Gao, New Insights into the Aging Behavior of Microplastics Accelerated by Advanced Oxidation Processes, Environ. Sci. Technol. 53 (2019) 3579–3588. https://doi.org/10.1021/acs.est.9b00493.

[45] M.L. Goodson, R. Lagle, P. Guggilla, X-Ray Photoelectron Spectroscopy of Polystyrene Composite Films, J Adv Mater Sci Eng 2 (2022). https://doi.org/10.33425/2771-666X.1007.

[46] X. Chen, X. Wang, D. Fang, A review on C1s XPS-spectra for some kinds of carbon materials, Fullerenes, Nanotubes and Carbon Nanostructures 28 (2020) 1048–1058. https://doi.org/10.1080/1536383X.2020.1794851.

[47] M. Smith, L. Scudiero, J. Espinal, J.-S. McEwen, M. Garcia-Perez, Improving the deconvolution and interpretation of XPS spectra from chars by ab initio calculations, Carbon 110 (2016) 155–171. https://doi.org/10.1016/j.carbon.2016.09.012.

[48] W. Guo, Q. Zhao, J. Du, H. Wang, X. Li, N. Ren, Enhanced removal of sulfadiazine by sulfidated ZVI activated persulfate process: Performance, mechanisms and degradation pathways, Chemical Engineering Journal 388 (2020) 124303. https://doi.org/10.1016/j.cej.2020.124303.

[49] M. Tong, F. Liu, Q. Dong, Z. Ma, W. Liu, Magnetic Fe3O4-deposited flower-like MoS2 nanocomposites for the Fenton-like *Escherichia coli* disinfection and diclofenac degradation, Journal of Hazardous Materials 385 (2020) 121604. https://doi.org/10.1016/j.jhazmat.2019.121604.

[50] S. Mao, C. Liu, Y. Wu, M. Xia, F. Wang, Porous P, Fe-doped g-C3N4 nanostructure with enhanced photo-Fenton activity for removal of tetracycline hydrochloride: Mechanism insight, DFT calculation and degradation pathways, Chemosphere 291 (2022) 133039. https://doi.org/10.1016/j.chemosphere.2021.133039.

[51] J. Lu, R. Hou, Y. Wang, L. Zhou, Y. Yuan, Surfactant-sodium dodecyl sulfate enhanced degradation of polystyrene microplastics with an energy-saving electrochemical advanced oxidation process (EAOP) strategy, Water Research 226 (2022) 119277. https://doi.org/10.1016/j.watres.2022.119277.

[52] Y. Cai, F. Chen, L. Yang, L. Deng, Z. Shi, Degradation of Polystyrene Nanoplastics in UV/NaClO and UV/PMS Systems: Insights into Degradation Efficiency, Mechanism, and Toxicity Evaluation, Water 15 (2023) 1920. https://doi.org/10.3390/w15101920.

[53] Z. Cai, X. Hao, X. Sun, P. Du, W. Liu, J. Fu, Highly active WO3@anatase-SiO2 aerogel for solar-light-driven phenanthrene degradation: Mechanism insight and toxicity assessment, Water Research 162 (2019) 369–382. https://doi.org/10.1016/j.watres.2019.06.017.

6 Discussion and conclusions

6.1 Narrative discussion

The first study developed a FeNi alloy carbon aerogel (FeNi-CA) cathode, which exhibited excellent bifunctional properties by catalysing the $2e^-$ oxygen reduction reaction (ORR) for H_2O_2 production and activating H_2O_2 into reactive hydroxyl radicals (·OH). The incorporation of Fe and Ni into the carbon aerogel matrix resulted in improved electron transfer, oxygen utilisation, and catalytic efficiency, enabling effective acetaminophen degradation across a wide pH range (3-9). Through optimisation, the system achieved up to 99.9% ACT removal within 120 minutes, with the degradation process primarily driven by electro-Fenton oxidation and electro-sorption mechanisms. Furthermore, the FeNi-CA cathode demonstrated reproducible performance over five cycles without requiring external aeration, thus reducing the operative cost and enhancing its industrial applicability. Degradation intermediates were identified, and a possible degradation pathway was proposed. These results highlight FeNi-CA as a promising candidate for scalable and sustainable EF applications targeting organic contaminants.

Building on the success of FeNi-CA, the second study introduced a CuCo carbon aerogel (CuCo-CA) cathode to target tetracycline, a widely used antibiotic and representative micropollutant. The integration of Cu and Co significantly enhanced the cathode's performance, facilitating efficient H_2O_2 generation and activation without external oxygen input. This enhancement was attributed to the synergistic effects of Cu and Co, which improved conductivity, mass transfer, and ORR activity. The CuCo-CA EF system achieved 94% tetracycline removal within 2.5 hours at neutral pH, demonstrating superior efficiency and stability over a wide pH range (3–9). Importantly, the system maintained catalytic performance over six cycles and exhibited long-term stability over 48-hour continuous operation. The study also demonstrated the system's effectiveness against various micropollutants, showcasing its versatility for advanced water treatment applications.

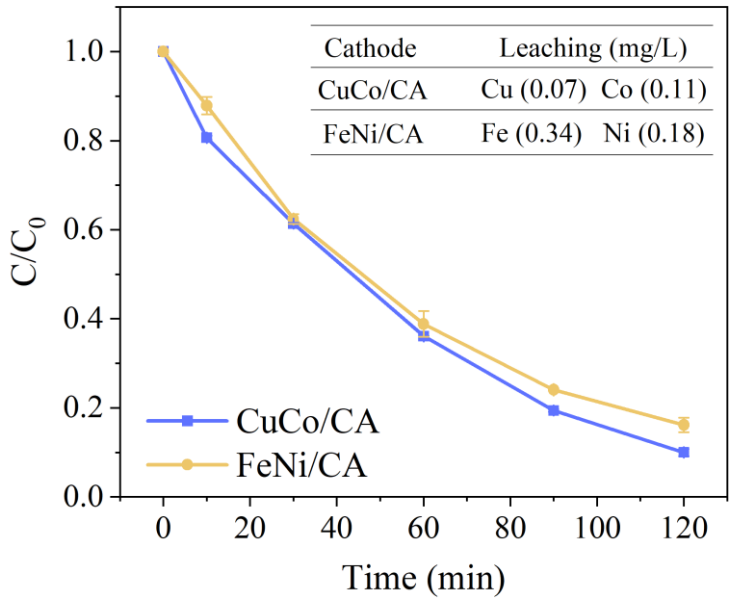

Figure 6.1. Comparison of acetaminophen removal and metal leaching using FeNi-CA or CuCo-CA as the cathode. Conditions: ACT-10mg/L, pH_0=7.0, 20mA, without aeration.

As shown in Figure 6.1, the CuCo-CA cathode performed better in the degradation of acetaminophen in the electro-Fenton system, and the amount of metal dissolved after the reaction was less than that of the FeNi-CA cathode under the same conditions. The third study extended the application of CuCo-CA to addressing emerging plastic contaminants, focusing on the degradation of polystyrene nanoplastics (PS-NPs). The CuCo-CA cathode enabled efficient *in situ* H_2O_2 generation and activation, resulting in effective ·OH production and PS-NP degradation without external aeration. The system achieved a reaction rate constant of 0.4906 h^{-1} and demonstrated robust recyclability across five consecutive runs. Structural and compositional changes in PS-NPs were characterised, revealing fragmentation of polymer chains, surface oxidation, and particle agglomeration. Hydroxyl radicals predominantly attacked the aromatic rings and carbon atoms in the polymer backbone, leading to the mineralisation of toxic intermediates into harmless end products. After six hours of treatment, the system achieved a total organic carbon (TOC) removal efficiency of 73.7%, ensuring the safety of treated water. These findings suggest the CuCo-CA EF system is a promising technology for small-scale nanoplastic treatment in water decontamination areas.

The comparative analysis of FeNi-CA and CuCo-CA cathodes underscores the significance of material design in EF technologies. While both cathodes exhibited

excellent bifunctional capabilities for H_2O_2 generation and activation, CuCo-CA demonstrated higher activity and lower metal leaching, making it a superior candidate for complex pollutants like PS-NPs. The studies collectively reveal key mechanistic insights, including:

- Enhanced ORR performance and Fenton catalytic activity driven by incorporating transition metal alloys.
- Synergistic effects of alloyed metals in improving oxygen utilisation, eliminating the need for external aeration.
- The carbon aerogel matrix encapsulates the metal particles, reducing metal leaching and expanding the pH application range.
- Effective degradation pathways are enabled by reactive oxygen species, with broad applicability across organic pollutants.

Overall, this work developed stable and efficient cathodes, expanded EF applicability across different pH ranges, reduced energy consumption, deepened mechanistic understanding, and highlighted the environmental safety of treated water. These findings provide a robust foundation for developing sustainable and efficient EF technologies for water treatment. Building on these advancements, the next step is to explore their implementation in large-scale systems, where operational efficiency, cost-effectiveness, and long-term stability become critical factors. A practical EF system for industrial applications would likely consist of a continuous-flow electrochemical reactor equipped with integrated cathodes optimised for *in situ* H_2O_2 generation and activation, such as FeNi-CA and CuCo-CA, and an anode. The system would also include pH control units, electrolyte recirculation, and automated monitoring for oxidation byproducts and metal leaching. Industrial-scale EF systems could be integrated into modular advanced oxidation process units, similar to commercialised ozonation or UV-Fenton systems, allowing flexibility for wastewater treatment plants or specialised chemical manufacturing sectors.

6.2 Conclusion and future work

This thesis explored the development and application of novel integrated cathode materials in heterogeneous electro-Fenton (EF) systems to address the environmental crisis of pharmaceutically active compounds (PhACs) and micro/nano-plastic (MP/NP). Across three studies, FeNi-CA and CuCo-CA bifunctional cathodes were synthesised and

systematically investigated for their performance in degrading representative pollutants—acetaminophen (ACT), tetracycline (TC), and polystyrene nanoplastics (PS-NP). The synergistic effects of componential metals on structural characteristics, electrochemical properties, and degradation performance were comprehensively investigated. Additionally, the degradation mechanisms, intermediates, and pathways of these pollutants were elucidated. The findings demonstrate the potential of EF systems employing these advanced cathodes as eco-friendly, efficient, and scalable solutions for water decontamination.

This thesis highlights the potential of advanced EF systems for addressing emerging water contaminants. The developed cathodes offer significant advantages, including scalability, operational stability, and adaptability to diverse pollutants. The established electro-Fenton processes have notable advantages in wastewater treatment, such as high efficiency in pollutant degradation and mineralisation, simple operation, and the use of readily available materials. However, several challenges need to be addressed, including the development of cost-effective and long-lasting electrode materials, optimisation of reactor design, and proper management of iron catalysts for disposal or reuse. Furthermore, most studies have been conducted on a small scale, highlighting the need for further research to support its application in large-scale industrial settings.

Future research could focus on the following aspects:

- **Scalability**: most studies are conducted in controlled laboratory environments, which does not account for the complexity of real wastewater treatment operations. The effects of scaling up EF technologies in practical conditions, such as municipal and industrial wastewater treatment plants, remain unexplored.
- **Complex matrixes**: wastewater matrixes are complex cocktails of different pollutants, future research should focus on evaluating the performance and stability of these catalysts in real wastewater matrixes, considering their interactions with diverse co-existing contaminants. Investigating catalyst selectivity and long-term efficiency under complex environmental conditions will be crucial for practical applications.
- **Combined pollutants**: plastics often act as carriers for other contaminants. Studies investigating the interaction of plastics with co-existing organic and inorganic pollutants in real water matrices, and their influence on EF degradation

performance and pathways are poorly studied.

- **Cost:** economic feasibility of EF related to reagents, apparatus, and electricity remains uncertain, especially for large-scale applications. Detailed techno-economic evaluations are necessary to assess the feasibility and competitiveness of Electro Fenton systems.
- **Integration with other methods**: hybridising EF with biological or adsorption processes to improve pollutant removal and lower operational costs needs further exploration. Research on integrating EF with other advanced oxidation processes (AOPs) or renewable energy sources to enhance cost-effectiveness and sustainability is limited.

Appendix A: Publication list

Journal Publications

1. **Qian Ye**, Timothy N. Hunter*, Hao Xu, David Harbottle, Girish M. Kale, Martin R. Tillotson*. Synergistic effect of Fe and Ni on carbon aerogel for enhanced oxygen reduction and H_2O_2 activation in electro-Fenton process. Separation and Purification Technology (IF 8.2). Volume 353, Part B, 2025, 128436. ISSN 1383-5866, https://doi.org/10.1016/j.seppur.2024.128436.

2. **Qian Ye**, Timothy N. Hunter*, Hao Xu, David Harbottle, Girish M. Kale, Martin R. Tillotson*. CuCo carbon aerogel as a bifunctional cathode for Electro-Fenton processes: Unveiling synergistic effects and catalytic mechanisms. Separation and Purification Technology (IF 8.2). Volume 361, Part 3, 2025. 131597, ISSN 1383-5866, https://doi.org/10.1016/j.seppur.2025.131597.

3. **Qian Ye**, Hao Xu, Timothy N. Hunter*, David Harbottle, Girish M. Kale, Martin R. Tillotson*. Advanced polystyrene nanoplastic remediation through electro-Fenton process: degradation mechanisms and pathways. Submitted to journal.

Conference Attendance

1. Postgraduate Researcher Annual Conference, Oral presentation, 1st May 2023, School of Civil Engineering, University of Leeds (UK).

2. 36th Topical Meeting of the International Society of Electrochemistry: Marine and environmental electrochemistry in the era of new technologies. Poster presentation, "Development of Novel Cathodes in Electrochemical Catalysis Systems for Water Treatment". 26-29th May 2024, Sibenik (Croatia).

Appendix B: Supplementary materials for chapter 3

Electronic Supplementary Materials (ESM) for Chapter 3 “Synergistic effect of Fe and Ni on carbon aerogel for enhanced oxygen reduction and H_2O_2 activation in electro-Fenton process”.

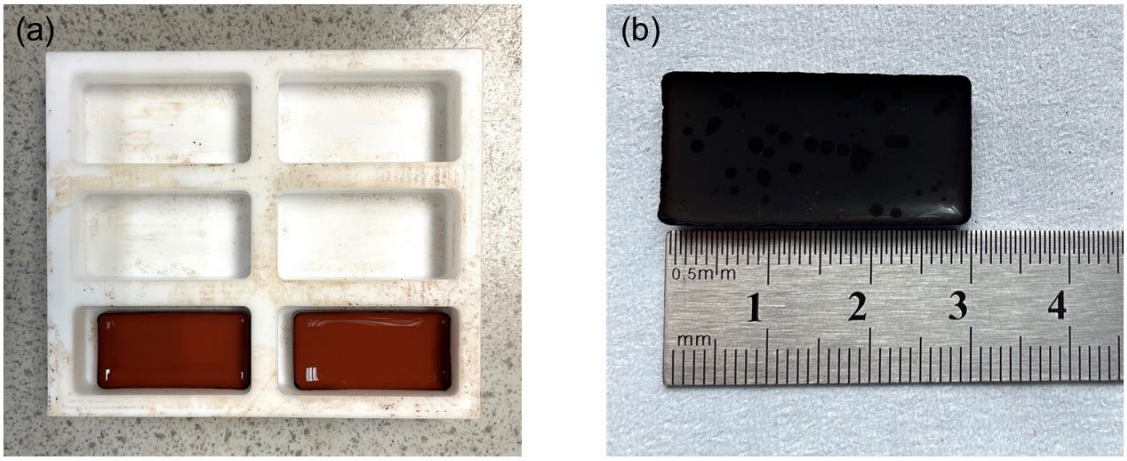

Fig S3.1. (a) Obtained wet gel after polymerisation and aging stage, and (b) FeNi-CA cathode after carbonisation.

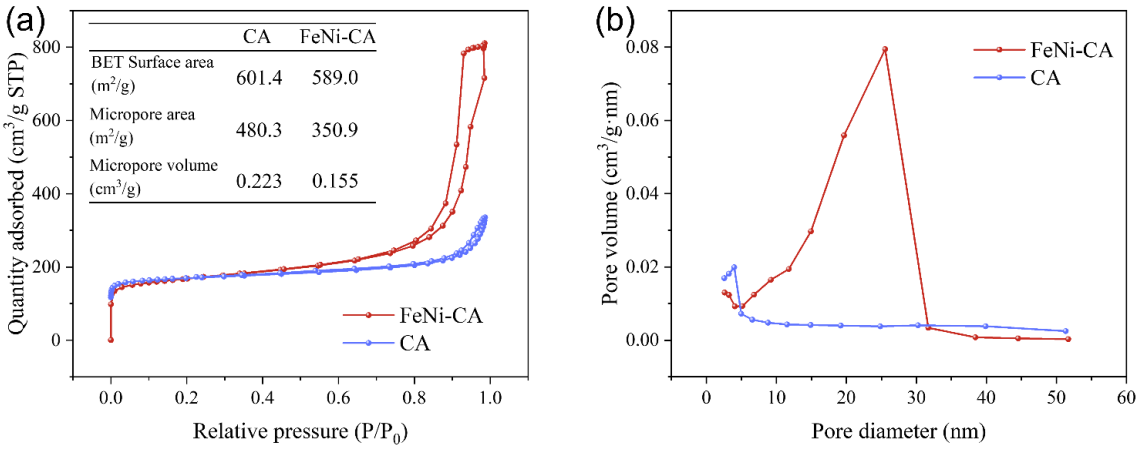

Fig S3.2. (a) N_2 adsorption–desorption isotherms. (b) Pore size distribution curves of pure CA and FeNi-CA.

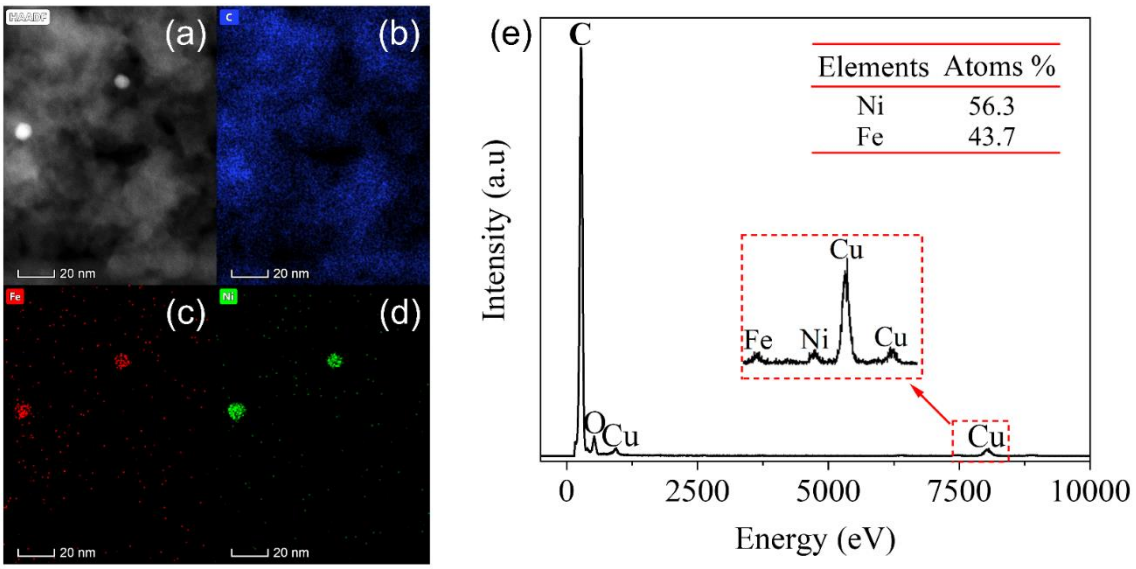

Fig S3.3. (a) STEM images of FeNi-CA, (b) EDS mapping of elemental C, (c) EDS mapping of elemental Fe, (d) EDS mapping of elemental Ni, and (e) EDS spectra of the selected area.

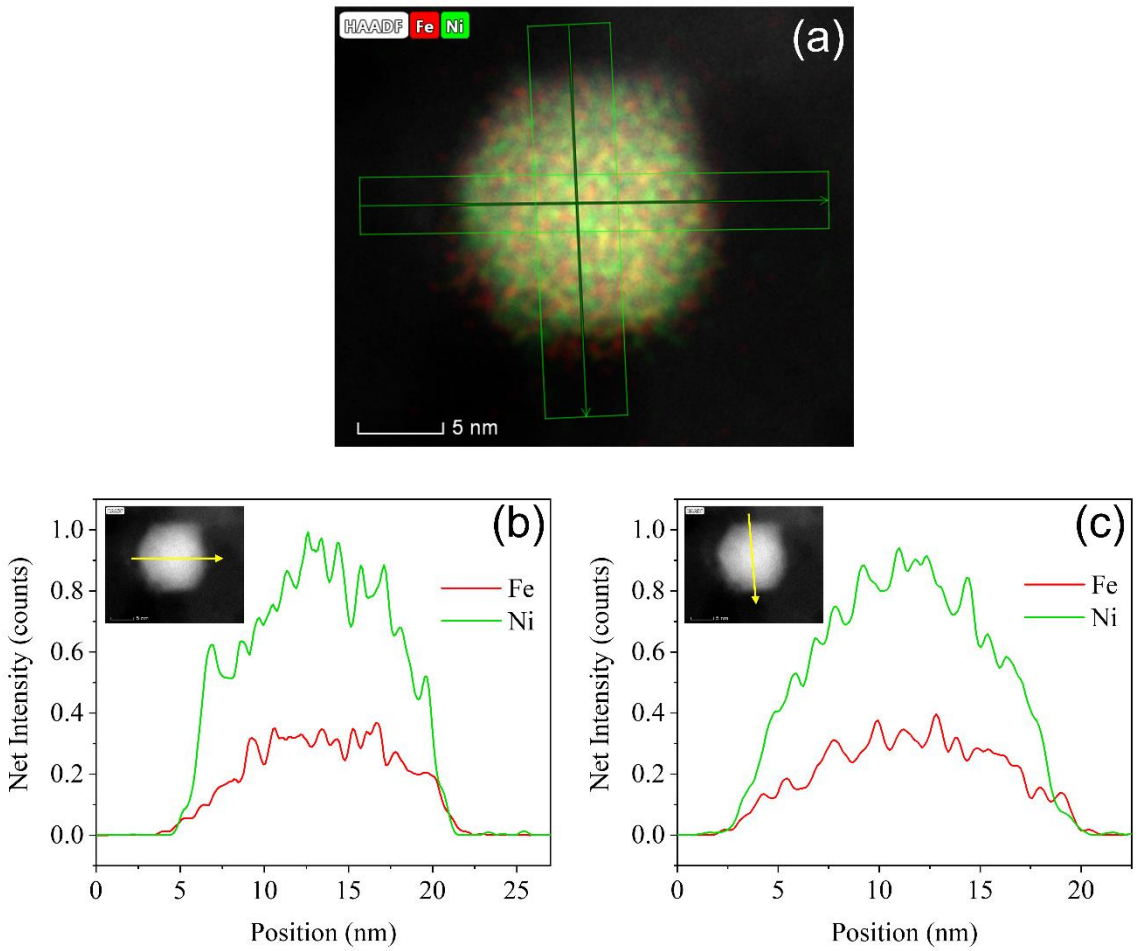

Fig S3.4. (a) EDS line scanning profiles of a single $FeNi_3$ alloy particle, at (b) horizontal direction, and (c) vertical direction.

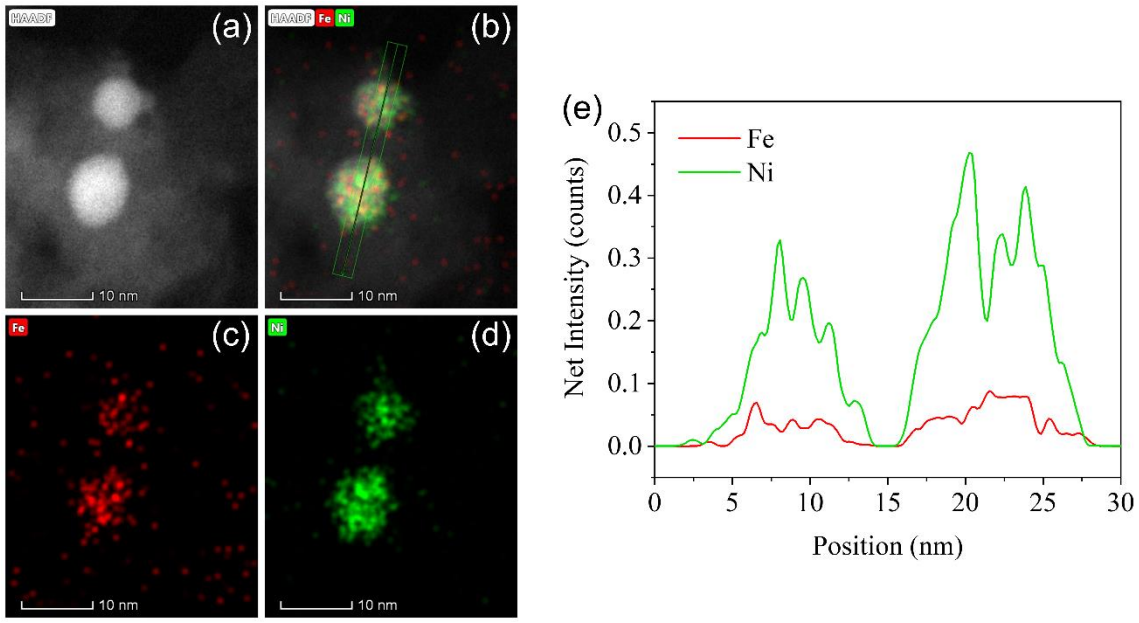

Fig S3.5. (a) HAADF-STEM images of FeNi-CA, (b) EDS line scanning, (c) EDS mapping of elemental Fe, (d) EDS mapping of elemental Ni, (e) Line scanning profile of Fe and Ni element.

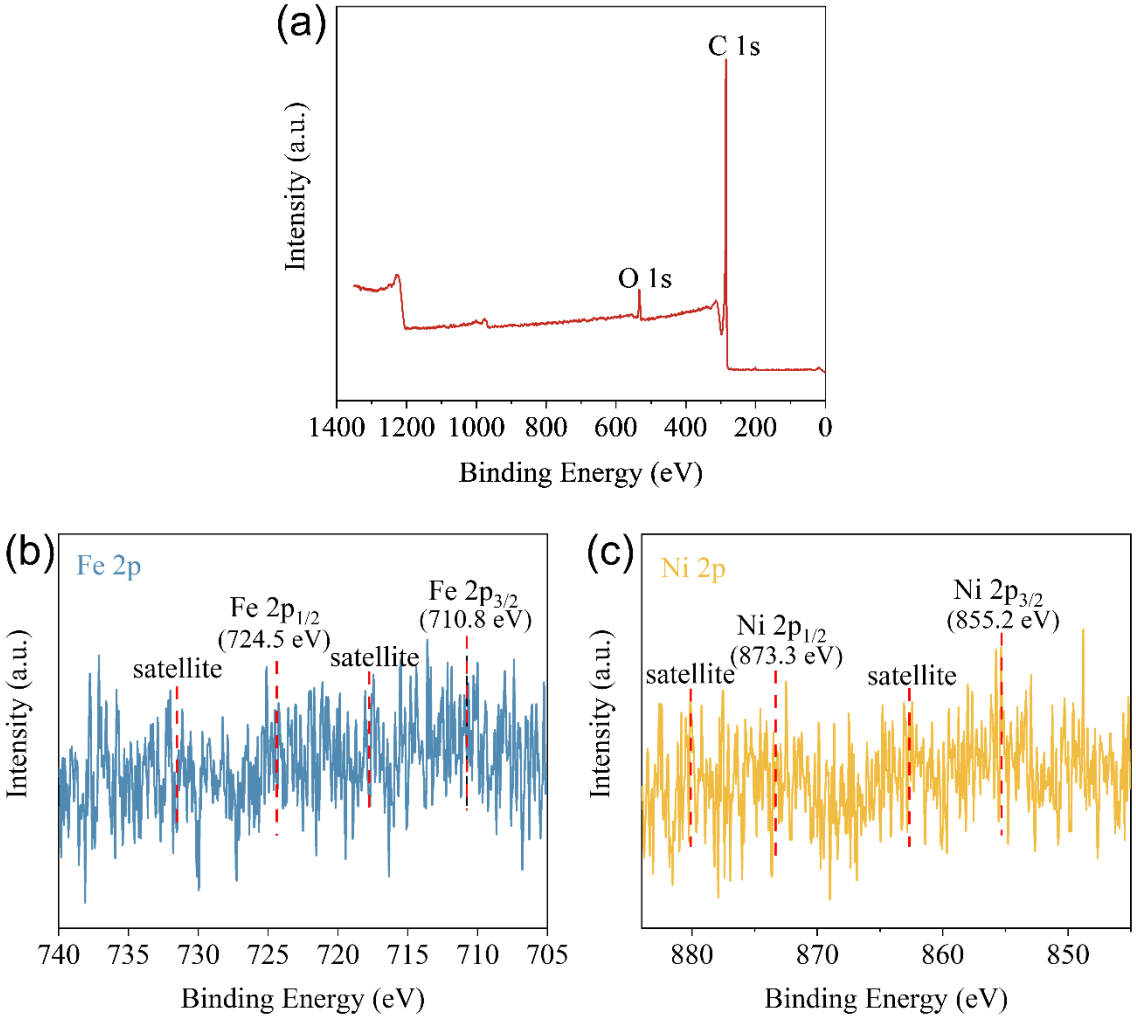

Fig S3.6. (a) XPS full spectrum of FeNi-CA, (b) Fe 2p XPS spectrum, and (c) Ni 2p XPS spectrum.

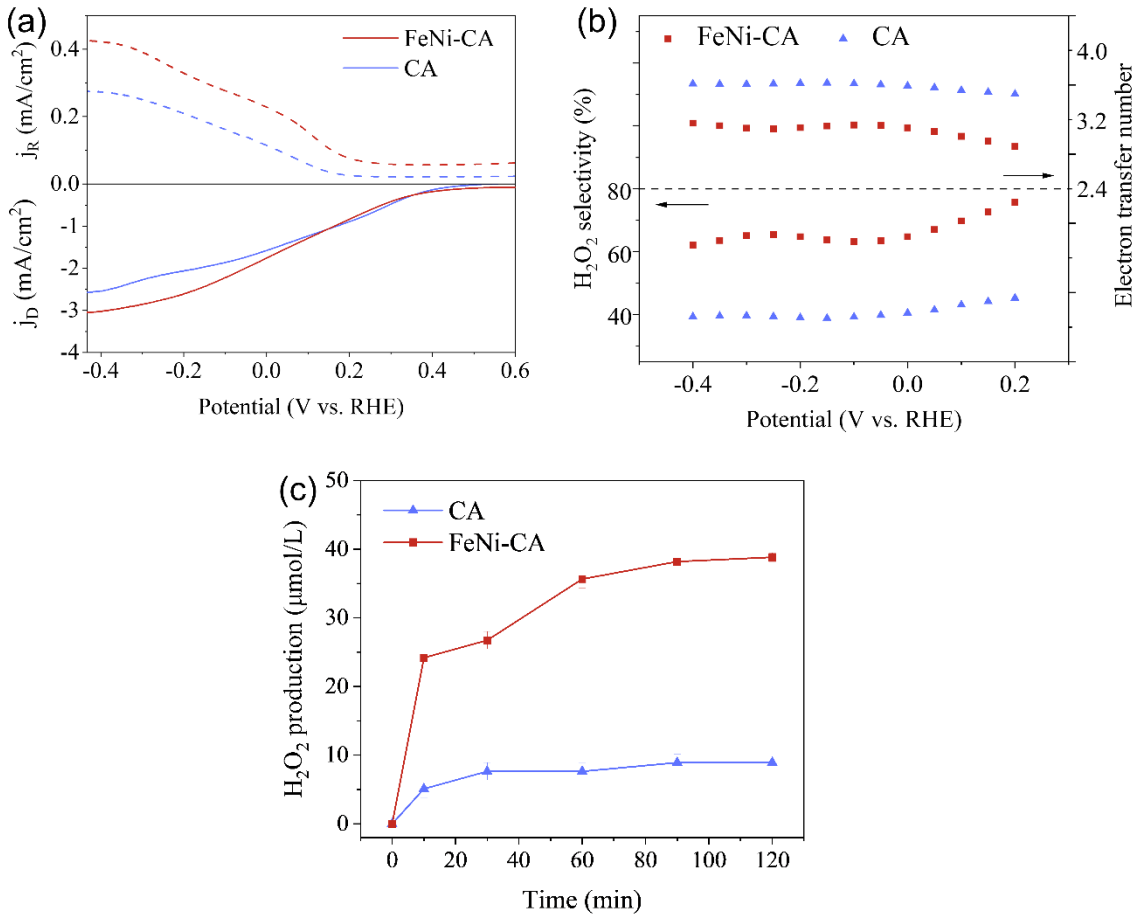

Fig S3.7. (a) Polarisation curves and simultaneous H_2O_2 oxidation currents at the ring electrode in 0.1 mol/L Na_2SO_4 at pH = 3. (b) Calculated electron transfer number and H_2O_2 selectivity. (c) H_2O_2 production in EF systems using FeNi-CA and CA as the electrode.

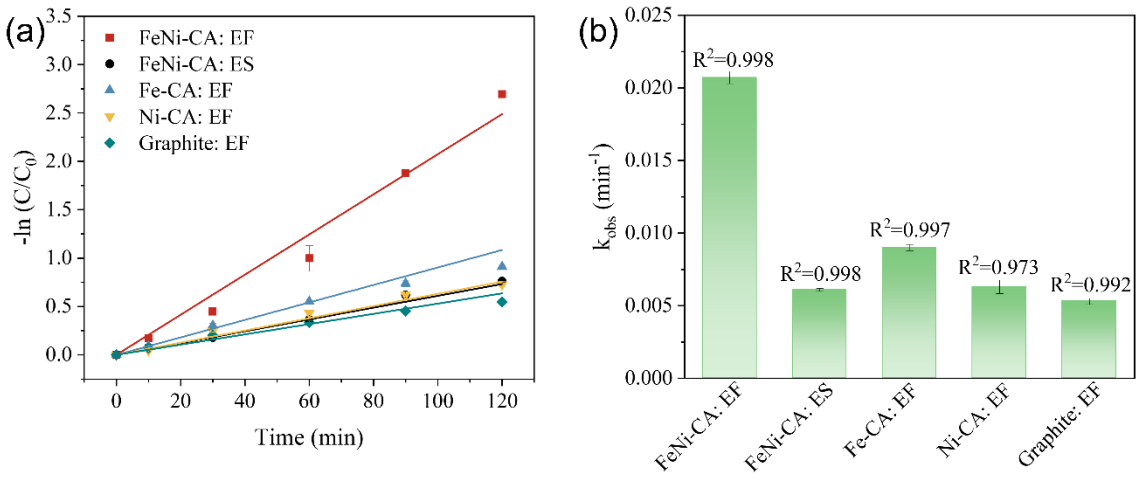

Fig S3.8. (a) Pseudo-first-order kinetics, and (b) Apparent rate constant of ACT degradation in electro-Fenton (EF) and electro-sorption (ES) system. Conditions: ACT-10 mg/L, Na_2SO_4-50 mM, pH_0-7.0, 0.4 L/min compressed air and 20 mA for EF system, 0.2 L/min N_2 and 1 mA for ES system.

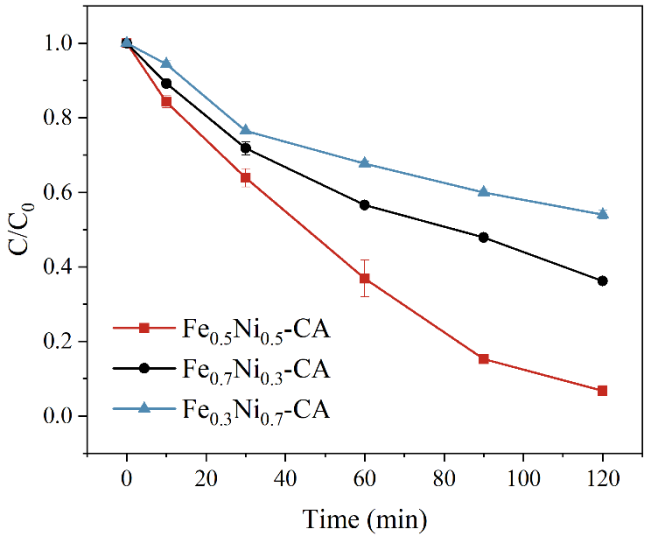

Fig S3.9. ACT degradation in EF systems using three cathodes with different metal contents. Conditions: ACT-10 mg/L, Na_2SO_4-50 mM, 20 mA, pH_0-7.0, 0.4 L/min compressed air.

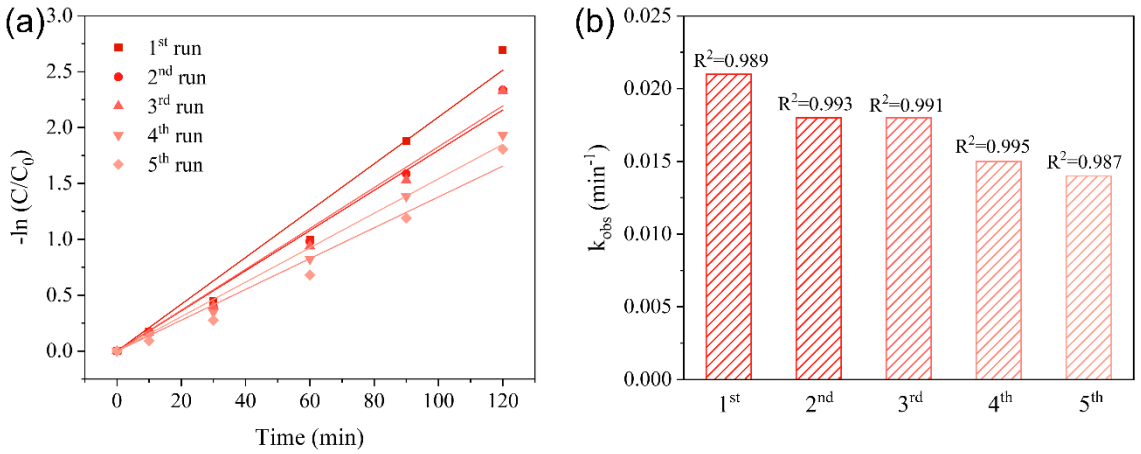

Fig S3.10. (a) Pseudo-first-order kinetics, and (b) Apparent rate constant of ACT degradation in recycle use of FeNi-CA cathode. Conditions: ACT-10 mg/L, Na_2SO_4-50 mM, pH_0-7.0, 20 mA, without aeration.

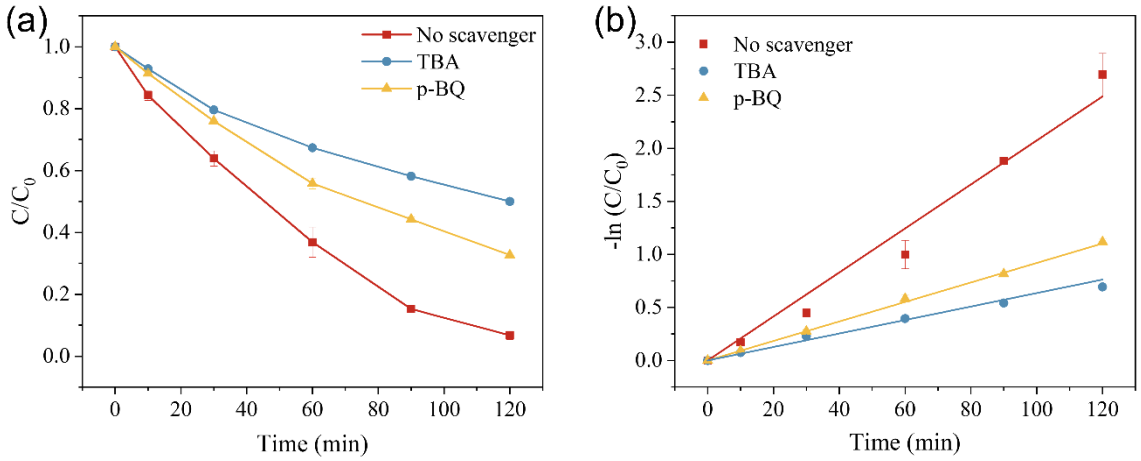

Fig S3.11. (a) The effect of radical scavengers on ACT degradation, and (b) Pseudo-first-order kinetics in FeNi-CA electro-Fenton system. Conditions: ACT-10 mg/L, Na_2SO_4-50 mM, TBA-1 M, p-BQ-2 mM, pH_0-7, 20 mA, 0.4 L/min compressed air.

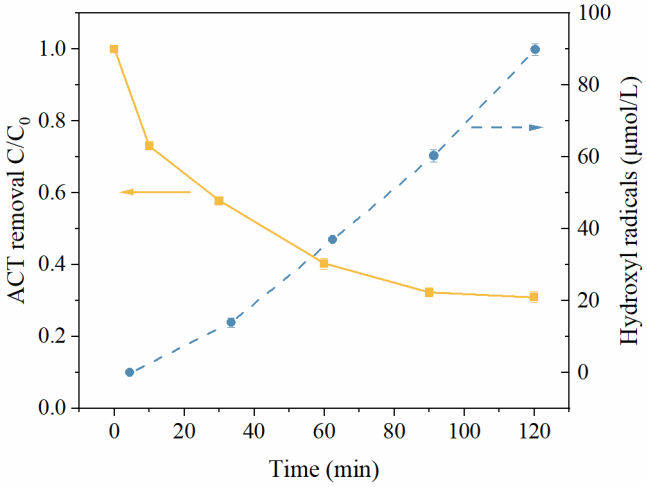

Fig S3.12. ACT removal (left) and hydroxyl radical generation (right) in the presence of FeNi-CA powder and externally supplied H_2O_2. Conditions: ACT-10 mg/L, H_2O_2-50 ppm, FeNi-CA-0.1 g/L, pH_0-5.4, salicylic acid-0.01 M.

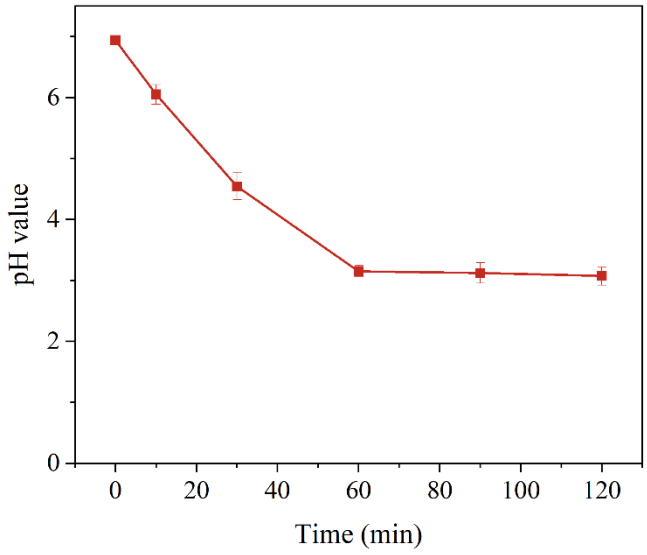

Fig S3.13. pH changes in FeNi-CA electro-Fenton system without contaminant. Conditions: Na_2SO_4-50 mM, 20 mA, compressed air-0.4 L/min.

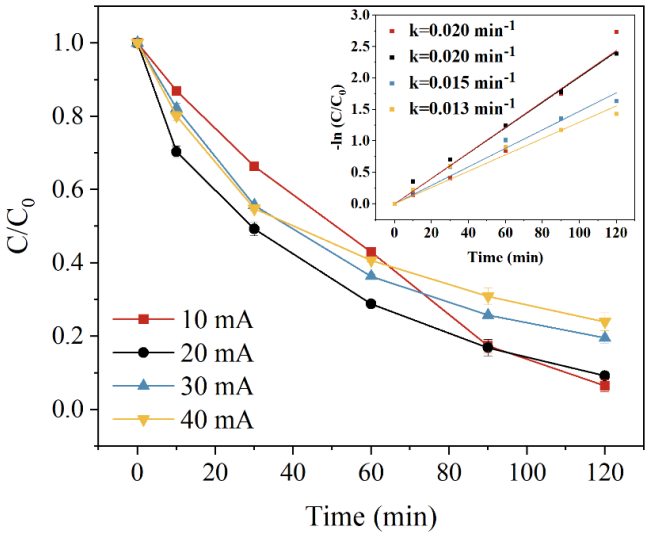

Fig S3.14. The effect of current on ACT degradation in FeNi-CA electro-Fenton system. Conditions: ACT-10 mg/L, Na_2SO_4-50 mM, pH_0-5.8, compressed air-0.4 L/min.

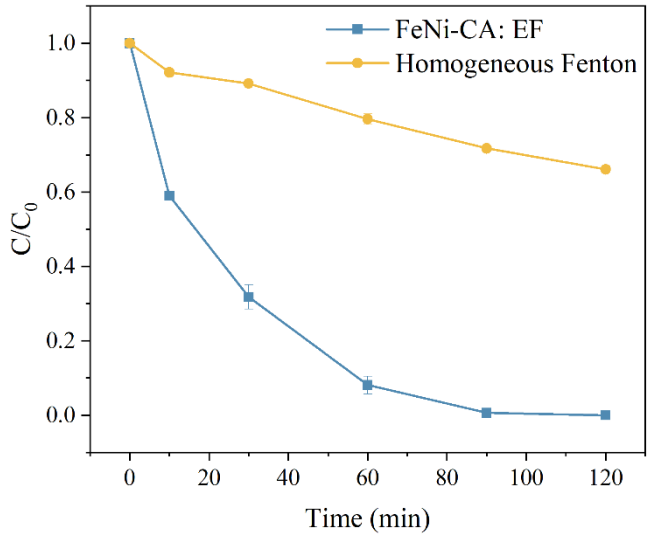

Fig S3.15. ACT degradation in FeNi-CA EF system and homogeneous Fenton system. Conditions in EF: ACT-10 mg/L, Na_2SO_4-50 mM, 20 mA, pH_0-3, compressed air-0.4 L/min. Conditions in homogeneous Fenton: ACT-10 mg/L, pH_0-3, Fe(III)-4 mg/L, Ni(II)-0.7 mg/L, H_2O_2-38.8 µmol/L.

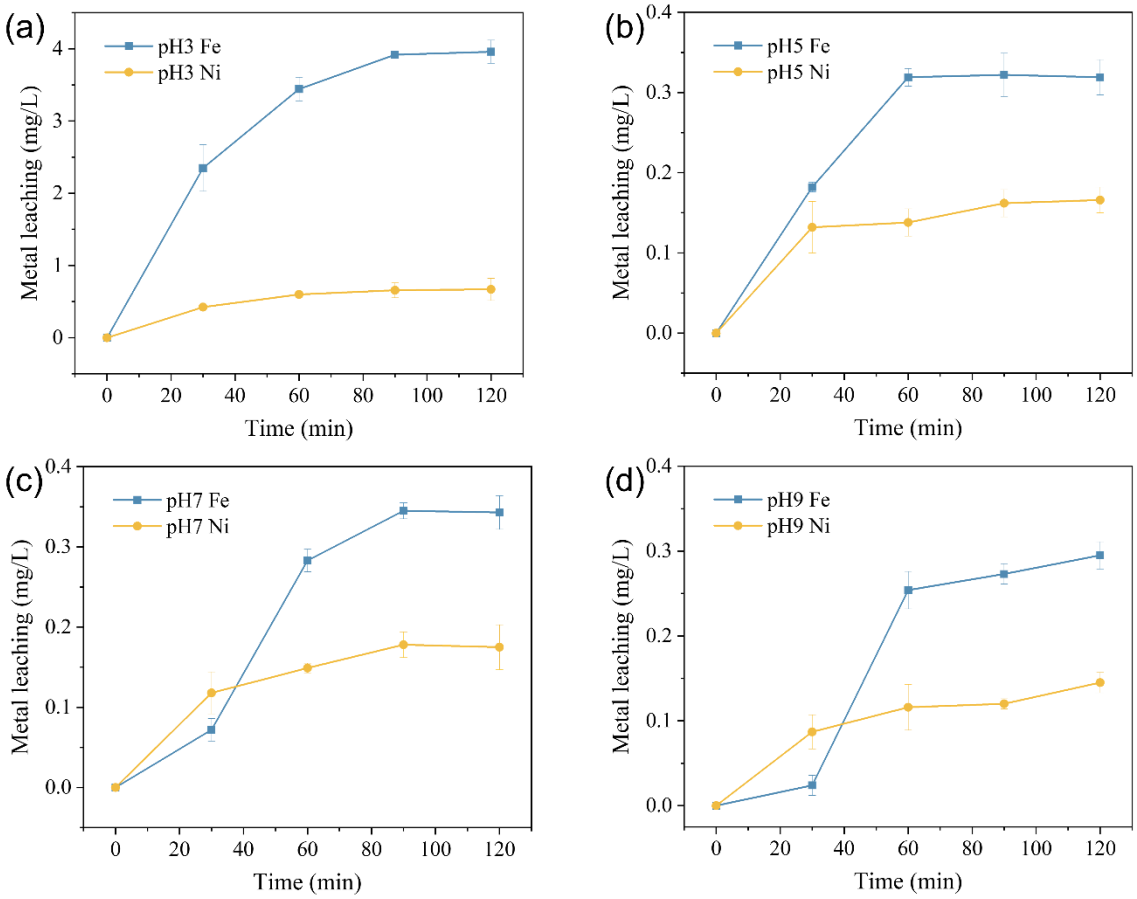

Fig S3.16. Metals leaching in FeNi-CA electro-Fenton system under (a) Initial pH of 3, (b) Initial pH of 5, (c) Initial pH of 7, and (d) Initial pH of 9. Conditions: ACT-10 mg/L, Na_2SO_4-50 mM, 20 mA, compressed air-0.4 L/min.

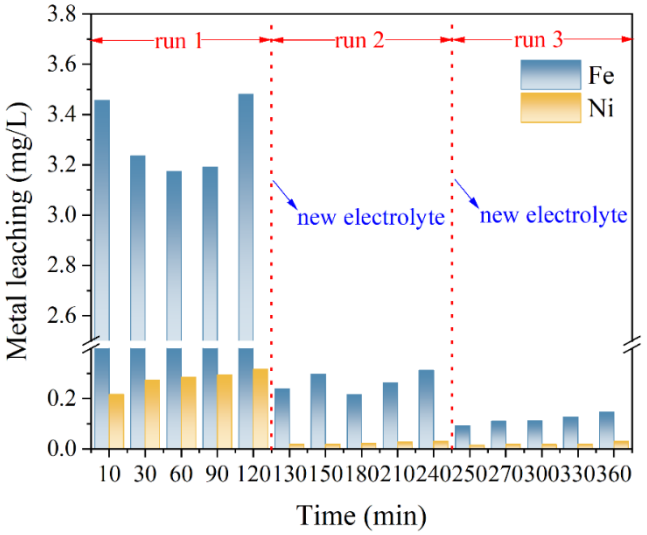

Fig S3.17. Metals leaching after pre-treatment in FeNi-CA electro-Fenton system. Conditions: pH_0-3, Na_2SO_4-50 mM, 20 mA, compressed air-0.4 L/min.

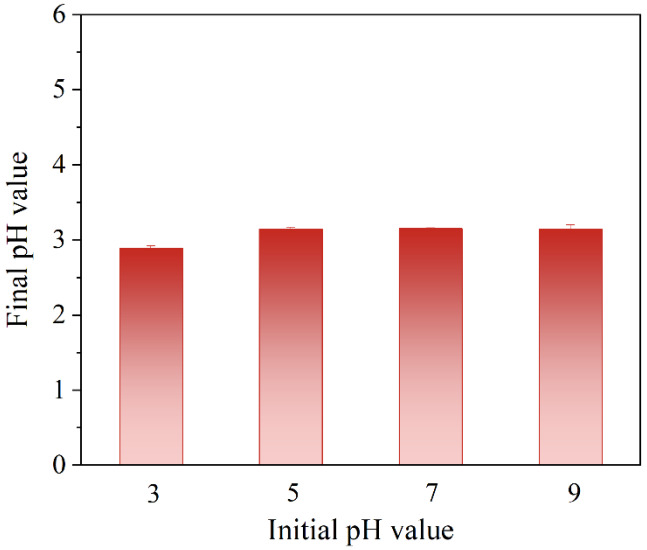

Fig S3.18. Final pH values after reaction in FeNi-CA electro-Fenton system under different initial pH. Conditions: ACT-10 mg/L, Na_2SO_4-50 mM, 20 mA, compressed air-0.4 L/min.

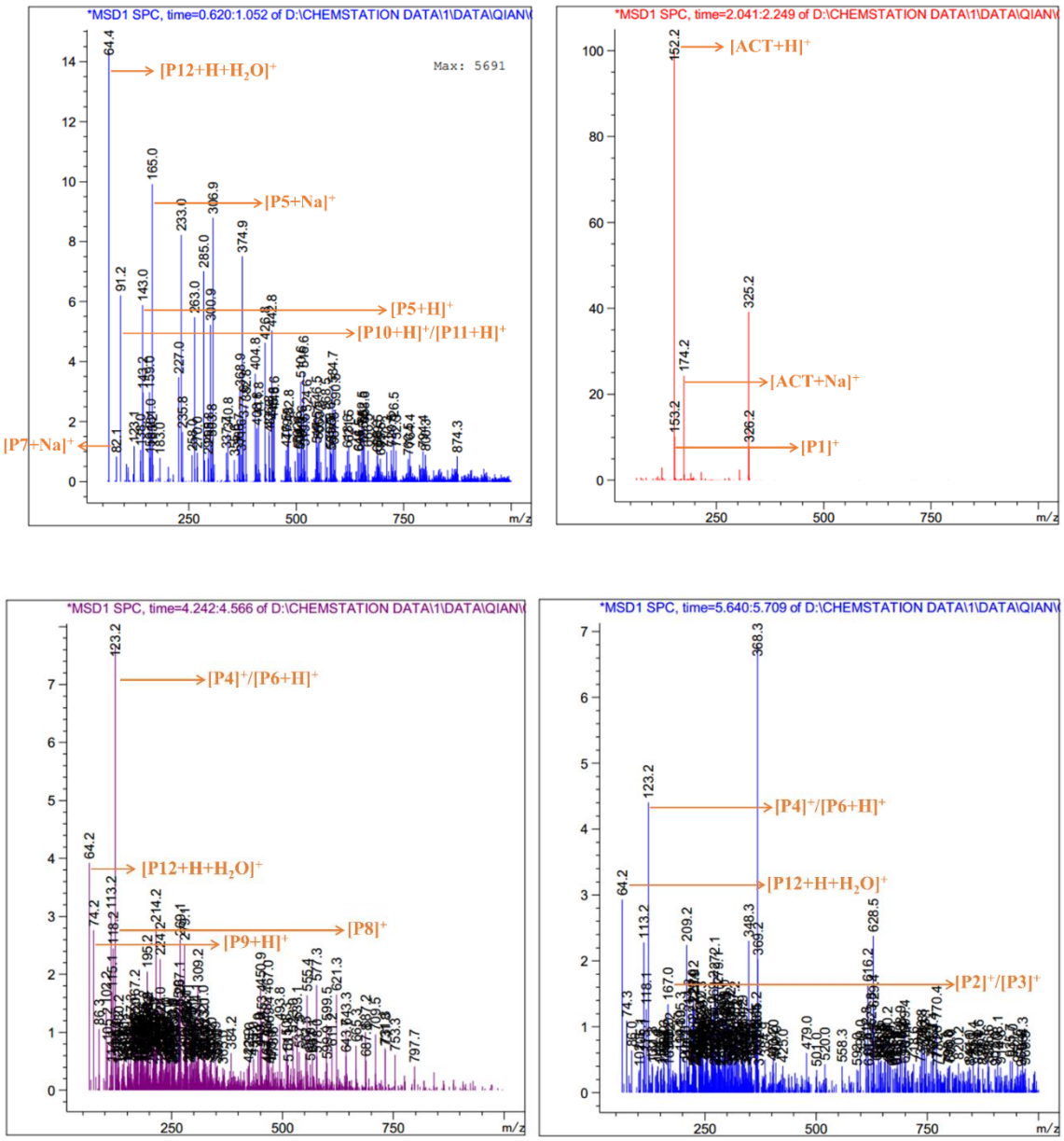

Fig S3.19. LC-MS spectra of ACT degradation intermediates.

Table S3.1. Structural information of identified intermediate products of ACT.

Products	m/z	Chemical name	Molecular formula	Structural formula
P1	153	N-(3,4-dihydroxyphenyl) formamide	$C_7H_7NO_3$	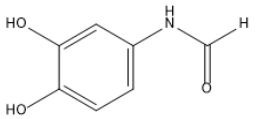
P2	167	N-(3,4-dihydroxyphenyl) acetamide	$C_8H_9NO_3$	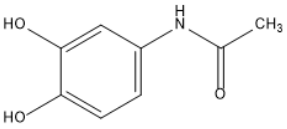
P3	167	N-(2,4-dihydroxyphenyl) acetamide	$C_8H_9NO_3$	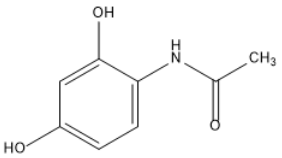
P4	123	4-(methylamino) phenol	C_7H_9NO	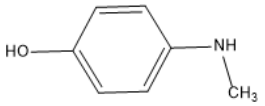
P5	142	(2Z,4Z)-hexa-2,4-dienedioic acid	$C_6H_6O_4$	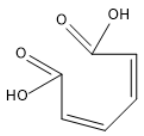
P6	122	Benzoic acid	$C_7H_6O_2$	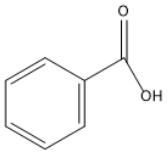
P7	59	Acetamide	C_2H_5NO	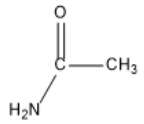
P8	118	Succinic acid	$C_4H_6O_4$	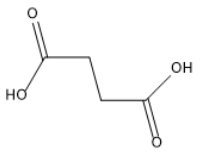
P9	73	Butan-1-amine	$C_4H_{11}N$	
P10	90	3-hydroxypropanoic acid	$C_3H_6O_3$	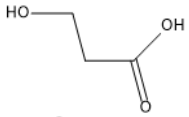
P11	90	Oxalic acid	$C_2H_2O_4$	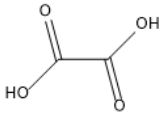
P12	45	Ethanamine	C_2H_7N	

Appendix C: Supplementary materials for chapter 4

Electronic Supplementary Materials (ESM) for Chapter 4 “CuCo carbon aerogel as a bifunctional cathode for Electro-Fenton processes: Unveiling synergistic effects and catalytic mechanisms”.

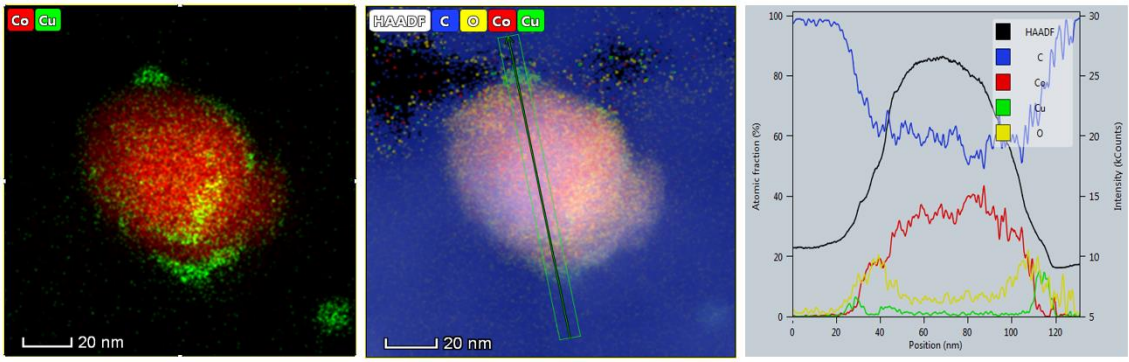

Figure S4.1. (a) EDS elemental mapping of Co and Cu; (b) and (c) EDS line scanning.

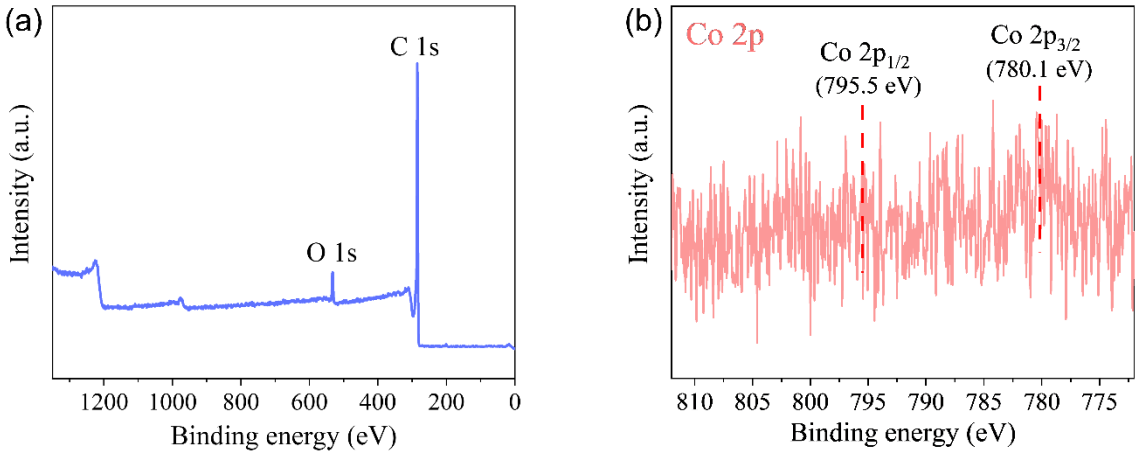

Figure S4.2. (a) Full XPS spectrum and (b) Co 2p XPS spectrum of CuCo/CA.

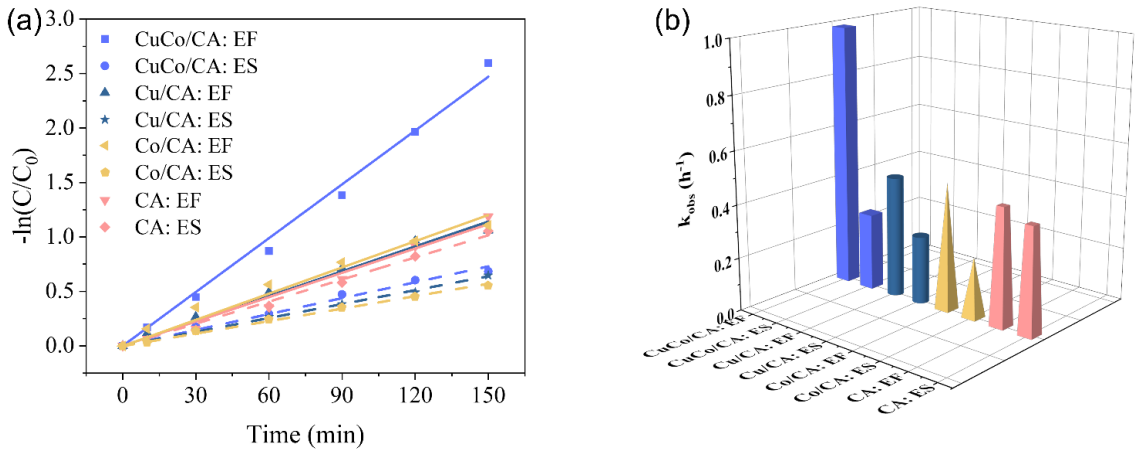

Figure S4.3. (a) Pseudo-first-order kinetics, and (b) apparent rate constant of TC degradation in different systems. Conditions: TC=10 mg/L, Na_2SO_4=50 mM, pH_0=7.0, no external aeration and 20 mA for EF systems; 0.2 L/min N_2 and 1 mA for ES systems.

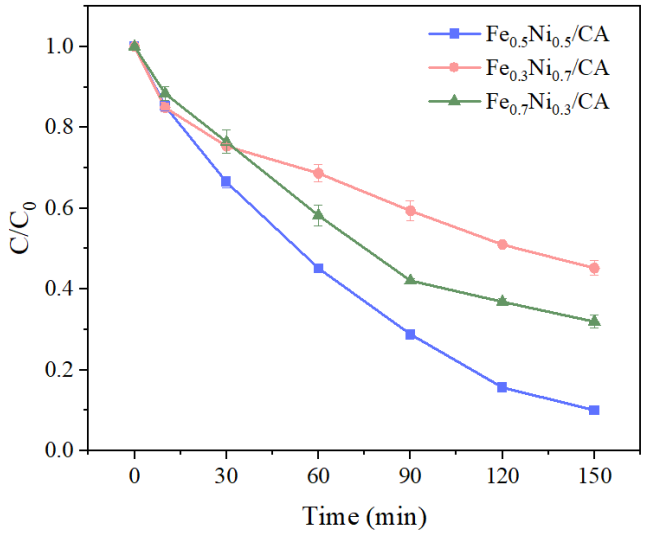

Figure S4.4. Investigation of Cu/Co ratio in CuCo/CA cathode. Conditions: pH_0-7.0, Na_2SO_4-50 mM, TC-10 mg/L, 20 mA, no external aeration.

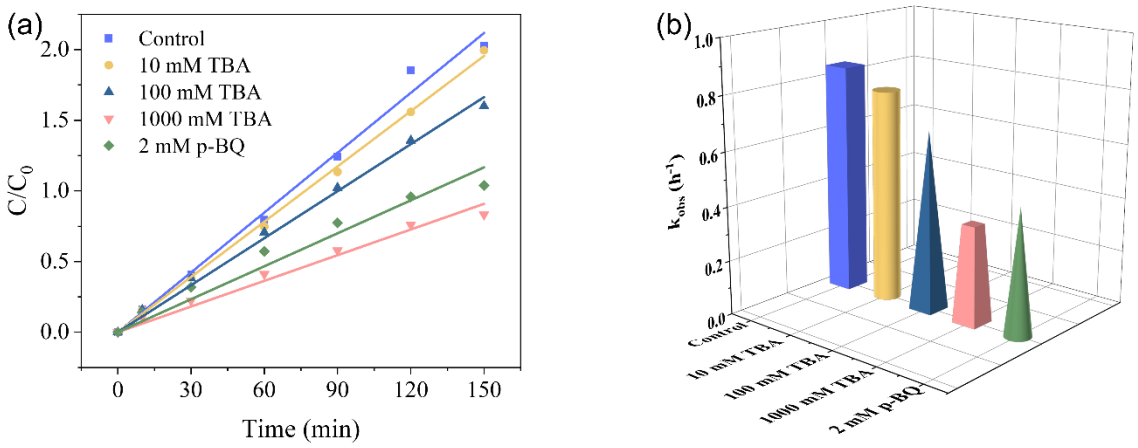

Figure S4.5. (a) Pseudo-first-order kinetics, and (b) apparent rate constant of TC degradation in CuCo/CA EF systems with and without radical scavengers. Conditions: pH_0-7.0, Na_2SO_4-50 mM, TC-10 mg/L, 20 mA, no external aeration.

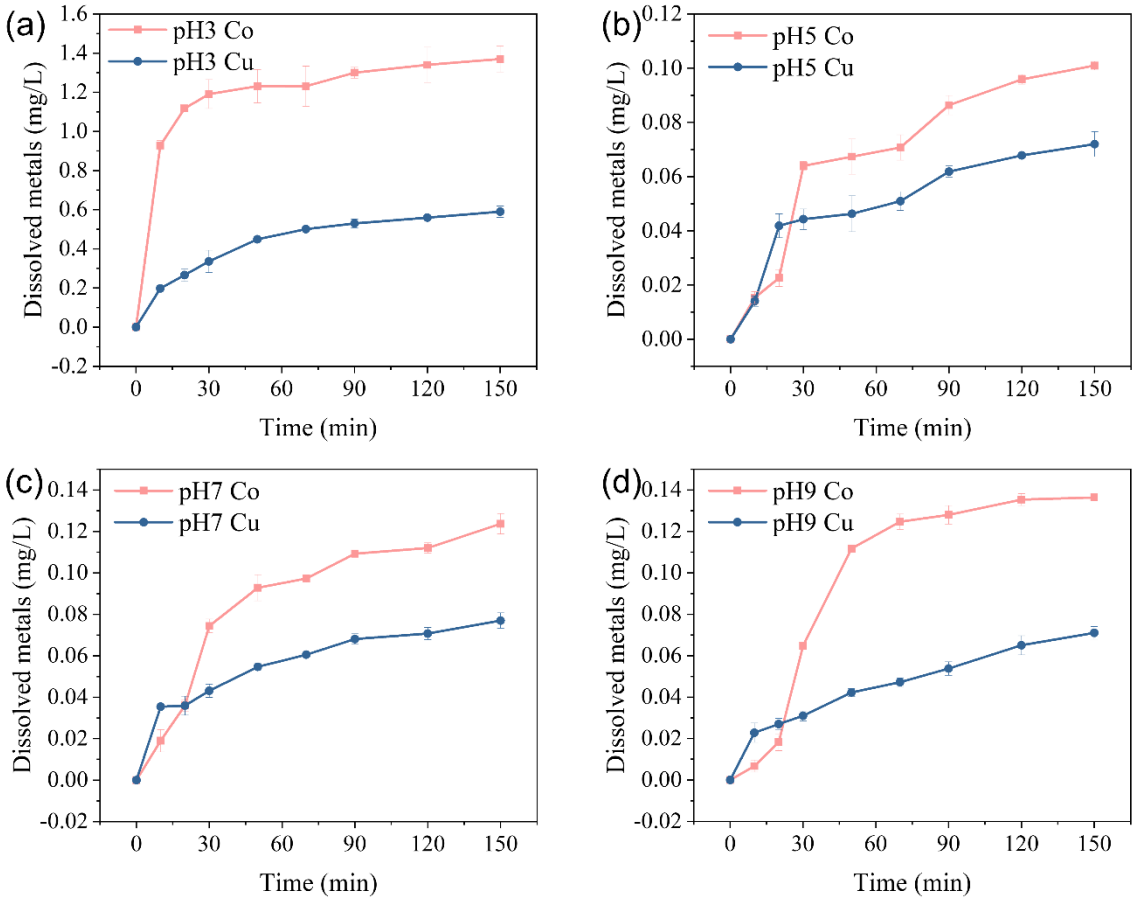

Figure S4.6. Metal leaching in the CuCo/CA EF system under initial pH of (a) 3, (b) 5, (c) 7 and (d) 9. Conditions: TC=10 mg/L, Na_2SO_4=50 mM, 30 mA, no external aeration.

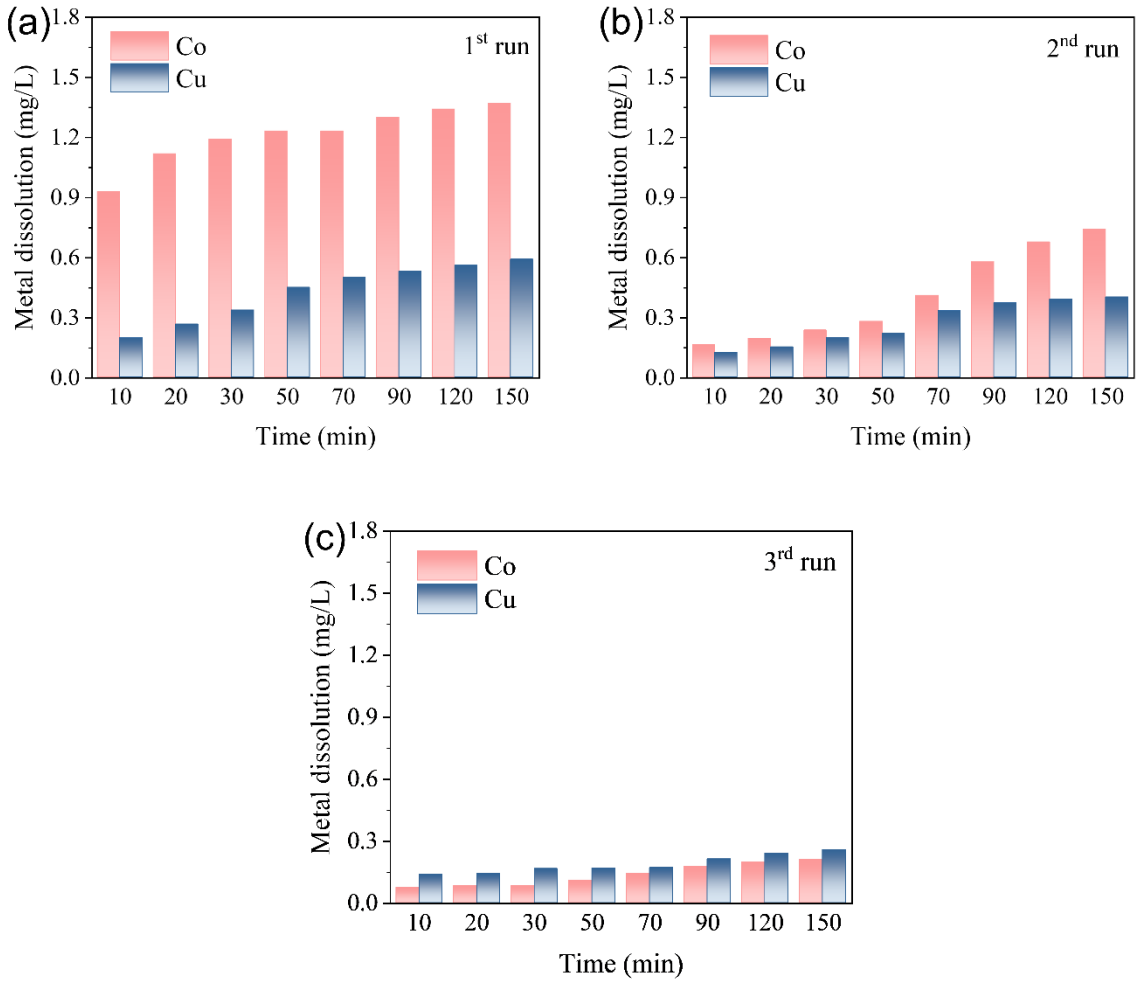

Figure S4.7. Concentrations of dissolved metals in three consecutive runs of the CuCo/CA EF system under initial pH of 3. Conditions: TC=10 mg/L, Na_2SO_4=50 mM, pH_0=3.0, 30 mA, no external aeration.

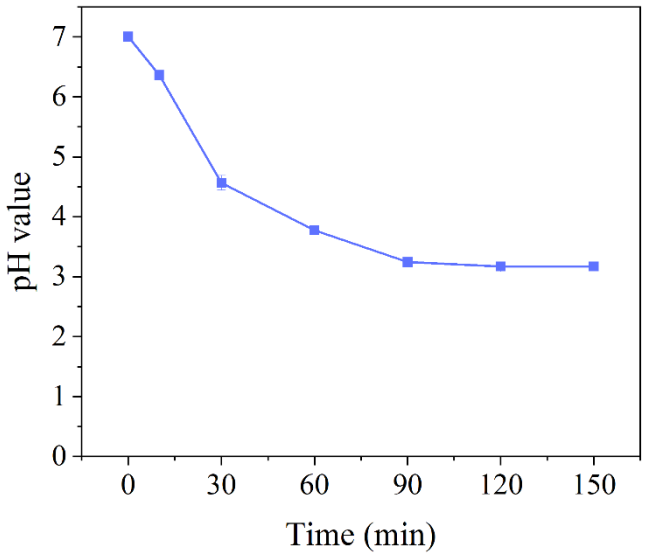

Figure S4.8. Change in pH value during TC degradation in the CuCo/CA EF system. Conditions: TC=10 mg/L, Na_2SO_4=50 mM, pH_0=7.0, 20 mA, no external aeration.

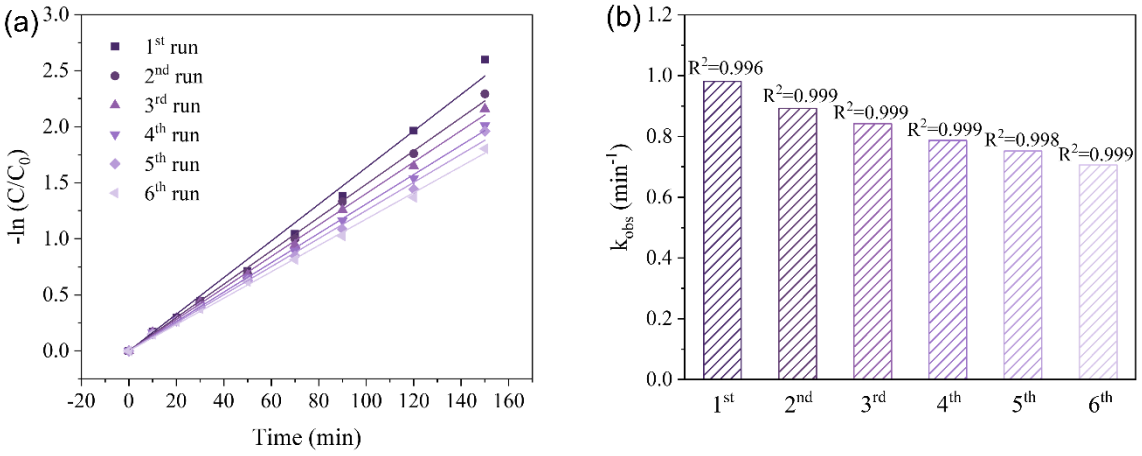

Figure S4.9. (a) Pseudo-first-order kinetics, and (b) Apparent reaction rate k_{obs} of TC degradation in 6 consecutive runs for the CuCo/CA EF system. Conditions: TC=10 mg/L, Na_2SO_4=50 mM, pH_0=7.0, 20 mA, no external aeration.

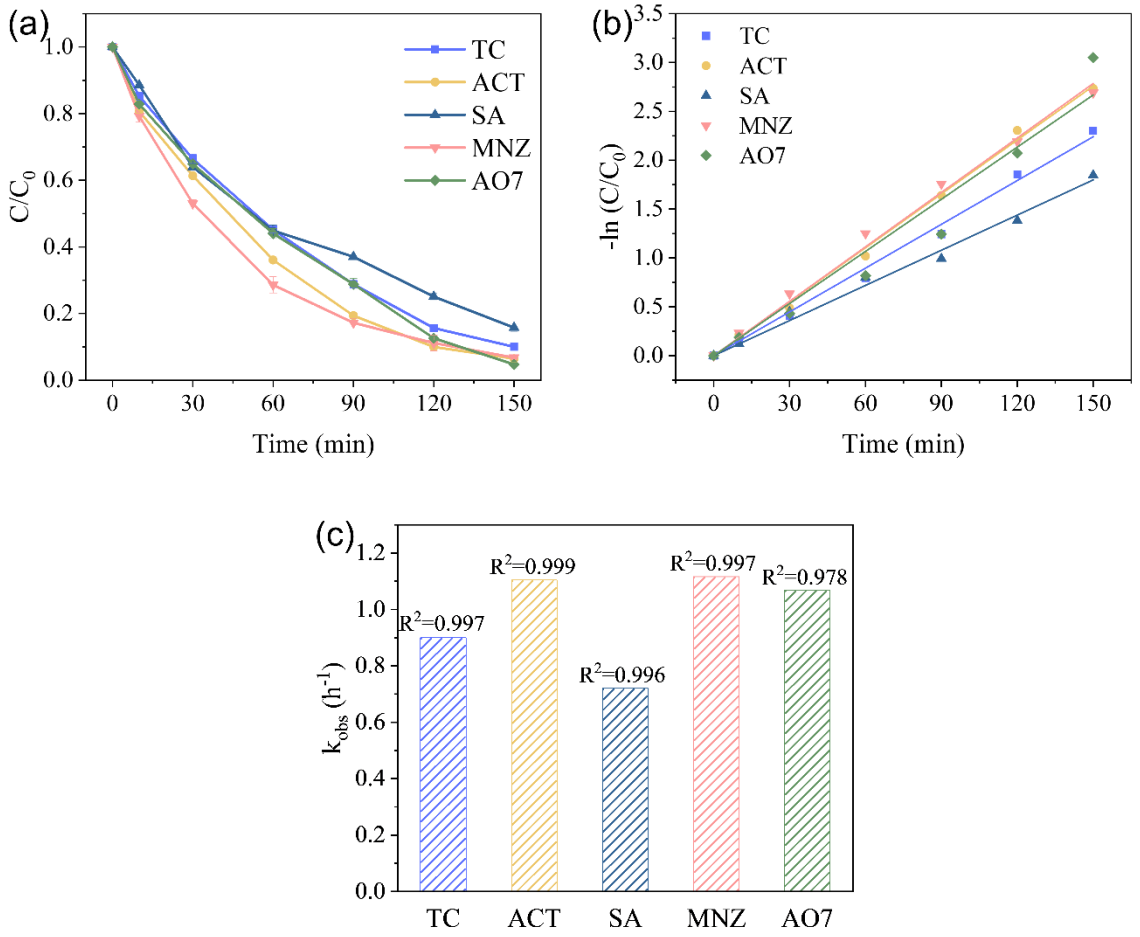

Figure S4.10. (a) Performances, (b) Pseudo-first-order kinetics, and (c) Apparent rate constants of various pollutants degradation in CuCo/CA EF system. Conditions: pollutant=10 mg/L, Na_2SO_4=50 mM, pH_0=7.0, 20 mA, no external aeration.

Table S4.1. Summary of ·OH production rate in other electro-Fenton systems.

Catalyst	Experimental conditions	Electrolyte	$k_{\cdot OH}$ (μM/min)	Ref.
Working: graphite felt Counter: platinum sheet Reference: saturated calomel electrode	7.5 wt% H_2O_2, 1.5 wt% Fe_3O_4, 0.75 V	0.3 M Na_2SO_4	0.604	[1]
Cathode: gas-diffusion-electrode Anode: iron plate	pH 3, 5.8 mA/cm^{-2}	0.05 M Na_2SO_4	0.183	[2]
Cathode: gas-diffusion-electrode Anode: Pt plate	1.5 L/min air rate, 100 mA, pH 3, 0.25 mM Fe^{2+}	0.05 M Na_2SO_4	0.5	[3]
Graphite sheet	1.0 V, 20 L/min air rate, pH 3, 10 μM Fe^{2+}	0.02 M Na_2SO_4	0.203	[4]
Cathode: CFF/CNT/Ni Anode: Ti/IrO_2-RuO_2	0.1 L/min air rate, pH 3, 40 mA/cm^2,	0.05 M Na_2SO_4	0.441	[5]
Cathode: Mn/Fe@porous carbon Anode: Pt	Air aeration, pH 3, 20 mA	0.1 M Na_2SO_4	0.733	[6]
Cathode: Ti mesh Anode: iron	0.04 L/min air rate, pH 4, 1.5 V, 50 mM H_2O_2	/	0.322	[7]
Cathode: CuCo/CA Anode: Pt	pH 3, 20 mA, no external aeration	0.05 M Na_2SO_4	0.834	This work

References

[1] J. Deng, J. Lu, Q. Yan, J. Pan, Basic research on chemical mechanical polishing of single-crystal SiC—Electro–Fenton: Reaction mechanism and modelling of hydroxyl radical generation using condition response modelling, Journal of Environmental Chemical Engineering 9 (2021) 104954. https://doi.org/10.1016/j.jece.2020.104954.

[2] D. Kubo, Y. Kawase, Hydroxyl radical generation in electro-Fenton process with in situ electro-chemical production of Fenton reagents by gas-diffusion-electrode cathode and sacrificial iron anode, Journal of Cleaner Production 203 (2018) 685–695. https://doi.org/10.1016/j.jclepro.2018.08.231.

[3] T. Yatagai, Y. Ohkawa, D. Kubo, Y. Kawase, Hydroxyl radical generation in electro-Fenton process with a gas-diffusion electrode: Linkages with electro-chemical generation of hydrogen peroxide and iron redox cycle, Journal of Environmental Science and Health, Part A 52 (2017) 74–83. https://doi.org/10.1080/10934529.2016.1229935.

[4] S. Qiu, D. He, J. Ma, T. Liu, T.D. Waite, Kinetic Modeling of the Electro-Fenton Process: Quantification of Reactive Oxygen Species Generation, Electrochimica Acta 176 (2015) 51–58. https://doi.org/10.1016/j.electacta.2015.06.103.

[5] T. Luo, H. Feng, L. Tang, Y. Lu, W. Tang, S. Chen, J. Yu, Q. Xie, X. Ouyang, Z. Chen, Efficient degradation of tetracycline by heterogeneous electro-Fenton process using Cu-doped Fe@Fe2O3: Mechanism and degradation pathway, Chemical Engineering Journal 382 (2020) 122970. https://doi.org/10.1016/j.cej.2019.122970.

[6] X. Zhou, D. Xu, Y. Chen, Y. Hu, Enhanced degradation of triclosan in heterogeneous E-Fenton process with MOF-derived hierarchical Mn/Fe@PC modified cathode, Chemical Engineering Journal 384 (2020) 123324. https://doi.org/10.1016/j.cej.2019.123324.

[7] Y. Chai, P. Qin, Z. Wu, M. Bai, W. Li, J. Pan, R. Cao, A. Chen, D. Jin, C. Peng, A coupled system of flow-through electro-Fenton and electrosorption processes for the efficient treatment of high-salinity organic wastewater, Separation and Purification Technology 267 (2021) 118683. https://doi.org/10.1016/j.seppur.2021.118683.

Appendix D: Supplementary materials for chapter 5

Electronic Supplementary Materials (ESM) for Chapter 5 “Advanced polystyrene nanoplastic remediation through electro-Fenton process: degradation mechanisms and pathways”.

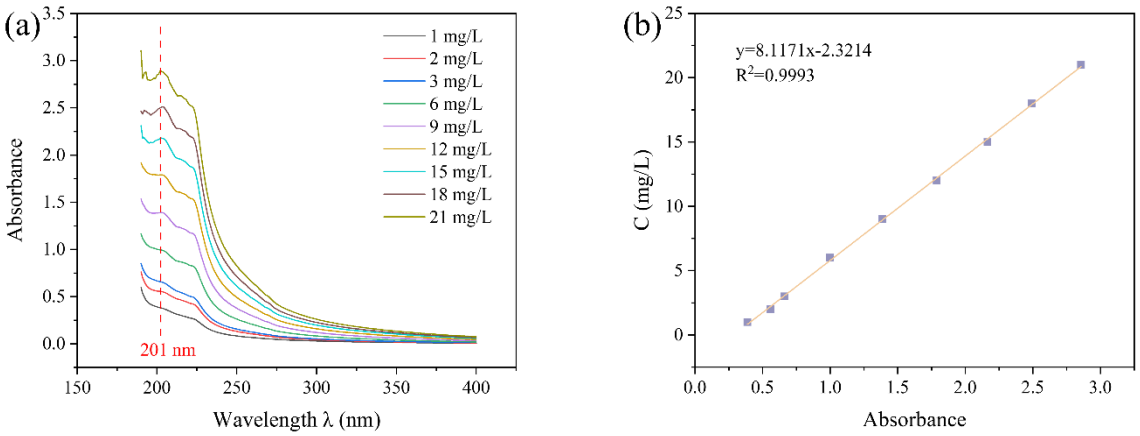

Fig S5.1. (a) Full wavelength scanning from 190 nm to 400 nm, and (b) Correlation between UV-vis absorbance and PS-NP concentration.

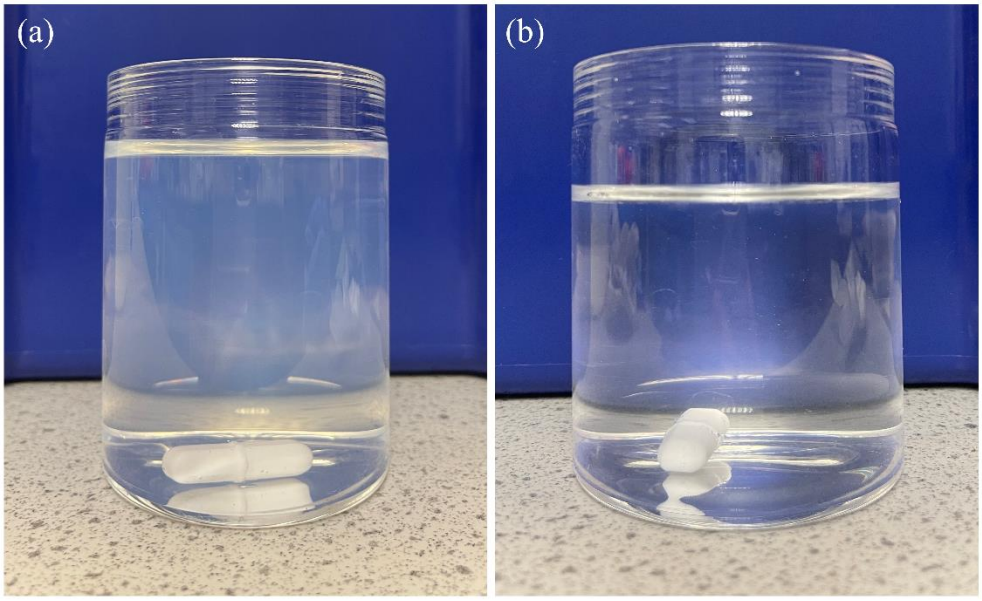

Fig S5.2. PS-NP suspension (a) pre-reaction, and (b) post-reaction. Conditions: [PS-NPs] = 20 mg/L, pH 7.0, applied current = 20 mA, [Na_2SO_4] = 0.05 mol/L, no aeration.

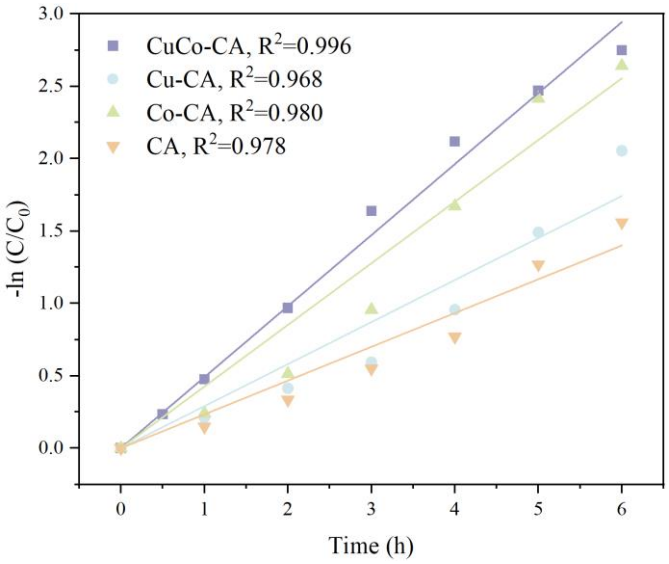

Fig S5.3. The pseudo-first-order kinetic fitting of PS-NP degradation in the electro-Fenton system with different cathodes. Conditions: [PS-NPs] = 20 mg/L, pH 7.0, applied current = 20 mA, [Na_2SO_4] = 0.05 mol/L, no aeration.

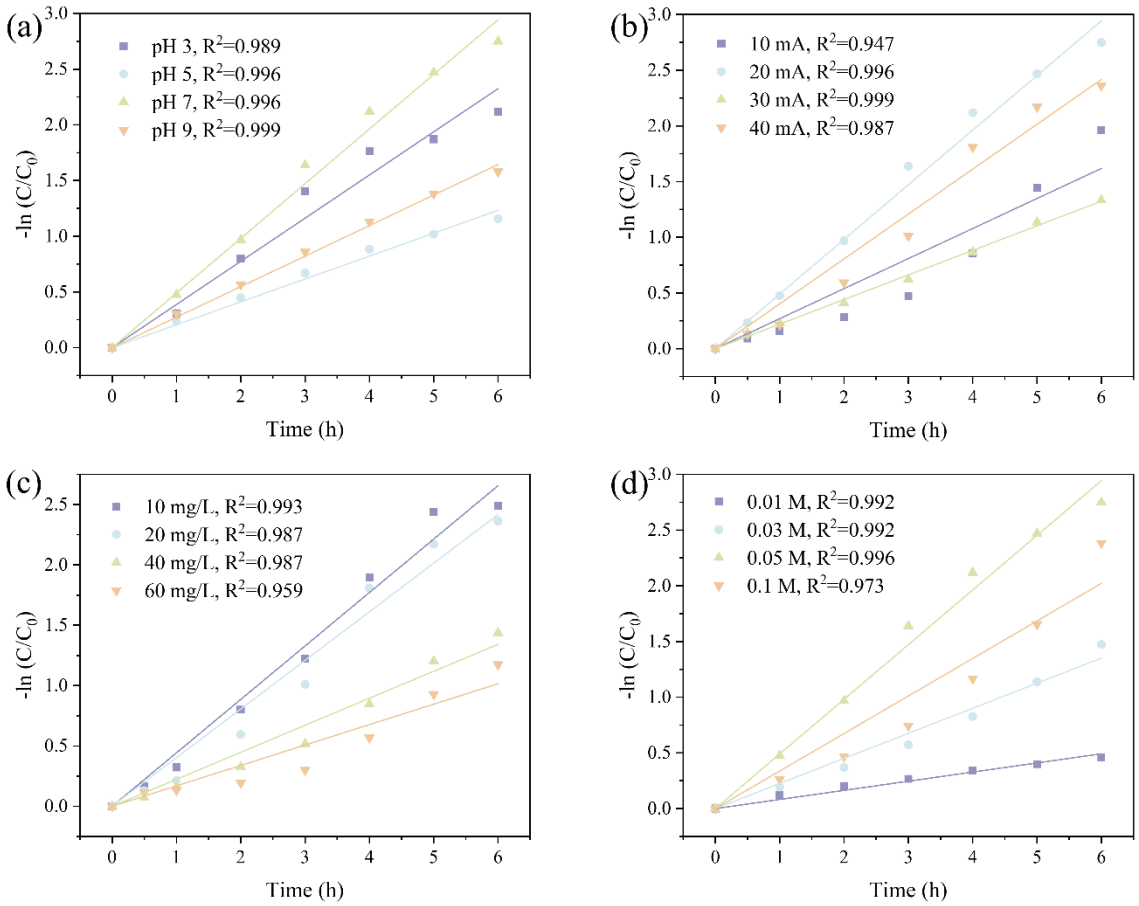

Fig S5.4. Pseudo-first-order kinetic fittings of PS-NP degradation under different conditions. (a) initial pH value; (b) applied current; (c) initial concentration of PS-NP; (d) Na_2SO_4 concentration.

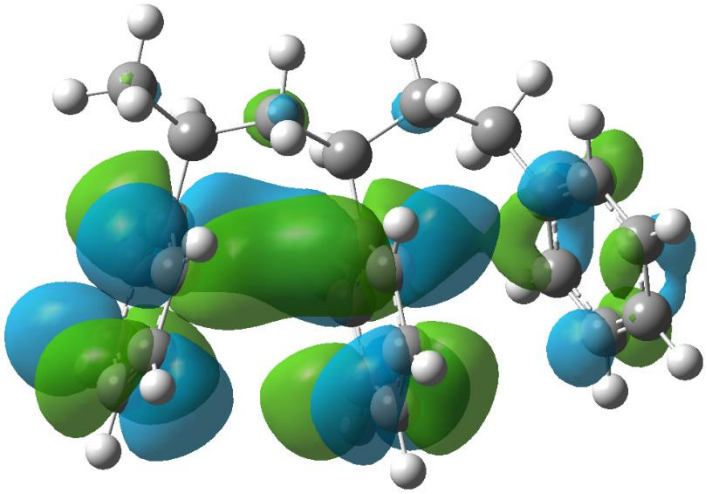

Fig S5.5. LUMO distribution map of the styrene molecule and polymer chain (n=3).

Fig S5.6. Mass spectra of PS-NP degradation intermediates.

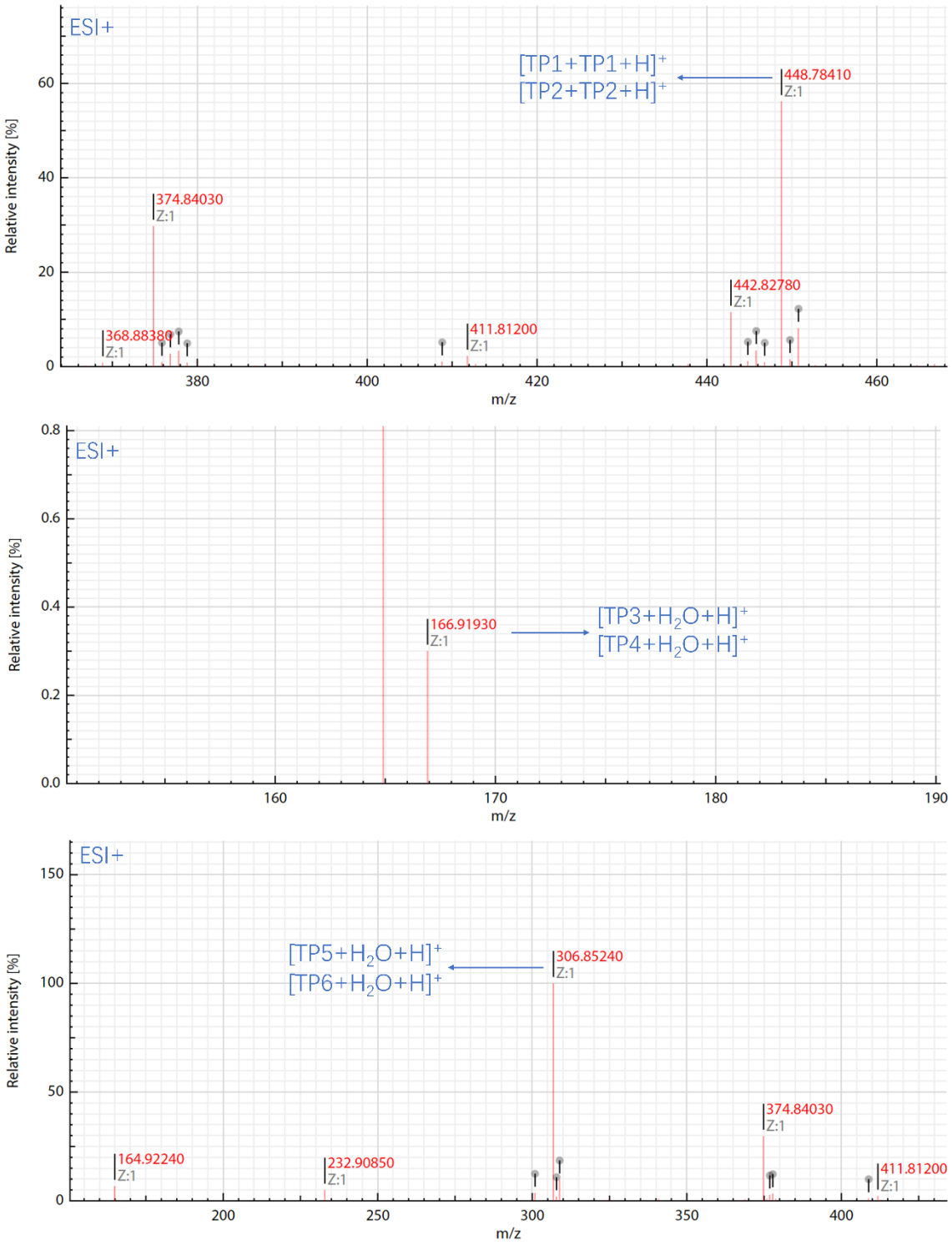

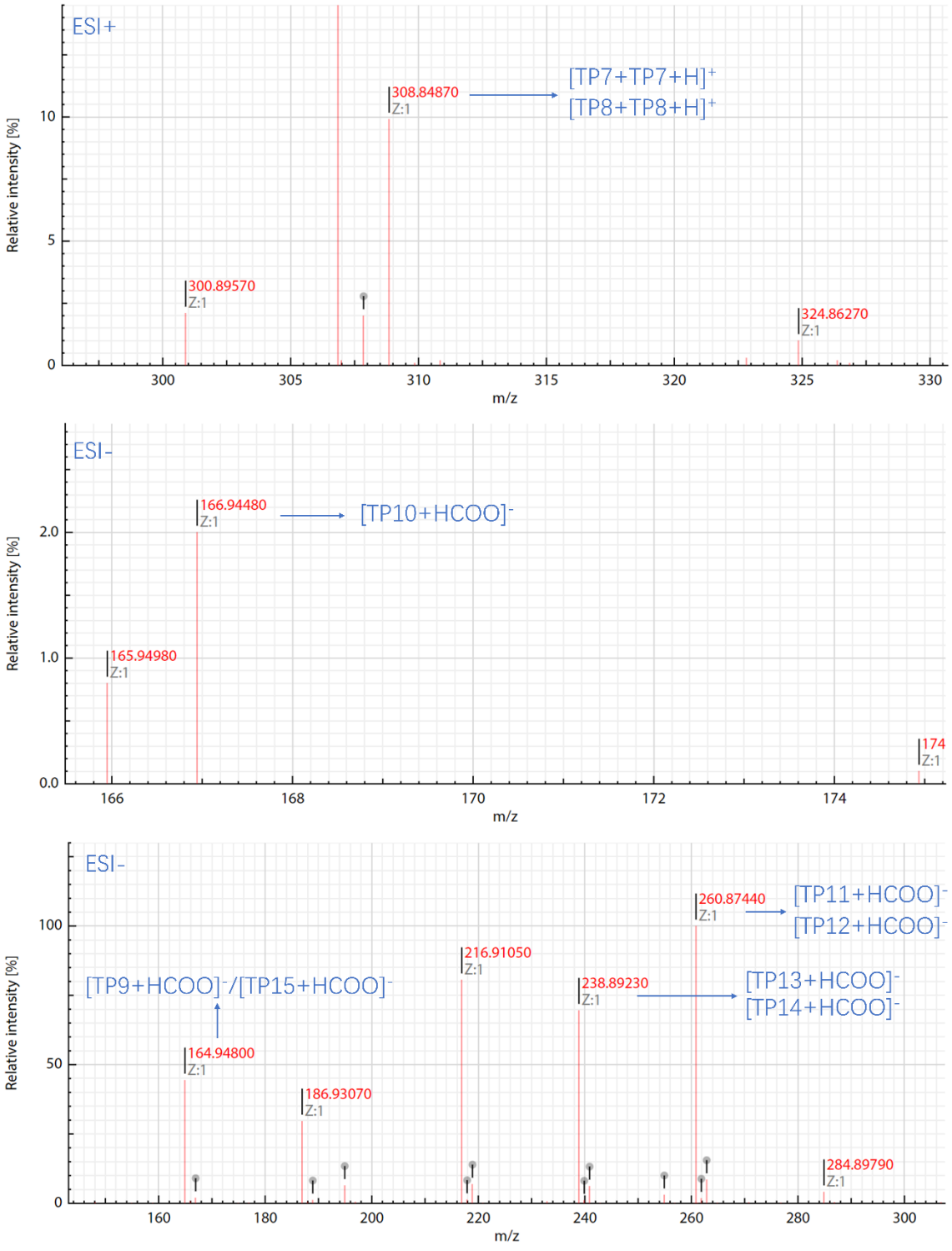
ESI+
308.84870
Z:1
[TP7+TP7+H]+
[TP8+TP8+H]+
300.89570
Z:1
324.86270
Z:1
Relative intensity [%]
m/z
ESI-
166.94480
Z:1
[TP10+HCOO]-
165.94980
Z:1
174
Z:1
ESI-
260.87440
Z:1
[TP11+HCOO]-
[TP12+HCOO]-
216.91050
Z:1
[TP9+HCOO]-/[TP15+HCOO]-
238.89230
Z:1
[TP13+HCOO]-
[TP14+HCOO]-
164.94800
Z:1
186.93070
Z:1
284.89790
Z:1

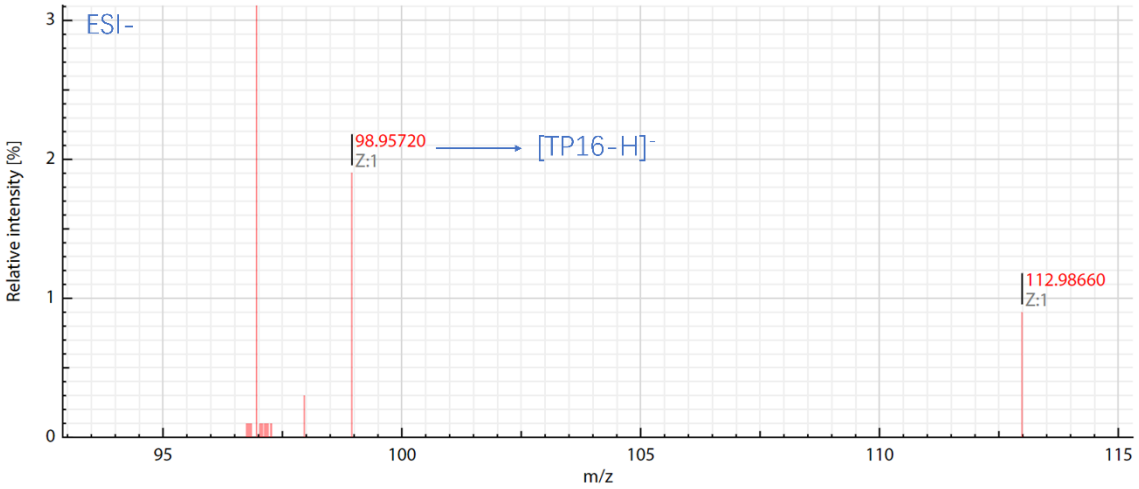
ESI-
98.95720
Z:1
[TP16-H]-
112.98660
Z:1
Relative intensity [%]
m/z
0
1
2
3
95
100
105
110
115

Table S5.1. Fukui index of atoms on polystyrene molecule.

Atom	Site	Charge (0) (e/Å)	Charge (-1) (e/Å)	Charge (+1) (e/Å)	f+	f-	f0
C	1	-0.39613	-0.3929	-0.40345	-0.00323	-0.00732	-0.00527
H	2	0.21063	0.19877	0.23606	0.01186	0.02543	0.018645
H	3	0.20033	0.19517	0.21152	0.00516	0.01119	0.008175
C	4	-0.35189	-0.35298	-0.34317	0.00109	0.00872	0.004905
H	5	0.19241	0.18875	0.20187	0.00366	0.00946	0.00656
H	6	0.19873	0.18902	0.21572	0.00971	0.01699	0.01335
C	7	-0.21863	-0.21419	-0.22922	-0.00444	-0.01059	-0.00752
H	8	0.19866	0.18954	0.21554	0.00912	0.01688	0.013
C	9	-0.36399	-0.36559	-0.35321	0.0016	0.01078	0.00619
H	10	0.19807	0.18483	0.21509	0.01324	0.01702	0.01513
H	11	0.194	0.19092	0.20258	0.00308	0.00858	0.00583
C	12	-0.20928	-0.20426	-0.21558	-0.00502	-0.0063	-0.00566
H	13	0.19769	0.18797	0.20938	0.00972	0.01169	0.010705
C	14	-0.55567	-0.55654	-0.55024	0.00087	0.00543	0.00315
H	15	0.19664	0.18855	0.20531	0.00809	0.00867	0.00838
H	16	0.19785	0.19212	0.20621	0.00573	0.00836	0.007045
H	17	0.19183	0.18817	0.19754	0.00366	0.00571	0.004685
C	18	-0.01161	-0.00839	0.03419	-0.00322	0.0458	0.02129
C	19	-0.20481	-0.20261	-0.19416	-0.0022	0.01065	0.004225
C	20	-0.21797	-0.2482	-0.18511	0.03023	0.03286	0.031545
C	21	-0.19699	-0.22467	-0.18711	0.02768	0.00988	0.01878
H	22	0.20716	0.20265	0.21903	0.00451	0.01187	0.00819
C	23	-0.20349	-0.21648	-0.19092	0.01299	0.01257	0.01278
H	24	0.20347	0.19755	0.21659	0.00592	0.01312	0.00952
C	25	-0.22157	-0.2321	-0.14167	0.01053	0.0799	0.045215
H	26	0.20425	0.19677	0.21793	0.00748	0.01368	0.01058
H	27	0.20457	0.19836	0.21755	0.00621	0.01298	0.009595
H	28	0.20464	0.19845	0.21601	0.00619	0.01137	0.00878
C	29	-0.01661	-0.02297	0.0708	0.00636	0.08741	0.046885
C	30	-0.20399	-0.21949	-0.18012	0.0155	0.02387	0.019685
C	31	-0.20871	-0.31046	-0.17517	0.10175	0.03354	0.067645
C	32	-0.20031	-0.30777	-0.17419	0.10746	0.02612	0.06679
H	33	0.20462	0.18754	0.22522	0.01708	0.0206	0.01884
C	34	-0.19633	-0.23249	-0.18503	0.03616	0.0113	0.02373
H	35	0.20482	0.1877	0.22467	0.01712	0.01985	0.018485
C	36	-0.21534	-0.24247	-0.10619	0.02713	0.10915	0.06814
H	37	0.20384	0.18399	0.22319	0.01985	0.01935	0.0196
H	38	0.20326	0.18466	0.22294	0.0186	0.01968	0.01914
H	39	0.20364	0.18553	0.22057	0.01811	0.01693	0.01752

C	40	-0.01677	-0.03186	0.02559	0.01509	0.04236	0.028725
C	41	-0.21035	-0.23724	-0.19486	0.02689	0.01549	0.02119
C	42	-0.21053	-0.32528	-0.19333	0.11475	0.0172	0.065975
C	43	-0.20078	-0.3172	-0.18088	0.11642	0.0199	0.06816
H	44	0.20401	0.18608	0.21572	0.01793	0.01171	0.01482
C	45	-0.198	-0.23877	-0.19199	0.04077	0.00601	0.02339
H	46	0.20651	0.18864	0.21707	0.01787	0.01056	0.014215
C	47	-0.21805	-0.24596	-0.15588	0.02791	0.06217	0.04504
H	48	0.20545	0.18577	0.21621	0.01968	0.01076	0.01522
H	49	0.20517	0.18619	0.21631	0.01898	0.01114	0.01506
H	50	0.20556	0.18718	0.21506	0.01838	0.0095	0.01394

Table S5.2. Structural information of identified intermediate products from polystyrene.

Products	m/z	Chemical name	Molecular formula	Structural
TP1	224.12	1,3-diphenylbutan-1-one	$C_{16}H_{16}O$	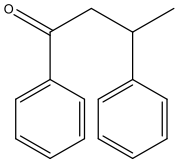
TP2	224.08	1,3-diphenylpropane-1,3-dione	$C_{15}H_{12}O_2$	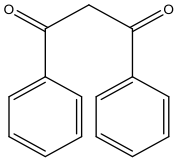
TP3	148.09	1-phenylbutan-1-one	$C_{10}H_{12}O$	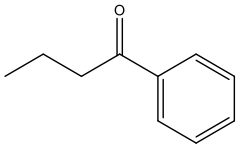
TP4	148.09	Isobutyrophenone	$C_{10}H_{12}O$	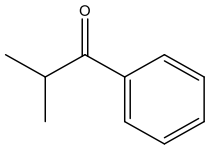
TP5	288.14	2,4-bis(3-hydroxyphenyl)pentane-1,5-diol	$C_{17}H_{20}O_4$	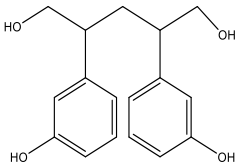
TP6	288.14	2-(2-hydroxyphenyl)-4-phenylpentane-1,3,5-triol	$C_{17}H_{20}O_4$	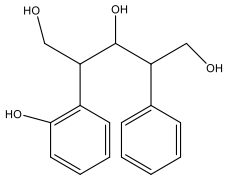
TP7	154.06	3-Hydroxyphenyl Ethylene Glycol	$C_8H_{10}O_3$	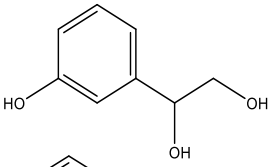
TP8	154.06	1-(2-hydroxyphenyl)ethane-1,2-diol	$C_8H_{10}O_3$	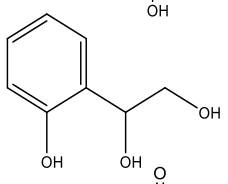
TP9	120.06	Acetophenone	C_8H_8O	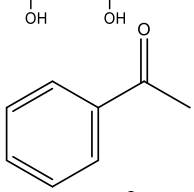
TP10	122.04	Benzoic acid	$C_7H_6O_2$	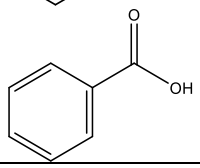

TP11	216.14	propane-1,1-diyl dibutyrate	$C_{11}H_{20}O_4$	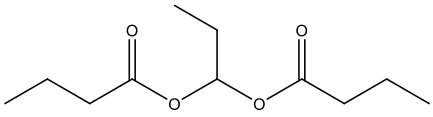
TP12	216.14	propane-1,2-diyl bis(2-methylpropanoate)	$C_{11}H_{20}O_4$	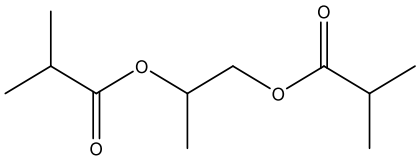
TP13	194.08	2,4,5,6-tetrahydroxy-3-methoxyhexanal	$C_7H_{14}O_6$	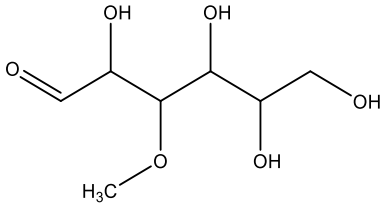
TP14	194.08	1,4,5,6-tetrahydroxy-3-methoxyhexan-2-one	$C_7H_{14}O_6$	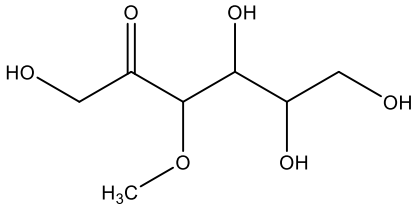
TP15	120.08	pentane-1,2,3-triol	$C_5H_{12}O_3$	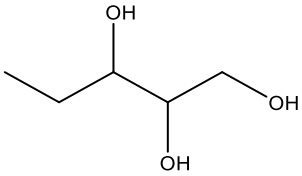
TP16	100.09	2-Butanone, 3,3-dimethyl-	$C_6H_{12}O$	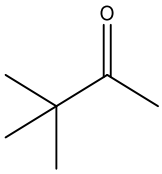

Table S5.3. Acute toxicity calculation of styrene and degradation products.

Products	Chemical name	Fathead minnow LC_{50} /mg L^{-1}	Tetrahymena pyriformis IGC_{50}/mg L^{-1}
	Styrene	6.09	64.96
TP1	1,3-diphenylbutan-1-one	1.43	7.91
TP2	1,3-diphenylpropane-1,3-dione	1.35	6.24
TP3	1-phenylbutan-1-one	7.79	43.18
TP4	Isobutyrophenone	8.26	50.97
TP5	2,4-bis(3-hydroxyphenyl)pentane-1,5-diol	2.98	29.78
TP6	2-(2-hydroxyphenyl)-4-phenylpentane-1,3,5-triol	7.89	89.55
TP7	3-Hydroxyphenyl Ethylene Glycol	473.01	703.43
TP8	1-(2-hydroxyphenyl)ethane-1,2-diol	303.81	747.74
TP9	Acetophenone	45.01	197.23
TP10	Benzoic acid	101.50	473.30
TP11	propane-1,1-diyl dibutyrate	5.05	59.90
TP12	propane-1,2-diyl bis(2-methylpropanoate)	10.15	85.29
TP13	2,4,5,6-tetrahydroxy-3-methoxyhexanal	7221.57	N/A
TP14	1,4,5,6-tetrahydroxy-3-methoxyhexan-2-one	17052.34	28899.81
TP15	pentane-1,2,3-triol	4247.71	9144.38
TP16	2-Butanone, 3,3-dimethyl-	361.86	1009.17